Faculty of Science and Engineering
Department of Chemical Engineering

Modelling and Simulation of Carbon-in-Leach Circuits

Divyamaan Wadnerkar

This thesis is presented for the Degree of
Doctor of Philosophy
of
Curtin University

April 2013

Declaration

To the best of my knowledge and belief this thesis contains no material previously published by any other person except where due acknowledgment has been made.

This thesis contains no material, which has been accepted for the award of any other degree or diploma in any university.

Signature : ………………………………………….

Date : ………………………...

Biography of the Author

Divyamaan Wadnerkar completed his Bachelor in Chemical Engineering from Malaviya National Institute of Technology Jaipur in 2008 . In 2008, he joined Department of Chemical Engineering, Curtin University, Western Australia as a research scholar. He has extensively worked in the area of multiphase flows, numerical modeling, chemical engineering design and process simulations for the past three years. His research interests lie in stirred tank reactors, multiphase flows, drag modeling, hydrodynamic simulations and dynamic process modeling. In the course of his PhD research, his work has been refereed at international journals and conferences which include:

Journal Publications:

a) Wadnerkar, D., Utikar, R. P., Tade, M. O., & Pareek, V. K. (2010). Prediction of Terminal Velocity of a Particle Falling in Non-Newtonian Fluids using the Macroscopic Particle Model. *Proceedings of ICMF*, 2010, Florida (USA).
b) Wadnerkar, D., Utikar, R. P., Tade, M. O., & Pareek, V. K. (2012). CFD Simulation of Solid–Liquid Stirred Tanks. *Advanced Powder Technology* (0). doi: 10.1016/j.apt.2012.03.007
c) Wadnerkar, D., Utikar, R. P., Tade, M. O., & Pareek, V. K. (2012). Macroscopic Particle Model: Application in Simulating Motion of Particles in Non-Newtonian Fluids. *To be submitted.*
d) Wadnerkar, D., Utikar, R. P., Tade, M. O., & Pareek, V. K. (2012). CFD simulation of high solid loading stirred tanks.. *To be submitted.*

Conferences and Workshops:

a) Wadnerkar, D., Utikar, R. P., Tade, M. O., & Pareek, V. K. (2012). Simulation and Analysis of Carbon-in-Leach (CIL) Circuits. *Presented at PSE,* 2012,Singapore.
b) Wadnerkar, D., Utikar, R. P., Tade, M. O., & Pareek, V. K. (2011). CFD Simulation of Solid–Liquid Stirred Tanks. *Presented at CHEMECA, 2011,* Sydney (Australia).

c) Wadnerkar, D., Utikar, R. P., Tade, M. O., & Pareek, V. K. (2010). Prediction of Terminal Velocity of a Particle Falling in Non-Newtonian Fluids using the Macroscopic Particle Model. *Presented at ICMF, 2010,* Florida (USA).

d) Wadnerkar, D., Utikar, R. P., Tade, M. O., & Pareek, V. K. (2012). Simulation of solid-liquid flow in stirred tanks at high solid loading. *Submitted at CFD 2012.*

Abstract

A CIL circuit is a process of continuous leaching of gold from ore to liquid using a counter-current adsorption of gold from liquid to carbon particles in a series of tanks. It concentrates gold from 2.5-3.5 g/t in ore to 10000 to 15000 g/t on carbon, thus playing an important role on the economics of a gold refinery.

In this study, a dynamic model of CIL circuits has been developed to study the transient nature of the system. The effect of various operating parameters on the performance of the system has also been assessed. For example, the particle size and cyanide concentration were predicted to play a critical role on the gold leaching. A decrease in the particle size increased the efficiency of the process, whereas an opposite effect was observed on increasing the cyanide concentration. The recovery also increased on increasing the carbon transfer interval. On the other hand, oxygen concentration did not show a significant effect on the efficiency.

The hydrodynamics of CIL tanks is also a complex phenomenon, and it affects both leaching and adsorption kinetics. Current models account for the effect of hydrodynamics in lumped manner. One needs to incorporate the hydrodynamic parameters explicitly in order to make the model applicable over a wider range of operating conditions. Therefore, rigorous CFD simulations of CIL tanks have also been carried out in this study. However, current multiphase CFD simulations require validation especially for interphase closures (such as drag). Therefore, simulations have been conducted using a number of drag models. The modified Brucato drag model was found to be the most appropriate for the CIL tanks, and hence was used in conducting the majority of the simulations in this study. Subsequently, the simulations were conducted to study the effect of various parameters, such as solid loading, and impeller speed and type, on the hydrodynamics of CIL tanks. At low solid loadings, the effect of it on the liquid hydrodynamics was minimal, however, at high solid concentrations, substantial impact on the hydrodynamics was predicted. For example, ‘false bottom effect’ was predicted at very high solid concentration indicates the presence of dead zones. Similarly, at higher solid loadings, higher slip velocities were observed below the impeller, near the wall and near the impeller rod. Finally, the higher solid loadings also caused the dampening of turbulence due to the presence of particles, thus resulting in significant power consumption to counteract this dampening.

Other than ore particles, CIL tanks also contain the larger carbon particles. The flow of carbon particles is affected by the flow of ore-liquid slurry. No model is currently available for calculating the drag force on the carbon particles. For obtaining the drag force, a novel macroscopic particle model (MPM) based on RDPM approach was used after validation. The predictions from the MPM model were compared with the available experimental data, and a new drag model has been proposed for the carbon particles in the CIL slurry.

The research develops a phenomenological model, validates the drag model for ore particles and proposes a drag model for carbon particles. These models along with the methodology presented in the thesis can be applied on the industrial scale CIL tanks for any ore type provided the rate terms and kinetic constants are known.

Acknowledgements

First and foremost, I would like to thank my supportive supervisor Prof. Vishnu Pareek for the freedom and faith he bestowed on me during my research. This made me an independent researcher. He not only provided in-depth advice in the discussions but he also made sincere efforts to provide all resources required including industrial meetings and visits. This provided me necessary exposure and the opportunity to explore the practical problems faced in the industry. He has motivated and encouraged during difficult times. It was a privilege and honour working with him. I would like especially to thank Dr. Ranjeet Utikar for providing invaluable new research ideas and healthy brainstorming during the research. I sincerely thank him for showing me the way and helping me reach this destination through motivation, encouragement and advice. I would also like to thank Prof. Moses Tade for his timely support and advice. I would also like to thank my thesis chairperson, Prof. Ming Ang for his valuable support and guidance.

I would like to thank Parker Centre for their financial and professional support. I am thankful to the Parker Centre Education Program Manager, Nadine Smith, for her encouragement and support for participation in conferences.

I also take this opportunity to thank my colleagues, Dr. Tejas Bhatelia, Dr. Ganesh K. Velluswamy and Dr. Milin Kumar Shah for their enormous support in learning the CFD tools and participating in research discussions. I would like to thank Emmanuel Obanijesu for moral support and ‘pushing’ that served to renew my spirit and refocus my attention and energy. I would like to express my gratitude to the department secretaries Stephenie Blakiston, Naomi Mockford, Jann Bolton and Tammy Atkins for always been supportive and helping whenever needed. I want to acknowledge my friends Harisinh and Abhishek for providing me a creative and pleasant working environment.

Above ground, I am indebted to my parents and brother who have provided me their unequivocal support and motivation throughout, as always, for which my mere expression of thanks likewise does not suffice. I would like to thank my wife Sneha for being my strength and enduring the frustration and loneliness during the final phase of my research.

Table of Contents

Abstract iii

Acknowledgements v

Table of Contents vi

List of Figures xi

List of Tables xvi

Nomenclature xvii

Chapter 1 Introduction 1

1.1 Phenomenological Modeling of CIL Circuit 3

1.2 Hydrodynamic Modeling of Stirred (CIL) Tanks 3

1.3 Objectives 5

1.4 Contributions of this thesis 6

1.5 Thesis Organization 6

Chapter 2 CIL Process 8

2.1 Leaching 8

2.1.1 Mechanism 8

2.1.2 Factors Affecting Leaching 11

2.1.3 Kinetics 14

2.2 Adsorption 19

2.2.1 Mechanism 19

2.2.2 Factors Affecting Adsorption 20

2.2.3 Kinetics 22

2.3 Preg-robbing 25

2.4 Carbon-in-Pulp and Carbon-in-Leach Tanks 26

2.5 Hydrodynamics of CIL Tanks 28

2.5.1 Regimes 36

2.5.2 Experiments and Correlations for Just Suspension Speed 39

2.5.3 Experimental Hydrodynamic Studies..42

2.5.4 Computational Hydrodynamic Studies 51

2.5.5 Solids Distribution and Homogenisation 55

2.5.6 Radial Concentration Profiles...60

2.5.7 Axial Concentration Profiles 65

2.5.8 Cloud Height..68

2.5.9 Flow Field..69

2.5.10 Slip Velocities...73

2.5.11 Drag Models 74

2.5.12 Scale-up 76

2.6 Drag for Carbon Particles 77

2.7 EL and LL Multiphase Simulation Approaches....................................78

2.8 Summary and Research Direction..80

Chapter 3 Phenomenological Modeling of CIL Circuit 81

3.1 Phenomenological Model 81

3.2 Model Development 82

3.3 Assumptions for CIL Model 83

3.4 Kinetics 83

3.4.1 Leaching 83

3.4.2 Adsorption 84

3.4.3 Cyanide Consumption...85

3.5 CIL Equations...85

3.6 Results and Discussion 87

3.6.1 Comparison with the Literature Data...87

3.6.2 Dynamic Simulation of CIL in Series 89
3.6.3 Effect of Process Parameters 90
3.6.4 Cyanide Concentration 91
3.6.5 Oxygen Concentration 93
3.6.6 Volume Fraction 93
3.6.7 Carbon Transfer Interval 94
3.6.8 Residence Time 96
3.7 Conclusion 97
Chapter 4 Hydrodynamic Simulation of CIL Tanks 98
4.1 CFD Model 99
4.1.1 Model Equations 99
4.1.2 Equations for Turbulence 100
4.1.3 Turbulent Dispersion Force 102
4.1.4 Basset Force, Virtual Mass Force and Lift Force 102
4.1.5 Interphase Drag Force 103
4.2 Methodology and Boundary Conditions 106
4.2.1 Vessel Geometry 106
4.2.2 Numerical Simulations 107
4.3 Results and Discussion 108
4.3.1 Preliminary Numerical Simulations 108
4.3.2 Flow Field 110
4.3.3 Analysis of Drag Models 112
4.3.4 Turbulent Kinetic Energy (TKE) 121
4.3.5 Slip Velocity 126
4.3.6 Cloud Height and Homogeneity 129
4.3.7 Power Number 131

4.4 Simulation of CIL Tank 132
  4.4.1 Flow Field and Velocity Components 133
  4.4.2 Slip Velocity 135
  4.4.3 Turbulence Kinetic Energy 136
4.5 Conclusion 138
Chapter 5 Macroscopic Particle Model and Drag Formulation for Carbon Particles 140
5.1 A brief review of particle motion in stagnant fluids 141
  5.1.1 Newtonian Fluids 141
  5.1.2 Non-Newtonian Fluids 143
5.2 Hydrodynamics Model 147
  5.2.1 Continuity Equations 147
  5.2.2 Fluid Rheology 148
  5.2.3 Macroscopic Particle Model 148
5.3 Methodology 151
5.4 Results and Discussions 152
  5.4.1 Effect of Simulation Parameters 152
  5.4.2 Comparison with Experimental Data 157
  5.4.3 Effect of Particle Diameter on Terminal Velocity in Newtonian Fluids 158
  5.4.4 Effect of Particle Diameter, Particle Density and Fluid Properties on Terminal Velocity in non-Newtonian Fluids 158
  5.4.5 Comparison of Fall Velocities for Newtonian and Non-Newtonian Fluids 160
  5.4.6 Comparison of Drag Coefficient for Newtonian and Non-Newtonian Fluids 161
5.5 Drag model 163

5.6 Conclusion....165
Chapter 6 Closure....166
6.1.1 Phenomenological Modelling of Carbon in Leach Circuit....166
6.1.2 Hydrodynamic Simulation of CIL Tanks....167
6.1.3 Macroscopic Particle Model and Drag Formulation for Carbon Particles....168
6.2 Recommendations for future work....169
Appendix I. MATLAB Code for Phenomenological Model....170
Appendix II. UDF for Modified Brucato Drag Model....176
References....178

List of Figures

Figure 1.1. CIL tanks in series in a gold extraction plant in Eritrea, Africa (Resources, 2010). 1

Figure 1.2. Flow of ore slurry and carbon particles across CIL in series. 2

Figure 1.3. Diagram illustrating macro-mixing and micro-mixing in stirred tanks. 4

Figure 1.4. Thesis Structure 7

Figure 2.1. Schematic representation of gold cyanidation (Habashi, 1966). 9

Figure 2.2. Gold surface illustrating various reaction paths. 17

Figure 2.3. Schematic diagram of equilibrium model (Nicol et al., 1984). 23

Figure 2.4. The studies conducted below 10% volumetric concentration. 29

Figure 2.5. The studies conducted above 10% volumetric concentration. 30

Figure 2.6. Regimes and states of suspension in a stirred vessel (Kraume, 1992).....38

Figure 2.7. Comparison of radial concentration between z/Z 0.0 to 0.1 (at low concentration). 61

Figure 2.8. Comparison of radial concentration between z/Z 0.0 to 0.1 (at high concentration). 61

Figure 2.9. Comparison of radial concentration between z/Z 0.1 to 0.2...................62

Figure 2.10. Comparison of radial concentration between z/Z 0.2 to 0.3 (at low concentration). 62

Figure 2.11. Comparison of radial concentration between z/Z 0.2 to 0.3 (at high concentration). 64

Figure 2.12. Comparison of radial concentration between z/Z 0.3 to 0.4.................64

Figure 2.13. Comparison of radial concentration at z/Z =0.65. 65

Figure 2.14. Comparison of axial concentration between r/R 0.0 to 0.3 (at high concentration). 66

Figure 2.15. Comparison of axial concentration between r/R 0.0 to 0.3 (at low concentration). 66

Figure 2.16. Comparison of axial concentration between r/R 0.3 to 0.6 (at low concentration). 67

Figure 2.17. Comparison of axial concentration between r/R 0.3 to 0.6 (at high concentration). 67

Figure 2.18. Comparison of axial concentration above r/R = 0.6. 67

Figure 2.19. Resolution of phases using (a) UDPM (b) RDPM and (c) L-L approach (Beetstra et al., 2006). 80

Figure 3.1. Schematic of CIL cascade. 82

Figure 3.2. Comparison of leaching rates. 84

Figure 3.3. Comparison with literature data..........88

Figure 3.4. Gold loading on carbon as a function of time for the six tanks of CIL circuit. 90

Figure 3.5. Effect of (a) cyanide concentration and (b) oxygen concentration on gold recovery..........92

Figure 3.6. Effect of ore volume fraction on gold recovery. 94

Figure 3.7. Effect of carbon transfer interval on gold recovery..........95

Figure 3.8. Effect of total residence time on gold recovery. 96

Figure 4.1. Solution domain for flow simulated through regularly arranged cylinders by Khopkar et al. (2006) for determination of drag..........105

Figure 4.2. Computational domain and grid distribution in stirred tank of with Rushton turbine..........108

Figure 4.3. Computational domain and grid distribution in stirred tank with PBTD. 109

Figure 4.4. Solid velocity vectors on the plane between the baffles for a solid volume fraction of 0.01 and 1000 RPM using RT. 111

Figure 4.5. Normalised velocity maps and velocity vectors at mid-baffle plane using PBTD for N = N_{js} of (a) single phase, (b) solid phase (20 wt%) and (c) solid phase (40 wt%). 112

Figure 4.6. Radial velocity at the impeller plane for 0.01 solid volume fraction and 1000 RPM using RT. 113

Figure 4.7. Radial velocity at axial plane r/R -0.5 for 0.01 solid volume fraction and 1000 RPM using RT. 114

Figure 4.8. Tangential velocity at axial plane r/R – 0.5 for 0.01 solid volume fraction and 1000 RPM using RT...114

Figure 4.9. Axial velocity at axial plane r/R – 0.5 for 0.01 solid volume fraction and 1000 RPM using RT. 115

Figure 4.10. The three velocity components of solids in a horizontal plane at z/H = 0.2 for 20 wt% and N=N_{js} using PBTD. 117

Figure 4.11. The three velocity components of solids in a horizontal plane at z/H = 0.2 for 40 wt% and N=Njs using PBTD. 117

Figure 4.12. Slip velocity on an impeller plane for a solid volume fraction of 0.01 and 1000 RPM using RT...120

Figure 4.13. Turbulent kinetic energy contours in stirred tanks at 1000 RPM using RT. 122

Figure 4.14. Turbulent kinetic energy profiles at impeller plane at 1000 RPM using RT. 123

Figure 4.15. Normalised turbulent kinetic energy contours at mid-baffle plane using PBTD for N = N_{js} of (a) single phase, (b) solid phase (20 wt%) and (c) solid phase (40 wt%)...125

Figure 4.16. Normalised slip velocity maps and velocity vectors at mid-baffle plane using PBTD for N = Njs of (a) 20 wt% solid and (b) 40 wt% solids. 128

Figure 4.17. The cloud height in stirred tanks using RT. (a) 0.01 volume fraction 1000 RPM (b) 0.07 volume fraction 600 RPM (c) 0.07 volume fraction 800 RPM (d) 0.07 volume fraction 1000 RPM. 130

Figure 4.18. Normalised velocity maps and velocity vectors at mid-baffle plane using PBTD for N = Njs of CIL tanks (50 wt %). 133

Figure 4.19. The three velocity components of solids in a horizontal plane at z/H = 0.2 for CIL tanks (50 wt%) and N=Njs..135

Figure 4.20. Normalised slip velocity maps and velocity vectors at mid-baffle plane for N = Njs of CIL tanks (50 wt %). 136

Figure 4.21. Normalised turbulent kinetic energy contours at mid-baffle plane for N = Njs of CIL tanks (50 wt %). 137

Figure 5.1. Schematic rheogram showing viscosities and shape factor areas. (Wilson et al., 2003) 146

Figure 5.2. Apparent viscosity as a function of shear rate using the Casson and Herschel- Bulkley models. 147

Figure 5.3. Flowchart showing calculation algorithm in MPM (Agrawal et al., 2009). 149

Figure 5.4. Fluid cells touched by particle and patching of particle velocity (Agrawal et al., 2004). 150

Figure 5.5. (a) Initial position of the particle. (b) Contours of fluid velocity around the particle. 153

Figure 5.6. Particle velocity as a function of time ($\rho_p = 8876$ kg/m^3, $\rho_f = 999$ kg/m^3, $\mu = 0.905$ Pa.s, $d_p = 0.00635$ m). 154

Figure 5.7. Effect of time-step size on simulation predictions ($\rho_p = 1550$ kg/m^3, $\rho_f = 999$ kg/m^3, $\mu = 1$ Pa.s, $d_p = 0.01$ m). 154

Figure 5.8. Effect of mesh size on simulation predictions ($\rho_p = 1550$ kg/m^3, $\rho_f = 999$ kg/m^3, $\mu = 1$ Pa.s, $d_p = 0.01$ m). 155

Figure 5.9. Effect of domain extent on the particle velocity prediction for Newtonian Fluids ($\rho_p = 7638$ kg/m^3, $\rho_f = 999$ kg/m^3, $\mu = 0.736$ Pa.s, $d_p = 0.00794$ m). 155

Figure 5.10. Effect of domain extent on the particle velocity prediction for Non-Newtonian Fluids ($\rho_p = 7638$ kg/m^3, $\rho_f = 999$ kg/m^3, $d_p = 0.00794$ m). 156

Figure 5.11. The Validation of terminal velocity predictions for Non-Newtonian Fluids by MPM model with the experimental values provided by Wilson et. al. (2003). 157

Figure 5.12. Variation in terminal velocity predictions with particle diameter for Newtonian fluids ($\rho_p = 1500$ kg/m^3, $\rho_f = 999$ kg/m^3, $\mu = 1$ Pa.s). 158

Figure 5.13. The Comparison of velocity predictions for the non-Newtonian fluids and their variation with particle diameter. (ρ_f = 999 kg/m3)....................................159

Figure 5.14. The Comparison of velocity predictions for the non-Newtonian fluids and their variation with fluid properties. (d_p = 0.00794 m, ρ_f = 999 kg/m3, µ = 0.736 Pa.s)..160

Figure 5.15. Sphere free fall velocity in non-Newtonian and Newtonian fluid with corresponding equivalent viscosity (2.093 Pa. s). 161

Figure 5.16. Drag coefficient as a function of particle Reynolds number. 162

List of Tables

Table 2.1 Availability of cyanide in compounds and their respective solubility in water (Marsden and House, 2006)..10

Table 2.2. Summary of Hydrodynamic studies at high solids concentration.............31

Table 2.3. Summary of advantages and limitations of experimental techniques used in the study of solid-liquid stirred tanks (Chaouki et al., 1997, Roy et al., 2002, Stevenson et al., 2010). 46

Table 3.1. Operating parameters for the simulation of CIL process 87

Table 3.2. Values of flow rate and carbon transfer cycle studied. 94

Table 4.1. Dimensions of domain and properties of materials used in this study. ...107

Table 4.2. Details of cases simulated...110

Table 5.1. Details of cases simulated using MPM model. 151

Table 5.2. Results from the cases simulated using MPM model............................162

Nomenclature

A_{Au}	Surface area of exposed gold, m^2
A_c	surface area per unit mass of carbon, m^2
Bi_{HB}	Bingham number for Herschley-Bulkley fluid
B_l	Blade length, m
B_w	Blade width, m
C	Impeller Clearance, m
C_x	Concentration in volume percent or weight percent
C_D	drag coefficient
C_{Do}	particle drag coefficient in still fluid
C_{CN} or $[CN]^-$	Cyanide Concentration, mg / l
C_{O2} or $[O_2]$	Oxygen Concentration, mg / l
C_{Au}	Gold Concentration in liquid, g / m^3
C^*_{Au}	Residual gold concentration, g / m^3
C_e	Equilibrium gold concentration in solution. g / kg
C_H	Cloud Height, m
D_{CN}	diffusivity of cyanide, m^2 / s
D_{O2}	diffusivity of oxygen, m^2 / s
D or D_i	impeller diameter, m
d_P	particle diameter, m
F	Faraday’s constant, C/mol
$\vec{F}_{td}$	force due to turbulent dissipation, kg m /s^2
$\vec{F}_q$	external force, kg m /s^2
$\vec{F}_{lift}$	lift force, kg m /s^2

$\vec{F}_{vm}$	virtual mass force, kg m /s^2
$\vec{F}_{12}$	interphase interaction force, kg m /s^2
g	acceleration due to gravity, m / s^2
G_k	production of turbulence kinetic energy, kg m^2 / s^2
H	tank height, m
$\bar{\bar{I}}$	unit stress tensor.
k	turbulence kinetic energy per unit mass, m^2 / s^2
k_f	film mass transfer coefficient
M	torque, N m
n	Number of moles
N	impeller speed, RPM
N_{js}	speed of just suspension, RPM
N_{Re}	Reynolds number
N_P	Power number
N_Q	Pumping number
p	pressure and is shared by both the phases, Pa
P	power delivered to the fluid, W
q	gold loading on carbon, g / kg
q^+	maximum gold loading on carbon, g kg
Q_{fs}	downflow stream, m^3 / s
Q_f	slurry feed stream, m^3 / s
Q_s	flow rate of slurry with carbon transfer, m^3 / s
R	Particle radius, m
Re_p	particle Reynolds number
Re_{PL}	Reynolds number for power law fluids
T	tank diameter, m

$\vec{u}$	velocity vector, m / s
$\vec{u}_{dr}$	drift velocity, m / s
V_{tip}	Impeller tip velocity, m / s
W	Baffle width, m
X	reaction conversion

Greek Letters

α	volume fraction
γ	shear rate, 1 / s
ε	turbulence dissipation rate, m^2 / s^3
ε_b	bulk turbulence dissipation rate, m^2 / s^3
ε_l	volume fraction of liquid
ε_c	volume fraction of carbon
ε_o	volume fraction of ore
λ	Kolmogorov length scale, m
χ	Ratio of stoichiometric constants of CN^- to oxygen
μ	shear viscosity, Pa s
μ_t	turbulent viscosity, m^2 / s
ρ	density kg / m^3
σ	Prandtl numbers
σ_{sl}	dispersion Prandtl number
τ	shear stress, Pa
$\bar{\bar{\tau}}$	stress tensor because of viscosity and velocity fluctuations
θ_m	mixing time, s
υ	bulk viscosity

Subscripts

l	continuous phase
m	mixture properties
q	1 or 2 for primary or secondary phase respectively
s	dispersed phase

Abbreviations

ASM	Algebraic Slip Model
CFD	Computational Fluid Dynamics
CARPT	Computer Automated Radioactive Particle Tracking
CIL	Carbon-in-Leach
CIP	Carbon-in-Pulp
DPM	Discrete Particle Model
EL	Eulerian-Langrangian
HSDM	Homogeneous Surface Diffusion Model
LES	Large Eddy Simulation
LL	Langrangian-Langrangian
MPM	Macroscopic Particle Model
PBTD	Pitched Blade Turbine (pumping Downwards)
PIV	Particle Image Velocimetry
PEPT	Positron Emission Particle Tracking
RDPM	Resolved Discrete Particle Model
UDF	User Defined Function
UDPM	Unresolved Discrete Particle Model
RANS	Reynolds Averaged Navier Stokes
RT	Rushton Turbine

RSM	Reynolds Stress Model
TKE	Turbulent Kinetic Energy

Chapter 1 Introduction

The Carbon-in-Leach (CIL) process concentrates gold from 2.5-3.5 g/t in ore to 10000 to 15000 g/t on carbon. Although the cyanide process was first used in South Africa in 1890, CIL was introduced in industries in 1949 at San Andreas (Honduras). Due to their inherent economical and metallurgical advantages, currently CIL circuits have been widely adopted in the Gold extraction industry (Marsden and House, 2006). A typical CIL circuit is shown in Figure 1.1.

Figure 1.1. CIL tanks in series in a gold extraction plant in Eritrea, Africa (Resources, 2010).

A CIL circuit is a process of continuous leaching of gold from ore to liquid and counter-current adsorption of gold from liquid to carbon particles in a series of tanks (see Figure 1.2). It also involves leaching and adsorption of competing species, influence of cyanicides, oxidizing agents and passivating agents and attrition of carbon. Moreover, mixing is important for uniform distribution of solids in the tanks and to avoid bypassing, short-circuiting and creation of dead-zones in the tanks. For such a complex process, formulation of a phenomenological model is difficult but indispensable for understanding the dynamics of the process.

Present models are based on empirical plant data, which are difficult to measure or interpret. While these models work for a specified plant, they cannot be generalized and used across the industry (Coetzee and Lalloo, 2005, Lima and Hodouin, 2005). Most of the kinetic models are not useful for performance evaluation, as the effect of many critical parameters is lumped in one variable. In this study, a phenomenological model has been developed. It includes rate kinetics with parameters that are easily measurable, and is suitable for performance evaluation.

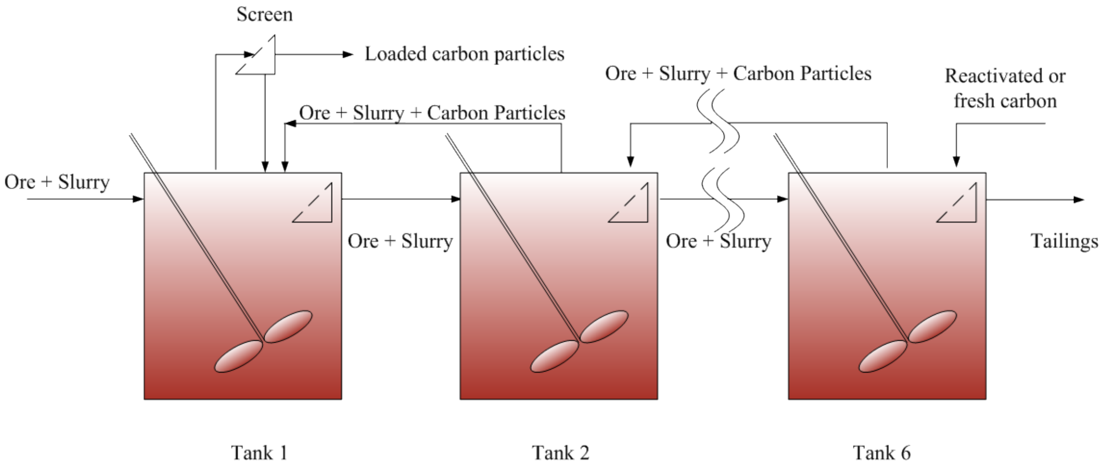

Figure 1.2. Flow of ore slurry and carbon particles across CIL in series.

Since CIL tanks typically have high solid loadings, their hydrodynamics also plays a critical role in governing their efficiency. Computational Fluid Dynamics (CFD) simulations have been extensively used for hydrodynamic study of multiphase systems (Micale et al., 2000, Micale et al., 2004, Ochieng and Lewis, 2006, Fradette et al., 2007, Kasat et al., 2008). However, conducting CFD simulation of CIL tanks is a challenging task, particularly the modelling the drag in the presence of turbulence.

In this research, both phenomenological and CFD models have been developed for CIL circuit. The phenomenological model has captured the dynamic nature of the process. For CFD modelling, the drag models suitable for the hydrodynamics of the CIL tanks were investigated. Afterwards, the CFD model was applied for studying the effect of solid loading on the hydrodynamics of CIL tanks.

1.1 Phenomenological Modeling of CIL Circuit

The quality of gold ores have deteriorated from around 12 grams per tonne in 1950 to current average value of only 3 grams per tonne in the many parts of the US, Canada, and Australia (Evans-Pritchard, 2009). Therefore, an in-depth understanding of the process is necessary to fine-tune the process parameters for improving the overall efficiency of the process. Hence, comprehensive phenomenological models encompassing detailed kinetics of the process are essential.

In the past, several models have been proposed for determining the effect of leaching, adsorption and preg-robbing rates (Walt and Deventer, 1992), studying different carbon transfer sequence strategies (Lima, 2007), designing the CIL process (Kiranoudis et al., 1998) and optimising reactor volumes, reactor network and plant configurations (Stange, 1991, Lima and Hodouin, 2005, Lima, 2006). However, currently there is no model for successfully simulating the complete non-linear behaviour of the CIL process. Reuter et al. (1991) used a knowledge based system, and van Deventer et al. (2004) used semi-empirical regression network kinetic model to simulate the process. But this restricted the use of these models only in the domain of the data collected. Fouling of the adsorbent, preg-robbing, hydrodynamics and competitive adsorption are the prime factors for the mismatch between the laboratory and plant data (Walt and Deventer, 1992, Rees and Deventer, 2001), and these must be taken into account in any realistic model of the process. Numerous kinetic models for leaching and adsorption have explicitly taken into account the process parameters affecting the process such as cyanide concentration, oxygen concentration, etc. (Lima and Hodouin, 2005). The phenomenological model developed in this study has incorporated the kinetics of leaching and adsorption. The model was validated, and then used for analysis of critical process parameters.

1.2 Hydrodynamic Modeling of Stirred (CIL) Tanks

The CIL tanks are multiphase poly-dispersed stirred systems with very high concentration of small ore particles (approximately 40-50% by weight and 50-150 μm in diameter) and very low concentration of large carbon particles (approximately

1.5 - 2.5 mm) (Deventer et al., 2004, Lima and Hodouin, 2005). This leads to several undesirable effects such as settling of solids, bypassing of inlet stream, and creation of dead-volumes in the tank, all of which then affect the leaching and adsorption kinetics. These factors can be incorporated as lumped parameters in a phenomenological model to make it more applicable over a wide range of operating conditions. This requires a hydrodynamic modelling of CIL tanks, which is a difficult task because of the presence of rotating internals, high concentration of solid particles (ore and carbon), presence of turbulence in the domain and absence of models representing the physics of the system.

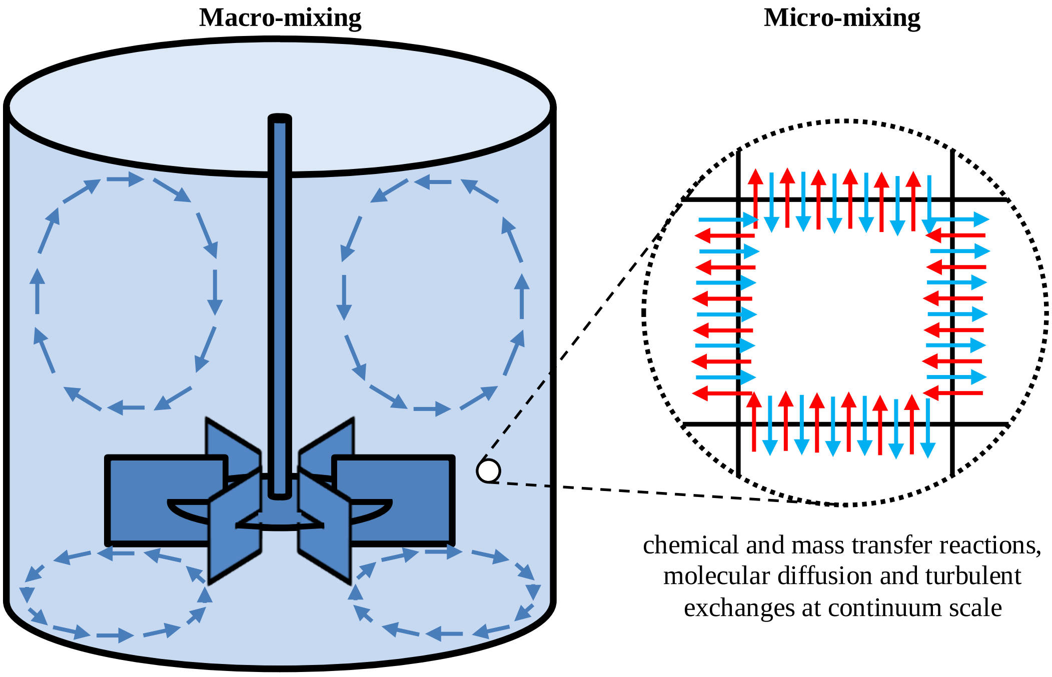

Figure 1.3. Diagram illustrating macro-mixing and micro-mixing in stirred tanks.

In a process involving stirred tanks, the mixing occurs at two levels namely macro-level and micro level as shown in Figure 1.3. At the micro level, micro-mixing governs the chemical and mass transfer reactions and occurs due to the molecular diffusion and turbulent exchanges. Micro-mixing is facilitated by mixing at the macro level that typically takes place through convection (Kasat et al., 2008). CFD can provide significant insight into these mixing processes. However, solids suspension and distribution in CIL tanks is also highly dependent on the turbulence and interphase drag in the tank. At low impeller speeds, the turbulent fluctuations are less and hence do not affect the predictions much. However, at higher impeller speeds, the drag and turbulence become increasingly important. While many drag models are available, there is no consensus on the appropriate drag model for liquid-solid stirred tanks (Ochieng and Onyango, 2008). In this thesis, different drag models have been assessed for a range of concentrations in CIL tanks. The validated drag model was then used for conducting hydrodynamic simulation of CIL tanks, using which flow field, slip velocity, turbulent kinetic energy, cloud height and power number were examined.

The challenges in conducting CFD simulations of CIL tank are due to the poly-dispersed nature of the drag formulation. Firstly, the drag formulation used for ore particles cannot be applied to carbon particles due to the size difference of several orders of magnitudes in the diameter. Secondly, the concentration of carbon particles in the ore slurry is very low as compared to the number of ore particles in the slurry. Therefore, not only the effect of liquid, but also the effect of the high concentration of ore particles on carbon particles should be incorporated. Therefore, a different modelling technique is required to capture the effect of carbon particles, for which, we have used the so-called, macroscopic particle model (MPM), which is a novel technique for simulating larger particles having diameters of the order of a few millimetres. The model findings were validated and a drag model for simulating the behaviour of carbon particles in ore slurry was developed.

1.3 Objectives

The over aim of this project was to study the hydrodynamics of a CIL circuit with specific objectives to:

a) develop a full mechanistic phenomenological model of Carbon-in-Leach circuit;

b) conduct a parametric study on the developed model and assess the effect of ore particle diameter, cyanide concentration and oxygen concentration on the efficiency of the process;

c) evaluate and validate multiphase drag models by comparing the predictions of different drag models with experimental data;

d) study the interdependence of drag and turbulence models on the hydrodynamics of CIL tanks, and;

e) investigate the MPM model for simulating hydrodynamics of CIL tanks and develop a drag model for simulating the large carbon particles of CIL tanks.

1.4 Contributions of this thesis

To achieve the above objectives, a range of modelling, simulation and analysis methods were employed, and major contributions of this thesis may be summarized as below:

a) A phenomenological model was developed for simulating the complete CIL circuit. The model can be used for optimizing industrial-scale CIL circuits as function of cyanide and oxygen concentrations, and ore particle diameter.

b) In Eulerian-Eulerian simulations, different drag models were investigated and their effect on the flow field in stirred tanks was assessed.

c) Simulations at both low and high solid concentration were carried out and their impact on the flow field and concentration were analyzed.

d) The novel MPM model has been used for simulating the hydrodynamics of carbon particles in CIL tanks. This, for the first time, has provided a greater insight into the drag experienced by carbon particles in the presence of ore and liquid.

1.5 Thesis Organization

As shown in Figure 1.4, the thesis has been organised in six different chapters each covering different but interlinked aspects of the research carried out in this study. In chapter 2, a critical literature review of various aspects of CIL circuits, such as the mechanisms and kinetics of leaching and adsorption, as well as hydrodynamics has been presented.

Using the most appropriate kinetics from chapter 2, a phenomenological has been presented in Chapter 3. Chapter 4 discusses hydrodynamics of CIL tanks using detailed CFD simulations. The hydrodynamics of carbon particles in the CIL tank using the MPM model has been presented in Chapter 5. Finally, in Chapter 6, a summary of the key findings of this research along with recommendations for future research has been presented.

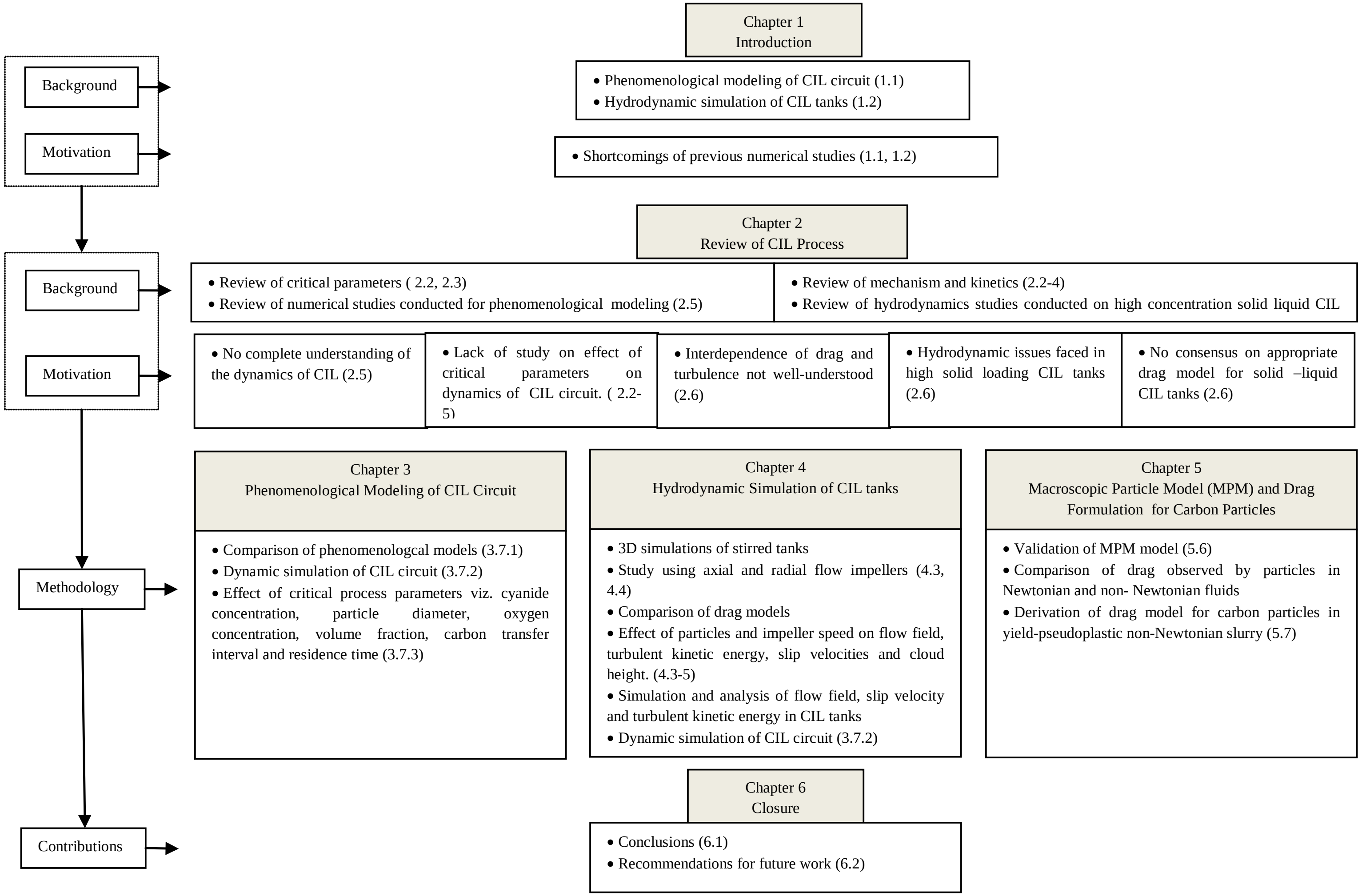

Figure 1.4. Thesis Structure

Chapter 2 CIL Process

Because of its importance in the gold extraction process, the CIL circuits have received significant attention of both academia and industry. Both cyanidation mechanism and factors affecting it, as well as adsorption mechanism has been examined. There have been studies on the leaching and adsorption processes for which phenomenological models using the kinetic equations have also been developed. However, there is currently no study on the modelling of CIL circuits based on critical parameters using first principles. Moreover, hydrodynamics of CIL tanks at high solid loading has been largely ignored. In this chapter the current state-of-art of CIL modelling and analysis has been presented.

2.1 Leaching

In the context of CIL circuit, leaching is the dissolution of gold from the ore into cyanide solution. In this section, review of leaching mechanisms, factors affecting leaching and its kinetics have been discussed.

2.1.1 Mechanism

The mechanism of gold dissolution in cyanide was first studied by Elsner (1946) and the reaction is given as (Marsden and House, 2006):

$$4\mathrm{Au} + 8\mathrm{CN}^- + \mathrm{O}_2 + 2\mathrm{H}_2\mathrm{O} \rightarrow 4\mathrm{Au(CN)}_2^- + 4\mathrm{OH}^- \qquad \text{……....(2.1)}$$

Later on, the reactions were further analysed, and in-depth studies were conducted to develop detailed mechanisms of the reactions (Habashi, 1966, Finkelstein, 1972, Zurilla et al., 1978, Nicol, 1980) of both anodic and cathodic reactions. In anodic reactions, gold oxidises and dissolves to form Au(I) complex $Au(CN)_2^-$, but Au(III) complex is also formed. However, further studies using electrochemical means have indicated that Au(I) is more stable than the Au(III) complex by 0.5V (Nicol, 1980). The schematic of this mechanism is shown in Figure 2.1, and the reactions may be expressed as:

$$Au + 2CN^- \Leftrightarrow Au(CN)_2^- + e^- \qquad \text{………(2.2)}$$
$$E = -0.60 + 0.118\text{pCN} + 0.059\log a_{Au(CN)_2^-} \ (V)$$

At cathode, oxygen reduces and forms hydrogen peroxide in solution.

$$O_2 + 2H^+O + 2e^- \Leftrightarrow H_2O_2 \qquad \text{………(2.3)}$$
$$E = 0.69 - 0.059pH - 0.0295pO_2 \qquad (V)$$

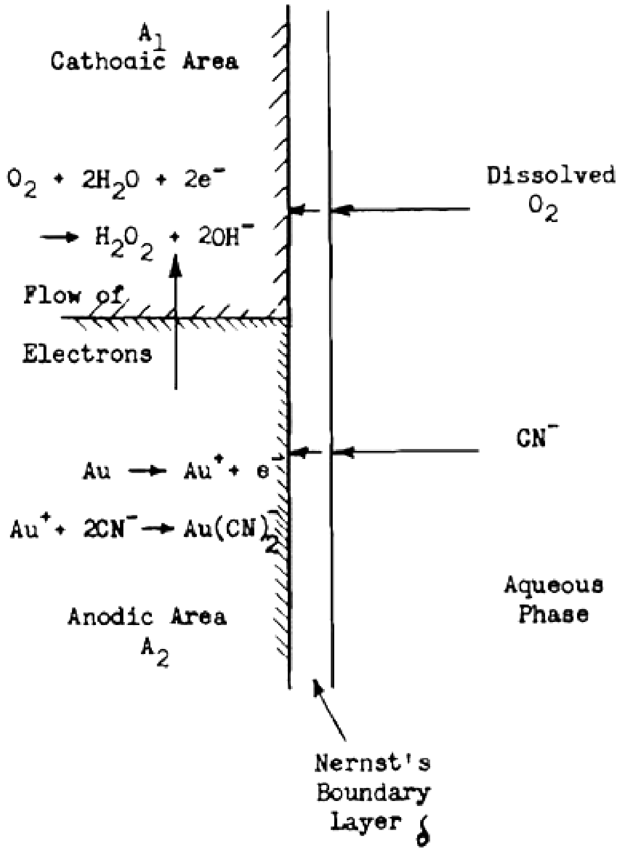

Figure 2.1. Schematic representation of gold cyanidation (Habashi, 1966).

Side reactions:

$$H_2O_2 + 2e^- \Leftrightarrow 2OH^- \qquad E^o = 0.88V \qquad \text{………(2.4)}$$

$$2H_2O_2 \Leftrightarrow O_2 + 2H_2O \qquad \text{………(2.5)}$$

$$O_2 + 2H_2O + 4e^- \Leftrightarrow 4OH^- \quad E^o = 0.401V \qquad \text{………(2.6)}$$

The intermediate gold species formed in the cyanidation reaction were investigated by Senanayake (2005). The author compared the stability constants of various anticipated intermediate species, and concluded that $Au(OH)(CN)^-$ was a more plausible intermediate.

The cyanidation of gold can be achieved by using sodium cyanide, potassium cyanide or calcium cyanide. Table 2.1 shows the solubility of these compounds in water and the amount of cyanide available in the compounds as a mass percent.

Table 2.1 Availability of cyanide in compounds and their respective solubility in water (Marsden and House, 2006)

Compound	Availability Cyanide %	Solubility in water at 25°C (g/100cc)	Comments
NaCN	53.1	48	NaCN and KCN are more readily soluble than $Ca(CN)_2$.
KCN	40.0	50	
$Ca(CN)_2$	56.5	Decomposes	

Dissolution of cyanide in the solution:

$$CN^- + H_2O \Leftrightarrow \underset{(weak\ acid)}{HCN} + OH^- \qquad \text{………(2.7)}$$

HCN has a relatively high vapour pressure (100 kPa at 26°C), and therefore, it volatilizes readily at the liquid surface under ambient conditions, causing a loss of cyanide from the solution. Therefore, most cyanide leaching systems are operated at a pH>10 which minimizes cyanide loss. Although adverse effects, such as decrease in reaction rates due to increase in the rate of interfering reactions, may be caused by excessively high pH.

$$HCN \Leftrightarrow H^+ + CN^- \qquad \text{………(2.8)}$$

$$\mathrm{K_a}(25^{\mathrm{o}}\mathrm{C}) = 6.2\times10^{-10} \quad ; \quad pKa = 9.31$$

Moreover,

Undesirable reactions $\left\{ \begin{array}{r} 4HCN + 3O_2 \Leftrightarrow 4CNO^- + 2H_2O \\ 3CN^- + 2O_2 + H_2O \Leftrightarrow 3CNO^- + 2OH^- \end{array} \right.$ ………(2.9)

These reactions reduce the free cyanide concentration and the cyanate species formed does not dissolve gold.

With respect to the choice of an oxidation agent, oxygen is preferred over hydrogen peroxide because of the following reasons:

a) H_2O_2 is very sensitive to the pH fluctuations during cyanidation and at certain conditions may act as cyanicide (Guzman et al., 1999).
b) Reduction of H_2O_2 on gold surfaces has been shown to be kinetically hindered.
c) The dissolution rate of gold in oxygen-free solutions containing H_2O_2 is very slow.
d) 85 % of H_2O_2 formed by O_2 reduction diffuses away from the reaction site, with only a small proportion reduced to OH^-.

2.1.2 Factors Affecting Leaching

The diffusion rates of cyanide and oxygen decide the limiting rate. Whichever species has the slower diffusion rate will provide the rate limiting factor (Kondos et al., 1995, Marsden and House, 2006).

$$0.5D_{CN^-}.[CN^-]/\delta_{[6]} = (2D_{O_2}.[O_2])/\delta_{[6]} \qquad \text{……..(2.10)}$$

$$\Rightarrow \quad D_{CN^-}.[CN^-] = 4DO_2.[O_2]$$

For $\mathrm{D_{CN^-}} = 1.83\times10^{-9}$, $\mathrm{D_{O_2}} = 2.76\times10^{-9}$

Therefore, $\dfrac{[CN^-]}{[O_2]} = 6$

In aerated alkaline cyanide solution, the dissolution rate is normally mass transport controlled with E^o =8-20 kJ/mol and depends upon the diffusion rate of CN^-, O_2 or both, to the gold surface (Marsden and House, 2006).

Cyanide concentration is easier to control than the oxidant concentration because of the low solubility of O_2 in water under atmospheric conditions. Under such conditions, dissolved oxygen is 8.2 mg/L and $[CN^-]$ for maximum gold dissolution is 0.005% or 0.002M CN^-. However, higher cyanide levels may be required because of the competition with other species for cyanide. Cyanide concentrations are usually maintained above those at which a decrease in extraction is observed. At low concentrations, cyanide is rate limiting but rate approaches a plateau value at high cyanide concentrations (Wadsworth, 2000). Increase in dissolved oxygen concentration implies increase in the rate of dissolution. The cost of increasing dissolved oxygen concentration must always be weighed against the cost of providing extra leaching time.

Temperature rise results in the increase of cyanidation (Guzman et al., 1999). The gold dissolution rate increases with temperature up to 85^{o}C. Temperature increase from 25^{o}C to 85^{o}C increases the dissolution rate by 20-25%. The cost associated with temperature increase can be somehow justified for high grade materials but not for low grade (Marsden and House, 2006).

Gold dissolution is maximised at pH values between approximately 9 and 9.5. Excessive loss of cyanide by hydrolysis is prevented by maintaining pH above 9.4. The practical importance of keeping pH below 9.5 is too little. It can be used to either reduce cyanide concentration in leach systems or to reduce the rate and extent of other undesirable reactions, e.g., dissolution of antimony and arsenic minerals. (Deschenes and Wallingford, 1995, Marsden and House, 2006). On the other hand, Guzman et al. (1999a) found a slight increase in the cyanidation as pH rises from 10 to 12 but afterwards observed a sudden decline in the cyanidation. Between 0.012 M and 0.0125 M, the cyanidation rates rose abruptly after which it attained a stable value. The acute effect due to change in pH and cyanide concentration was related to the transition from diffusion controlled process to chemical reaction controlled process. Therefore, the optimum pH for leaching depends on a number of related factors and must be derived independently for each ore type and leaching system.

Dissolution rate is directly related to the exposed surface area of gold. It is further related to the particle size distribution and liberation characteristics. In other words, the efficiency of the comminution process preceding leaching is the factor on which the exposed surface area of gold depends. Though it is a generalisation that the rate is going to increase with the decrease in the particle size, it is also observed that the rate decreases with the decrease in the particle size due to the presence of cyanicides and increasing rate of competing, reagent consuming materials.

Gold dissolution is usually mass transport controlled. Therefore, the rate depends on diffusion layer thickness and mixing characteristics of the bulk solution. Increasing agitation increases the dissolution rate up to a maximum, above which agitation has little or no further benefit (Marsden and House, 2006).

Copper and iron in the ores result in consumption of cyanide meant for gold dissolution. The poisonous effect of sulphides can be counteracted by adding lead during cyanidation. The cyanide consumption has also been observed to decrease when oxygen and lead were added. Gold dissolution was found to be very sensitive to the free cyanide below 380 ppm. Excess free cyanide results in unnecessary cyanide consumption. So an optimum value for the free cyanide level was determined, which came out to be 480 ppm (Deschenes and Wallingford, 1995). Oxygen and lead nitrate were found to have recuperating effect on cyanidation. Only oxygen dissolution is not much effective. However, the concurrent presence of lead nitrate improves the cyanidation rate and extent of cyanidation (Jeffrey and Ritchie, 2001, Deschenes et al., 2002, Guo et al., 2005). It is because the addition of lead nitrate completely stops the precipitation of arsenic species on gold and significantly reduces the formation of sulphide (Deschenes et al., 2002).

Lin and Chen (2001) used cyclic voltametric and potential step chronoamperometric techniques in order to perform electrochemical study of gold dissolution in cyanide solution and passivation of gold surface. The expected reaction was the CNO^- formation by cyanide and hydroxide. As the voltage is increased, the passivative layer formation was found to be dominant that completely covers the electrode surface at the vertex potential of 0.7V. The passivation reaction was proposed as

$$Au + OH^- \Leftrightarrow AuOH + e^-$$

The presence of another passivation species, auric hydroxide, was suggested that was formed by the disproportionation reaction of aurous hydroxide.

$$3AuOH \Leftrightarrow 2Au + Au(OH)_3$$

At the cathodic peak, the passivative layer was observed to be broken and more fresh gold is exposed. The cyanidation reaction is suggested to be diffusion controlled and chemical or electrochemical controlled as well. It was supposed that a faster passivation reaction may occur at higher pH (Lin and Chen, 2001). Crudwell and Godorr(1997) considered that gold passivation is due to formation of AuCN precipitate on the gold surface. But Guzman et al. (1999) suggests the role of Au_2O_3 in it. Jeffrey and Ritchie (2001) suggest the role of both AuOH and AuCN for the same.

Pyrites have also shown a significant effect on the leaching kinetics at a concentration lower than 10%. Low leaching rates at low oxygen concentration is attributed to the lack of oxidants for the process while at high oxygen concentration, contamination of gold surface by intensified dissolution of antimony was argued. The mechanism of lead nitrate was proposed by Guo et al. (2005) that involves the precipitation of antimony species out of the leaching solution. The passivation film was likely an antimony oxide (Guo et al., 2005).Chemical equilibrium effects were not found to restrict gold leaching due to irreversibility of Elsner equation (Brittan, 2008).

2.1.3 Kinetics

As is discussed in the previous section, cyanidation reaction is found to be diffusion controlled or reaction rate controlled. Based on the findings, different rate equations have been proposed, which are discussed in detail in this section.

Habashi (1966) conducted a thorough study of the reaction kinetics and found the reaction to be diffusion rate controlled. They derived a rate equation that demonstrated the dependence of the rate of leaching on the concentration of oxygen and cyanide quite well. As $C_{CN} << 4.4\ C_{O2}$, the reaction entirely becomes cyanide concentration dependent. When the case is right opposite, the reaction rate becomes entirely dependent on the concentration of oxygen.

$$\frac{dn_{Au}}{dt} = \frac{2A_{Au}D_{CN^-}C_{CN^-}D_{O_2}C_{O_2}}{\delta\left(D_{CN^-}C_{CN^-} + \chi D_{O_2}C_{O_2}\right)} \qquad \text{……..(2.11)}$$

where, n is number of moles, A_{Au} is the surface area of exposed gold, D_{O2} is the diffusivity of oxygen in water, and C_{O2} and C_{CN} are the concentration of oxygen and cyanide respectively in pulp, χ is the ratio of stoichiometric constants of CN^- to oxygen i.e. 4.4.

Schubert et al. (1993) modified the above equation given by Habashi (1966) including a dimensionless occlusion factor, s, in the equation and reduced the reaction rate to a realistic one.

$$\frac{dn_{Au}}{dt} = \frac{6s\mu_{Au}D_{O_2}}{\rho_{Au}\overline{R}_{Au}\delta}n_{Au}\left[\frac{1}{C_{O_2}} + \frac{1.5\chi}{C_{CN^-}}\right]^{-1} = -k_{Au}n_{Au}\left[\frac{1}{C_{O_2}} + \frac{1.5\chi}{C_{CN^-}}\right]^{-1} \qquad \text{……..(2.12)}$$

where, R_{Au} is the average radius of gold or metal particle, ρ_{Au} is the density, μ_{Au} is molecular mass.

Another kinetic equation was proposed by Crundwell and Godorr (1997) that was dependent on electrochemical mechanism, surface passivation and the shrinkage of gold particle. Crundwell and Godorr (1997) considered the reaction at the surface as the rate controlling and heterogeneous reaction with a diminishing surface area and modelled it using shrinking-particle model along with the electrochemical reaction. They assumed that all the particles are spherical and presence of uniform size distribution of particles in the system. The dissolution of gold has been described by the simultaneous solution of the following equations:

$$\frac{dX}{dt} = k_s(1-X)^{2/3}(1-f) \qquad \text{……..(2.13)}$$

$$\frac{df}{dt} = k_2(1-f) - k_{-2}f + \frac{2}{3}k_s f(1-f)(1-X)^{-1/3} \qquad \text{……..(2.14)}$$

where, X is the reaction conversion, k_s is the variable rate coefficient, f is the fraction of total surface area covered with passivating film, k_2 and k_{-2} are rate constants.

k_s is given by:

$$k_s = \frac{3(k_a k_c)^{1/2} C_{O_2}{}^{1/2} C_{CN^-}{}^{1/2}}{\rho_{Au}RF} \qquad \text{……..(2.15)}$$

where, k_a is the anodic rate constant, k_c is the cathodic rate constant, R is the gas constant and F is Faraday constant. The mechanism indicates that the rate of reaction is proportional to the square root of the concentrations of both oxygen and cyanide (Crundwell and Godorr, 1997).

Guzman et al. (1999) conducted experiments and observed a transition from diffusion controlled process to chemical reaction controlled process. As a result, acute effects were observed with the change in pH and cyanide concentration. The activation energy for the process was calculated and was found to be 8.8 kJ/mol. It typically lies in the range of diffusion rate control processes i.e. 8-20 kJ/mol (Guzman et al., 1999).

The limitation of all these rate equations is the high probability of error in the exact determination of exposed and passivated surface area through experiments. Moreover, the practical use of such equations in the plant design, scale-up and optimisation is limited (Lima and Hodouin, 2005). For these purposes, empirical rate equations only dependent on parameters that can be accurately obtained from experiments are necessary.

Such an equation was proposed by Brittan (1975). They proposed a variable activation energy model for gold cyanidation which involved a pseudo-first order mechanism.

$$\frac{dC_{Au}}{dt} = -\exp\left\{b_1\left(C_{Au} - C^*_{Au}\right) - b_2\right\} \times \left(C_{Au} - C^*_{Au}\right) \qquad \text{……..(2.16)}$$

Where, C_{Au} is the instantaneous gold concentration, C^*_{Au} is residual gold concentration, b_1 and b_2 are constants.

Nicol et al. (1984) proposed a second order rate equation based on the leaching rate observed for most of the South African ores, and this equation is also known as Mintek model:

$$\frac{dC_{Au}}{dt} = -k\left(C_{Au} - C^*_{Au}\right)^2 \qquad \text{……..(2.17)}$$

where, k is the rate constant.

Wadsworth (2000) studied surface processes in gold cyanidation and found that surface processes including oxygen diffusion, surface adsorption, charge transfer and chemical reactions to be rate controlling. Based on this observation, a model including surface imperfections (kinks and edges) has been proposed by Wadsworth (2000). Figure 2.2 illustrates steps that may occur in these types of processes where (a) is an atom dissolved in an electrolyte, (b) is an ad-atom or ad-ion on the planar surface, and (c) and (d) are kink and edge sites.

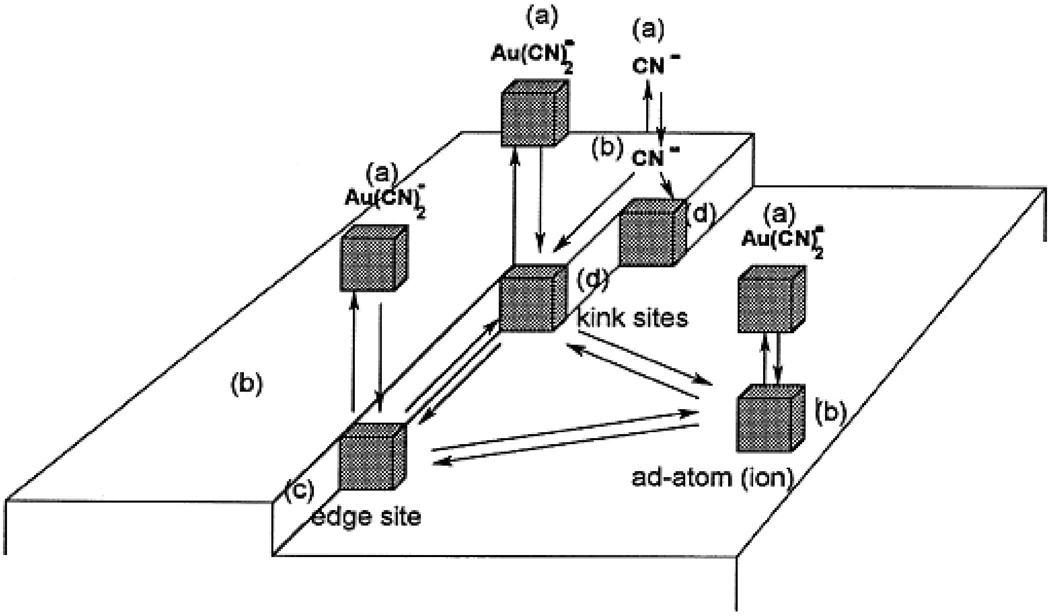

Figure 2.2. Gold surface illustrating various reaction paths.

The kinetics of gold dissolution was found to be a two-electron process (Wadsworth et al., 2000). A dissolution mechanism was proposed in which the active sites contain two or more gold atoms. The kinetics was determined in the presence and absence of activator in the solution. The rate was found to increase in the presence of nitrogen and sulphur aromatic heterocyclic compounds. The reactive intermediate complex is considered to be $Au_x(CN)_n^{-n}$. The rate expression obtained was:

In the absence of activation agents,

$$-r_{Au} = \left(\frac{K_3 \left(C_{CN^-} \right)^3}{1 + K_3 \left(C_{CN^-} \right)^3} \right) k_1 \qquad \text{……..(2.18)}$$

In the presence of activation agents

$$-r_{Au} = \left(\frac{K_3 \left(C_{CN^-} \right)^3}{1 + K_3 \left(C_{CN^-} \right)^3 + K_5 \left(A \right)^2} \right) \times \left(k_1 + k_2 \frac{(A)}{\left(C_{CN^-} \right)} \right). \qquad \text{……..(2.19)}$$

where r_{au} is the rate of gold dissolution, A is the activator concentration, k_1, k_2, K_5 and K_3 are the rate constants. At high concentration of cyanides, they found the initial rate of the reaction as $6.9\times10^{-6}\,mol\,m^{-2}\,s^{-1}$. They also proposed an expression to calculate optimum activator concentration by differentiating the following equation:

$$(\mathrm{A}) = -0.463(\mathrm{CN}^-) + \left[21.1 + 0.214(\mathrm{CN}^-)^2 + 0.0292(\mathrm{CN}^-)^3\right]^{1/2} \qquad \text{……..(2.20)}$$

Jeffrey and Ritchey (2001) observed that AuCN will not be formed in the case of impure gold. It will result in shorter chain lengths, more chain ends per unit area, and a faster dissolution rate. Considering the conditions employed, it was discovered that the gold dissolution reaction is chemical controlled and not diffusion controlled. The activation energy they calculated came out to be 47 ± 4 kJ mol^{-1}, which is a characteristic of a chemically controlled reaction. The rate equation for gold cyanidation proposed by Jeffrey and Ritchie (2001) is based on the following proportionality relation:

$$-r_{Au} \propto C_{CN^-}{}^2 \qquad \text{……..(2.21)}$$

Coetzee and Lalloo (2005), while simulating a simplified CIP model in excel, used a leaching rate assuming it to have linear relationship with the concentration gradient between metallic gold and aurocyanide.

$$\frac{\mathrm{dC_{Au}}}{\mathrm{dt}} = -\mathrm{k_1}\left(\mathrm{K_L C_{Au}} - \frac{\mathrm{C_{Au(CN)_2^-}}}{\mathrm{C_{Au}}}\right)^2 \qquad \text{……..(2.22)}$$

Particle diameter and reagent concentration are critical for the leaching rate kinetics. But, these parameters were not considered in these models. Considering the critical importance of these parameters in gold cyanidation, Ling et al. (1996) developed an empirical equation which included cyanide and oxygen concentration.

$$\frac{\mathrm{dC_{Au}}}{\mathrm{dt}} = -\mathrm{k}\left(\mathrm{C_{CN^{-1}}}\right)^a\left(\mathrm{C_{O_2}}\right)^b\left(\mathrm{C_{Au}} - \mathrm{C^*_{Au}}\right)^c \qquad \text{……..(2.23)}$$

Where k, a, b and c are constants.

This work was followed by Lima and Hodouin (2005), who developed a lumped kinetic model that takes into account the cyanide consumption, mean particle diameter of ore, oxygen concentration and unleachable gold concentration of the ore. They characterised ore and then conducted experiments in closed batch reactors. The kinetic equation parameters were estimated from the experimental results by minimizing the sum of squared error function. The expression was the same as Ling et al. (1996), but k and C_{Au}^* were functions of particle diameter.

$$\frac{dC_{Au}}{dt} = -k\left(C_{CN^-}\right)^a\left(C_{O_2}\right)^b\left(C_{Au} - C_{Au}^*\right)^c$$

……..(2.24)

In the expression of Ling et al. (1996), k was a constant and the value of C_{Au}^* depended on particle diameter. The order of reaction with respect to the gold concentration of ore was 1.5. But, in the expression proposed by Lima and Hodouin (2005), both k and C_{Au}^* were presented as a function of particle diameter. Moreover, the order of reaction with respect to the gold concentration of ore was 2.13, which is near the commonly accepted value of 2.

C_{Au}^* and k in terms of ore particle diameter (d_{ore}) is given as:

$$C_{Au}^* = 0.357\left(1 - 1.49e^{-0.0176 d_{ore}}\right)$$

……..(2.25)

$$k = 1.13\times10^{-3} - 4.37\times10^{-11} d_{ore}^{2.93}$$

……..(2.26)

At the same time, an expression for cyanide consumption kinetics was also determined dependent upon the free cyanide concentration and particle diameter (Lima and Hodouin, 2005).

$$-r_{CN^-} = \left(\frac{1.69\times10^{-8}}{\bar{d}^{0.547} - 6.40}\right)[CN^-]^{3.71}$$

……..(2.27)

2.2 Adsorption

2.2.1 Mechanism

Jordi et al. (1991) found the adsorption of gold cyanide from clear solutions to be characterized by intra-particle diffusion rate control, limited by a finite film mass transfer rate at low gold loadings.

Vegter (1992) conducted experiments and reported similar findings. They concluded that kinetic model will have to take into account both film and intraparticle mass transfer. The distribution of gold in the activated carbon particle was investigated quantitatively and suggested that reasonably uniform intra-particle mass transfer characteristics exist within individual carbon particles (Cook et al., 1989, Vegter, 1992). The rate steps in the process were found by Vegter (1992) are as follows:

a) The mass transport of gold cyanide and cations across the solution film surrounding the carbon particle,
b) Transport in the solution filling the pores,
c) The adsorption reaction and transport of the adsorbed cation gold cyanide ion pair along the pore walls by surface diffusion.

McDougall et al. (1980) suggested that the mechanism can be determined by analysing the nature of adsorbed gold. They used X-ray photoelectron spectroscopy to find the oxidation state and concluded that the adsorption of aurocyanide onto activated carbon occurs by some reduction mechanism. They suggested the formation of either a sub-stoichiometric $Au(CN)_x$ surface species or a cluster-type compound of gold. Later on it was suggested that it occurs via an ion-pair mechanism in which the ion-pairs of the type $M^{n+}[Au(CN)_2^-]_n$ are adsorbed onto the carbon surface without chemical change (Adams et al., 1987, Adams, 1990, Adams et al., 1992, Kongolo et al., 1997).

Kongolo et al. (1997) further examined the mechanism by measuring the zeta potential and described the process occurring in the electrical double layer and on the surface of the solid during adsorption. They suggested that adsorption can proceed by way of chemisorptive interactions at uncharged active sites. In the acidic pH range, the adsorption occurs by electrostatic interactions where the co-adsorbed monovalent ions contribute to the formation of adsorption centres.

From these findings, it can be concluded that the gold adsorption on carbon is limited both by mass transfer across the solution film surrounding the carbon particle and by diffusion inside the carbon.

2.2.2 Factors Affecting Adsorption

Numerous factors such as pH, temperature, structure, size and properties of carbon particles, presence of ions, aromaticity, etc. affect adsorption. The large surface area provides the adsorption sites and charring and partial oxidation are believed to give rise to the chemical properties of activated carbon. While the carbon macropores get blinded by the fine particles present in the solution and may result in the decrease in the absorption rate (Jordi et al., 1991).

The sodium and potassium ions increase the rate of gold adsorption which is found to further increase at the same concentration of calcium in the solution. The equilibrium loading of gold remains virtually independent of the pH value in the range of 6 to 12, whereas it increases strongly with pH values in the range of 1 to 5. The temperature was found to have an inverse effect on the equilibrium loading of gold. (Adams, 1990, Adams et al., 1992).

The influence of cyanide and oxygen on the adsorption has been studied by Woollacott and Guzman (1993). This effect was significant at low cyanide concentrations. At high oxygen (>5.5 ppm) and low cyanide (<100ppm) levels, adsorption was very sensitive to the changes in both the concentrations of oxygen and cyanide. However, when the concentration of both oxygen (>3.6 ppm) and cyanide (>100 ppm) are high, the opposite effect is observed (Woollacott and Guzman, 1993). At low oxygen levels, the process is found relatively insensitive to cyanide but is sensitive to the changes in concentration of oxygen (Adams, 1990, Woollacott and Guzman, 1993). On a contrary, Ibrado & Fuerstenau (1992) showed in their results that oxygen content is not good for adsorption.

The effects of variation in carbon porous structure and heteroatom functional group were studied by Jia et al. (1998). The gold adsorption capacities increased appreciably with increasing extent of activation. Treatment of carbon with nitric acid reduced the gold adsorption capacity but it dramatically increased when treated with ammonia. However the gold capacity was still lower than untreated carbon. Alcohols showed adverse effects on gold cyanide adsorption on carbon. It was suggested that hydrophobic organic solvents have destructive effects on gold adsorption. An increase in the adsorption was noticed with an increase in aromaticity and that decreased with increase in the H/C ratio (Ibrado and Fuerstenau, 1992). It is also agreed upon that excess free cyanide has little effect on gold adsorption capacity. The role of nitrogen functional groups present in the active carbon on gold adsorption was found out to be negligible. The graphene layers play a key role in the adsorption (Ibrado and Fuerstenau, 1992, Jia et al., 1998, Lagerge et al., 1999). The chemically activated carbons were found out to be more disordered than active carbons prepared by gasification. The dimension of $Au(CN)_2^-$ ion is ~ 500 pm in spherical cross-section by 1 nm long. It was indicated that the porosity< 2 nm is probably responsible for adsorption of gold cyanide species. The conclusion was made that adsorption of gold cyanide on active carbon is a function of solution equilibria, carbon porous structure and the bonding in the metal cyanide species (Jia et al., 1998).

2.2.3 Kinetics

In attempt to account for the phenomenon discussed above, various models of adsorption kinetics have been developed. The first few models were based on the film-diffusion mass transfer between the bulk fluid and the surface of the carbon. In these models, adsorption was dependent on the gradient between the gold in liquid and the equilibrium concentration of gold on carbon. The model is given by:

$$\frac{dq}{dt} = A_c k_f \left(C - C_e\right) \qquad \text{……..(2.28)}$$

where, C is the gold concentration in solution, C_e is the equilibrium gold concentration in the solution, A_c is the surface area per unit mass of carbon and k_f is the film mass transfer coefficient.

The equilibrium gold concentration, C_e, is described using its relationship with the gold on carbon. For the purpose, the data from the experiments is used to fit in the isotherms. For expressing the relationship three isotherms have been used in the literature.

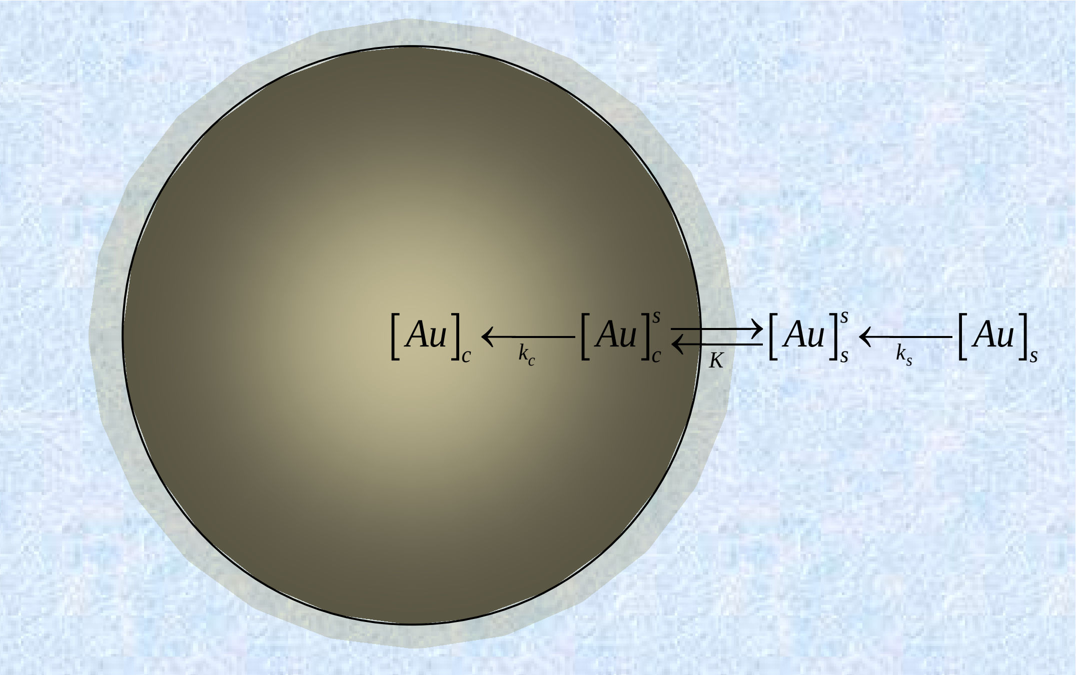

Figure 2.3. Schematic diagram of equilibrium model (Nicol et al., 1984).

Nicol et al.(1984) came out with a linear equilibrium isotherm for gold adsorption based on the assumption that equilibrium is established at the supposed homogeneous outer surface, and that mass transport of the gold into the bulk of the carbon particle can be characterized by a single pseudo-mass-transport coefficient (k_c) and a corresponding quantity (k_s) for the solution phase. This is illustrated in Figure 2.3. They proposed a linear isotherm for the equilibrium between gold on the carbon and that in the solution at the interface. The isotherm is given as:

$$q = AC_e \qquad \text{.......(2.29)}$$

where, A is adsorption parameter.

On the basis of adsorption-desorption reaction rate-control, Langmuir adsorption isotherm was assumed. It is widely used in the modelling of adsorption in CIP/CIL circuit due to its simplicity (Dixon et al., 1976, Stange, 1991, Kiranoudis et al., 1998). Langmuir isotherm is given as:

$$C_e = \frac{bq}{q^+ - q} \qquad \text{........(2.30)}$$

where, b is adsorption parameter and q^+ is the maximum gold concentration on carbon.

Based on the diffusion of gold cyanide inside the carbon particles, Freundlich isotherms were described for the adsorption equilibrium (Cho et al., 1979, Deventer, 1986, Vegter, 1992). Freundlich isotherm is given as:

$$q = A\left(C_e\right)^b \qquad \text{……..(2.31)}$$

where, A and b are adsorption parameters.

The rate equation takes the following form after substituting the isotherms into it:

Linear $$\frac{dq}{dt} = A_c k_f \left(C - q/A\right) \qquad \text{……..(2.32)}$$

Freundlich $$\frac{dq}{dt} = A_c k_f \left(C - \left(\frac{q}{A}\right)^{1/b}\right) \qquad \text{……..(2.33)}$$

Langmuir $$\frac{dq}{dt} = A_c k_f \left(C - \frac{bq}{q^+ - q}\right) \qquad \text{……..(2.34)}$$

For certain specific conditions in which the carbon is loaded to a greater extent, the kn model was proposed by Nicol et al. (1984). The model presents a direct relationship between the gold adsorbed on carbon and the gold concentration in solution and is given as:

$$\mathrm{q} = \mathrm{k_2 C t^n} \qquad \text{……..(2.35)}$$

The Dixon model was developed by Dixon, Cho and Pitt (1976) and is given by:

$$\frac{dq}{dt} = k_a C\left(q^+ - q\right) - k_d q \qquad \text{……..(2.36)}$$

where k_a and k_d are adsorption and desorption rate constants.

A model based on intra-particle mass transfer was proposed by Jordi et al. (1991). This porous particle model is called homogeneous surface diffusion model (HSDM), used for the gold adsorption kinetics on activated carbon. It was modelled by external film transfer and internal diffusion within the particle which was modelled by a single effective diffusion coefficient. Since, this model was not effective near equilibrium conditions. Therefore, it was modified by introducing the concept of blinding of carbon micropores in the equation and a new diffusion coefficient was introduced (Ahmed et al., 1992).

Kn model takes the form of film diffusion model with linear isotherm for n = 1, if the gold concentration in solution is constant. Kn model is independent of the gold loading on carbon and the model is based on the assumption of a constant gold concentration in liquid. It provides highly inaccurate adsorption rate especially in CIL circuits, where, the gold concentration in liquid changes considerably. Moreover, it has a time variable in the model not suitable for dynamic simulations. Therefore, Kn model is only suitable for very short duration simulations in batch operation. Similar results were obtained from the first order rate equation that was found to be applicable in the initial lower gold concentrations (Le Roux et al., 1991). The porous particle models are mathematically complex introducing additional parameters to be solved for and hence increasing numerical difficulties and practical inapplicability. Moreover, verification of such models is also a problem due to a large number of parameters to be compared from different sets of experimental data.

For small values of gold concentration on carbon, Dixon model becomes similar to the model based on Langmuir isotherm. Freundlich isotherm, Langmuir isotherm and Dixon model provided a better fit over a range of data, but only deviated for a comparatively large value of gold concentration, which is practically not faced in the industry (Woollacott et al., 1990).

2.3 Preg-robbing

Preg-robbing is considered as one of the factors affecting gold extraction, which is competed by the adsorption on activated carbon resulting in enhanced gold extraction. Another factor is the continual removal of leached species from the solution disturbing the solid-liquid equilibrium and favouring further gold dissolution, in accordance with the Le Chatelier’s principle. It was found that enhancement of gold extraction was due to the activated carbon adsorbing gold that would have otherwise been pregrobbed (Rees and Deventer, 2000). It was postulated that preg-robbing was caused by initial weak adsorption or precipitation of aurocyanide to silicate minerals in the case of silicate ore and initial fast adsorption in the case of sulphide ore which was followed by the reversal as the system comes to equilibrium (Goodall et al., 2005).

The preg-robbing behaviour of sulphide ores was determined by analysing pyrite and chalcopyrite ores. Quartz, silicate and clay minerals were not found to be preg-robbing, whereas pyrite ores were found to be preg-robbing. Formation of copper complexes and $Fe(CN_6)^{4-}$ does not lead to preg-robbing by precipitating in preference to the stronger $Au(CN)_2^-$ complex and it results in accelerating the leach process. This stabilizes $Au(CN)_2^-$ complex in liquid. Presence of excess free cyanide resulted in enhanced loading of gold onto activated carbon rather than the mineral sample. Adsorption of $Au(CN)_2^-$ on activated carbon was noticed to be a physical adsorption. Preg-robbing was detected as an irreversible process and has been observed being not inhibited by a blocking of active adsorption sites on the mineral surface. It was suggested that gold is reduced at the surface of ores, with the subsequent release of zinc and copper in solution. The mechanism of cyanidation and reduction are as follows:

$$Au(CN)_2^- \Leftrightarrow Au(CN)_{ads} + CN^- \qquad \text{……..(2.37)}$$

$$Au(CN)_{ads} + e^- \Leftrightarrow Au(CN)_{ads}^- \qquad \text{……..(2.38)}$$

$$Au(CN)_{ads}^- \Leftrightarrow Au + CN^- \qquad \text{……..(2.39)}$$

Oxidation of Chalcopyrite:

$$CuFeS_2 \Leftrightarrow Cu^{2+} + Fe^{2+} + 2S^0 + 4e^- \qquad \text{……..(2.40)}$$

The copper(II) formed reacts with the cyanide ions released by the gold reduction (Rees and Deventer, 2000).

$$Cu^{2+} + 3CN^- \Leftrightarrow Cu(CN)_2^- + 0.5(CN)_2 \qquad \text{……..(2.41)}$$

2.4 Carbon-in-Pulp and Carbon-in-Leach Tanks

Stange (Stange, 1991) used a linear model for adsorption and CIP process, which was optimised based on the minimisation of capital and operating cost function for the different number of stages. In another study, three basic process operating modes viz. carousel, continuous, and sequential were analysed. The optimisation study was conducted by economic evaluation of total gold loss and total annual cost as minimization object for each case (Kiranoudis et al., 1998). A simplified CIP model was simulated in EXCEL where leaching and adsorption rates were assumed to have linear relationship with the concentration gradient between metallic gold and aurocyanide, and aurocyanide and gold adsorbed onto the activated carbon respectively (Coetzee and Lalloo, 2005).

Van Deventer and Ross (1991) reviewed the developments in CIP systems and concluded that despite preg-robbing being an important phenomenon in the process incurring losses to the industry, it has been largely neglected. The researchers took this into account and the process was simulated using the flexibility of knowledge based systems because of the ill-defined and dynamic nature of the process (Reuter et al., 1991). Although the simulations provided data close to the experimental values, but its accuracy was heavily dependent on the accuracy and the available data.

Rees and Van Deventer (2001) conducted batch experiments and obtained the value of reaction constants for four different types of ores. In a subsequent paper (Rees et al., 2001), these values were applied in the rate equations and were combined for a series of tanks creating CILs. Mintek rate equation, film diffusion model with Langmuir isotherm and film diffusion with Freundlich isotherm were used for leaching, adsorption and Preg-robbing, respectively. The data were compared with the experimental data in terms of the gold concentration profile along the circuit.

Schubert et al. (1993) evaluated the performance of plant by simulating the process and varying few parameters. It was found that carbon attrition plays a major role in affecting the efficiency. The type of carbon transfer through the cycle is not that important, but the high loading of carbon at the bottom of the cascade is beneficial. For leaching, the equation given by Habashi (1966) was modified and used. Other than this, the oxidation of cyanide to cyanate (CNO^-) was included in the cyanide concentration balance and a linear equation for oxygen dissolution in the pulp was also incorporated and solved simultaneously. A linear equation for the adsorption of aurocyanide onto activated carbon was chosen. The degradation of carbon due to attrition was also solved by another first order equation given below:

$$\frac{dn_{Cf}}{dt} = k_{ab} n_{Cg} \qquad \text{……..(2.42)}$$

where, n_{cf} is the number of moles of carbon in fine size, k_{ab} is the coefficient of abrasion rate and n_{cg} is the number of moles of carbon in coarse size.

Lima (2007) used lumped kinetic models as the rate equation of leaching and cyanide consumption and for adsorption Langmuir isotherm was used. Other than simulation several carbon transfer strategies were analysed to find the best recovery strategy for the plant. Reactor volume optimisation, reactor network analysis and optimal distribution of cyanide in leaching tanks were also studied (Lima and Hodouin, 2005, Lima, 2006, Lima and Hodouin, 2006).

The modelling approach used in most of the studies has been aimed for modelling of the CIL series to simulate the outputs of CIL process. There is still need to simulate the process using suitable equations that not only can simulate the outputs of CIL, but also provide the flexibility to identify the process parameters that affect the process as a whole. Particle diameter and reagent concentration are critical for the leaching rate kinetics. In order to increase the recovery rate, understanding real time response to changes in these operating parameters is essential. This will help to find an optimised value of those parameters for attaining the highest efficiency achievable with the reasonable resources employed in the CIL series.

2.5 Hydrodynamics of CIL Tanks

Stirred tanks are used as CIL tanks in gold extraction industries. For the process, the efficiency of the operation depends on the contact between the constituents and suspension quality (Kasat et al., 2008). The mass transfer is facilitated by the extent of contact between the phases. The contact is the maximum if the solids are completely and homogeneously suspended in the entire tank. The problems that are faced in the stirred tanks causing poor interaction between the phases are settled solids, dead zones, accumulation of solids near the wall, dampening of the flow field, etc. This can be quantified by the hydrodynamics study in the stirred tanks. For this purpose, the minimum speed at which the solids are completely off the bottom of stirred tank, just suspension speed, is of major importance (Zwietering, 1958, Baldi et al., 1978, Sardeshpande et al., 2009). Below this point, a large proportion of solids remain settled in the tank. The more amount of solid has settled at the bottom of the tank, the lesser is its contact with the fluid. At the just suspension speed, the efficiency of the processes is high as it results in near homogeneous suspension. Knowledge of just suspension speed is necessary, as very high impeller speeds (above the just suspension speeds) may not provide a far better homogenisation and attribute to the loss of energy (Angst and Kraume, 2006).

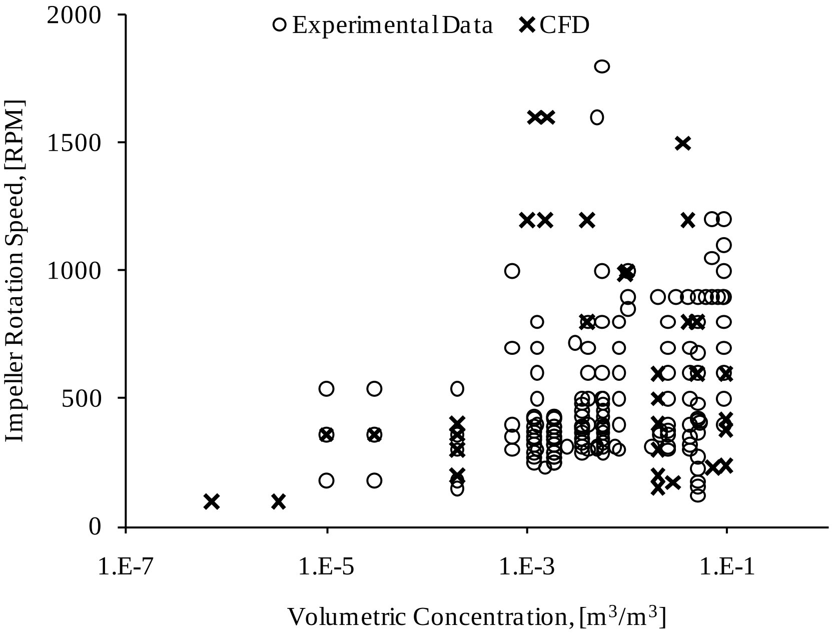

Figure 2.4. The studies conducted below 10% volumetric concentration.

Among the process parameters on which the performance of stirred tanks depends, impeller speed and solid concentration are the most important. Research studies have been conducted for a wide range of impeller speeds. However, the range of solids concentration for which the research has been conducted still needs to be reviewed. When the concentration data collected from numerous studies were plotted against the impeller speeds, the focus of most of the studies was found to be on the low concentration range (Figure 2.4 and Figure 2.5). The reason behind the lesser number of studies in the high concentration range is due to the limitation of experimental techniques. The reason is the lack of tools and techniques that could measure the data with high spatial and temporal resolution at high solid loading. As the concentration of solids increases, the opacity of the system increases as well. This renders inability to the non-intrusive optical techniques to provide accurate data for such systems. The intrusive techniques are very sensitive with respect to the sample tube angle, sample withdrawal velocity, sample tube design, orientation of the sample tube and the design. In such cases, the margin of error while the collection of the samples also increases with the increase in the solid concentration.

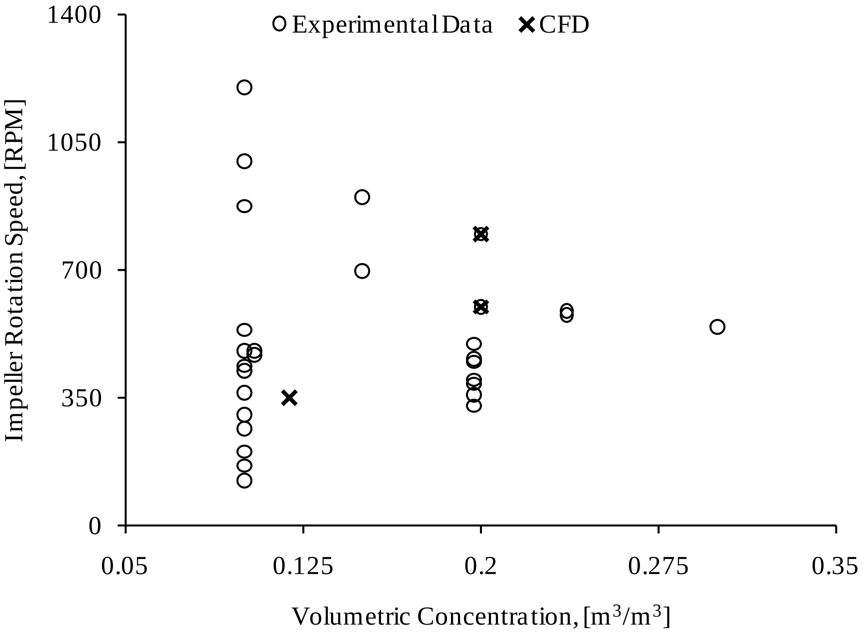

Figure 2.5. The studies conducted above 10% volumetric concentration.

Few experimental techniques such as CARPT and PEPT can prove useful for the measurements. These techniques have been analysed recently and the outcomes are quite favourable (Guha et al., 2007, Guida et al., 2010). The advantages and limitations of the experimental techniques are discussed in detail later in the section 2.5.3 of this chapter. As compared to the experimental investigations, far fewer CFD studies in high concentration are due to the lack of experimental data for validation of models. With the availability of reliable experimental data, there is a higher possibility of more simulation studies at high solid concentration. This will enhance the understanding of highly concentrated systems like CIL tanks. For high solid loading stirred tanks, a brief review of studies is summarised in Table 2.2 and an extensive review is presented in the following sections.

Table 2.2. Summary of Hydrodynamic studies at high solids concentration.

Author and year	**Solid Loading**	**Impeller Speed**	**Measurements**	**Techniques**	**Geometry**				**Impeller**			**Particle**		**Liquid**
	% v/v or % w/w or g/l	**(in RPM)**			**Tank Type**	**T**	**H**	**W**	**Impeller Type**	**D**	**C**	**Material (density)**	**Diameter (in mm)**	
Chudacek (1985)	6.1%, 12.2% and 24.4% v/v	80-1450 variable	Power	Strain Gauge	Profile Bottomed Vessel	0.5	T	T/10	3-PBT	0.33T	T/6 or T/2	Silica Sand 2650 kg m-3	0.29 and 0.116	Water
			Slurry Height	Visual or Photographic Method	Flat Bottomed Vessel						T/12 or T/3			
					Cone and Fillet Vessel						T/4 or T/2			
Buurman et al. (1986)	0-15% v/v	530	Flow measurement	Ultrasonic Doppler Velocitymeter	Elliptical Bottomed Cylindrical Vessel	4.26	T	T/10	4-PBTD	0.4T	T/3	Sand Particles 2550 kg m-3	0.157	Water
			Solid concentration	Sampling										
Yamazaki et al. (1986)	0-30%	300-1200	Solid concentration profile	Photo-electric method of measurement	Flat-bottomed Cylindrical Tank	0.3	T	-	RT	0.23T	0.3T	Glass particle 2470 kg m-3	0.087, 0.135 and 0.264	Water
				Analytical Method: Sedimentation-dispersion model					4-blade marine propeller	T/3				
Ayazi Shamlou and Koutsakos (1989)	1, 2, 3 and 6% w/w	300-800	Local solid concentration	Laser transmitter and receiver	Spherical Bottomed Cylindrical Vessel	0.225	1.64T and 2.9T	T/10	6-PBT	0.44T, 0.8T and 0.29T	H/5 or H/31	Glass particles 2450 kg m-3	0.175 – 1.1	Water
Yamazaki et al. (1992)	15 % v/v	700 and 900	Solid Concentration	Backscattering-type probe	Flat Bottomed Cylindrical Vessel	0.3	T	-	RT	0.23T	T/5	Glass particle 2470 kg m-3	0.135	Water
									4-blade marine propeller	T/3				
MacTaggart et al. (1993)	10 and 30% v/v	440 and 545	Solid Concentration	Conductivity Probe	Flat Bottomed Cylindrical Vessel	0.292	T	T/10	RT	0.33T	0.33T	Sand Particles 2650 kg m-3	0.255, 0.3 and 0.41	Water
Rasteiro et al. (1994)	5 and 20 % v/v	600	Concentration Profiles	Analytical: Settling/dispersion model	Flat Bottomed Cylindrical Vessel;	0.3 and 0.5	T	-	Axial Flow impeller	T/3	T/5	Glass particle 2370 kg m-3	0.087 and 0.416	Water
Nasr-El-Din et al. (1996)	10 and 30 % v/v	440 or 545	Solid Concentration	Conductivity probe	Flat Bottomed Cylindrical Vessel	0.292	T	T/10	RT	0.33T	0.33T	Sand particle 2650 kg m-3	0.082, 0.255, 0.41, 0.5 and 1	Water

Author and year	**Solid Loading**	**Impeller Speed**	**Measurements**	**Techniques**	**Geometry**				**Impeller**			**Particle**		**Liquid**
	% v/v or % w/w or g/l	**(in RPM)**			**Tank Type**	**T**	**H**	**W**	**Impeller Type**	**D**	**C**	**Material (density)**	**Diameter (in mm)**	
Bujalski et al. (1999)	up to 40% w/w	0-600 Variable	Power	Air-bearing Technique	Flat Bottomed Cylindrical Vessel	0.29	T	T/10	A310	0.52T	T/4	Glass or Sand Particles 2500 kg m-3	0.1-1.0	Water
			Suspension Behaviour	Visual Observation		0.72			A315	0.42T		ion exchange resins 1350 kg m-3		
			Mixing time	Decolorization Technique								Zircon sand 4450 kg m-3		
Wu et al. (2001)	20%, 22.5% and 32% v/v	0-1000; mostly conducted at 250 or 300 RPM	Power	Torque Transducer	Flat Bottomed Cylindrical Vessel	0.39	T	T/12	DT (2, 3, 4, 5, 6 or 8 bladed); PBTD (2, 3, 4, 5 or 6 bladed with angle 20, 25, 30, 35, 40 or 45 degrees); 6-bladed concave shaped radial turbine; 6-bladed radial disc turbine with hole at centre of each blade; Lightnin A310;	0.41T	T/3	Glass Ballotini particles 2500 kg m-3	0.07 or 0.105	Water
			Impeller Speed	Speed detector										
			Velocity and flow measurement	Laser Doppler Velocimetry										
			Settled solid height measurement	Ruler										
Altway et al. (2001)	5 and 20% v/v	800	Solid Concentration	Fluent; Algebraic Slip Model;	Flat-bottomed cylindrical tank	0.3	T	T/10	RT	T/3	T/3	Glass beads 2360 kg m-3	0.087, 0.05 and 0.01	Water
Rieger (2002)	2.5, 5, 10, 15 and 20% v/v	-	Critical impeller speed	Visual Observation	Dish-bottomed Cylindrical tank	0.2	T	T/10	6-PBT	0.3T	0.15T	Ballotini particles 2500 kg m-3	0.133 - 4	Water
Bittorf and Kresta (2003)	24 to 55% w/w	530	Velocity measurement	Laser Doppler Velocimetry	Flat Bottomed Cylindrical Vessel	0.24	T	T/10	4-PBT and Lightnin A310	T/2	T/4 and T/6	Sand Particles 2550 kg m-3	0.3	Water
Micheletti (2003)	1.8% - 15.5% v/v;	50, 100, 150, 200, 250, 300, 350, 400 and 450	Particle Concentration and mixing time	Conductivity Probe	Flat Bottomed Cylindrical Vessel	0.29m	T	T/10	RT	0.338T	T/3 or 0.15T	Glass Bead particles 2470 kg m-3	0.15-0.71	Water
			Power	Strain Gauges								Polystyrene particle 1050 kg m-3	0.4-1.4	
												Diakon Particles 2470 kg m-3	0.5-1.18	
Brunazzi et al. (2004)	up to 40% w/w	0-600	Solids concentration	Impedance Probe	Flat Bottomed Cylindrical Vessel	0.5	T	T/10	A310 impeller	0.346, 0.386 and 0.5T	0.25T	Spherical glass beads 2500 kg m-3	0.09-0.6	Water
			Power	Strain Gauges										

Author and year	Solid Loading	Impeller Speed	Measurements	Techniques	Geometry				Impeller			Particle		Liquid
	% v/v or % w/w or g/l	(in RPM)			Tank Type	T	H	W	Impeller Type	D	C	Material (density)	Diameter (in mm)	
Micale et al. (2004)	0.48, 2.4, 4.8, 9.6 and 20% v/v	300, 380 and 480	Suspension height	Visual Inspection	Flat Bottomed Cylindrical Vessel	0.19	1.5T	T/10	RT	T/2	0.095T	Silica particles 2580 kg m-3	0.212-0.25	Water
				Ansys CFX 4.4: Eulerian-eulerian approach										
Spidla et al. (2005)	5 to 10% v/v	159, 166, 122, 125, 225, 267, 176 and 205	Solid Concentration	Conductivity probe	Flat Bottomed Cylindrical Vessel	1	T	T/10	6-PBTD	T/3	T/3 and T/6	Glass particles 2500 kg m-3	0.14 and 0.35	Water
			Impeller Speed	Opto-electronic disc system										
Angst and Kraume (2006)		H90 criterion	Solid concentration	Endoscope	Dished Bottomed Cylindrical Vessel		T	T/10	6-PBTD	0.3125T	0.3125T	Glass Bead particles 2500 kg m-3	0.2	Water
	5% v/v	678				0.2								
	10%v/v	877				0.2								
	5% v/v	419	Power	Torque meter		0.4								
	10% v/v	538				0.4								
	5% v/v	275				0.9								
Ochieng and Lewis (2006)	1-20% w/w	200-700 RPM	Velocity and Flow	Laser Doppler Velocimetry	Elliptical Bottomed Cylindrical Vessel	0.38	T	T/10	Four blade Mixtec HA735 propeller	0.33T	0.15T	Nickel Particles 8908 kg m-3	0.23, 0.4 and 0.75	Water
			Solids concentration distribution	Non-intrusive Optical Attenuation Technique (OAT)										
			Particle size distribution	Sampling and analysis by Laser Diffraction Technique										
				CFX: Sliding Grid approach;										
Ochieng and Lewis (2006)	1-20% w/w	200-700	Velocity and flow field measurement	Laser Doppler Velocimetry	Elliptical Bottomed Cylindrical Vessel	0.378	-	T/10	Four Blade Hydrofoil Propeller (MIXTEC HA735)	0.33T	0.13T – 0.33T	Nickel Solids 8912 kg m-3	0.075-1.0	Water
			Solids concentration	Optical Attenuation Technique										
				CFX 5.6/5.7: Eulerian-Eulerian aproach										

Author and year	Solid Loading	Impeller Speed	Measurements	Techniques	Geometry				Impeller			Particle		Liquid
	% v/v or % w/w or g/l	(in RPM)			Tank Type	T	H	W	Impeller Type	D	C	Material (density)	Diameter (in mm)	
Fradette et al. (2007)	2.8% v/v	173	Solid concentration profiles	Analytical: SIMM model	Flat Bottomed Cylindrical Vessel	0.072	0.903T	-	Down-pumping Marine Propeller	T/4	0.36T	Ballotini Particles 2500 kg m-3	1	Corn Syrup (ρl = 1360 kg/m3; µ = 1.05 Pa.s)
	7.1% v/v	230												
	11.9% v/v	350												
Ochieng and Onyango (2008)	1-20% w/w	200-700	Solid concentration distribution and settling velocity	Optical Attenuation Technique	Flat Bottomed Cylindrical Vessel	0.378	T	T/10	Four blade Mixtec HA735 propeller	0.33T	0.15T	Nickel particles 8908 kg m-3	0.23, 0.4 and 0.75	Water
			Particle size distribution	Laser Diffraction Technique										
			Particles morphology	Scanning electron microscope (SEM)										
				CFX; Multiple frames of Reference and Sliding Grid approach										
Kasat et al. (2008)	10% v/v	120-2400		CFD Simulation: Fluent Eulerian-eulerian approach.	Flat Bottomed Cylindrical Vessel	0.3	T	T/10	RT	T/3	T/3	Glass particles 2470 kg m-3	0.264	Water
Guida et al. (2009)	0.025, 0.052 and 0.104	360, 405 and 480	Velocity measurements and solid concentration	Positron Emission Particle Tracking (PEPT)	Flat Bottomed Cylindrical Vessel	0.288	T	T/10	6-PBTD	T/2	T/4	Glass Particles 2485 kg m-3	2.85 – 3.3	Water with NaCl added (ρs= 1150 kg m-3)
		375, 410 and 470							6-PBTU					
Fletcher and Brown (2009)	9.6% v/v	240, 420 and 600		ANSYS CFX 11 Eulerian-Euleriam Model Algebraic Slip Modelling (ASM)	Flat Bottomed Cylindrical Vessel	0.19	1.5T	T/10	RT	T/2	0.095T	Silica Particles 2580 kg m-3	0.212-0.25	Water

Author and year	Solid Loading	Impeller Speed	Measurements	Techniques	Geometry				Impeller			Particle		Liquid
	% v/v or % w/w or g/l	(in RPM)			Tank Type	T	H	W	Impeller Type	D	C	Material (density)	Diameter (in mm)	
Tamburini et al. (2009)	9.6% v/v	380	Transient particle distribution data	High-resolution digital camera (19 fps);	Flat Bottomed Cylindrical Vessel	0.19	1.5T	T/10	RT	T/2	0.089T	Silica particles 2580 kg m-3	0.212-0.25 and 0.231	Water
				Ansys-CFX4.4; Eulerian–Eulerian MFM;										
Stevenson et al. (2010)	5 and 10% v/v	306, 366, 426, 480 and 366	Solid concnetration	MRI and ERT	Flat Bottomed Cylindrical Vessel	0.06	1.083T	T/12	RT	0.417T	0.278T	Ballotini particles 2200 kg m-3	0.054 and 0.102	Water
												Nylon particles 1100 kg m-3	0.513	
Guida et al. (2010)	0.025, 0.052, 0.104 and 0.236	360, 405, 480 and 590	Velocity measurements and solid concentration	Positron Emission Particle Tracking (PEPT)	Flat Bottomed Cylindrical Vessel	0.288	T	T/10	6-PBTD	T/2	T/4	Glass Particles 2485 kg m-3	2.85 – 3.3	Water with NaCl added (ρs= 1150 kg m-3)
		375, 410, 470 and 580							6-PBTU					
Hosseini et al. (2010)	5 to 30% w/w	250-800	Solid Concentration	Electrical Resistance Tomography (ERT)	Flat Bottomed Cylindrical Vessel	0.4	1.5T	T/12	A100, A200, A310 and A320	0.445T	T/5- T/2	Glass Particles 2500 kg m-3	0.21-1.5 mm	Water

In the following sections, a review of experimental and computational work in the field of solid – liquid stirred tanks (CIL tanks) has been presented.

2.5.1 Regimes

The challenging aspect in the turbulent multiphase flow is that it is very unpredictable due to velocity fluctuations and the presence of additional phase. Different flow conditions can result in a different flow pattern, which then affects the quality of suspension. Depending on the combination of the different properties, different regimes may be observed in a stirred tank. Broadly, the flow regimes can be classified into four categories, viz. below the just suspension speed, at the just suspension speed, at the speed of homogeneous suspension and above the speed of homogeneous suspension. The suspension state and the corresponding regimes are shown in Figure 2.6.

At the impeller speed below the just-suspension, the particles remain settled at the bottom of the tank resulting in the formation of a 'false bed' (Sardeshpande et al., 2009). High solid concentration may result in increased thickness of the bed leading to a pseudo-low impeller clearance situation (Figure 2.6 (a)). As a result, the Rushton turbines, that are known to create upper circulation loop and a lower circulation loop, may create a single circulation loop. The concentration of the particles above the bed is low and is not large enough to significantly affect the flow field. Due to the low impeller speed, the kinetic energy possessed by the liquid phase is not enough to counteract the inertia, and suspend the particles.

In the experiments conducted involving visual observation, the just-suspension speed has been defined as an impeller speed at which the particles do not remain settled at the bottom for more than 2 seconds (Zwietering, 1958). As the impeller speed attains just-suspension speed, the particles present in the bulk increases (Figure 2.6 (b)). The particles suspend due to the kinetic energy of the liquid phase getting converted into the kinetic energy of particles (Shamlou and Koutsakos, 1989). As a result the flow field is highly affected by the presence of particles. The liquid phase kinetic energy and the velocity decrease resulting in the dampening of the turbulence (Derksen, 2003, Ochieng and Lewis, 2006, Sardeshpande et al., 2009). However, the effect on the turbulence depends on the size of the turbulent eddies and the particle size. If the particle size is significantly smaller than the turbulent eddies, the particles have no resistive effect on the liquid phase and flow along the motion (Magelli et al., 1990, Ochieng and Onyango, 2008). The kinetic energy of the liquid phase is shared by the particle phase. But, on a contrary, larger size particles resist the turbulent eddies and hence, reduce the vigour. Moreover, the loss of kinetic energy is greater in the case of large size particles due to collisions because of the larger inertia. As a result, turbulence decreases significantly. A sudden variation in the concentration in the tank at a particular axial height is observed (Bittorf and Kresta, 2003, Brunazzi et al., 2004, Spidla et al., 2005, Ochieng and Lewis, 2006, Kasat et al., 2008, Fletcher and Brown, 2009). This is due to the circulation loop and the inward jets forcing the solids inwards and downwards near the axis. The height of this sudden concentration variation is also termed as cloud height. The cloud height at the just suspension conditions is approximately 0.45 – 0.55 times the height of the tank (Brunazzi et al., 2004). The variation in the solid concentration is the maximum at the cloud height. The velocity vectors above the cloud height, or in other words near the top surface, are very weak (Kasat et al., 2008).

The suspension is said to be homogeneous in a stirred tank, if the standard deviation of the concentration at various points of the tank is not greater than 0.2. In this particular condition, the cloud height is greater than 0.9 times the height of the tank (Figure 2.6 (c)). In these conditions, no clear demarcation of the cloud height is possible because of the very high variation near the top surface due to the infusion of air (Buurman et al., 1986).

At the impeller speed above the speed of just suspension, the flow field remains the same as in the case of just suspension. More of kinetic energy possessed by the liquid phase is transferred to the particles. The centrifugal force exerted on the solid particles increase to such an extent that the concentration of particles near the wall increases (Figure 2.6 (d)). As a result a decrease in the homogeneity is observed (Angst and Kraume, 2006, Hosseini et al., 2010).

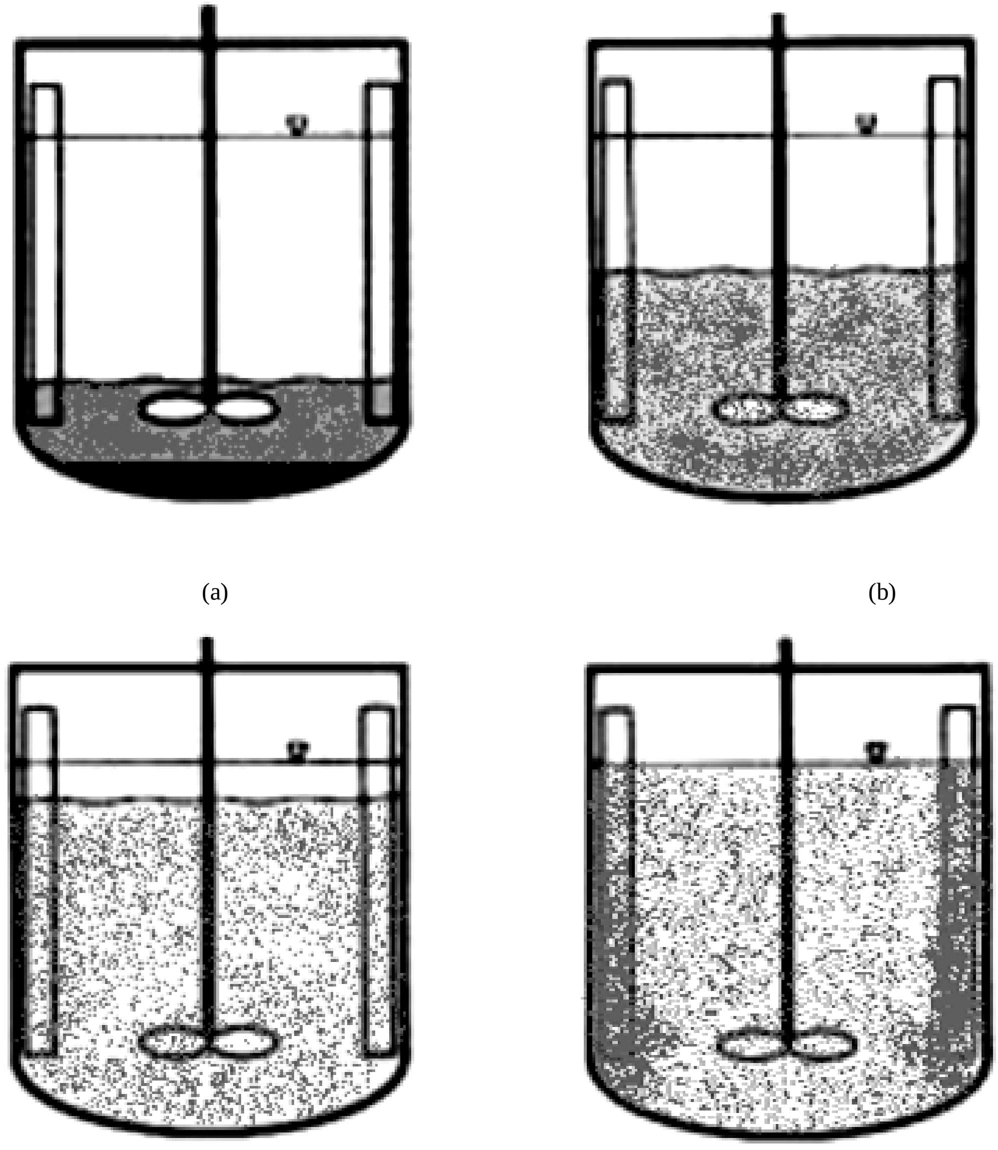

(a) (b)

(c) (d)

Figure 2.6. Regimes and states of suspension in a stirred vessel (Kraume, 1992)

Not much difference in the impeller speed is observed between the second and third regimes specified above. Moreover, speed of just suspension provides a near approximation of homogeneity. The speed of just suspension is used as an initial design parameter by the engineers and is also used as a common operating parameter for the performance evaluation of stirred tanks for different impellers, concentrations, particle sizes, etc. Therefore, the study of the just suspension speed is important in solid-liquid stirred tanks. Such study will provide an initial basis of the appropriate operating conditions for CIL tanks.

2.5.2 Experiments and Correlations for Just Suspension Speed

Conventionally, solid suspension in stirred reactors is characterized by impeller speed required for just off bottom suspension (N_{js}). Just suspension impeller speed (Njs) is the speed at which all particles are lifted up from the bottom of the vessel and particles do not spend more than 1 or 2 seconds on the bottom of the vessel (Zwietering, 1958). Based on the experiment conducted for different solid loadings, stirred tanks and solid types, Zwietering (1958) proposed a correlation for estimation of just suspension speed. The correlation is given as:

$$N_{js} = Sd_p^{0.2}\left(\frac{\mu}{\rho_l}\right)^{0.1}\left(\frac{g\left(\rho_s-\rho_l\right)}{\rho_l}\right)^{0.45} X^{0.13}D_i^{-0.85} \qquad \text{……..(2.43)}$$

where S is constant for a given system geometry, d_p is the particle diameter, μ is the fluid viscosity, ρ_l is the fluid density, g is the acceleration due to gravity, X is the weight percent of solids and D_i is the impeller diameter.

Baldi et al. (1978) proposed a new model for the determination of the minimum stirrer speed for complete suspension. Particles with mono- and bi-modal size distribution were examined in fluids with different physical properties. With regard to turbulence dissipation near bottom, ε_b, Baldi et al. (1978) observed that it is surely different from the average value ε of the dissipated power per unit volume. For the assumption of $\varepsilon_{b\sim}$ ε, Z was found to be a constant for a given geometry:

$$\mathrm{Z} = \sqrt{\left(\frac{\Delta\rho \mathrm{g}}{\rho_1}\right)\frac{\mathrm{Td}_\mathrm{p}^{1/6}}{\mathrm{N}_\mathrm{p}^{1/3}\mathrm{D}_\mathrm{i}^{5/3}\mathrm{N}_\mathrm{js}}} = \text{constant} \qquad \text{……..(2.44)}$$

where T is tank diameter and ψ is power number.

Since, the ratio $\varepsilon_{b/}$ ε depended on the steer velocity, therefore it was expressed as:

$$\frac{\varepsilon_b}{\varepsilon} = f\left[\frac{1}{N_{\mathrm{Re}}}\left(\frac{D_i}{C}\right)^2\right] \qquad \text{……..(2.45)}$$

where f is proportionality constant, N_{Re} is Reynolds number and C is the impeller clearance.

$\varepsilon_{b/}$ ε was found to be a constant when the stirrer was very near to the bottom, while it was more and more affected by the hydrodynamic conditions as C increased. Baldi et al. (1978) proposed a complex model which takes into effect the off-bottom clearance and geometrical complexities such that no any parameter estimation was required from experiments as was required for the estimation of S =S(D/T) in the Zwietering' s correlation. The correlation was given as:

$$N_{js} \propto d_p^{0.14} \mu^{0.17} \rho_l^{-0.16} \left(\frac{g\left(\rho_s - \rho_l\right)}{\rho_l} \right)^{0.42} X^{0.125} D_i^{-0.89} \qquad \text{……..(2.46)}$$

Witcherle (1988) proposed a model of particle suspension in an agitated vessel considering that the process regime is determined by the ratio of the particle settling velocity to the characteristic velocity around the particle at the tank bottom. The model proposed was:

$$N_{js} = \left(\frac{B_{js}}{A_{\min}} \right)^{2/3} \left[\frac{d_p^*}{\left(18 + 0.6 d_p^{*3/2}\right)} \right]^{2/3} \left(d_p^*\right) \qquad \text{……..(2.47)}$$

where B_{js} and A_{min} are model parameters and d_p^* is the dimensionless particle diameter.

Dimensionless particle diameter is given as:

$$d_p^* = \left(\frac{d_p^3 \rho_l g\left(\Delta\rho\right)}{\mu^2} \right)^{1/3} \qquad \text{……..(2.48)}$$

For A_{min}, the shear rates were calculated at the bottom of the tank and it was assumed to summarize all the effects of the mixing equipment geometry. For common geometries, the value of A_{min} was found to be 2.5-3.5. The value of B_{js} was approximately 10, as estimated from empirical data and is supposed to be dependent on the particle shape and the particle concentration.

Rieger (2002) studied the effect of particle content on agitator speed for off-bottom suspension in dish bottomed vessel. Experimental results for a given volumetric concentration were plotted in the form of a modified Froude number (Fr) showing its dependence on relative particle diameter, d_p/T. The correlation for Fr at the just suspension speed is given as:

$$Fr = \frac{A_1\left(d_p/T\right)^a}{\left[1+\left\{A_2\left(d_p/T\right)^a\right\}^{10}\right]^{1/10}}$$ ……..(2.49)

where, A_1 and A_2 are model parameters.

Modified Froude number is defined as:

$$Fr = \frac{n^2 d_p \rho_l}{g\Delta\rho}$$ ……..(2.50)

N. Sharma and A. Shaikh (2003) studied the factors that were responsible for the discrepancies in the just suspension speeds and power required for just suspension. Critical speed as well as the critical power was found to increase with the increased clearance. Low clearance result in a fast velocity impinging the bottom suspending the solids at low impeller speed and low power input. At low clearance, the ratio of the local energy to the average energy dissipated per unit volume was found to be constant. At intermediate and high clearance, the power increased and hence, a determination of a different scale-up criterion for each of the impeller clearance regions was suggested. For the increase in the tank diameter, the critical suspension speed increased due to the more energy required to suspend solids. However, the increase in impeller diameter increased tip speed and hence, a lower critical speed was required.

Brucato et al. (2010) studied the particle suspension and power requirements in an unbaffled stirred tank. The N_{js} values for the unbaffled tanks were found to be smaller than those in baffled tanks due to the lesser dissipation of liquid phase kinetic energy (because of baffles). But there is no change in dependency of N_{js} on particle concentration and density difference in the absence of baffles. This is because the presence of particles, its amount and density impacts the velocity flow field adversely. The settled solids resulted in the formation of ‘false bed’ at low impeller speeds, hence, decreasing clearance and the power number. Another reason for high power number at low agitation speeds was attributed to the increase in the local density due to the presence of suspended solids in the lower part of the vessel. With the increase in impeller speed, particle suspension increased and the power number decreased. Power requirements to achieve just-suspension conditions were found to be significantly smaller in top-covered unbaffled tanks as compared with the more common baffled vessels.

Instead of the modifications in the correlations and the newly proposed correlations, the prediction of N_{js} is still not precise due to its variation with several parameters ranging from the geometrical parameters to particle properties. However, most of the recently conducted studies still make the use of Zwietering's correlation (Sardeshpande et al., 2009, Unadkat et al., 2009, Brucato et al., 2010, Guida et al., 2010, Stevenson et al., 2010).

2.5.3 Experimental Hydrodynamic Studies

Chudacek (1985) studied the impact of the settled solids on the complete off-bottom suspension and the effect of the modified bottom of the tank on the power consumption for complete suspension. They observed that the unsuspended solids are present in the centre and periphery at the bottom of the tank due to the induced recirculation loops. The powers for the suspension of solids were compared for different geometries. The profiled bottom tank was found to be the most efficient as a smoother profile of high velocity and the absence of sharp flow diversions and low velocity field at the bottom of the tank leads to the complete suspension. The 'cone and fillet' bottomed geometry was inefficient only for the easily suspended solids i.e. finer particles. In conditions above the complete off-bottom threshold, the performance of 'cone and fillet' geometry was better than the 'profiled bottom' geometry as the presence of cone was effective for flow diversions. The complete off-bottom suspension criterion applied to the flat bottom tank was inadequate for modelling solids suspension. So, it was also suggested that a smoother flow pattern was easier for theoretical analysis of solids suspension.

Yamazaki et al. (1986) measured the concentration profile of solids suspended in the slurry tank in high solids concentration regions, using a photo-electric method. They observed the radial concentrations to be nearly constant. The increase in particle suspension resulted in turbulence damping in the liquid phase. The concentration near the surface was noticed to decrease as the settling velocity near the top surface overcomes the dispersion force. The ratio of the liquid flow velocity to the falling velocity of the solid particles was found to be approximately proportional to the impeller speed under the complete suspension conditions. This is mainly due to the decreased upflow velocity in the liquid phase caused by the strong interference by the solid particles. Although it was that the agitation with the radial flow impeller was more effective for solids suspension in comparison with the agitation with the axial flow impeller on an impeller speed basis, but it was recommended that the efficiency of agitation should be compared on an energy basis.

Ayazi Shamlou and Koutsakos (Shamlou and Koutsakos, 1989) studied the change of suspension behavior of solids with the change in impeller speed and concentration in a stirred tank. A near exponential increase in the solids concentration with the decrease in the height from the top was observed as the concentration of solids is low in the clear liquid layer. An increase in homogeneity was observed with the increase in the impeller speed as the mean kinetic energy and hence, turbulence in the flow increased. However, the presence of high concentration of solids resulted in loss of kinetic energy and reduced velocity field and hence, resulted in poor suspension. The distribution of the particles was characterized by a ratio of the turbulent diffusion coefficient and terminal settling velocity of particle in stirred tank that provided linear relationship with impeller speed, impeller diameter and terminal velocity.

Yamazaki et al. (1992) proposed a method for measuring continuously the local solids concentrations in a high solids loading (1-40% v/v) stirred tank. The solids concentration in slurries is determined by measuring the intensity of the light reflected from the surface of solids, on which the light of a chosen wave length and constant intensity from a light source was projected. The intensity of the reflected light was found to be affected by the particle diameter, particle shape, particle colour and so on due to the superimposition of a considerable fraction of light scattered on the reflecting light, and the extinction coefficient defined by Lambert-Beer’s law is not constant for higher concentration slurries. A proper calibration is required for the measurement of solids concentration at high concentration. In a glass beads-water system, this method could be applied to the measurement of the local and high solids concentration in the region of $5\% < C_{av} < 40\%$ at $d_p > 100$ µm.

MacTaggart et al. (1993) developed a four-electrode conductivity probe to measure solids concentrations. An efficient procedure based on graduated cylinder was established for calibration. Errors in measurement were observed near the boundary as the presence of walls affects sensor voltage. The probe was used for the measurement of solids concentration. They found low solid concentrations at the top and high solid concentrations in the impeller plane.

Ferreira et al. (1994) validated the use of the light scattering technique (LST), associated with Refractive index measurement (RIM), for the experimental measurement of solids concentration in a mixing tank The measurements were compared with data collected from an intrusive light-reflection technique and a sampling technique given in the literature along with values predicted by the settling-dispersion model. For very low solid loading (0.3% v/v), no variation in the radial and axial concentration profiles was noticed. It was concluded that the LST is adequate for the study of solid/liquid suspensions with higher solids content, but it will need rigorous matching of refractive index.

Nasr-El-Din et al. (1996) used sample withdrawal technique in a stirred tank for the measurement and analysis of solids concentration. The concentration profiles were found dependent on the particle size, overall concentration and the impeller rotation speed. A variation in the solids concentration at radial and axial positions was observed. A suspension quality decreased with an increase in particle size. A homogeneous suspension at low particle size was obtained, whereas, at a high particle size a clear liquid layer was observed near the top surface. It was due to the higher settling velocity of larger particles. Increasing the impeller speed also resulted in an increase in the suspension quality because of the higher turbulence and dispersion force counteracting the force due to gravity. At high impeller speeds, liquid possesses high kinetic energy which is transferred to the particles, hence, resulting in their suspension.

Brunazzi et al. (2004) developed a new probe based on the measurement of electrical impedance to measure solid/liquid hold-up in stirred tank reactors working with high solid concentration (up to 40% by weight). The probe was designed to measure the whole cross section of the stirred vessel, as the two electrodes were two rings positioned on the vessel wall and shaft. The main advantage of the probe was that it was fairly non-intrusive and can be used for both laboratory-scale and industrial stirred tank reactors. The spatial resolution of the probe was found to be 3cm.

Barigou (2004) investigated the capabilities of non-intrusive techniques such as PET and PEPT for the flow field and circulation study in stirred tanks (opaque system). PET is a technique used in medicine, where a positron-emitting radioactive tracer is introduced and its distribution is determined by detecting the pairs of back-to-back γ-rays arising from electron-positron annihilation. PEPT is a technique working on the same principle whereby a single tracer particle can be tracked at high speed within operating equipment. They found that PET and PEPT offer a far superior approach for analysis of such systems.

Guha et al. (2007) used CARPT for the flow field measurement at two solid concentrations of 1% and 7% by volume. CARPT is a powerful non-invasive monitoring technique capable of providing the actual trajectories of a tracer particle in “opaque” multiphase flows. This yields the Lagrangian information about the velocity vector along the particle trajectory from which the complete 3-D velocity distributions and turbulence parameters can be obtained.

Pianko-Oprych et al. (2009) measured the flow field in a stirred tank with pitched blade turbine using PIV and PEPT and compared the results. The agreement between the data produced by PIV and PEPT was very good. For the measurements with the solids present, velocity data could not be collected by PIV both because of lack of penetration and of severe scattering of the light beam. For the PEPT technique, data were obtained as effectively for both phases as under the two previous operating conditions. Overall, the ability of PEPT to give good quantitative results when PIV was unable to provide any information at all in the presence of even a small quantity of solids and air was confirmed.

Stevenson et al. (2010) studied solid concentration in a stirred tank using magnetic resonance imaging(MRI) and electrical resistance tomography (ERT) and compared the results. ERT is similar to conductivity probe, but it is non-invasive and needs accurate calibration and reconstruction. MRI has high resolution (up to 10 mm). Its reconstruction is well defined, non-invasive and can observe transport phenomena. But, it cannot be used for ferrous material and is limited to bore of the magnet (often <70mm). The two techniques presented complementary attributes, with ERT better suited to larger length-scales and faster temporal resolutions whilst MRI provided better spatial resolution and quantitative velocity mapping.

Table 2.3 provides a summary of the experimental methods prominently used in the study of stirred tanks. It is clear from this table, that the hydrodynamics of CIL systems can be quantified by CARPT and PEPT which are non-intrusive, have sufficient resolution and can operate in opaque systems.

Table 2.3. Summary of advantages and limitations of experimental techniques used in the study of solid-liquid stirred tanks (Chaouki et al., 1997, Roy et al., 2002, Stevenson et al., 2010).

Method	**Spatial Resolution**	**Advantages**	**Limitations**	**References for more details**
Visual	Very Low	Simple and accurate, although element of subjectivity in determining N_{js}. Non-invasive	Can only be applied to low volume fractions of solids (<10%) and clear suspension solutions	(Zwietering, 1958, Sardeshpande et al., 2009)
Direct sampling	Low	Not limited to opacity or solids concentration	Invasive. Affected by withdrawal velocity, sample geometry and relative position in the flow field	(Barresi and Baldi, 1987, Nasr-El-Din et al., 1996)
Conductivity probe	Low	Conductivity can be related to volume fraction through the Maxwell relation, with accurate determination	Invasive. Disrupts flow field	(MacTaggart et al., 1993, Nasr-El-Din et al., 1996, Bujalski et al., 1999, Micheletti, 2003, Spidla et al., 2005)
ERT	Low	Similar to conductivity probe, but non-invasive. Large amounts of information captured easily and quickly	Need accurate calibration and reconstruction. Resolution limited to 5% (typically) of vessel diameter	(Hosseini et al., 2010, Stevenson et al., 2010)
Optical and PIV (laser, LED)	Good	Can be accurately calibrated allowing multiple sampling positions. Non-invasive	Limited to low solid conc. (4 wt%-typically) due to opacity limitations	(Fan et al., 2005, Pianko-Oprych et al., 2009, Unadkat et al., 2009)
PEPT	Medium (8 mm)	Non-invasive and long experimental times due to very low temporal resolutions	Medium resolution. Resolution decreases with increasing particle velocity.	(Barigou, 2004, Guida et al., 2009, Pianko-Oprych et al., 2009)
CARPT	Medium (7 mm)	High data collection rate and trackability of more than one solids type.	Medium resolution (due to errors in position reconstruction and “Steric” Limitation))	(Guha et al., 2007, Guha, 2008)
MRI	High (0.1 mm)	High resolution (up to 10 μm). Reconstruction well defined. Non-invasive. Can observe transport phenomena	No ferrous material. Limited to bore of magnet (often <70 mm). Experiments can range from minutes to hours	(Stevenson et al., 2010)

Bujalski et al. (1999) studied the clear liquid layer formed near the top surface in a mixing tank. The effect of the layer on the suspension and mixing time was observed. The layer resulted in elongated mixing time due to lesser turbulence dissipation. With the finer solids, the suspension occurred at low impeller speeds and hence, the phenomenon of clear liquid layer was prominent. A high average concentration increased the clear liquid layer as it dampened the turbulence resulting in weak velocity vectors in the upper region of stirred tanks. In the case of scale-up, the aspect ratio of the stirred tank increased and the zone of the clear liquid layer increased resulting in further elongation of mixing time.

Wu et al. (2001) analyzed the pumping velocity, flow turbulence and other flow characteristics in relationship to the impeller geometric parameters and proposed few correlations relating pumping rate, just suspension speed and Power. No change in the shape of the velocity profiles was observed with the change of the geometrical parameters like pitch angle, number of blades and blade thickness for both PBTs and RTs. Based on the data obtained, the authors proposed a correlation for the pumping rate produced for a given power input. They also recommended the use of pumping rate, $N_Q \sim 0.70\ P_o^{1/3}$ for PBTD and $N_Q \sim 0.42\ P_o^{1/3}$. After analysing the just suspension speeds for various geometries, a relationship between impeller pumping and solids suspension was given as $N_{js}* N_Q=$ constant. The impeller pumping was also correlated with solids suspension using the relation $N_Q*S = K$, where S is a parameter in Zweitering’s correlation and K is a dimensionless constant independent of solid/liquid property.

Bittorf and Kresta (2003) proposed a model for the prediction of cloud height based on a mean flow assumption. Turbulent fluctuations and macroinstabilities were measured in the clear fluid layer and were found to be negligibly small. It was due to the turbulence damping as the presence of solids resulted in the reduced velocity field. It was observed that the impeller discharge jet impinges on the bottom of the tank and then spread radially towards the wall. The combination of this stream with the swirling flow, also driven by the impeller and constrained by the baffles, produced a three-dimensional wall jet along the baffle. The jet reached its maximum velocity at a height of $0.2<z/T<0.3$. Beyond this point, the velocities in the jet began to decay. The decreased velocities could drag the solids up to a certain height called cloud height. Given the local maximum velocities in the wall jet and the suspension properties of the system, the interface height can be predicted using U_m,C_H/V_{tip},N_{js}=0.08 for dimensionless cloud heights from 0.6 to 0.8. The correlation of cloud height using the velocity of just suspension, C/T ratio and D/T ratio was proposed.

Micheletti (2003) investigated the effects of off-bottom clearance, solids concentration, particle size and the particle density in a solid-liquid stirred tank. Solids radial concentration data indicated the presence of variation at radial points. The higher off-bottom clearance resulted in a longer mixing time because it creates a weaker circulation loop below the impeller that takes more time to suspend the particles. At speeds well below Njs, the suspension was low and hence, the product of impeller speed and mixing time ($N^*\theta_m$) was the same as in single phase flow. With the increase in impeller speeds, $N^*\theta_m$ increases because the velocities in the vessel are reduced in the presence of particles, hence increasing the overall mixing time. After a certain speed, the solids were completely suspended and the vessel started behaving like a single phase system and the $N^*\theta_m$ again approaches a single phase value. The value of $N^*\theta_m$ increased with the increase in solids concentration and particle diameter for the same reason of solids damping the turbulence in the vessel. A sensitivity study of power number was performed and it was found to be a function of both concentration and impeller clearance. The low density particles were found to suspend at lower impeller speeds as the settling velocity is less and is easily counteracted by dispersion force.

Brunazzi et al. (2004) measured solid/liquid hold-up in stirred tank reactors at high solid concentration (up to 40% by weight).It was observed that the cloud height at just suspension speed for various concentration remains in the range of 0.45 – 0.55 T. Larger impellers showed a better performance with respect to homogenisation with lower speeds, as increased diameter increases the tip speed of the impeller. Preliminary results show that dimensionless axial dispersion coefficient, D_{es}/ND^2, decreases with increasing solid load.

Spidla et al. (2005) studied the particle distribution in a stirred tank with moderate solids concentration (5 and 10% by volume). The fluctuations in solids concentration were less and constant below the cloud height. Due to the turbulent flow and the macro-instabilities, maximum fluctuations were noticed at the cloud height. The level of the cloud height decreased with the increase in solid concentration and decreasing impeller clearance as both of these weaken the flow in the upper part of the vessel. The height of the interface between the clear-liquid layer and the suspension layer was lower in the region above the impeller as the recirculating jet (elliptical flow field) forced solids downwards near the axis.

Angst and Kraume (2006) compared the experimental results of power consumption and solid profiles in stirred tanks for different scale geometries. Since, the suspension speeds were taken for that satisfying the 90% homogeneity criteria, a fairly homogeneous distribution was found irrespective the scale of geometry. High solid concentrations were observed in the secondary vortex below the shaft and along the wall region as the solid particles get dragged by the liquid due to high liquid velocity. A peak was also observed in the bottom centre resulting due to the settling and low velocity region formed just below the secondary vortex. Lower than mean particle concentration regions were found above the impeller near the shaft as the low kinetic energy of the continuous phase in this region renders very little energy to the dispersed phase. Very low concentrations were found near the top surface because of the same reason. Irrespective of the scale of the geometry used, the power numbers were observed to be low due to the presence of solids as compared to single phase systems as the particles dissipate more kinetic energy and reduce turbulence. A homogeneous suspension of the smaller particles at a smaller impeller speed was due to the additional mass of the particles, more kinetic energy is dissipated and the turbulence of the continuous phase is reduced. For impeller speeds higher than H90, an increasing stirrer speed leaded to rising suspension height resulting in a decreasing solids concentration around the stirrer and an increasing velocity of the circulated continuous phase which both result in a rising power number.

Guida et al. (2009) studied the suspension and the effect of solids suspension on the flow field of PBTD and PBTU for a moderately concentrated suspension (up to 10.6% by weight). The high degree of vertical non-uniformity of the suspension was observed with a minimum at the impeller level and a maximum above it, near the central plane. Particle velocities were found to be relatively high in the impeller region and around the centre of the flow loops but low in the upper parts of the tank and in the centre of the loops as the particle gained kinetic energy from the fluid velocity and follow the same trend. The presence of the solid phase caused a reduction in the flow number. Homogeneity increased with the increase in solid concentration for both modes of impeller operation. The radial profiles of the PBTD lie above those of the PBTU due to the higher accumulation of particles beneath the impeller in the case of the PBTU.

Guida et al. (2010) conducted experiments on dense suspensions (up to 40% by weight) using PEPT and studied the flow field and concentration profiled in a stirred tank. The presence of solids has great impact on turbulence. For PBTD, with the increase in the solid concentration, the velocity of impeller discharge stream decreased due to the damping of turbulence. As a result, the point of impact on the bottom moved radially outwards and a slight radially inward and axially upwards shift of the position of circulation loop was observed. For PBTU, with the increase in solids concentration, the lower flow loop was observed to contract with the centre shifting downwards, while the upper flow loop virtually disappeared. At a low solids concentration, the systems tend towards homogeneity with the particles in suspension. At a high solids concentration (above 20 wt%), the rate of increase in homogeneity reduced dramatically for the PBTU as it was not able to disperse the solids settled at the bottom of the tank. For PBTD, the jet was found capable to create turbulent dispersion at the bottom of the tank, hence dispersing the settled solids.

Hosseini et al. (2010) examined the solid –liquid mixing efficiency in a stirred tank with an intermediate to high solids loading (5-30 wt%). The Electrical Resistance Tomography (ERT) was used to find the solid concentration profiles. The effect of the impeller type, off-bottom clearance, impeller speed, power and particle size on the homogeneity was studied. The impeller with the highest pumping rate resulted in the achievement of homogeneity with the least power consumption. A very small off-bottom clearance resulted in the low velocity zone at the bottom centre of the tank. In the case of high off-bottom clearance, fluid strike with low velocities at the bottom. In both of these cases, low homogeneity was observed. The homogeneity was observed to increase with the increase in the impeller speed. The impeller speed greater than that required for the maximum homogeneity was observed to be detrimental because the strong centrifugal forces create a low solids concentration region in the centre. The large size as well as high density particles has large settling velocities and hence, were harder to suspend as compared to finer solids.

Stevenson et al. (2010) studied solid concentration in a stirred tank using ERT and MRI and noticed that the overall particle concentration was found to influence the radial concentration resulting in non-uniform radial profiles. The particle concentration was observed to decrease with increasing agitation speeds due to increasing suspension. Homogeneity is achieved well before achieving Zwietering's N_{js} correlation, suggesting the overprediction by the correlation. No any improvement in homogeneity was found by increasing impeller speed above N_{js}.

2.5.4 Computational Hydrodynamic Studies

Rasteiro et al. (1994) examined the solid concentration profiles using the sedimentation-dispersion model. The axial variation in concentration was studied for the change in the average concentration, particle size and impeller clearance. The increase in average concentration resulted in the axial variation in concentration profiles for the same impeller speed, as the higher concentration led to more turbulent dispersion and hence, the continuous phase velocities decreased. The lesser continuous phase velocity resulted in suspension of lesser solids. The larger particles, having experienced larger force due to gravity and have a high inertial mass, result in a less uniform axial distribution. For the low clearance, the critical impeller speed was lesser due to a high velocity jet from the axial impeller hitting the bottom. At the same time an increase in the power number for a homogeneous suspension was required as the weak velocity flow field was observed to be present in the upper part of the mixing tank.

Altway et al. (2001) performed simulations to predict solid concentration profile in stirred tanks. The simulation results were verified using Yamazaki et al. (1986). The agreement using the Algebraic Slip Model (ASM) was found to be especially excellent for systems with low solid concentration. The largest deviation occurred in the region near the shaft where the downward axial velocity comes in contact with the rotation of the shaft. The solid concentration profiles show that the highest solid concentration occurs on tank bottom centre, as the kinetic energy of the liquid was not able to overcome the potential energy of the particles at the bottom. In the region near to the liquid surface, the solid concentration decreases sharply due to the negative buoyant jet behavior. The simulation results showed the presence of concentration peak on impeller plane. The results were compared for different particle sizes and a more uniform suspension was found with smaller diameter particles. The larger particles have more force due to gravity acting on it.

Micale et al. (2004) used Multiple Reference Frame (MRF) and Sliding Grid (SG) approach to study the clear liquid layer and the suspension height for dense solid–liquid systems. Not much difference between the MRF and SG approach was observed. With the increase in solid concentration, the clear liquid layer was observed to reduce progressively with increasing impeller speed. Increase in impeller speed resulted in the increase in liquid axial velocity that exceeded the particle settling velocity. The flow field structure progressively changes with the increase in the particle concentration resulting in shorter and sharper suspension layers. Simulated power numbers were 2.98, 2.74 and 2.68 for N = 5, 6.33 and 8 rps respectively (particle loading of 9.6% v/v), which were significantly smaller than the experimental values of 4.59, 4.37 and 4.23. The imperfection in the solid suspension prediction was attributed to all those second order effects (particle drag modifications due to liquid turbulence as well as to the presence of other particles, particle–particle direct interactions, etc.) that were neglected in the study.

Brunazzi et al. (2004) compared the dispersion values of solid and liquid phases with experimental values and found that the assumption of $D_{es} = D_{el}$ in modelling was found to be only true in low solid concentration systems and was declared unacceptable for high solid concentration (above 20% by weight) systems.

Ochieng and Lewis (2006) employed Computational Fluid Dynamics (CFD), Laser Doppler Velocimetry (LDV) and optical attenuation methods to investigate the nickel solids off-bottom suspension and cloud height in a fully baffled elliptical bottomed tank agitated by a hydrofoil propeller Mixtec HA735. The cloud height was visualised as a sudden concentration gradient and was a result of negative buoyant jet behaviour. In a fully developed flow field, there was one major circulation loop and a minor one with its centre at about x=0.2T, r=0.8R. The minor circulation loop was a result of the deflection of the horizontal stream by the wall at x=0.2T and represented a region of poor mixing. There were voids behind the impeller blades, which represent the trailing vortices. In front of the blades there were small regions of high solid concentration. It was concluded that a low clearance results in better mixing because the turbulence dissipation occurs along a short path between the impeller blade tip and the tank bottom. The CFD simulation under-predicted Njs especially for the larger particles (dp=150μm). For the much larger particles (dp N300μm), both the Zwietering correlation and CFD under-predicted Njs. The CFD predictions were better than Zwietering correlation for the smaller particles. The high Njs can be attributed to the curvature at the bottom of the tank. Higher liquid kinetic energy is required to overcome the overall potential energy of solids for solid suspension and larger particles with more inertia lose more kinetic energy on collision as compared to smaller particle. In both of these cases, higher liquid kinetic energy and hence, higher just suspension speed was needed. For the same reason, a rapid increase in the cloud height is observed with an increase in the impeller speed and the decrease in cloud height with an increase in the solids loading.

Ocheing and Lewis (2006) investigated the solids concentration distribution in stirred tanks with high solids loading (0-20% by weight) using Eulerian-Eulerian simulations. The flow field in the presence of particles was observed to change because of the high density of the particles and their interaction with wall jet. A decrease in the axial velocity was observed. At a high solid concentration, the turbulence and drag become very important parameters in solid suspension. The turbulent structure provides energy to disperse the high concentration of solid particles, but at the same time the solid particles may result in the dampening of the turbulence. These depend on the integral length scale and the diameter of the particles. The cloud height was observed to decrease with an increase in the particle concentration. This is due to weak velocities present in the upper part of the tank because of the dissipation of kinetic energy of the fluid to suspend a larger number of particles. The study on the polydisperse particles suggested the larger kinetic energy dissipation due to collisions of larger particles and resulting in settling. The concentration profiles were studied and the suspension of smaller particles was evident.

Kasat et al. (2008)used a computational fluid dynamics (CFD) based model to understand the complex interactions between the suspension quality and the fluid mixing process and compared predictions with the experimental data of axial solid concentration profile reported by Yamazaki et al. (1986). The mixing time, calculated from the tracer concentration history recorded at eight different locations, is the time required for the tracer concentration to lie within (±5%) of the final concentration ($C\infty$). Cloud height marked by the sudden concentration gradient leaves a clear liquid layer near top surface. The kinetic energy in this zone is very low which leads to high values of mixing time in the clear liquid layer. The computational model has also predicted significant reduction in liquid velocity values in this region. Beyond N = 25 rps, the dimensionless mixing time decreases gradually with an increase in the impeller rotational speed because the clear liquid layer disappears and the system shows a behaviour, similar to the single-phase stirred reactor. A single loop flow pattern at low impeller speed is because of the presence of solid bed resulting in an apparent low clearance (i.e., false bottom effect), which vanishes with increasing rotational speed above 300 RPM.

Ocheing and Onyango (2008) employed an Eulerian based polydispersed multiphase simulation approach to investigate the effects of drag models and operating parameters on nickel solids concentration distribution. The CFX built-in drag models and the Brucato drag were studied. The solids concentration distribution and settling velocity were analysed by the non-intrusive optical attenuation technique (OAT). The prediction by the Gidaspow and Schiller–Naumann models observed to be similar in most parts of the tank. The better results provided by the Brucato drag model was attributed to the mixing due to turbulent eddies or turbulent dispersion, which was not accounted for by both the Gidaspow and Schiller–Naumann models. It has been mentioned that for $d_p/\lambda>10$, the interaction between energy dissipating eddies and particles become important for the solids concentration distribution. The effect of the method of obtaining εCFD on the solids concentration distribution was also assessed. The results of the solids concentration distribution obtained with εCFD (based on the assumption of homogeneous turbulence level in the complete system) were indistinguishable from those of the Schiller–Naumann model. This was due to the fact that these values represent a gross under-prediction of the turbulent kinetic energy dissipation rate, and hence, an over-prediction of λ, leading to a small value of the free stream turbulence correction term in the Brucato model. Consequently, the Brucato model effectively became Schiller–Naumann model. Power consumption increased exponentially with an increase in the particle loading as a large number of particles required more power to lift from the tank bottom. The under-prediction of the power was consistent with that of the impeller speed required to achieve just off bottom solids suspension (Njs) and this can be attributed to the assumption of regular spherical particles in the simulations. Slip velocity was observed to increase with the particle size as the drag experienced by the particle is opposed by the increased inertial force. The high slip velocity in the impeller region was due to the high fluid velocity relative to that of the solids in the impeller stream. As a result, the particles in the impeller region lagged behind the liquid. Similarly, those in the upward stream in the region closer to the surface lagged behind the liquid, whilst, for the downward stream, particles led the fluid.

Tamburini et al. (2009) conducted CFD simulations adopting Eulerian-Eulerian approach and predicted the transient behaviour of off-bottom suspension for high concentration systems. The results were also compared with the experimental data generated. The observed decrease in suspension height in the central part of the tank up on the impeller disk and movement of solid particles towards more peripheral zones was due to the impeller revolution resulting in the vortex formation behind impeller and the outward jet forcing solids towards the walls. For first two revolutions, the velocities in the vessel were significant near impeller. Later, it was observed that the velocity diffuse into the upper part of the tank because of the velocity jet striking the wall and splitting in axial components. The particles were observed to be present in the regions where the velocities were significant due to the drag. Different drag factors and correlations, viz. fixed $C_D = 6.01$, C_D for particle falling in quiescent liquid (slip-C_D), Wen and Yu and Brucato drag were assessed for the system. Suspension height near the sidewall is slightly overestimated. This may well depend on some drag overestimation when using the Ergun equation under high particle concentration conditions. The introduction of the model Brucato drag, produces a little increase in suspension height. Model slip-C_D, does not yield any significant difference with respect to model fixed-C_D. Any effect of the drag model is not local. The solids volume fraction was noticed to have a uniform value throughout the vessel height at high speed.

2.5.5 Solids Distribution and Homogenisation

Lower concentrations were found near the top and high concentrations were found in the impeller plane (MacTaggart et al., 1993, Barigou, 2004, Angst and Kraume, 2006). Therefore, a high concentration peak was observed on the impeller plane (Altway et al., 2001, Derksen, 2003). High solid concentrations were observed also in the secondary vortex below the shaft and along the wall region as the solid particles get dragged by the liquid due to high liquid velocity (Micale et al., 2000, Derksen, 2003, Angst and Kraume, 2006). A peak was also observed in the bottom centre, resulting due to the settling and low velocity region formed just below the secondary vortex and the low kinetic energy of the liquid was not able to overcome the potential energy of the particles at the bottom (Altway et al., 2001, Angst and Kraume, 2006, Khopkar et al., 2006). As a result, high solids sojourn times were found in the bottom of the reactor (Guha, 2008). Lower than mean particle concentration regions were found above the impeller near the shaft as the low kinetic energy of the continuous phase in this region renders very little energy to the dispersed phase (Micale et al., 2000, Angst and Kraume, 2006). The observed decrease in suspension height in the central part of the tank up on the impeller disk and movement of solid particles towards more peripheral zones was due to the impeller revolution resulting in the vortex formation behind impeller and the outward jet forcing solids towards the walls (Tamburini et al., 2009). In the region near to the liquid surface the solid concentration decreases sharply due to the negative buoyant jet behaviour (Shamlou and Koutsakos, 1989, Altway et al., 2001). In axial impellers, the concentrations above average concentration were found in and below the impeller plane (Barresi and Baldi, 1987, Barigou, 2004). The high degree of vertical non-uniformity of the suspension was observed with a minimum at the impeller level and a maximum above it, near the central plane (Guida et al., 2009).

A variation in the solids concentration at radial and axial positions was observed in stirred tanks (Nasr-El-Din et al., 1996, Micheletti, 2003). But, for very low solid loading, no variation in the radial (Yamazaki et al., 1986, Barresi and Baldi, 1987, Ferreira et al., 1994) and axial concentration profiles was noticed (Ferreira et al., 1994). For the radial impellers, the concentration gradient at radial positions was found to increase with an increase in the particle size. It was due to the increased effect (settling) of gravity in the radial regions where velocity magnitude is low (Barresi and Baldi, 1987). Radial gradient in the concentration was negative in the upper part of the vessel and positive in the lower part. The reason behind these observations is, firstly, the clockwise velocity loop in lower part resulting in a solid accumulation in the centre of the tank and anticlockwise in the upper region, and secondly, the presence of higher magnitude and gradients of velocity in lower part (Micale et al., 2000). A comparatively flat axial concentration profile was obtained for Rushton turbine in the upper part of the vessel, as the solid concentration was below average concentration and most of the solids present in the lower region of the vessel. In very dilute suspensions, the concentration profiles were independent of the mean concentration and attain homogeneity at low impeller speeds (Barresi and Baldi, 1987, Guida et al., 2010). When the solid concentration was high, the homogeneity got worse due to loss of kinetic energy and reduced velocity field and dampening of turbulence (Barresi and Baldi, 1987, Shamlou and Koutsakos, 1989). It also resulted in the axial variation in concentration profiles for the same impeller speed, as the suspension of solids decreased due to reduced continuous phase velocity field (Rasteiro et al., 1994). At a high solids concentration (above 20 wt%), the rate of increase in homogeneity reduced dramatically for the PBTU as it was not able to disperse the solids settled at the bottom of the tank. For PBTD, the jet was found capable to create turbulent dispersion at the bottom of the tank, hence dispersing the settled solids (Guida et al., 2010). The overall particle concentration was found to influence the radial concentration resulting in non-uniform radial profiles. The particle concentration at the bottom was observed to decrease with increasing agitation speeds due to increasing suspension (Stevenson et al., 2010).

Homogeneity is achieved well before achieving Zwietering's N_{js} correlation, suggesting the overprediction by the correlation. No any considerable improvement in homogeneity was found by increasing impeller speed above N_{js}. (Chudacek, 1985, Ibrahim and Nienow, 1999, Stevenson et al., 2010). With the increase in the stirrer speed and the decrease in particle diameter, the variation in the axial concentration decreased as it increased the homogeneity. An increase in homogeneity was observed with the increase in the impeller speed as the mean kinetic energy and hence, turbulence in the flow increased (Shamlou and Koutsakos, 1989, Sessiecq et al., 1999, Tamburini et al., 2009, Hosseini et al., 2010). Another reason for this behaviour was attributed to the higher turbulence and dispersion force counteracting the force due to gravity (Nasr-El-Din et al., 1996). At Re>10000 values, the movement of particles was generally similar to that observed in water as the dispersed phase follows the continuous phase because of its high kinetic energy (Ibrahim and Nienow, 1999, Kasat et al., 2008). At very high impeller speeds, an increasing stirrer speed lead to rising suspension height resulting in a decreasing solids concentration around the stirrer and an increasing velocity of the circulated continuous phase (Angst and Kraume, 2006). The impeller speed greater than that required for the maximum homogeneity was observed to be detrimental because the strong centrifugal forces create a low solids concentration region in the centre (Hosseini et al., 2010). Little or no hysteresis in particle suspension was observed when the speed was taken to N_{js} and then lowered down (Ibrahim and Nienow, 1999). A hysteresis was observed in achieving the same complete suspension in the case tip speed was increased from low speed from the case in which tip speed was decreased from a high speed of homogeneous suspension (Geisler et al., 1993). At low impeller speeds, a concentration profile with the maximum concentration in the impeller plane was observed as the highly turbulent flow drag particles in this region (Sessiecq et al., 1999). Larger impellers showed a better performance with respect to homogenisation with lower speeds, as increased diameter increases the tip speed of the impeller (Brunazzi et al., 2004). The solids suspension was found to be inversely proportional to the impeller pumping rate (Wu et al., 2001). The impeller with the highest pumping rate resulted in the achievement of homogeneity with least power consumption (Hosseini et al., 2010).

The unsuspended solids are present in the centre and periphery at the bottom of the tank due to the induced recirculation loops. The modified geometries with ‘fully-profiled’ and ‘cone & fillet’ bottom geometries were found effective in reducing the amounts of unsuspended solids. The unsuspended solids present due to sharp flow diversions and low velocity field at the bottom of the tank were absent in such profiled geometry. The ‘cone and fillet’ bottomed geometry was inefficient only for the easily suspended solids i.e. finer particles. In conditions above the complete off-bottom threshold, the performance of ‘cone and fillet’ geometry was better than the ‘profiled bottom’ geometry as the presence of cone was effective for flow diversions (Chudacek, 1985).

A suspension quality decreased with an increase in particle size and had a lower mean axial velocity in the upward flow because of the higher magnitude of the force due to gravity on particles (Nasr-El-Din et al., 1996, Guiraud et al., 1997, Ochieng and Lewis, 2006, Hosseini et al., 2010). It also resulted in less uniform axial distribution (Rasteiro et al., 1994) and decrease in circulation length(Sbrizzai et al., 2006). Large particles accumulate around the bottom centre due to the intermittent spiral vortex formation. As this vortex bursts out of the Ekman layer, many particles moved upwards. With time, the concentration of particles at the bottom increases due to both gravity and their inertia. The vortex was observed to be able to resuspend smaller particles with diameter 0.03 mm as the axial dispersion force counteracted the gravity and inertia of the small particles (Lavezzo et al., 2009). A homogeneous suspension at low particle size was obtained at low impeller speeds (Nasr-El-Din et al., 1996, Altway et al., 2001, Angst and Kraume, 2006, Sbrizzai et al., 2006, Sardeshpande et al., 2009), whereas, at a high particle size a clear liquid layer was observed near the top surface. It was due to the higher settling velocity of larger particles (Nasr-El-Din et al., 1996). The higher off-bottom clearance resulted in a longer mixing time because it creates a weaker circulation loop below the impeller that takes more time to suspend particles (Micheletti, 2003, Ochieng and Lewis, 2006). For axial impellers, a very small off-bottom clearance resulted in the low velocity zone at the bottom centre of the tank. In the case of high off-bottom clearance, fluid strike with low velocities at the bottom. In both of these cases, low homogeneity was observed (Hosseini et al., 2010).

At speeds well below N_{js}, the suspension was low and hence, the product of impeller speed and mixing time ($N*\theta_m$) was the same as in single phase flow. With the increase in impeller speeds, $N*\theta_m$ increases because the velocities in the vessel are reduced in the presence of particles, hence increasing the overall mixing time. After a certain speed, the solids were completely suspended and the vessel started behaving like a single phase system and the $N*\theta_m$ again approaches a single phase value. The value of $N*\theta_m$ increased with the increase in solids concentration and particle diameter for the same reason of solids damping the turbulence in the vessel.

The low density particles were found to suspend at lower impeller speeds as the settling velocity is less and is easily counteracted by dispersion force (Micheletti, 2003). High density particles have large settling velocities and hence, were harder to suspend as compared to low density particles (Hosseini et al., 2010). In the lower part of the vessel, heavy particles tend to be trapped in low-velocity circulation regions which were unable to re-suspend particles toward the high mixing region around the impeller (Sbrizzai et al., 2006). The study of the polydisperse particles suggested the higher kinetic energy dissipation due to collisions of larger particles that resulted in settling (Ochieng and Lewis, 2006). At larger scale, $N^2D^{1.55}$ is constant for a homogeneous suspension, and hence homogeneity is attained at a lower specific power input than on a small scale (Buurman et al., 1986).

2.5.6 Radial Concentration Profiles

Radial concentration profile below 0.1 dimensionless height is shown in Figure 2.7 and Figure 2.8 for low solid loading and high solid loading cases. The concentration profiles demonstrate the presence of peaks in the bottom centre of the stirred tank. Low concentrations are visible in the periphery regions and show little accumulation. Homogenisation at very low concentration at low impeller speeds is also clearly visible, as it is evident from the concentration values near the bottom that lie around the average concentration in the stirred tank and the flat nature of the profile. The concentrations above the speed of just suspension are near the average concentration. But, this is not evident by the experimental data available in the literature. Moreover, no any difference in the concentration profiles was observed with the increase in the impeller speeds. At higher concentrations, different patterns were observed in the experimental data. The trend that was observed by Stevenson et al. (2010) is right opposite to that observed by Guha et al. (Guha, 2007). The differences are due to the limitations of the experimental techniques through which reliable and accurate values cannot be obtained with the experiments conducted on stirred tanks.

When the concentration profiles between the dimensionless height 0.1 and 0.2 were plotted, the impact of the concentration peak on the profiles was not evident in this zone. At the speeds above the just suspension speed, a flat profile with concentration approximately equal to the average concentration was observed (Figure 2.9). Barresi et al. (1987) observed a radial decrease in concentration. But the gradient in the concentration was not steep. A high quality suspension is noticed at comparatively higher levels in stirred tanks within this zone as it approaches the impeller. The increase in concentration dampens the turbulence and hence the drag observed by the particles is less. Therefore, the suspension quality is poorer at 10% average concentration than the 5% concentration.

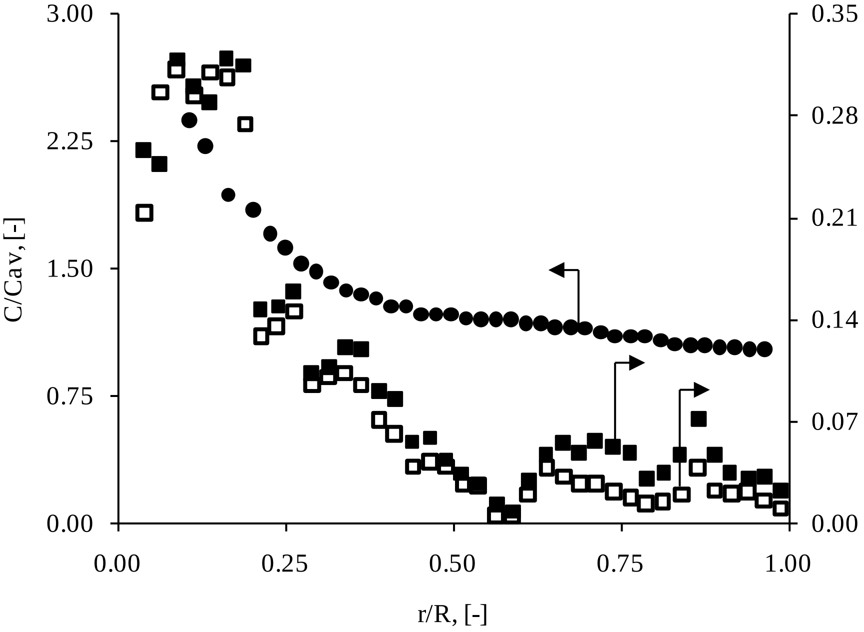

● - z/Z = 0.1 RPM = 390 Cav = 0.0056 Barresi et al. (1987) ■ - z/Z = 0.075 RPM = 850 Cav = 0.01 Guha et al. (2007) □ - z/Z = 0.075 RPM = 1000 Cav = 0.01 Guha et al. (2007)

Figure 2.7. Comparison of radial concentration between z/Z 0.0 to 0.1 (at low concentration).

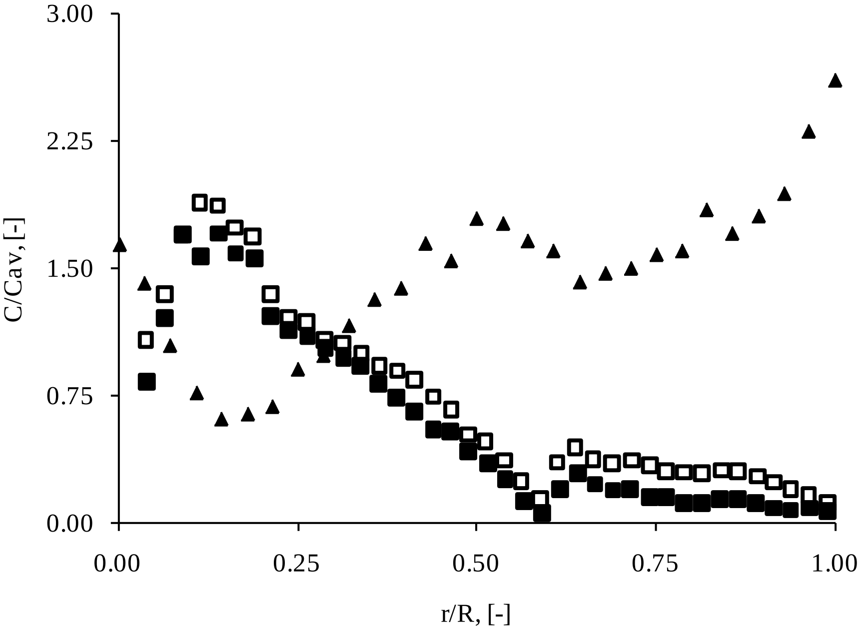

▲ - z/Z = 0.02 RPM = 480 Cav = 0.1 Stevenson et al. (2010) ■ - z/Z = 0.075 RPM = 1050 Cav = 0.07 Guha et al. (2007) □ - z/Z = 0.075 RPM = 1200 Cav = 0.07 Guha et al. (2007)Between dimensionless height 0.1 and 0.2

Figure 2.8. Comparison of radial concentration between z/Z 0.0 to 0.1 (at high concentration).

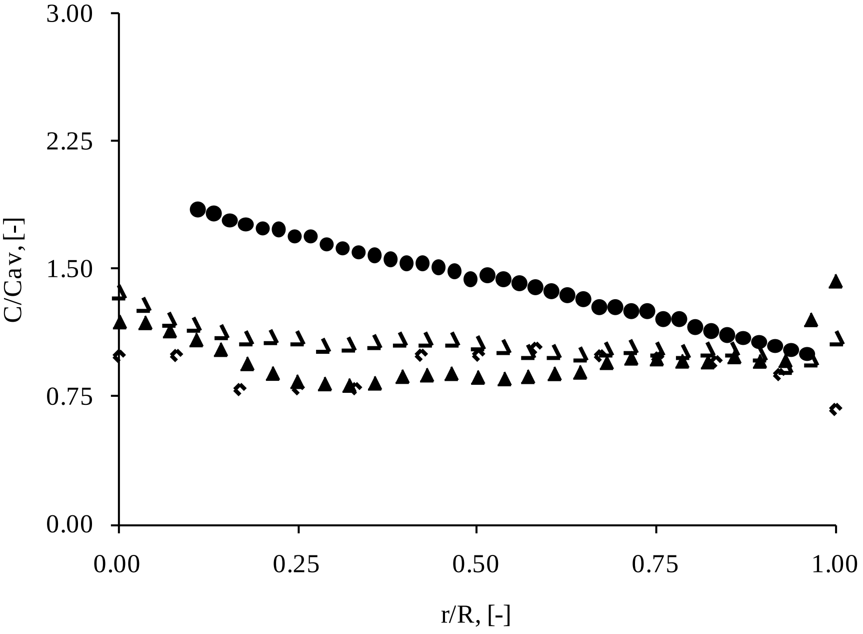

● - z/Z = 0.19 RPM = 390 Cav = 0.0056 Barresi et al. (1987) ◊ - z/Z = 0.14 RPM = 480 Cav = 0.05 Stevenson et al. (2010) ▲ - z/Z = 0.14 RPM = 480 Cav = 0.1 Stevenson et al. (2010) Δ - z/Z = 0.18 RPM = 480 Cav = 0.1 Stevenson et al. (2010)

Figure 2.9. Comparison of radial concentration between z/Z 0.1 to 0.2.

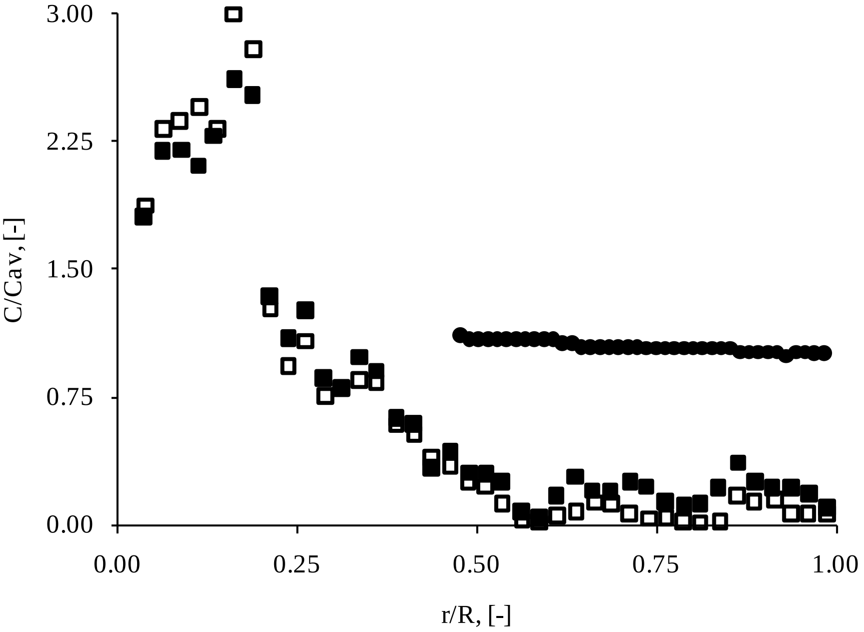

● - z/Z = 0.29 RPM = 390 Cav = 0.0056 Barresi et al. (1987) ■ - z/Z = 0.25 RPM = 850 Cav = 0.01 Guha et al. (2007) □ - z/Z = 0.25 RPM = 1000 Cav = 0.01 Guha et al. (2007)

Figure 2.10. Comparison of radial concentration between z/Z 0.2 to 0.3 (at low concentration).

The region just below the impeller, i.e. dimensionless height between 0.2 and 0.3, is under the influence of high turbulence and flow field. Due to this, the concentration in this zone is uniform at speeds near or above the just suspension speeds irrespective of the concentration (Figure 2.10 and Figure 2.11). A very slight radial decrease in the velocity is observed due to the gradient in the axial velocities pushing the solids from the region of high axial velocities to the region of lower axial velocities. Relatively high concentration region adjacent to the walls denotes the accumulation of solids near the wall due to no slip condition on the wall and centrifugal force applied on the particles.

In the impeller zone (between dimensionless height 0.3 and 0.4), the turbulence and flow field are the maximum. It is the region with the highest slip velocities, as the particles experience opposite turbulent and inertial forces. The quality of suspension depends on the impeller speed. The impeller draws the particles from the top and bottom in the centre region and then thrusts it radially outwards with the jet. Therefore, the concentration in this zone is uniform and the profile obtained is flat (Figure 2.12). In the studies just above the impeller plane, a radial increase in concentration was observed due to the migration of particles from the zone of higher axial velocities to lower axial velocities.

The zone of dimensionless height 0.65 is the region far above the impeller plane, where the flow field starts to diminish (Figure 2.13). The magnitude of the velocity in this region is far lower as is observed in the region of impeller plane. Flat concentration profiles were observed by Yamazaki et al. (1986). However, this was not the case as was found in other studies conducted in this field (Guha, 2007). Guha (2007) noticed that the concentrations are far lower than the average concentration as the fluid is not able to drag the particles to this height and the suspension has not achieved homogeneity.

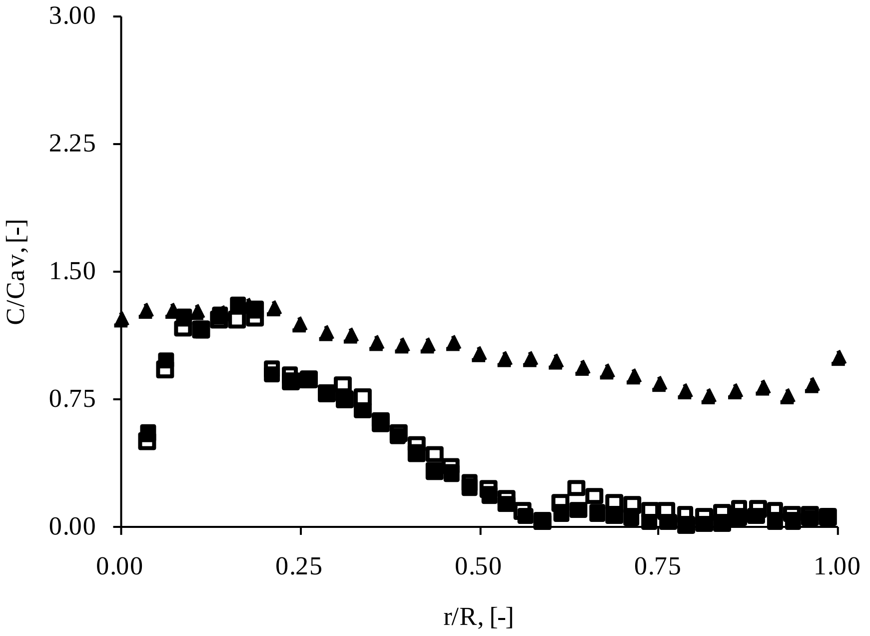

▲ - z/Z = 0.29 RPM = 480 Cav = 0.1 Stevenson et al. (2010) ■ - z/Z = 0.25 RPM = 1050 Cav = 0.07 Guha et al. (2007) □ - z/Z = 0.25 RPM = 1200 Cav = 0.07 Guha et al. (2007)

Figure 2.11. Comparison of radial concentration between z/Z 0.2 to 0.3 (at high concentration).

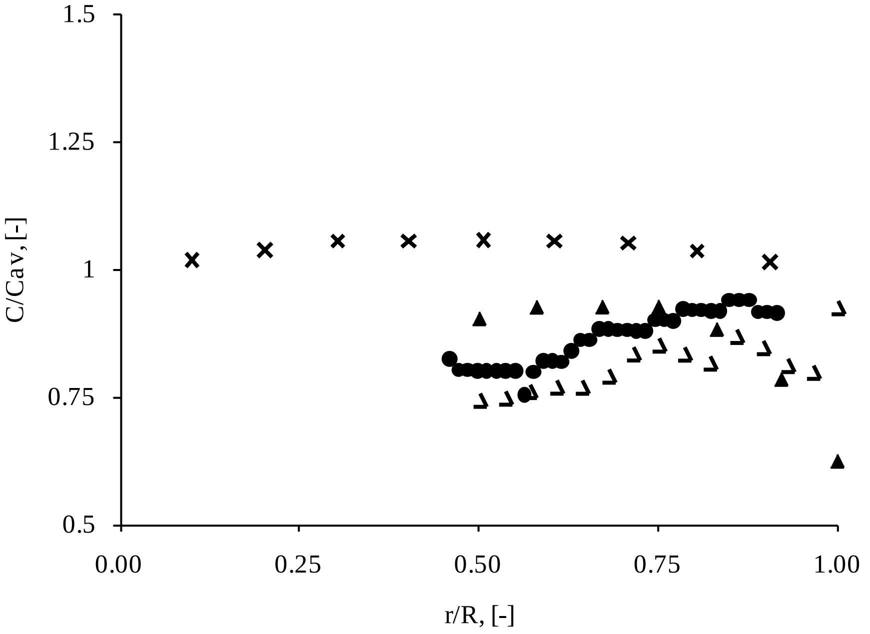

● - z/Z = 0.39 RPM = 390 Cav = 0.0056 Barresi et al. (1987) ▲- z/Z = 0.38 RPM = 480 Cav = 0.05 Stevenson et al. (2010) Δ - z/Z = 0.38 RPM = 480 Cav = 0.1 Stevenson et al. (2010) X - - z/Z = 0.35 Cav = 0.15 Yamazaki et al. (1986)

Figure 2.12. Comparison of radial concentration between z/Z 0.3 to 0.4.

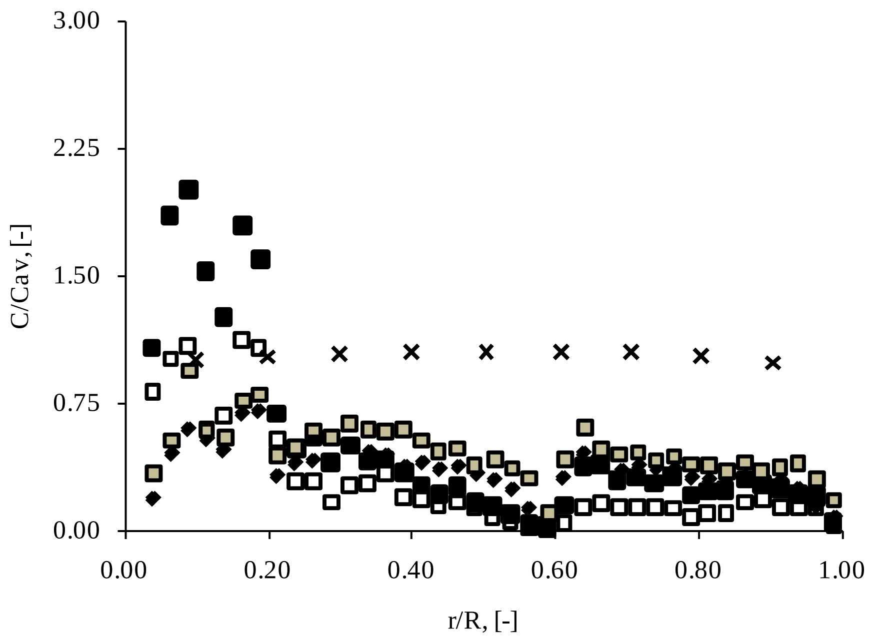

X - z/Z = 0.65 Cav = 0.15 Yamazaki et al. (1986) ■ - z/Z = 0.65 RPM = 850 Cav = 0.01 Guha et al. (2007) □ - z/Z = 0.65 RPM = 1000 Cav = 0.01 Guha et al. (2007) ♦ - z/Z = 0.65 RPM = 1050 Cav = 0.07 Guha et al. (2007) ▣ - z/Z = 0.65 RPM = 1200 Cav = 0.07 Guha et al. (2007)

Figure 2.13. Comparison of radial concentration at z/Z =0.65.

2.5.7 Axial Concentration Profiles

On comparing the axial concentration profiled in radius below 0.3, flat profiles are observed in the cases the impeller speed is well above the just suspension speed. This also shows that no cloud height is present at high impeller speeds (Figure 2.14 and Figure 2.15). On a contrary, the concentration is near the average concentration in the lower part of the stirred tank system. But, at higher axial locations, the concentration diminishes and approaches near zero values at low impeller speeds. The axial velocities in these cases are not that high to lift the particles to the top of the tank. As a result, a sudden drop of concentration in the upper portion of the tank and presence of cloud height is observed. At any of these impeller speeds, the concentration near the surface is always lower than the average concentration due to the comparatively low velocity magnitude and the air entrapment. With the same impeller speed, the low concentration solids show greater homogeneity. The low impeller speed is able to provide enough momentum to the particles that it gets carried to the top part of the tank and renders homogeneity.

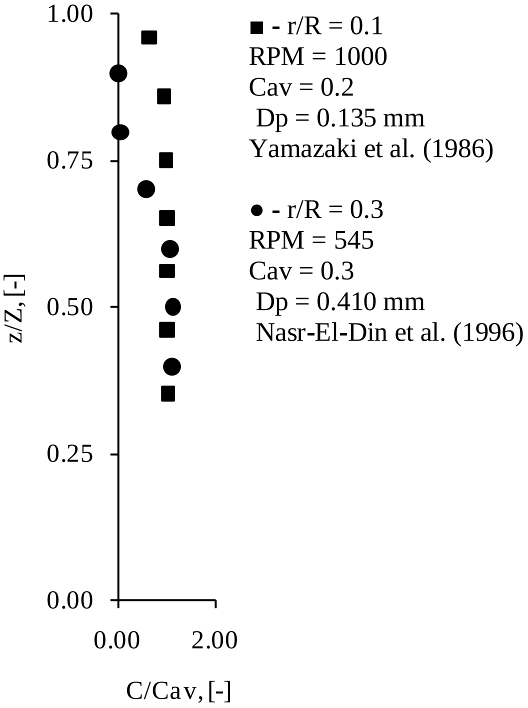

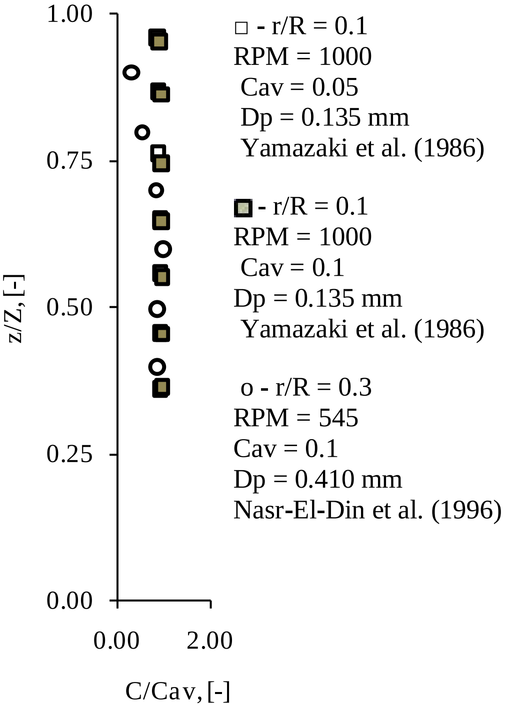

Figure 2.14. Comparison of axial concentration between r/R 0.0 to 0.3 (at high concentration).

Figure 2.15. Comparison of axial concentration between r/R 0.0 to 0.3 (at low concentration).

The influence of high velocity impeller tip is visible in the concentration profiles in the region between radius 0.3 and 0.6. At the impeller tip a ‘belly shaped’ profile is obtained (Figure 2.16 and Figure 2.17). The reason for this behaviour can be attributed to the high turbulence and velocities thrusting the solid particles out of the impeller zone, and the phase of deceleration starts as the particles cross the impeller zone. As a result the accumulation is evitable in this region. The same impact of the concentration and impeller speed was also observed in the profiles of this zone.

In the region above the dimensionless radius of 0.6, the concentration profile at high impeller speed is flat all over except the impeller zone (Figure 2.18). In the impeller zone, the fluctuations in the concentration are visible even above the radius of 0.6 the tank radius. Near the bottom, the concentration of solids is very high at low impeller speeds due to accumulation (not shown here). At high impeller speeds and high concentration, the concentration near the wall increases due to the centrifugal force experienced by the particles. At the same time the measurement of concentration near the walls is complicated, as the intrusive techniques interferes with the rapid change in the flow behaviour of the particles and the non-intrusive techniques not able to resolve the data near walls.

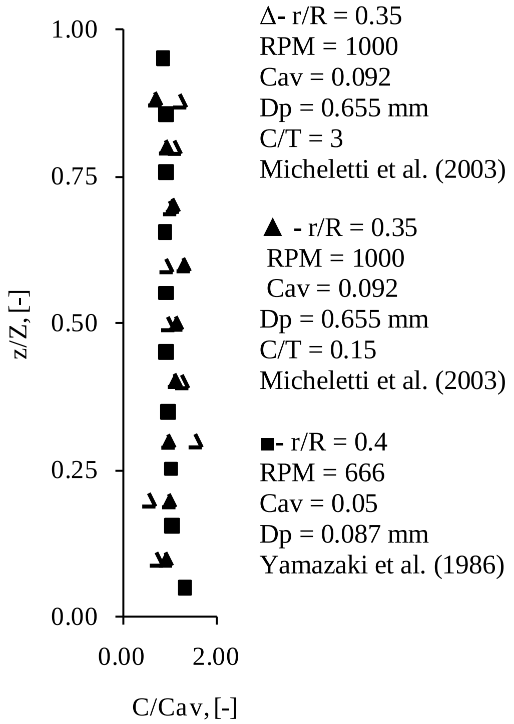

Figure 2.16. Comparison of axial concentration between r/R 0.3 to 0.6 (at low concentration).

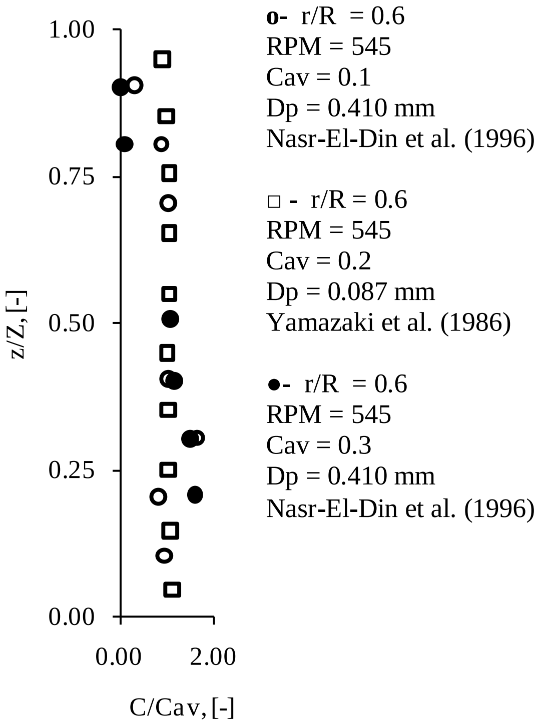

Figure 2.17. Comparison of axial concentration between r/R 0.3 to 0.6 (at high concentration).

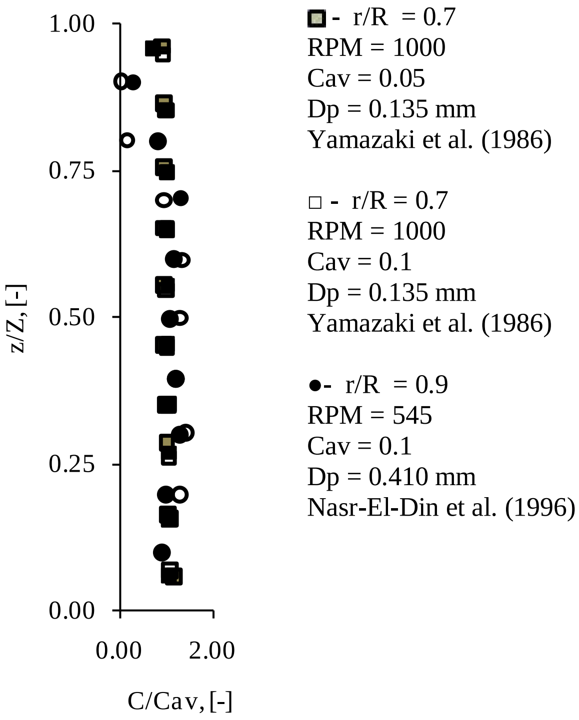

Figure 2.18. Comparison of axial concentration above r/R = 0.6.

2.5.8 Cloud Height

Turbulent fluctuations and macroinstabilities were measured in the clear fluid layer and were found to be negligibly small. It was due to the turbulence damping as the presence of solid result in the reduced velocity field. Beyond a certain height, the velocities in the jet began to decay. The decreased velocities could drag the solids up to a certain height called cloud height (Bittorf and Kresta, 2003). The cloud height was visualised as a sudden concentration gradient and was a result of negative buoyant jet behaviour (Ochieng and Lewis, 2006, Kasat et al., 2008, Fletcher and Brown, 2009). The fluctuations in solids concentration were less and constant below the cloud height. Due to the turbulent flow and the macro-instabilities, maximum fluctuations were noticed at the cloud height (Spidla et al., 2005). It was observed that the cloud height at just suspension speed for various concentrations remains in the range of 0.45 – 0.55 T (Brunazzi et al., 2004). The cloud height was observed to increase with the increase in the impeller speed till it reached 90% of the tank height above which the air entrapment in the top layer resulted in unpredictability (Buurman et al., 1986). At lower solid loading, the cloud height remained unaffected because of the homogeneity attained at a lower impeller speed (Sardeshpande et al., 2009).

The level of the cloud height decreased with the increase in solid concentration (Spidla et al., 2005, Ochieng and Lewis, 2006, Ochieng and Lewis, 2006) and decreasing impeller clearance as both of these weaken the flow in the upper part of the vessel (Spidla et al., 2005). With the increase in solid concentration, the cloud height was observed to rise progressively with increasing impeller speed. Increase in impeller speed resulted in the increase in liquid axial velocity that exceeded the particle settling velocity. The flow field structure progressively changes with the increase in the particle concentration resulting in shorter and sharper suspension layers (Micale et al., 2004). The cloud height first decreased and then increased with the increase in impeller speed due to the formation of false bottom resulting from the settled bed of particles which disappears when the speed is increased (Ochieng and Lewis, 2006, Sardeshpande et al., 2009). The height of the interface between the clear-liquid layer and the suspension layer was lower in the region above the impeller as the recirculating jet (elliptical flow field) forced solids downwards near the axis (Spidla et al., 2005).

Mixing time (θ_m) was found to depend on cloud height and on solid loading (when solid loading is above 3% v/v). The mixing time initially increased with an increase in impeller speed due to the increasing suspension of solids (reduction in pumping number) and then decreased due to the attainment of homogeneous suspension and acquiring the flow field of a single phase flow (Sardeshpande et al., 2009). The clear liquid layer above the cloud height resulted in elongated mixing time due to little turbulence dissipation (Bujalski et al., 1999, Kasat et al., 2008, Sardeshpande et al., 2009). Beyond N = 25 rps, the dimensionless mixing time decreases gradually with an increase in the impeller rotational speed because the clear liquid layer disappears and the system shows a behaviour, similar to the single-phase stirred reactor (Kasat et al., 2008).

With the finer solids, the suspension occurred at low impeller speeds and hence, the phenomenon of the clear liquid layer was prominent. A high average concentration increased the clear liquid layer as it dampened the turbulence resulting in weak velocity vectors in the upper region of stirred tanks. In the case of scale-up, the aspect ratio of the stirred tank increased and the zone of the clear liquid layer increased resulting in further elongation of mixing time (Bujalski et al., 1999).

2.5.9 Flow Field

For radial impellers, a high velocity jet plunge the solids outside, that hit the wall and loses kinetic energy (Derksen, 2003). After hitting the wall, jet splits into two axial streams and forms two loops (Sbrizzai et al., 2006). A single loop flow pattern at low impeller speed is because of the presence of solid bed resulting in an apparent low clearance (i.e., false bottom effect), which vanishes with increasing rotational speed (Kasat et al., 2008). The stronger lower circulation loop is observed because of the high magnitude axial velocities striking the bottom, which is not the case in the region above impeller (Guha, 2008). Due to the trailing vortices and high velocity, large velocity fluctuations were observed in the vicinity of the impeller. Turbulent kinetic energy and the dissipation rate were found to be the maximum at blade tip because of the same reason (Sbrizzai et al., 2006). The turbulence of the flow dampened due to the presence of particles. Because of the presence of higher concentration of particles, this influence is strongest in the impeller plane. High concentration of particle reduced suspension and hence, a higher concentration below the impeller reduced the strength of the lower vortex. The case is just the opposite in the upper region for the same reason (Derksen, 2003).

For axial impellers, the flow of the jet was observed to hit the bottom after being pumped, which then moved radially out towards the walls in the presence of particles, and jet velocity decreased due to the dampening of turbulence (Guiraud et al., 1997, Bittorf and Kresta, 2003, Virdung and Rasmuson, 2007, Guida et al., 2010). The combination of this stream with the swirling flow, also driven by the impeller and constrained by the baffles, produced a three-dimensional wall jet along the baffle (Bittorf and Kresta, 2003). The fluid moves upwards forming a complete loop. The absence of the vortex was due to the axial impeller and baffles in the system. The tangential velocity increased linearly from the axis due to the degradation of the axial component, reached a maximum of 0.15Vtip at r/D = 0.32 and then decreased near the wall due to baffles (Guiraud et al., 1997). There were voids behind the impeller blades, which represent the trailing vortices (Ochieng and Lewis, 2006, Sbrizzai et al., 2006). Particle velocities were found to be relatively high in the impeller region and around the centre of the flow loops but low in the upper parts of the tank and in the centre of the loops as the particle gained kinetic energy from the fluid velocity and follow the same trend (Guida et al., 2009). With axial impellers, a distinct flow pattern consisting of two flow loops, one above and one below the impeller plane, was established up to solids concentrations of 3 wt% (Barigou, 2004). For PBTU, with the increase in solids concentration, the lower flow loop was observed to contract with the centre shifting downwards, while the upper flow loop virtually disappeared (Guida et al., 2010).

Particle velocity reduced in the central bulk region probably because of particle crowding in this area (Barigou, 2004). As the study of the secondary phase was conducted for very low volume fraction (0.5 volume %), negligible change in the flow behaviour was observed. Even at high Reynolds numbers, the circulation patterns of the dispersed phase seemed to be modified when the rotation speed is changed (Guiraud et al., 1997, Unadkat et al., 2009). No significant change in the shape of the velocity profiles was observed with the change of the geometrical parameters like pitch angle, number of blades and blade thickness for both PBTs and RTs (Wu et al., 2001).

A significant reduction in liquid velocity values was also observed for solid liquid flows near the top surface (Khopkar et al., 2006). The radial velocity profiles of the PBTD lie above those of the PBTU due to the higher accumulation of particles beneath the impeller in the case of the PBTU which reduces the velocity (Guida et al., 2009). Although the impellers used were hydrofoil axial impellers, the discharge from the impeller was found to be radial. This was because of the viscous power law fluid which shortened the axial velocity flow. Higher fluid recirculation and longer trajectory were obtained at higher speeds and higher impeller clearance, as it increased the trajectory length and provided more space below the impeller. The momentum transfer performance was superior for A320 impeller because of the greater width that increased the pumping rate (Barigou, 2004).

The presence of particles decreases the velocity gradients in the immediate vicinity of the impeller blades, as well as causing a general decrease in the fluctuating velocities throughout the jet stream (Unadkat et al., 2009). An increase in particle loading reduced the frequency of particle circulation substantially in a more or less linear fashion and the motion of particles became less ordered. These effects were explained by an increase in particle–particle interactions as circulation increased, which would lead to longer more tortuous particle trajectories (Barigou, 2004). Higher (compared to the bulk) particle velocities were reported underneath the impeller blade and in the discharge stream (Unadkat et al., 2009). The turbulent structure provides energy to disperse the high concentration of solid particles, but at the same time the solid particles may result in the dampening of the turbulence (Barresi and Baldi, 1987, Nouri and Whitelaw, 1992, Bittorf and Kresta, 2003, Ochieng and Lewis, 2006). These depend on the integral length scale and the diameter of the particles (Ochieng and Lewis, 2006). The settling velocity changes in the stirred tank in the conditions where the particle diameter was comparable to the Kolmogoroff microscale and eddies have significant influence on particle motion (Magelli et al., 1990). For $dp/\lambda>10$, the interaction between energy dissipating eddies and particles become important for the solids concentration distribution (Ochieng and Onyango, 2008). Only when the particle size is sufficiently close to the eddy length microscale, the particle behaviour was unaffected by external turbulence. The eddy–particle interaction was reasoned as the basic mechanism for solids distribution in a stirred liquid (Pinelli et al., 2004). It is the reason that the settling velocity near the top surface overcomes the dispersion force and the concentration near the surface decreases. The air entrapment phenomenon was also found to be delayed due to the damping effect of turbulence (Micale et al., 2002). But close to the tank walls, increased turbulence was noticed because of the shorter integral length scale (Ljungqvist and Rasmuson, 2004).

The ratio of the liquid flow velocity to the falling velocity of the solid particles, u/uf, which coincides with the model parameter ratio P_{ef}/P_{es}, is approximately proportional to the impeller speed under the complete suspension conditions. This is mainly due to the decreased upflow velocity in the liquid phase caused by the strong interference by the solid particles. Although it was that the agitation with the radial flow impeller was more effective for solids suspension in comparison with the agitation with the axial flow impeller on an impeller speed basis, but it was recommended that the efficiency of agitation should be compared on an energy basis (Yamazaki et al., 1986). With the increase in impeller speed the turbulence increased, and the decrease in particle diameter resulted in low inertial effects (Barresi and Baldi, 1987). R.M.S. velocities were found to be higher in the presence of solids than in the single phase flow. But, R.M.S. velocities decreased with the increase in particle size. Both of these observations were based on the effect of the ratio of particle diameter to integral length scale on the turbulent intensity. If this ratio is less than 0.1, the turbulent intensity decreases while if it is greater than 0.2, the turbulent intensity increases. This is expected as smaller particle follows the trend of the fluid, thus dissipating its kinetic energy, while larger particles will result in a bigger wake, in turn resulting in more energy being transformed from mean flow to turbulent kinetic energy (Virdung and Rasmuson, 2007).

The study of the polydisperse particles suggested the larger kinetic energy dissipation due to collisions of larger particles (Ochieng and Lewis, 2006). The profiled bottom tank was found to be the most efficient as a smoother profile of high velocity led to the complete suspension (Chudacek, 1985). No influence of the particle shape on the flow and orientation was observed because of the strong turbulence in stirred tanks. As a result, the influence of particle shape is negligible in contrast to the effects of the impeller. In the region far from the impeller, the turbulence effects are low and the orientations of the particle change little with impeller speed and remain steady with the increasing radial coordinates (Fan et al., 2005).

2.5.10 Slip Velocities

The mass transfer is directly related to the slip velocities. High mass transfers were observed in the regions of high slip velocities (Ljungqvist and Rasmuson, 2001, Ljungqvist and Rasmuson, 2004). For radial impellers, Slip velocities were observed to be the maximum in an impeller plane as a result of vigorous turbulent motion and the particle inertia (Derksen, 2003). The vortices behind impeller reduce the kinetic energy of the particles due to erratic behaviour and collisions, and hence, decrease its velocity (Khopkar et al., 2006). For axial impellers, the large values of radial slip velocities were observed in the impeller plane because of the presence of high turbulent jet and the particle inertia (Guiraud et al., 1997). The largest slip velocities in the investigated part of the vessel were obtained just beneath the impeller as the particles experience both inertial and gravitational forces (Ljungqvist and Rasmuson, 2001, Ljungqvist and Rasmuson, 2004, Ochieng and Onyango, 2008). The values of slip velocities for the radial and tangential component obtained were also not significant (Guiraud et al., 1997). Radial transport of particles from a region with high axial fluid velocity into a region of lower axial fluid velocity caused the large particles to move faster than the surrounding fluid and vice versa (Ljungqvist and Rasmuson, 2004). The slip velocities increased with the increase in the density of particles as high density particles possess more inertia than low density particles. Increased particle size had a greater effect on the axial slip than increased particle density. This was explained by taking the Stokes theory into account according to which the settling velocity is proportional to the square of particle diameter but only a factor of density difference of the phases (Ljungqvist and Rasmuson, 2004). With the increase in the concentration, the slip velocity increased because of the loss of solid phase kinetic energy due to particle-particle collision and particle-wall collisions (Nouri and Whitelaw, 1992). In the regions where the axial velocity is upward, the particles were found to lag behind the fluid while particles led in the regions of downward axial velocities due to directions of gravity and inertia effects. This is the region that the axial slip velocity decreases with downflow and increases in upflow (Nouri and Whitelaw, 1992, Guiraud et al., 1997, Ljungqvist and Rasmuson, 2001, Ljungqvist and Rasmuson, 2004, Ochieng and Onyango, 2008, Pianko-Oprych et al., 2009). The axial velocity was found to be very sensitive to D/T and C/T when the results from the literature were compared (Pianko-Oprych et al., 2009).

2.5.11 Drag Models

Micale et al. (2000) predicted particle concentration distribution in stirred tanks using two modelling approaches - Settling velocity model (SVM) and multi-fluid model (MFM). For both the models, it was concluded that the increase in particle drag coefficient due to turbulent flow must be accounted for to give a good simulation of experimental data. Ljungqvist and Rasmuson (2001) tested four different drag models viz. Schiller-Nauman, Ishii-Zuber, Ihme and Brucato and found that these four models give very similar results for the cases simulated. However, the radial and tangential slip velocities were under-predicted while the axial slip velocities were over-estimated in the major part of the vessel. This was due to the free-stream turbulence in the vessel which increases the drag on the particles. Derksen (2003) suggested the inclusion of the particle drag coefficient based on the Reynolds number and solid volume fraction to take into account the hydrodynamic interactions between multiple particles. Micale et al. (2004) used Multiple Reference Frame (MRF) and Sliding Grid (SG) approach to study the clear liquid layer and the suspension height for dense solid–liquid systems. They attributed the imperfection in the solid suspension prediction to all those second order effects (particle drag modifications due to liquid turbulence as well as to the presence of other particles, particle–particle direct interactions, etc.) that were neglected in the study. Khopkar et al. (2006) modified Brucato drag model and simulated the solid suspension in a fully baffled reactor and compared the results with experimental results of Yamazaki et al. (1986) and Godfrey and Zhu (1994). They performed a computational study to understand the drag observed by the particles as a result of the high turbulence in the stirred tanks, flow through a bank of regularly arranged cylinders. Ignoring the possible influence of the solid volume fraction and particle Reynolds number, the predicted results were correlated considering the sole dependence on dp/λ for a range of solid holdup values (5 -25%). The results obtained provided a factor of 0.1 to the Brucato Drag correlation and the new correlation was termed as Modified Brucato Drag. The computational model with both the formulations reasonably predicted the solid holdup distribution and shows a relatively small influence of the drag coefficient formulation on the predicted results. The solid holdup distribution using the modified correlation showed the presence of more solids at the bottom of the reactor compared to that predicted using the Brucato drag coefficient formulation. The modified Brucato correlation was also able to predict the presence of a clear liquid layer. Ochieng and Lewis (2006) employed Computational Fluid Dynamics (CFD) to investigate the nickel solids off-bottom suspension and cloud height in a fully baffled elliptical bottomed tank agitated by a hydrofoil propeller Mixtec HA735 using Gidaspow drag model. Ocheing and Lewis (2006) investigated the solids concentration distribution in stirred tanks with high solids loading (0-20% by weight) using Eulerian-Eulerian simulations with Gidaspow and Lopez de Bertodano models. They noticed that at the high solid concentration, the turbulence and drag become very important parameters in solid suspension. Ocheing and Onyango (2008) employed an Eulerian based polydispersed multiphase simulation approach to investigate the effects of drag models and operating parameters on nickel solids concentration distribution. The CFX built-in drag models and the Brucato drag were studied. The prediction by the Gidaspow and Schiller–Naumann models observed to be similar in most parts of the tank. The better results provided by the Brucato drag model was attributed to the mixing due to turbulent eddies or turbulent dispersion, which was not accounted for by both the Gidaspow and Schiller–Naumann models. Kasat et al. (2008) used a computational fluid dynamics (CFD) based model to understand the complex interactions between the suspension quality and the fluid mixing process and compared predictions with the experimental data of axial solid concentration profile reported by Yamazaki et al. (1986). The modified Brucato drag model was validated and used in the study. Guha (2008) conducted numerical simulations and assessed different approaches viz. LES and Eulerian-Eulerian to simulate turbulent solid–liquid flow in a low solid loading (1% by volume) stirred tank by comparing with the results from the CARPT experiment. LES predicted radial velocities better than the Euler-Euler in the impeller plane. It was because of the high turbulent fluctuations in this region that was not taken into account by the drag formulation used (Schiller-Nauman model). Fletcher and Brown (2009) predicted the cloud height in a stirred tank and analyzed the role of various modelling approaches, turbulence modelling and particle drag law formulations on the predictions of CFD models. No significant difference was reported by them in the use of Schiller Naumann and Richardson and Zaki drag models for the prediction of cloud height. Tamburini et al. (2009) conducted CFD simulations adopting Eulerian-

Eulerian approach and predicted the transient behaviour of off-bottom suspension for high concentration systems. Different drag factors and correlations, viz. fixed Cd = 6.01, Cd for particle falling in quiescent liquid (slip-Cd), Wen and Yu and Brucato drag were assessed for the system. Suspension height near the sidewall is slightly overestimated. This may well depend on some drag overestimation when using the Ergun equation under high particle concentration conditions. The introduction of the Brucato drag model produces a little increase in suspension height. Model slip-CD, does not yield any significant difference with respect to model fixed-CD. Any effect of the drag model is not local.

2.5.12 Scale-up

Buurman et al. (1986) derived a scaling up rule for the stirred tanks assuming the turbulence to be isentropic. The scale-up rule was given as, $N_{js} \propto D^{-0.666}$. The power consumption was found to be sensitive to the blade thickness. An increase in the blade thickness increased the pumping rate and resulted in the decrease in stirrer speed, and hence, power for achieving the same suspension. The cloud height was observed to increase with the increase in the impeller speed till it reached 90% of the tank height above which the air entrapment in the top layer resulted in unpredictability. At larger scale, $N^2D^{1.55}$ is constant for a homogeneous suspension, and hence homogeneity is attained at a lower specific power input than on a small scale.

Magelli et al. (1990) investigated the solids distribution in high aspect ratio stirred tanks under batch and semibatch conditions. The system was modelled using sedimentation-dispersion model. Not much difference was observed between the profiles of batch and semi-batch systems. An increase in impeller speed, liquid velocity and a decrease in particle size and density resulted in the flat concentration profiles. All these factors resulted in lowering of the slip velocities between the phases resulting in a homogeneous suspension. The scale-up rules were also derived and found that a constant tip speed or a constant $ND^{0.93}$ was appropriate. The main discrepancy lies in the extent of the influence of power consumption. The settling velocity changes in the stirred tank in the conditions where the particle diameter was comparable to the Kolmogoroff microscale and eddies have significant influence on particle motion.

Montante et al. (2001) conducted computational analysis and validated it with experiments for a high aspect-ratio baffled tank agitated with pitched blade turbines. The solid concentration was analyzed. Higher concentration of solids was found above the impeller as the axial impeller creates a single loop forcing the solid below the impeller to the peripheral regions, from where they circulate and move above the impeller. Pinelli drag model and the standard drag models were also evaluated and Pinelli drag model provided a better comparison with the solid hold-up distribution. The overall power number was 20% less than that calculated for each of the impeller as the power dissipated in the overall volume is lowered due to scale-up. In scaled up geometries, the particle dispersion process was noticed to be dominated by convective mixing (related to average velocities) and only to a minor extent by turbulent dispersion.

Montante et al. (2003) analyzed the scale-up criteria for stirred tanks based on the dependency of minimum impeller speed as a function of impeller diameter or the dependency of settling velocity on the λ/d_P. The results were also compared with the data available in the literature. A constant tip speed was deduced as a reliable criterion for the scale-up for λ/d_P in the range outside 0.01 and 0.2. In other intermediate complex conditions, the tip speed was suggested to have a factor less than 1. Another scale-up criteria for $N_{js} \propto D^{-n}$, was derived from the experimental data (n=0.93) and provided a value of n different from that provided in literature (n=0.63). The difference in the scale-up parameters in the different studies was due to change in geometrical parameters such as bottom shape (torispherical vs. flat), the use of one vs. multiple impellers and the size of the vessels.

It is evident from the review that the scale-up rule for the stirred tanks presented by different authors is the same with ND^{-n} to be constant as the scale up criterion and n varying between 0.63 and 0.93.

2.6 Drag for Carbon Particles

Other than ore particles, CIL tanks also contain large carbon particles. The concentration of carbon particles (~1% v/v) is much lower than the ore particles (~ 25% v/v). Therefore, the interaction of carbon particles with the ore particles is considerable and the flow of carbon particles will get affected. No any different drag model is available to address such a huge difference in volume fraction in bidisperse systems. Moreover, the drag experienced by the carbon particles is different in the presence of high concentration of ore than that in stagnant fluid.

In order to calculate drag on the carbon particles a different outlook of the problem can be used. Rather than considering the CIL system as a mixture of ore particles, carbon particles and liquid, it has also been considered as a mixture of non-Newtonian slurry and larger carbon particles (Jones and Horsley, 2000). Osan (1990) investigated the rheological characteristics of ore slurries in CIL circuit and found it as yield-pseudoplastic non-Newtonian fluid.

The drag force acting on the large carbon particles can be obtained by either conducting experiments or by conducting numerical simulations that resolve the forces acting on the particle. Experiments can provide accurate results but are time consuming and expensive. Numerical simulations enable the accurate calculation of drag force after validation in an inexpensive way. Eulerian-Langrangian (EL) and Langrangian-Langrangian (LL) approaches can be used for such simulations. The criteria of selection of the suitable numerical approach used will be accuracy and numerical inexpense. In the next section, the different numerical approaches are discussed and analysed in detail. In the 5th chapter, the selected technique will be validated using experimental data and then the results from the simulations will be used for the modelling of drag for large carbon particles.

2.7 EL and LL Multiphase Simulation Approaches

In Eulerian-Lagrangian approach, the fluid phase is considered as a continuum and Reynolds averaged Navier-Stokes equations are solved, while the solid phase is considered as a collection of discrete particles obeying Newton’s law. The particles dissipate energy either by collision or by surface friction (Walton, 1993). The inelastic collision between the particles is calculated by the spring-dashpot model by Cundall and Strack (Cundall and Strack, 1979). In case of collisions, the energy dissipation is usually described via the coefficient of normal restitution e, which is defined as the factor by which the postcollisional relative velocity of two particles in the normal direction is reduced as a result of dissipation, compared with a fully elastic collision. The surface friction is governed by the friction coefficient, f, and affects the relative tangential velocity at the contact point, at which both sticking and sliding can occur. One can also include the dissipation of energy in the tangential direction, governed by a coefficient of tangential restitution, e_t (Walton, 1993).

Eulerian-Lagrangian approach again consists of two approaches based on the description of the solid phase viz. unresolved discrete particle model (UDPM) and resolved discrete particle model (RDPM) (Figure 5.1 (a) and (b)). In RDPM, the stick boundary condition is applied in which the fluid velocity disappears at the surface of solid spheres. For this, Lagrangian force points are defined which are uniformly distributed on the surface of a particle. The velocity of each force point is calculated from the linear and angular velocity of the sphere. The fluid-solid interaction is then controlled by a force density which is added to the momentum conservation equation. The force densities are calculated from the constraint that at each force point, the local fluid velocity should match the local particle velocity.

In UDPMs, the size of the grid is typically an order of magnitude larger than the size of particles. Therefore, the particles act as only the point sources and sinks of momentum. Or in other words, the particles in the domain act as Lagrangian force points. The force density is also calculated from a correlation rather than force balance. Moreover, the volume of the fluid phase is not occupied by the solid particles, and therefore, it is artificially incorporated (Hoef et al., 2008). Again, the correlations for the fluid-solid interaction are critical for the accuracy of the simulations.

The Lagrangian-Lagrangian approach considers both the solid and fluid phases as particles and so the interaction are accounted for by the collisions of fluid and solid particles (Figure 5.1 (c)). No empirical correlations are used for the calculation of interactions. Moreover, the grid size is an order smaller than the size of particles. LL is expected to resolve the forces around carbon particles and be the most accurate method for drag force calculation but it would be computationally more expensive. Due to its computational intensity, the LL approach is limited to obtain the interaction parameters between the two phases which are then used in the EE/EL model (Beetstra et al., 2006).

From the above discussion, it is evident that the fluid-solid models are significantly different from each other in their ability to capture the physics and requirement of the computational power. Since, UDPM considers particle as a point mass which makes it unsuitable to take into account the actual drag and lift forces. RDPM approach provides the accuracy at a lesser computational expense when compared to DNS. In this study, MPM (Agrawal et al., 2009) will be used for drag calculations, which is based on RDPM approach.

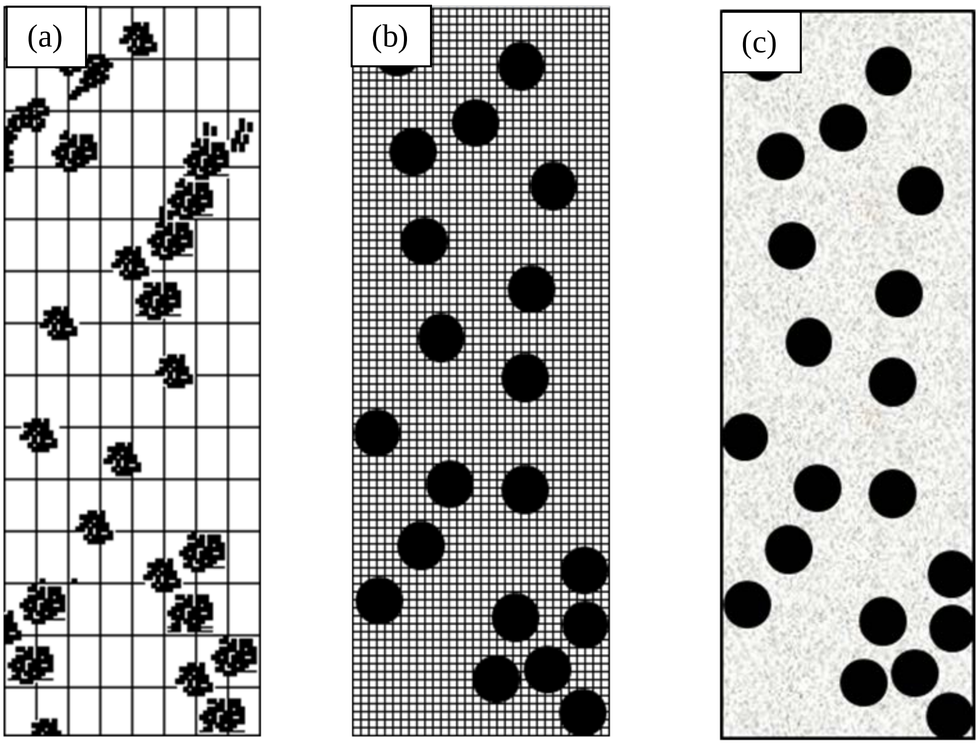

Figure 2.19. Resolution of phases using (a) UDPM (b) RDPM and (c) L-L approach (Beetstra et al., 2006).

2.8 Summary and Research Direction

In this chapter, various aspects of CIL tanks , such as the mechanism of leaching and adsorption, hydrodynamics of tanks used for this process have been discussed.

Since a significant amount of research has already been conducted on developing novel kinetic and mechanism for gold adsorption, the objective of this research was not study this aspect but to employ the most suitable mechanism into a range of multi-scale models. It is also clear from the above literature review that the existing phenomenological models for CIL tanks do not include the reaction kinetics and mechanism suitable for industrial applications. Therefore, a new phenomenological model taking into account this factor has been developed in this research. In addition, currently, there is a clear lack of understanding on the hydrodynamics of CIL tanks especially at higher solid loadings typical of industrial applications. Finally, there is a significant knowledge-gap on the hydrodynamics of carbon particles in a CIL tank. In this research we have used a novel macroscopic particle model to impart a greater understanding on the flow and hydrodynamics of carbon particles.

Chapter 3 Phenomenological Modeling of CIL Circuit

In order to increase the recovery rate of CIL process, a clear understanding of its kinetics, mechanism and dynamics is necessary. While a lot of effort has been focused on understanding the kinetics and mechanism of leaching and adsorption (Stange, 1991, Walt and Deventer, 1992, Kiranoudis et al., 1998, Deventer et al., 2004, Coetzee and Lalloo, 2005, Lima and Hodouin, 2006, Lima, 2007), the system dynamics has not received due attention. The dynamics is affected by various operating parameters like cyanide and oxygen concentration, particle size and competitive adsorption.

This chapter presents a first principles based dynamic model that links system performance to the operating parameters. Transient simulations were carried out in order to understand real time response of the system. Effect of the operating parameters on the performance of the system was assessed.

3.1 Phenomenological Model

The schematic of CIL process is shown in Figure 3.1. In CIL in series, the crushed gold bearing ore is mixed with cyanide solution and lime and is passed through a series of stirred tanks. While passing through the process, gold continuously leaches in the cyanide solution. Subsequently, carbon is passed through the series of tanks counter-currently. Counter-current carbon transfer takes place using slurry pumps at regular intervals. The screens installed in each tank restrict carbon to flow in co-current direction and only allows smaller ore particles to pass through. During its counter-current passage through the tanks, carbon continuously adsorbs gold from the cyanide solution. Therefore, in the first tank, the concentration of gold on carbon is the highest. This carbon is sent to the elution circuit for gold removal. The slurry coming out of the last tank contains negligible quantity of gold in ore and in solution.

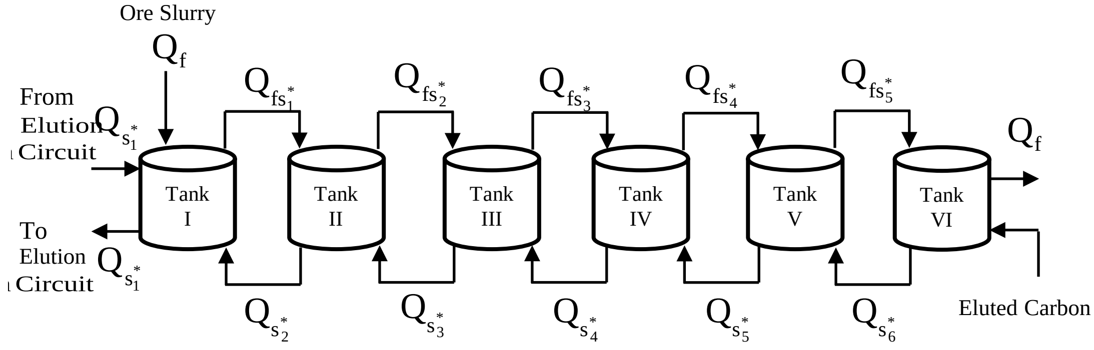

Figure 3.1. Schematic of CIL cascade.

3.2 Model Development

In order to achieve the objective of understanding the dynamics of the process, a simulation model was developed. The following aspects were considered:

a) The rate of leaching
b) The rate of adsorption
c) The rate of cyanide consumption
d) The exchange of mass between the tanks

The first three aspects involve the choice of an appropriate rate expression that can account for most of the process parameters explicitly. This will provide the flexibility to study the impact of the parameters like cyanide concentration, oxygen concentration and ore particle diameter on the process dynamics and in turn, to optimise it. The final aspect deals with the interaction between the tanks. The model includes mass balance of gold, ore, carbon and slurry over the whole process as well as individual units.

3.3 Assumptions for CIL Model

The CIL tanks were treated as CSTR with perfect mixing. In the current model, the hydrodynamic factors affecting leaching and adsorption kinetics are lumped in the kinetic parameters of leaching and adsorption. Bypass of the inlet feed of a tank to its outlet stream was considered negligible as the use of axial impellers generates a non-radial flow. The slurry flows down along the impeller, avoiding any significant bypass. The carbon considered, whether fresh or regenerated, has negligible deterioration or fouling while passing across the CIL circuit. No carbon loading profile is considered in the study and carbon transfer is considered to occur simultaneously at regular intervals, as it is not in the scope of current research. However, the proposed phenomenological model provides the flexibility to use a carbon loading profile or change the carbon transfer cycle. pH in the process is maintained above 10 and, therefore, the process is assumed to occur at a constant pH. The effect of the competitive species is not explicit in the kinetic models. However, the effect is lumped in the leaching rate equation.

3.4 Kinetics

3.4.1 Leaching

The model proposed by Lima and Hodouin (2005) includes most of the critical process parameters such as the cyanide consumption, mean particle diameter of ore, oxygen concentration and unleachable gold concentration of the ore. The leaching rate proposed by Lima and Hodouin (2005) is given as:

$$r_{leach} = \frac{dC_{Au}}{dt} = -k\left(C_{CN^-}\right)^{\alpha}\left(C_{O_2}\right)^{\beta}\left(C_{Au} - C_{Au}^{*}\right)^{\gamma} \qquad \ldots\ldots\ldots(3.1)$$

where, k is a rate constant, C_{CN^-} is the cyanide concentration, C_{O2} is oxygen concentration, C_{Au} is gold concentration in ore, C_{Au}^{*} is the residual gold concentration in ore and α, β and γ are the reaction order with respect to cyanide, oxygen and gradient of gold concentration respectively.

In this rate expression, both k and C_{Au}^{*} are functions of particle diameter.

$$C_{Au}^{*} = a\left(1 - be^{-c\bar{d}_{ore}}\right) \qquad \ldots\ldots\ldots(3.2)$$

$$k = k_{Au_1} - k_{Au_2}\,\bar{d}_{ore}^{\,\theta} \qquad \ldots\ldots\ldots(3.3)$$

where a, b, c, k_{Au_1}, k_{Au_2} and θ are model parameters and $\overline{d}_{ore}$ is mean diameter of ore particle.

There is a significant difference in the leaching rate calculated using different kinetic equations. In lieu of valid plant data, the Mintek rate equation (Nicol et al., 1984) was used as a reference. The leaching rate calculated from Lima and Hodouin (2005) is slower compared to the Mintek rate equation (see Figure 3.2). This deviation can be attributed to the dependence of the leaching kinetics parameters, especially residual gold concentration on ore type. The leaching rate was, therefore, modified so that the predicted reaction rate closely matches Mintek rate equation. The modified residual gold concentration and k values are given by:

$$C_{Au}^{*} = 0.357\times10^{-4}\left(1-1.49e^{-0.0176\overline{d}_{ore}}\right) \qquad \text{.........(3.4)}$$

$$k = 0.00513 - 2.28\times10^{-10}\overline{d}_{ore}^{\,2.93} \qquad \text{.........(3.5)}$$

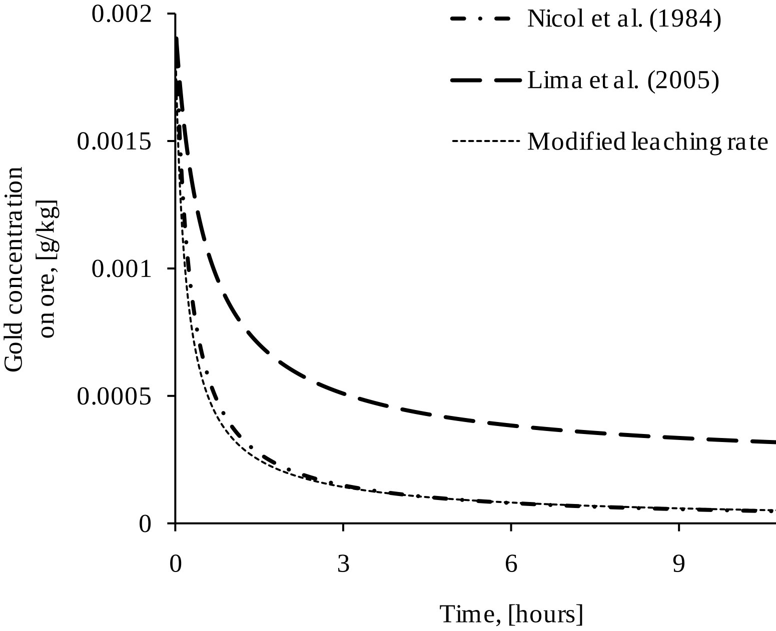

Figure 3.2. Comparison of leaching rates.

3.4.2 Adsorption

Numerous models for adsorption are available (Dixon et al., 1976, Fleming et al., 1980, Fleming and Nicol, 1984, Nicol et al., 1984, Woollacott et al., 1990, Kiranoudis et al., 1998). The film diffusion model with Langmuir isotherm was preferred over a detailed pore diffusion model as the latter is computationally intensive and demands information on many parameters that are not related to the process and are hard to estimate. The film diffusion model with Langmuir isotherm as described in Chapter 2 is given as:

$$\frac{dq}{dt} = A_c k_f \left(C - \frac{bq}{q^+ - q} \right) \qquad \text{………(3.6)}$$

where A_c is the surface area per unit mass of carbon, k_f is the film mass transfer coefficient, C is the concentration of gold in liquid, q is the concentration of gold on carbon, q^+ is the maximum gold loading on carbon and b is fitting parameter.

3.4.3 Cyanide Consumption

The cyanide consumption kinetics were determined using the free cyanide concentration and particle diameter by Lima et al. (2005). The expression is given as:

$$-r_{CN^-} = k_{CN^-} [CN^-]^{\eta} \qquad \text{………(3.7)}$$

where k_{CN^-} is the overall rate constant expressed as a function of ore particle diameter and η is the order of reaction.

The rate constant is expressed as:

$$k_{CN^-} = \frac{k_{CN_1^-}}{\bar{d}_{ore}^{\,\varphi} - k_{CN_2^-}} \qquad \text{………(3.8)}$$

where $k_{CN_1^-}$, $k_{CN_2^-}$ and φ are model parameters.

The value of the model parameters was found by Lima et al. (2005) and are used in the CIL model as it is. These values are given in Equation 3.15.

3.5 CIL Equations

Considering the assumptions stated in Section 3.3, the equations for CSTRs were written and the mass balance equations were written incorporating leaching and adsorption. The overall balance on a reactor i can be written as follows:

$$Q_{fs_i^*} = Q_{f^*} + Q_{s_{i+1}^*} \qquad \text{………(3.9)}$$

where Q_{fs^*} is the downflow stream, Q_{f^*} is the slurry feed stream and Q_{s^*} is the flow rate of slurry with carbon transfer.

The balance equations for Gold in liquid phase, in ore and on carbon are given by equations 3.10, 3.11, and 3.12 respectively.

$$\varepsilon_{li} V_i \frac{dC_i}{dt} = \frac{\varepsilon_{l(i+1)}}{\varepsilon_{l(i+1)} + \varepsilon_{o(i+1)}} Q_{s_{i+1}^*} C_{(i+1)} + \frac{\varepsilon_{l(i-1)}}{\varepsilon_{l(i-1)} + \varepsilon_{o(i-1)}} Q_{fs_{i-1}^*} C_{(i-1)} - \frac{\varepsilon_{li}}{\varepsilon_{li} + \varepsilon_{oi}} \left(Q_{s_i^*} + Q_{fs_i^*} \right) C_i + r_{leach} - r_{ads} \qquad \text{……..(3.10)}$$

$$M_i \frac{dG_i}{dt} = \frac{\varepsilon_{o(i+1)}}{\varepsilon_{l(i+1)} + \varepsilon_{o(i+1)}} Q_{s_{i+1}^*} \rho_o G_{(i+1)} + \frac{\varepsilon_{o(i-1)}}{\varepsilon_{l(i-1)} + \varepsilon_{o(i-1)}} Q_{fs_{i-1}^*} \rho_o G_{(i-1)} - \frac{\varepsilon_{oi}}{\varepsilon_{li} + \varepsilon_{oi}} \left(Q_{s_i^*} + Q_{fs_i^*} \right) \rho_o G_i - r_{leach} \qquad \text{……..(3.11)}$$

$$W_i \frac{dQ_i}{dt} = \frac{\varepsilon_{c(i+1)}}{\varepsilon_{l(i+1)} + \varepsilon_{o(i+1)}} Q_{s_{i+1}^*} \rho_c Q_{(i+1)} - \frac{\varepsilon_{ci}}{\varepsilon_{li} + \varepsilon_{oi}} Q_{s_i^*} \rho_c Q_i + r_{ads} \qquad \text{……..(3.12)}$$

The rate equations implemented in the mass balance equations are as follows:

Leaching: $$r_{leach} = k \left(C_{CN^-} \right)^{\alpha} \left(C_{O_2} \right)^{\beta} \left(C_{Au} - C_{Au}^* \right)^{\gamma} \qquad \text{……..(3.13)}$$

Adsorption: $$r_{ads} = \frac{6 k_{fj} W_i}{\rho_c d_c} \left(C_i - C_{i,s,c} \right) \qquad \text{……..(3.14)}$$

Cyanide Consumption: $$-r_{CN^-} = \left(\frac{1.69 \times 10^{-8}}{\bar{d}^{0.547} - 6.40} \right) [CN^-]^{3.71} \qquad \text{……..(3.15)}$$

where ε is the volume fraction, C is the gold concentration in leaching tank, Q is the gold concentration on carbon, G is the gold concentration in ore, ρ_o is the ore density and ρ_c is the carbon density, W is the mass of carbon in tank, M is the mass of ore in tank, $C_{i,s,c}$ is the equilibrium concentration on carbon given by Langmuir isotherm.

A MATLAB program was written for simulating the behaviour of the CIL battery.

The values of parameters and constants are tabulated in Table 3.1 given below:

Table 3.1. Operating parameters for the simulation of CIL process

Operating Parameters	Value
Flow Rate of ore and slurry, Q_f	0.2083 m^3 / s
Counter-current flow with carbon particles, Q_s	0.2083 m^3 / s
Stages, i	1 to n, where n is 6.
Volume of a tank, V	750 m^3
Volume fraction of liquid, ε_l	0.85
Carbon concentration in each tank	25 kg / m^3
Oxygen Concentration	28 mg / L
Initial Cyanide Concentration	280 mg / L
Gold Concentration in liquid in fresh feed	5 g / m^3
Gold Concentration on ore in fresh feed	0.001 g / kg
Gold Concentration on eluted carbon	0 g / kg
Constants for leaching reaction:	
α	2.13
β	0.961
γ	0.228
a	0.357×10^{-4}
b	1.49
c	-0.0176
k_{Au_1}	5.13×10^{-3}
k_{Au_2}	2.28×10^{-10}
θ	2.93
Constants for adsorption reaction (Langmuir isotherm)	
K_{fj}	0.00001
b	0.417
q^+	7.708
Constants for cyanide consumption reaction	
$k_{CN_1^-}$	1.69×10^{-8}
$k_{CN_2^-}$	6.4
φ	0.547
η	3.71
Particle properties	
Carbon particle diameter	0.0014 m
Carbon particle density	900 kg / m^3
Ore particle diameter	75 µm
Ore particle density	2550 kg / m^3

3.6 Results and Discussion

3.6.1 Comparison with the Literature Data

Due to lack of industrial data, the simulation results were compared to previous modelling studies of Deventer et al.(2004). Deventer et al. (2004) used Mintek leaching rate in their simulations which does not consider the effects of oxygen concentration and particle diameter. Results of simulations carried out using this rate equation shown in Figure 3.3a closely agree with Deventer's results. Simulations were also carried out using modified Lima and Hodouin (2005) kinetics given in Section 3.4.1. These simulations shown in Figure 3.3b match with Deventer's data.

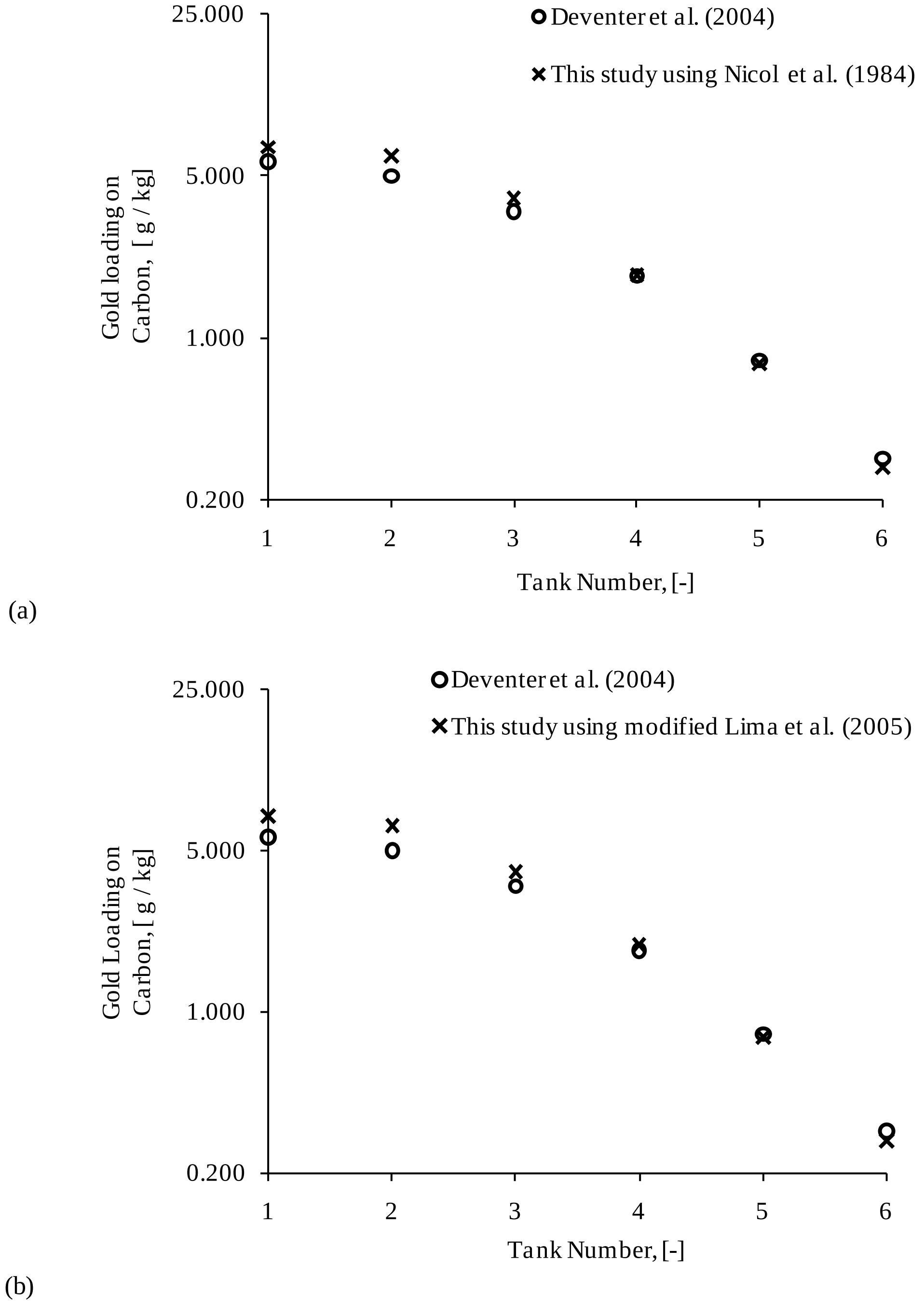

Figure 3.3. Comparison with literature data

The Carbon-in-leach process is a countercurrent leaching-adsorption process. The slurry containing ore, lime and cyanide enters the CIL circuit from the first tank and carbon enters from the last tank. The concentration of gold in the solution was observed to decrease across the tanks. This is due to the simultaneous adsorption by the carbon particles in the tank with countercurrent flow. The countercurrent flow ensures a consistent high concentration gradient of gold between the carbon particles and the liquid throughout the circuit. Consequently, according to Le Chatelier's principle, high adsorption rates are observed. As the carbon moves countercurrently across the circuit, the loading on the carbon increases exponentially with maximum loading observed in the first tank (see Figure 3.3). After the first tank the carbon is removed and is sent to the elution circuit. Even though the gold concentration in the liquid is low, the carbon is able to remove the remaining small quantity of gold leaving a low residual gold concentration.

3.6.2 Dynamic Simulation of CIL in Series

Simulations were carried out using the validated model with initial gold concentration in liquid = 5 g/m^3 and initial gold loading on carbon = 0 g/kg. While the ore and the liquid flow was continuous through the circuit from tank 1 to tank 6, carbon was transferred countercurrently (from tank 6 to tank 1) in a semi batch mode. The carbon transfer cycle was 12 hours with a loading time of 30 minutes. Figure 3.4 shows the dynamic behaviour of gold loading on carbon for in different tanks.

For tanks 1 to 3, the gold loading on carbon increased with time (Figure 3.4a). However, the loading was observed to increase quickly, and then decreased in tanks 4 to 6 (Figure 3.4b). With high gold loading ore entering tank 1, the gold leaching rate remains high, and the high gold concentration is maintained. In the consequent tanks, the gold concentration keeps on decreasing, resulting in an initial shoot up of gold loading in tanks 4 to 6, followed with a continuous decrease.

For all the tanks, the gold loading on carbon was found to increase in any given cycle. During a cycle, no carbon transfer takes place between the tanks, so the gold loading keeps on increasing due to adsorption. At the end of the cycle, the low gold loading carbon is transferred to the preceding tank. In general, the concentration in the initial tanks increases with time periodically dropping down as the transfer cycle kicks in. The loading vacillated within a band as a pseudo-steady state is reached. In the later tanks (tanks 4, 5, and 6), the loading first increases quickly (due to the high gradient in initial guess) and then dampen to reach a pseudo steady state value. For the first tank pseudo steady state is achieved within 108 hours (9 cycles). Longer time is required for the other tanks to achieve a pseudo steady state with the 6th tank taking the longest time.

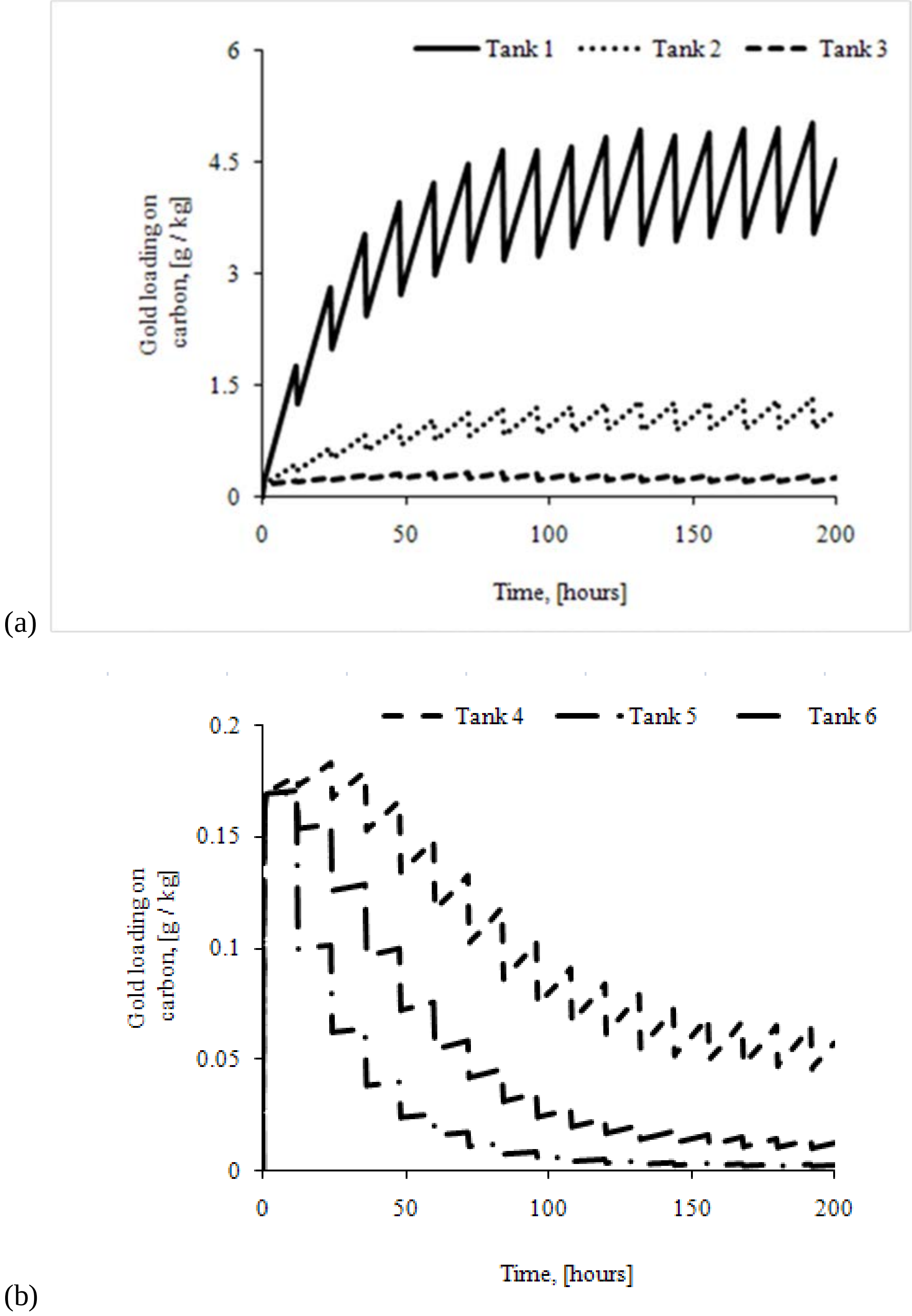

Figure 3.4. Gold loading on carbon as a function of time for the six tanks of CIL circuit.

3.6.3 Effect of Process Parameters

Ore particle diameter, cyanide and oxygen concentration have an effect on gold recovery. In order to assess their effect, dynamic simulations were carried out. The values reported below are the time averaged values after steady state was achieved.

The results of the simulations with respect to the influence of these process parameters on the efficiency of gold recovery are discussed in the subsections below.

3.6.4 Cyanide Concentration

Cyanide concentration has a prominent effect on the efficiency of the CIL circuit as shown in Figure 3.5a. With the increase in the cyanide concentration, the efficiency of the CIL circuit increases. Leaching rate kinetics is proportional to 2.13 power of cyanide concentration that results in the increase in leaching rate with its increase. It leads to a higher instantaneous gold concentration in liquid in each dynamic cycle. As a result more gold is available for adsorption on carbon and lesser residual gold is present in the ore. For a given particle diameter, the recovery was seen to increase initially with an increase in cyanide concentration. Further increase in cyanide concentration did not have any effect on recovery as a plateau was observed. Thus, increasing the cyanide concentration over a certain limit only result in incurring losses.

Size reduction increases the surface area of particles and hence, increases leaching. Therefore, decrease in particle diameter increases leaching and so the efficiency of CIL process is increased. The effect of particle diameter is incorporated in the model through rate constant and the residual gold concentration. The difference in the recovery is substantial, but the curve approaches a plateau for higher particle diameter. That means, the decrease in particle size greatly increases the recovery rate.

For low cyanide concentration (100 mg/l), a significant change (2.5%) in the recovery with respect to particle diameter was observed. At low cyanide concentration, although the recovery was low, the effect of particle diameter was dominant and rate was found to be more sensitive to the particle diameter. This shows that the impact of particle diameter on the CIL process is prominent. For the highest cyanide concentration studied (700 mg/l), although the improvement in recovery was 1.9% as compared to the maximum of 2.5%, but the recovery was also much higher. The rate of decrease in cyanide concentration is dependent on particle diameter. The rate of consumption of cyanide decreases with the increase in particle diameter. Therefore, the residual cyanide present is higher in the case of larger particles. This gives the reason for the change in the recovery that is slightly higher for the bigger particle than that for the smaller particle for any two cyanide concentrations.

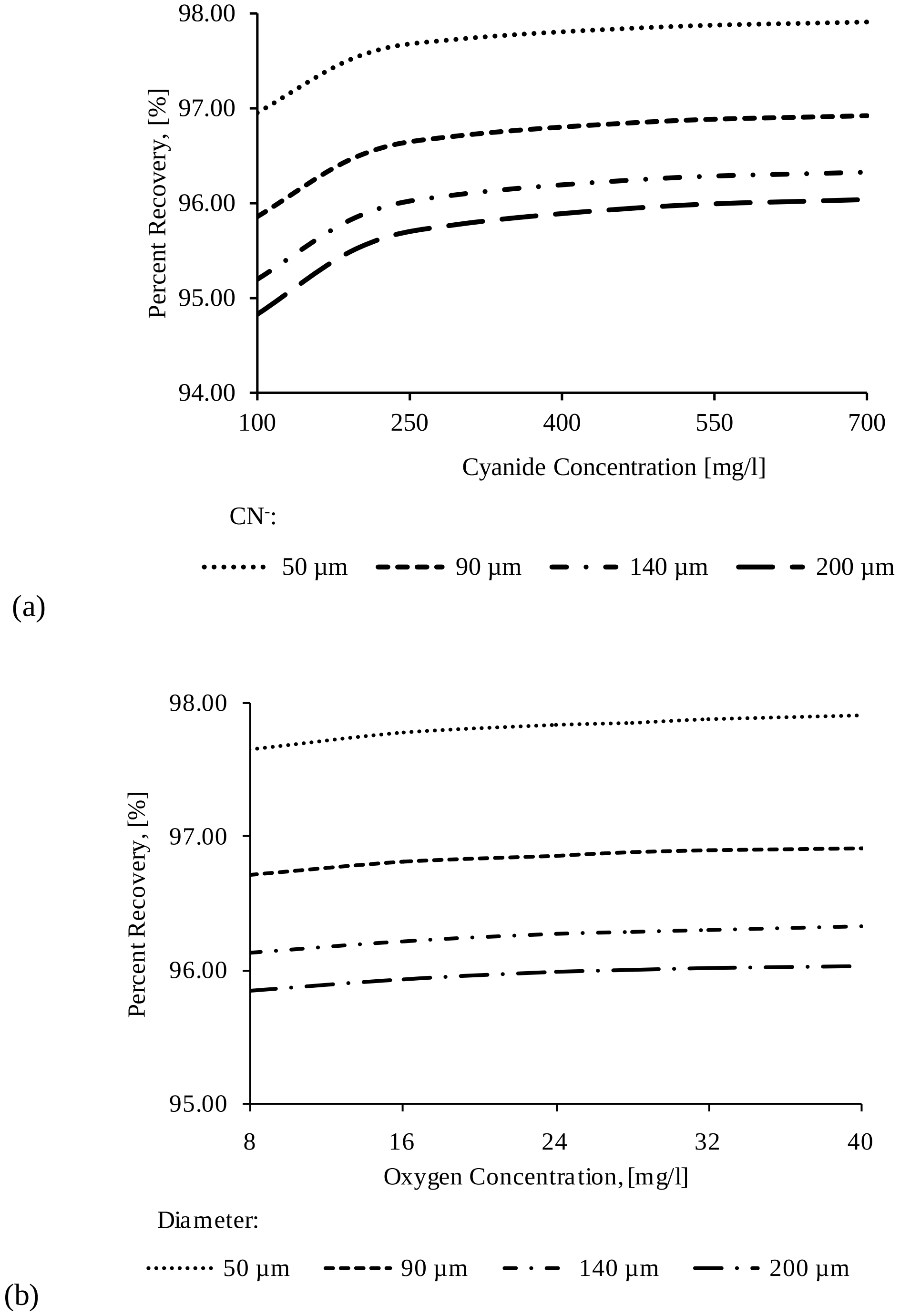

Figure 3.5. Effect of (a) cyanide concentration and (b) oxygen concentration on gold recovery

Various size reduction operations in industry, i.e. crushing, grinding, etc. are cost intensive, and in order to obtain a cost effective output, it becomes necessary to conduct an optimization study to obtain an appropriate value of particle diameter, as the size reduction cost increases with the fineness of the particle. Similar case applies to the cyanide concentration, where excess cyanide will only result in excessive running cost.

3.6.5 Oxygen Concentration

Figure 3.5b shows the effect of oxygen concentration at different particle diameters. For a given particle diameter, increasing oxygen concentration marginally improves gold recovery. This observation is the result of low solubility of oxygen in water. At the conditions in CIL, the dissolved oxygen is 8.2 mg/l. A concentration below this value will result in limiting the rate of leaching. Therefore, it becomes necessary to supply oxygen to maintain a minimum level in CIL tanks to facilitate leaching. Hence, similar to cyanide, excess oxygen will not result in any significant increase in the recovery. Oxygen is supplied in the CIL tanks through spargers. The flow rate through the sparger can be regulated in order to maintain the oxygen concentration in the CIL tank. To increase the airflow rate in order to gain only a marginal increase in the recovery only adds up to the running cost of the plant without any significant profit.

3.6.6 Volume Fraction

The solid volume fraction inside the CIL tank is a crucial parameter. A decrease in the solid volume fraction will result in the increase of the processing costs. The same amount of ore will take in considerably longer time to be processed. It is only beneficial, if the decrease in the volume fraction of solids results in a significant increase in the recovery rate. The increase in carbon loading with the increase in the ore volume fraction is evident from Figure 3.6. This increase is linear and is directly related to the solid volume fraction. As the solid volume fraction increases, there is an increase in the leaching rate. As a result the corresponding loading on carbon increases. On a contrary, when the residual concentration of gold in the ore was compared, there is a negligible decrease in the residual gold concentration. Another factor that has a significant impact on the leaching rates at higher volume fractions of ore is mixing. The present model assumes uniform mixing. Therefore, the effect of mixing cannot be captured. A detailed hydrodynamic study on CIL tanks has been conducted and discussed in chapter 4. Based on the results obtained, the increase in ore concentration in CIL circuit results in reducing the processing cost, without any significant losses as residual. Therefore, a high viable concentration is recommended to be used in CIL circuit.

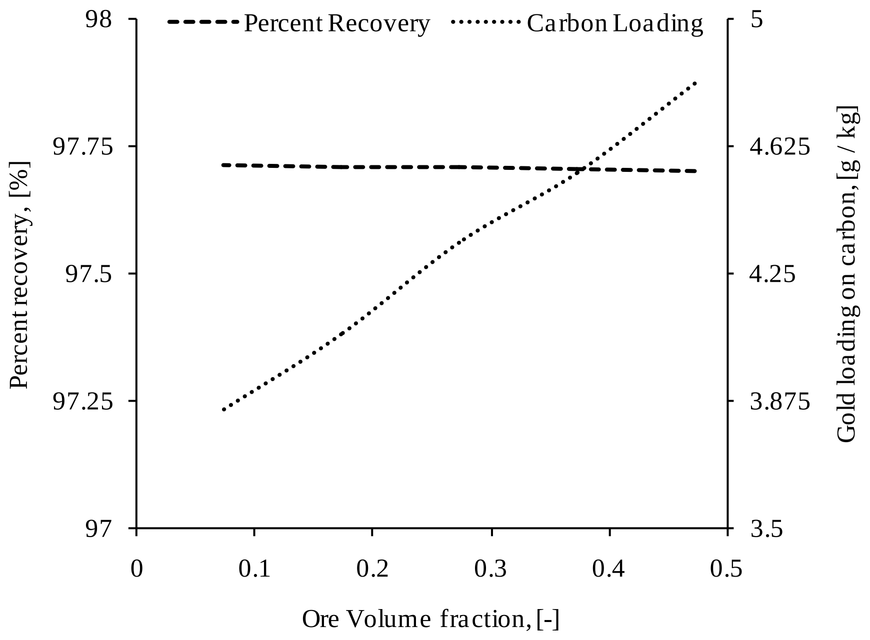

Figure 3.6. Effect of ore volume fraction on gold recovery.

3.6.7 Carbon Transfer Interval

In CIL process operations, the flow of ore and slurry is continuous through the tanks, but the carbon transfer occurs at regular intervals. The effect of carbon transfer on the amount of gold adsorbed on the carbon is presented (Figure 3.7). While changing the carbon transfer interval, the counter-current flow rate was changed such that for 72 hour period, the amount of flow was same for all the cases. In this way the same amount of carbon was used for the adsorption of gold in each case over a time-averaged basis. The flow rate and carbon transfer interval values of each case are tabulated in Table 3.2.

Table 3.2. Values of flow rate and carbon transfer cycle studied.

Carbon Transfer Interval (hours)	Flow Rate (m^3/s)
6	0.104
12	0.208
36	0.625
48	0.833
72	1.250

The gold concentration on carbon in the first tank increases with the increase in the carbon transfer interval. It is due to the increased residence time of carbon particles in the CIL circuit. As the residence time increases, the gold loaded on the carbon also increases due to additional contact time with the liquid. The high frequency of the carbon transfer results in the passing of carbon with low gold concentration to the elution circuit at a faster rate.

Deducing the inferences from results in three possibilities. Firstly, the decrease in the carbon transfer interval increases the operating costs as it results in more frequent transfer of carbon and operation of pumps. Secondly, the possibility of mixing of fresh carbon with the loaded carbon increases with the increase in the flow rate at increased carbon transfer interval. Thirdly, if as a solution to this, the nature of carbon transfer is changed from simultaneous to non-simultaneous configuration (like tank 1, tank 3 and tank 5 transferred first, than tank 2, tank 4 and tank 6 transferred in the second instant), the size of the tanks has to be substantially increased.

Therefore, the results show the advantage of higher carbon transfer interval but it is recommended to optimise it with respect to the operating cost and capital cost.

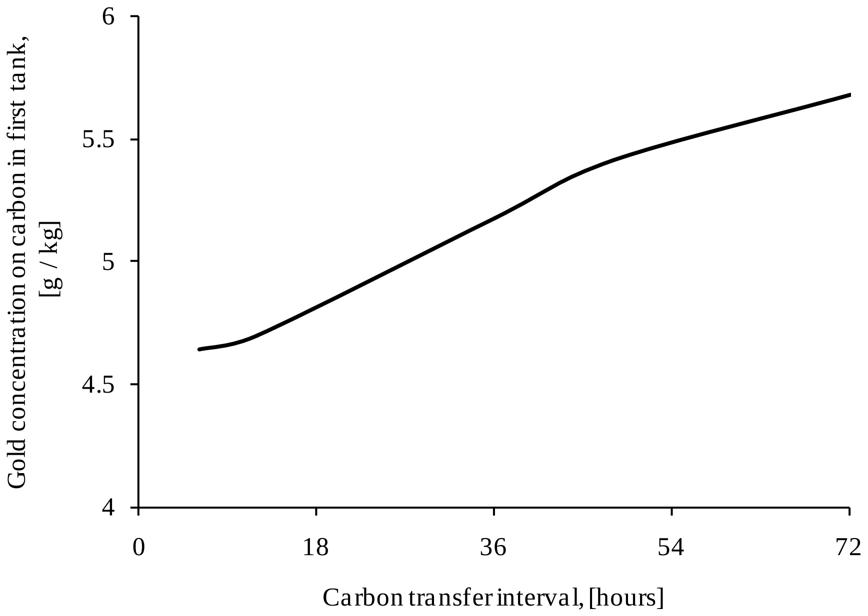

Figure 3.7. Effect of carbon transfer interval on gold recovery

3.6.8 Residence Time

Residence time is the time taken by the slurry to pass through all six tanks. Its value provides information about the contact time between the ore and cyanide solution. The higher is its value, the longer will be the contact time and the more gold will be leached.

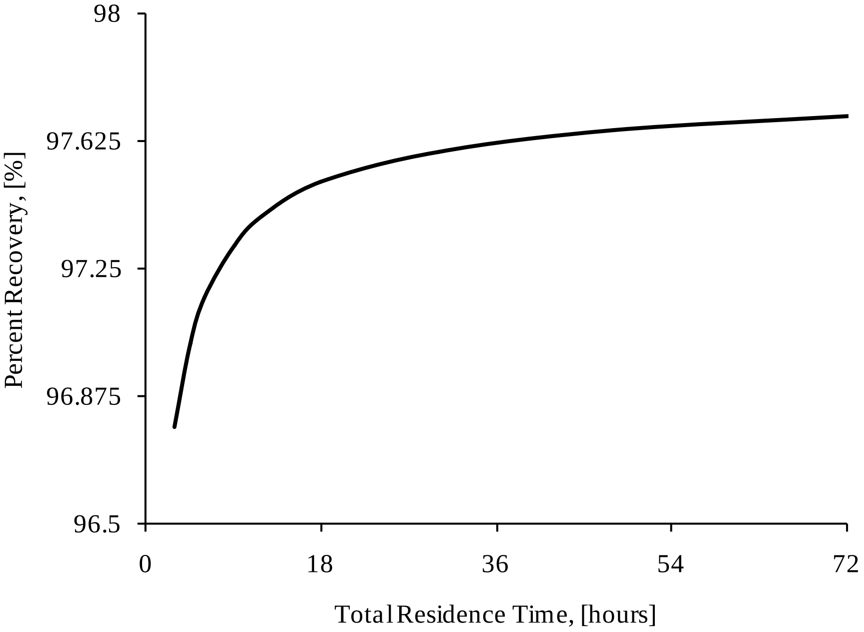

Figure 3.8. Effect of total residence time on gold recovery.

The residence time in the CIL circuit is critical for its efficiency and therefore, it is an important operational consideration. The effect of residence time on the efficiency was investigated by changing the flow rates of slurry. The increase in residence time showed an exponential increase in the recovery in the initial phase as is shown in Figure 3.8. At a very low residence time, the contact time between the ore and cyanide solution and pregnant solution and carbon particles is very less. Under these conditions, the slurry moves to the next tank without reaching an equilibrium value. As the residence time is increased, more contact time is available for the ore to get leached and carbon to adsorb aurocyanide. But, after a particular period, the residence time is sufficient to provide enough time to reach the gold concentration in liquid and on carbon to reach near the equilibrium value. In the system studied in the chapter, the optimal residence time is found to be 18 hours after which the improvement in recovery is less than 0.001%. In different gold mining industries its value lies between 12 hours to 20 hours.

3.7 Conclusion

Gold extraction process in a CIL circuit was modelled and simulated. A dynamic model of the CIL circuit was developed and used to study the variation in gold concentration in the liquid and on carbon. The impact of various process parameters on the residual gold in the ore was studied. The results obtained by the model were compared with existing literature and were found to be in close agreement. The particle size and cyanide concentration are critical for the gold leaching. Decrease in the particle size and an increase in cyanide concentration resulted in an increase in the efficiency of the process. It is necessary to obtain an optimized value of particle size and cyanide concentration with respect to the cost associated with it in order to save the running costs and obtaining higher efficiency of the process. Oxygen concentration did not show significant effect on the efficiency. The residence time and the number of tanks are interrelated. The current study shows the increase in the recovery with the increase in residence time and the number of tanks. The increased recovery is obtained with increased carbon transfer interval. Increased carbon transfer interval may result in increased capital costs if the tank configurations are changed. Low carbon transfer interval incurs higher operating costs. The conclusions from the study will help devise suitable strategies for optimizing gold extraction process.

In this chapter, lumped parameter model has been used and uniform mixing was assumed. However, the effect of flow and mixing on such systems has been recognised. In stirred tanks, scale up based on empirical correlations is often unreliable as these correlations depend on averaged flow properties and do not consider non-idealities in mixing. Distributed parameter models, based on the actual flow fields in the mixing tanks, are preferable, however, these require accurate estimation of the local flow field which can be obtained through hydrodynamic modeling. As pointed out in chapter 2, the current models to predict hydrodynamics are not mature specially for flow at higher concentration of solids. This makes quantifying hydrodynamics of such a system is a challenging task. Threrefore, in chapter 4 and 5, a detailed hydrodynamic study of the flow in CIL tanks is undertaken.

Chapter 4 Hydrodynamic Simulation of CIL Tanks

In the CIL processes, effective mixing is necessary at both micro and macro level for adequate performance. Numerous factors such as the just suspension speed, critical suspension speed, solids distribution, etc. dictate the mixing performance. The effect of these factors was not considered in the phenomenological model presented in the previous chapter. To make the model applicable over a wider range of operating parameters, a distributed parameter model is needed for CIL model, for which a hydrodynamic study is essential.

Computational Fluid Dynamics (CFD) is increasingly being used to predict the hydrodynamics and performance of multiphase stirred tanks. It has proved to be a useful tool in analysing the impact of these factors on the flow characteristics of such systems (Micale et al., 2000, Montante et al., 2001, Micale et al., 2004, Khopkar et al., 2006, Ochieng and Lewis, 2006, Fradette et al., 2007, Kasat et al., 2008). Accounting for the solid-liquid interaction is critical for accurate predictions of these systems. These interactions are governed by the turbulence and interphase drag. Therefore, a careful selection of models for turbulence and drag is required.

At low impeller speeds, turbulent fluctuations are less and hence do not affect the predictions much. However, at higher impeller speeds, the drag and turbulence become increasingly important. As is discussed in Section 2.5.11, despite of several studies there is no consensus on the appropriate drag for liquid-solid stirred tanks. Therefore, evaluation of different drag models for a given flow condition is necessary before applying the CFD to industrial scale CIL tanks. The available drag models are initially validated for low volume fraction and low Reynolds number (although turbulent) for which experimental data is available. The behaviour of turbulent kinetic energy, suspension quality and cloud height are also extensively discussed for these cases.

Continuous improvements in non-invasive electrical, magnetic and radioactive techniques have made it possible to capture experimental data on high solid loading stirred tanks. Barigou, (2004) Brunazzi et al. (2004), Guida et al. (2009), Pianko-Oprych et al. (2009) and Stevenson et al. (2010) have assessed the applicability of these techniques to determine flow field, measure concentration, investigate off-bottom suspension and the effect of particle size and concentration on it and generate valuable experimental data. For high solid loading, turbulence level distribution (responsible for the particle suspension) is not available. Distribution of turbulent kinetic energy, dissipation rate and slip velocity govern the quality of suspension e.g. zones of high slip velocity indicate high mass transfer rates (Ljungqvist and Rasmuson, 2001). Therefore, determining the scale of turbulence energy, dissipation rate and slips velocity distribution in the tank can be useful for evaluation of mixing efficiency of an impeller. CFD simulation can provide information on understanding of the solids concentration distribution in a stirred tank (Montante et al., 2001).

In this Chapter, Eulerian-based multiphase simulation has been employed to investigate the effect of high solid loading on the hydrodynamics of a stirred tank. The CFD simulation results were first compared with the experimental velocity field data (Guida et al., 2010) for both the phases. In the later part of the chapter, the flow field, velocity components, slip velocity and turbulence kinetic energy are used to evaluate the performance and the flow field distribution in tanks at high solid concentrations as in CIL.

4.1 CFD Model

4.1.1 Model Equations

The hydrodynamics is simulated using Eulerian-Eulerian multiphase model. The two phases are treated as interpenetrating continua represented by a volume fraction at each point of the system. The Reynolds averaged mass and momentum balance equations are solved for each of the phases. The governing equations are given below:

Continuity equation:

$$\frac{\partial}{\partial t}\left(\alpha_q \rho_q\right)+\nabla.\left(\alpha_q \rho_q \vec{u}_q\right)=0 \qquad \text{.........(4.1)}$$

Momentum equation:

$$\frac{\partial}{\partial t}\left(\alpha_q \rho_q \vec{u}_q\right)+\nabla.\left(\alpha_q \rho_q \vec{u}_q \vec{u}_q\right)=-\alpha_q \nabla P+\nabla.\overline{\overline{\tau}}_q+\alpha_q \rho_q \vec{g} \qquad \text{.........(4.2)}$$

$$+\left(\vec{F}_{td}+\vec{F}_q+\vec{F}_{lift,q}+\vec{F}_{vm,q}\right)+\vec{F}_{12}$$

Where q is 1 or 2 for primary or secondary phase respectively, α is volume fraction, ρ is density, $\vec{u}$ is the velocity vector, P is pressure and is shared by both the phases, $\overline{\overline{\tau}}$ is the stress tensor because of viscosity and velocity fluctuations, g is gravity, $\vec{F}_{td}$is force due to turbulent dissipation, $\vec{F}_q$ is external force, $\vec{F}_{lift,q}$ is lift force, $\vec{F}_{vm,q}$ is virtual mass force and $\vec{F}_{12}$ is interphase interaction force.

The stress-strain tensor is due to viscosity and Reynolds stresses that include the effect of turbulent fluctuations. Using the Boussinesq's eddy viscosity hypothesis the closure can be given to the above momentum transfer equation. The equation can be given as:

$$\overline{\overline{\tau}}_q=\alpha_q \mu_q\left(\nabla \vec{u}_q+\nabla \vec{u}_q^{\,T}\right)+\alpha_q\left(\lambda_q-\frac{2}{3} \mu_q\right) \nabla.\vec{u}_q \overline{\overline{I}} \qquad \text{.........(4.3)}$$

Where μ_q is the shear viscosity, λ is bulk viscosity and $\overline{\overline{I}}$ is the unit stress tensor.

4.1.2 Equations for Turbulence

Different turbulence models are available in the literature for estimation of turbulent viscosity. Standard k-ε turbulence model is the most preferred model for simulating single and multiphase flows in stirred tanks because of its capability to reasonably predict the turbulence in the system. Standard k-ε turbulence model assumes isotropy for turbulence. Other models such as Reynolds stress model (RSM) and the Large eddy simulation (LES) use anisotropic turbulence in the domain. However, RSM has shortcomings like non-universal model parameters and numerical difficulties. It does not capture the time dependent nature of flow and is computationally expensive (Murthy and Joshi, 2008). On the other hand, in LES, the flow field is explicitly solved at scales larger than the grid spacing for spatial scales and the time step for the temporal scales (Derksen et al., 1999). Therefore, LES models only the smallest scales, which are more or less isotropic. While at larger scales, the turbulence is fully resolved leading to higher accuracy (Murthy and Joshi, 2008). However, such simulations are computationally expensive and require significant computational power. Other than being computationally expensive, LES has no limitations and can yield better results. Derksen (2003) has used LES for the simulation of solid suspension in stirred tanks. The number of grid points in the system used to perform LES simulation was 14 million. The computational power used in this simulation is approximately 60 times higher than that conducted using the standard k-ε turbulence model. Jenne and Reus (1999) conducted a critical assessment by comparing the experimental results with simulation using different k-ε models and indicated that different temporal scales and anisotropic consideration are of minor importance and do not lead to significant improvement to the standard k-ε models. Considering practical applicability in terms of computational power and results by Jenne and Reuss (1999), the RANS based k-ε turbulence model was used.

k-ε mixture turbulence and k-ε dispersed turbulence models are used in the present study. The mixture turbulence model assumes the domain as a mixture and solves for k and ε values which are common for both the phases. In the dispersed turbulence model, the modified k-ε equations are solved for the continuous phase and the turbulence quantities of dispersed phase are calculated using Tchen-theory correlations. It also takes the fluctuations due to turbulence by solving for the interphase turbulent momentum transfer. For the sake of brevity, only the equations of mixture model for turbulence are given below. Other equations can be found in the Fluent user guide (ANSYS, 2009).

$$\frac{\partial}{\partial t}(\rho_m k) + \nabla.\left(\rho_m \vec{u}_m k\right) = \nabla.\left(\frac{\mu_{t,m}}{\sigma_k}\nabla k\right) + G_{k,m} - \rho_m \varepsilon \qquad \ldots\ldots\ldots(4.4)$$

$$\frac{\partial}{\partial t}(\rho_m \varepsilon) + \nabla.\left(\rho_m \vec{u}_m \varepsilon\right) = \nabla.\left(\frac{\mu_{t,m}}{\sigma_\varepsilon}\nabla \varepsilon\right) + \frac{\varepsilon}{k}\left(C_{1\varepsilon} G_{k,m} - C_{2\varepsilon}\rho_m \varepsilon\right) \qquad \ldots\ldots\ldots(4.5)$$

$C_{1\varepsilon}$ and $C_{2\varepsilon}$ are constants, σ_k and σ_ε are turbulent Prandtl numbers.

The mixture density, ρ_m and velocity, $\vec{u}_m$ are computed from the equations below:

$$\rho_m = \sum_{i=1}^{N} \alpha_i \rho_i \qquad \text{………(4.6)}$$

$$\vec{u}_m = \sum_{i=1}^{N} \alpha_i \rho_i \vec{u}_i \Big/ \sum_{i=1}^{N} \alpha_i \rho_i \qquad \text{………(4.7)}$$

Turbulent viscosity, $\mu_{t,m}$ and production of turbulence kinetic energy, $G_{k,m}$ are computed from equations below:

$$\mu_{t,m} = \rho_m C_\mu \frac{k^2}{\varepsilon} \qquad \text{………(4.8)}$$

$$G_{k,m} = \mu_{t,m}\left(\nabla \vec{u}_m + \nabla \vec{u}_m^{\,T}\right) : \nabla \vec{u}_m \qquad \text{………(4.9)}$$

4.1.3 Turbulent Dispersion Force

The turbulent dispersion force is significant when the size of turbulent eddies is larger than the particle size (Kasat et al., 2008). Its significance is also highlighted in some previous studies (Ljungqvist and Rasmuson, 2001). The role of this force is analysed in this study. It is incorporated along with the momentum equation and is given as follows:

$$\vec{F}_{t,d} = K_{pq} \vec{u}_{dr} \qquad \text{……..(4.10)}$$

Where drift velocity, $\vec{u}_{dr}$ is given by,

$$\vec{u}_{dr} = -\left(\frac{D_p}{\sigma_{pq}\alpha_p} \nabla \alpha_p - \frac{D_q}{\sigma_{pq}\alpha_q} \nabla \alpha_q \right) \qquad \text{……..(4.11)}$$

D_p and D_q are diffusivities and σ_{pq} is dispersion Prandtl number.

4.1.4 Basset Force, Virtual Mass Force and Lift Force

Basset force arises due to the formation of a boundary layer around the particles and is relevant only for unsteady flows. Its magnitude is much smaller than the interphase drag force (Khopkar et al., 2006). Moreover, its calculation involves a history integral, consuming more computational power without any additional advantage in accuracy.

The Lift force acts on a particle mainly due to the velocity gradient in the primary phase flow field and is exerted in the perpendicular direction of the flow field. The influence of the lift force is not significant as compared to the drag force unless in exceptional cases such as the phases separating quickly. Therefore, it is not recommended to include lift force as it is computationally expensive to converge.

Similar is the case observed in the case of virtual mass force, which is encountered by accelerating particles by the inertia of the primary-phase mass. It is significant only when the secondary phase density is much smaller than the primary phase density (ANSYS, 2009). Ljungqvist and Rasmuson (2001) studied the influence of interphase forces on the simulated holdup profiles in a stirred tank and found very little influence of lift and virtual mass forces. Therefore, in this study, these forces are not considered.

4.1.5 Interphase Drag Force

As is evident from the review presented in Chapter 2, there is no consensus on the appropriate drag force for multiphase flows. Therefore, in this chapter, the Gidaspow (1990), Wen and Yu (1966), Brucato (1998) and modified Brucato (2006) Drag models are assessed. Simulation results from these models are compared with experimental data of Guha et al. (2007) and Guida et al. (2010). The validated model will be used for the simulation of CIL tanks. The details of the drag force and drag models is given in the paragraphs below.

The drag force represents interphase momentum transfer due to the disturbance created by each phase. For dilute systems and low Reynolds number, particle drag is given by Stokes law and for high Reynolds number, the Schillar Nauman Drag Model can be used. In the literature, other drag models such as Gidaspow model (1990) and Wen and Yu model (1966) have also been discussed. These drag models are generally based on pressure drop measurements, bed expansion studies and numerical experiments (Mabrouk et al., 2007). As described earlier, Gidaspow drag model is a combination of the Ergun equation (1952) derived from the pressure drop data from packed bed and Wen-Yu equation (1966) derived from the settling of solids in liquid. For the voidage less than 0.8, the Ergun equation is used and for the voidage greater than or equal to 0.8, Wen-Yu equation is applied. Equations given below describe the model:

$$\beta_{\text{Wen-Yu}} = \frac{3}{4}\frac{\alpha(1-\alpha)}{d_p}\rho_f\left|\vec{u}_f - \vec{u}_s\right|C_{Do}\alpha^{-2.65} \qquad \text{for voidage} > 0.8 \qquad \text{……..(4.12)}$$

$$\beta_{\text{Ergun}} = 150\frac{(1-\alpha)^2\mu_f}{\alpha d_p} + 1.75\frac{(1-\alpha)\rho_f\left|\vec{u}_f - \vec{u}_s\right|}{d_p} \qquad \text{for voidage} \leq 0.8 \qquad \text{……..(4.13)}$$

where α is the liquid volume fraction, d_p is the particle diameter, ρ_f is the fluid density, $\vec{u}_f$ is the fluid velocity, $\vec{u}_s$ is the solid velocity, μ_f is the fluid laminar viscosity and C_{Do} is the drag coefficient in stagnant liquid.

C_{Do} is given as:

$$C_{Do} = \frac{24}{\alpha\,\text{Re}_s}\left[1 + 0.15\left(\alpha\,\text{Re}_s\right)^{0.687}\right] \qquad \text{if } \text{Re}_s < 1000 \qquad \text{……..(4.14)}$$

$$C_{Do} = 0.44 \qquad \text{if } \text{Re}_s \geq 1000 \qquad \text{……..(4.15)}$$

where Re_s is particle Reynolds number.

Re_s is expressed as:

$$\text{Re}_s = \frac{d_p\rho_f\left|\vec{u}_f - \vec{u}_s\right|}{\mu_f} \qquad \text{……..(4.16)}$$

But for stirred tank systems, high Reynolds number and increased eddy size impact drag force. Therefore, the drag model used should take turbulence into account. Considering the influence of turbulence on drag, Brucato et al. (1998) measured the residence time and average particle settling in turbulent conditions in a Taylor-Couette apparatus. Since the observed effect was found to increase with both particle size and mean turbulent energy dissipation rate, they proposed a new drag model making drag coefficient as a function of ratio of particle diameter and Kolmogorov length scales. So, with the change in the turbulence at some local point in the system, the drag will also change. The drag coefficient proposed by Brucato et al. (1998) is given below:

$$\left(\frac{C_D - C_{Do}}{C_{Do}}\right) = K\left(\frac{d_P}{\lambda}\right)^3 \qquad \text{……..(4.17)}$$

where, K is dimensionless constant with value of 8.76 × 10^{-4}, d_P is particle diameter and λ is Kolmogorov length scale.

Khopkar et al. (2006) performed DNS simulations for conditions closer to those in stirred tanks. To understand the drag observed by the particles as a result of the high turbulence in the stirred tanks, flow through a bank of regularly arranged cylinders was computationally studied (Figure 4.1). The fractional increase in the drag coefficient is a function of dp/λ, the particle Reynolds number and the volume fraction. Ignoring the possible influence of the solid volume fraction and particle Reynolds number, the predicted results were correlated considering the sole dependence on dp/λ for a range of solid holdup values (5 -25%). The results obtained provided a factor of 0.1 to the Brucato Drag correlation and the new correlation was termed as Modified Brucato Drag. This modified drag has a constant value of 8.76 × 10^{-5}.

Fajner et al. (2008) and Lane et al. (2005) have proposed drag correlations that also take the dependency of drag on volume fraction and density into consideration (Lane et al., 2005, Fajner et al., 2008). For the conditions studied in this chapter, the drag force calculated using these models was similar to the modified Brucato drag model. Therefore, Brucato and modified Brucato models were used for further study.

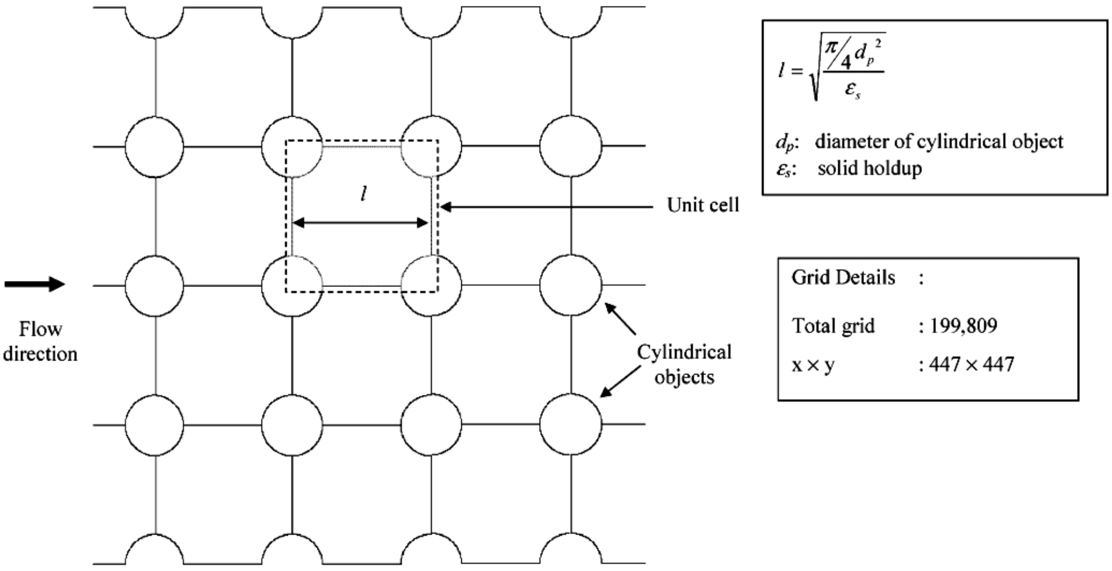

Figure 4.1. Solution domain for flow simulated through regularly arranged cylinders by Khopkar et al. (2006) for determination of drag.

For the simulation, Fluent’s built in Gidaspow and Wen and Yu models were used. User Defined Functions (UDFs) were written for Brucato and modified Brucato drag models. The implementation of Brucato drag model uses Kolmogorov length scale calculated for each cell, rather than using a value from the mean power dissipated in the system and applying it all over the domain as is commonly practiced. The use of mean power value can over-predict and under-predict drag in the system, resulting in increasing inaccuracy in the simulation results. Calculation at each cell resulted in the accurate calculation of drag using the localised values of Kolmogorov length scale.

4.2 Methodology and Boundary Conditions

The simulations were conducted for both low and high solid volume fractions in the stirred tanks. Due to lack of a uniform dataset, for low solid volume fraction, experimental setup and conditions of Guha et al. (2007) were used and for high solid loading, experimental setup and conditions of Guida et al. (2010) were considered for the hydrodynamic study. The simulations were first validated with the experimental data and then were used for the further analysis of the flow field, slip velocity, turbulence kinetic energy and turbulent dissipation.

4.2.1 Vessel Geometry

All the dimensions used in the study are the same as used by Guha et al. (2007) and Guida et al. (2010). Flat bottomed cylindrical tanks of diameter, T= 0.2 m for Guha et al. (2007) and T = 0.288 m for Guida et al. (2010) were used (Figure 4.2 and Figure 4.3). The tank height for both the cases was equal to its diameter and both tanks were mounted with four baffles of width 0.1T. The shaft of the impeller (of diameter = 0.01m) was concentric with the axis of the tank in both of these cases. Guha et al. (2007) used Rushton turbine with off-bottom clearance, C = T/3 and Guida et al. (2010) used pitched blade turbine with off-bottom clearance, C = T/4 in their studies. The dimensions of the impellers and the physical properties of the material used are tabulated in Table 4.1.

Table 4.1. Dimensions of domain and properties of materials used in this study.

Guha et al. (2007)				Guida et al. (2010)			
RT (in m)		Material		45^o PBTD (in m)		Material	
D	0.0667	ρ_l	1000 kg/m^3	D	0.144	ρ_l	1150 kg/m^3
B_l	0.0167	ρ_p	2550 kg/m^3	B_l	0.055	ρ_p	2485 kg/m^3
B_w	0.0133	d_p	0.0003 m	B_w	0.041	d_p	0.003 m
C	0.0667	C_x	0-7 vol %	C	0.072	C_x	0-40 wt%

4.2.2 Numerical Simulations

Owing to the rotationally periodic nature, half of the tank was simulated for all the cases. Multiple reference frame (MRF) approach was used. A reference moving zone with dimensions $r = 0.06$ m and $0.03995 < z < 0.09325$ was created for cases of Guha et al. (2007) and dimensions $r = 0.06$ m and $0.036 < z < 0.137$ was created for cases of Guida et al. (2010) (where z is the axial distance from the bottom). The impeller rod outside this zone was considered as a moving wall. The top of the tank was open, so it was defined as a wall of zero shear. The specularity coefficient is 0 for smooth walls and is 1 for rough walls. The walls of stirred tank were assumed to be smooth and a very small specularity coefficient of 0.008 was given to all other walls. In the initial condition of the simulation, a uniform average concentration of particles was taken in the tank. For modelling the turbulence, a standard k- ε mixture model was used. The model parameters were $C\mu$: 0.09, C_1 : 1.44, C_2 : 1.92, σ_k: 1.0 and $\sigma_\varepsilon = 1.3$. In a few cases the standard k- ε dispersion model was also used with the turbulence Schmidt number, σ, taken as equal to 0.8. The steady state numerical solution of the system was obtained by using the commercial CFD solver ANSYS 12.1 and 13.1 FLUENT. In the present work, Simple Pressure-Velocity coupling scheme was used along with the standard pressure discretization scheme.

The convergence of the simulation was verified by monitoring residual values as well as additional parameters namely turbulence dissipation over the volume and torque on the shaft. Once the residuals were below 0.001 and additional parameters become constant, a simulation was deemed to be converged. Then the time averaged data was used for the comparison of results.

4.3 Results and Discussion

4.3.1 Preliminary Numerical Simulations

The size and distribution of the grid is important for the accuracy for turbulence predictions in stirred tanks. Therefore, grid independency of the geometry was checked by conducting single phase flow simulations for each of the cases and comparing the power number.

The power number is a global criterion providing an estimate for the power dispersed in mixing by an impeller.

It is given as:

$$N_P = \frac{P}{\rho_m N^3 D_i^5} \qquad \text{……(4.18)}$$

The power delivered to the fluid can be derived by multiplying the torque delivered to the fluid with the impeller speed, 2πN. The torque (M) is obtained by integration of the pressure on the impeller blade. Therefore the power is given by:

$$P = 2\pi NM \qquad \text{…….(4.19)}$$

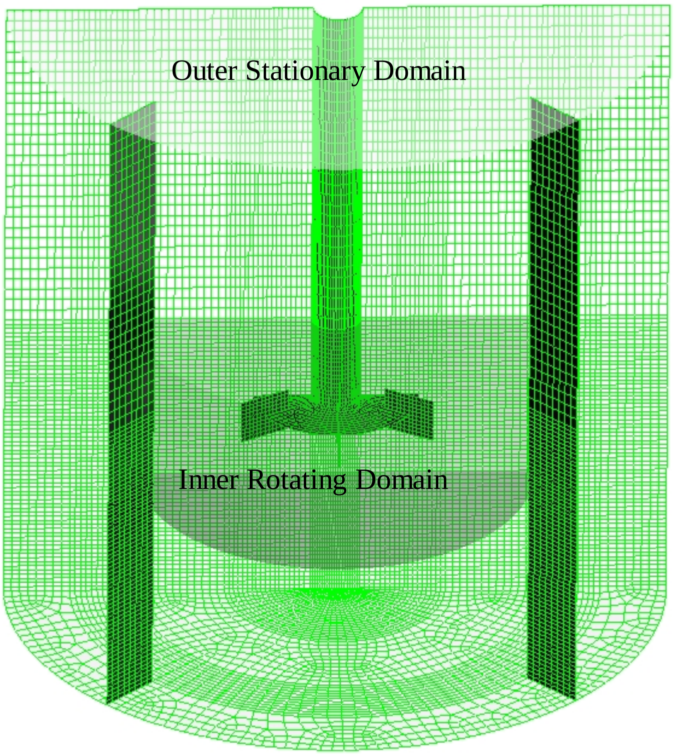

Figure 4.2. Computational domain and grid distribution in stirred tank of with Rushton turbine.

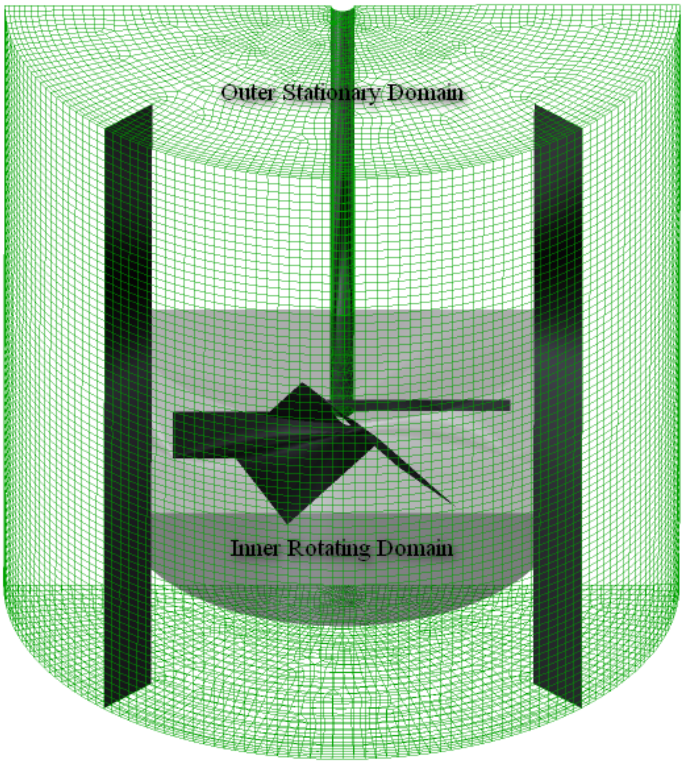

Figure 4.3. Computational domain and grid distribution in stirred tank with PBTD.

For the stirred tank setup of Guha et al. (2007), geometries with total number computational grid of 175460, 224280 and 428760 cells were checked. The grid of 224280 predicted a correct value of power number of 4.97. This value agrees reasonably well with the experimentally determined value of 5 reported by Bates et al. (Bates et al., 1963). This value didn’t change with further refinement of the grid. A similar study was conducted on the setup of Guida et al. (2010) using a geometry with 275036, 400246 and 648430 cells that predicted power number as 1.95, 1.69 and 1.67 respectively. As no considerable change in the power number was observed beyond the grid size of 400246 cells, it was used for further simulations. The details of cases simulated and discussed in the chapter are given in Table 4.2.

Initial simulations were conducted to assess the effect of the turbulence dispersion force. Negligible effect of the force was found for the case of 0.01 volume fraction. The turbulence dispersion force has a higher influence at greater concentration of solids where its magnitude will be high enough to be comparable with the other forces being exerted on the secondary phase (Ljungqvist and Rasmuson, 2001).

Table 4.2. Details of cases simulated.

Impeller Type	Case	N (RPM)	$N_{Re}(\times 10^5)$	N_P
RT	Single phase flow	1000	7.39	4.97
RT	1 % v/v	1000	7.51	4.95
RT	7% v/v	1000	8.19	4.63
PBTD	Single phase flow	330	1.31	1.67
PBTD	20 wt%	480 (N_{js})	1.91	2.11
PBTD	40 wt%	590 (N_{js})	2.34	2.34

4.3.2 Flow Field

Figure 4.4 shows the velocity vectors on a centre plane. For the Rushton turbine, an outward jet stream is formed due to the outward thrust of the impeller. This high velocity jet approaches towards the wall of the stirred tank and strikes it. The jet splits into two streams. One stream moves in axially upward and another in an axially downward direction. It creates an anticlockwise velocity field in the region above the impeller and a clockwise velocity field in the region below the impeller. The velocity near walls for the region above impeller is upwards and below the impeller is downwards. It is opposite when the velocity field is observed near the centre. The intensity of the recirculation in the region below the impeller is stronger than that above the impeller. The converged solution showed similar flow field (velocity field vectors) as compared to that available in the literature (Guha et al., 2007).

All the flow characteristics discussed above were captured by the CFD simulation and of the flow are clearly visible in Figure 4.4. The simulations were also able to capture the upward inclination of the jet and its asymmetry. This inclination is the result of the imbalance in the forces exerted on the flow due to the presence of bottom wall and absence of the top wall. In the simulations, different boundary conditions imposed on the vessel on the top wall (free slip) and bottom wall (no slip) result in this angular inclination. This effect was also shown in the simulation of Sbrizzai et al. (2006). The velocity vectors near the top surface of the stirred tank show a very weak flow field in this region.

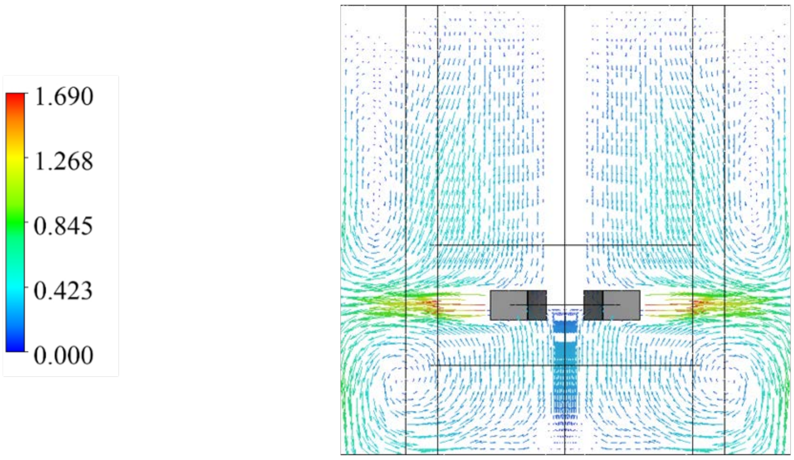

Figure 4.4. Solid velocity vectors on the plane between the baffles for a solid volume fraction of 0.01 and 1000 RPM using RT.

The flow field generated by the PBTD for single phase and the two concentrations viz. 20% and 40% by wt are shown in Figure 4.5. For the PBTD, a downward discharge jet is formed which is inclined radially outwards. The jet approaches the bottom of the tank and moves radially outwards towards the wall. The high velocity of the jet encounters the bottom and side wall of the vessel and then moves upwards forming a loop. The magnitude of the velocity was high in the impeller region and in the flow loop, but low velocity was observed in the centre of the loop and the upper parts of the tank. Similar behaviour was observed with the studies that used axial impellers for the investigations (Guiraud et al., 1997, Bittorf and Kresta, 2003, Virdung and Rasmuson, 2007, Guida et al., 2010).

In the presence of particles, a significant reduction in the jet velocity is observed due to dampening of turbulence (Figure 4.5b and c). A detailed examination shows a change in the flow structure. A shift in the centre of the flow loop can be observed from single phase to multiphase. The centre of the loop has shifted axially upwards and radially inwards. Guida et al. (2010) also observed similar phenomenon. The shift in the centre of the loop is a result of the change in the direction of discharge jet well before hitting the bottom wall. On analysing the presence of solids near the bottom wall, a high concentration zone of solid was observed. The high concentration of solid offered a low-clearance to the impeller generated flow and imposed resistance to the flow loop. Such a phenomenon has been observed by Kasat et al. (2008) and Sardeshpande et al. (2009) for radial flow impellers and termed it as "false-bottom effect". This is also the reason of decreasing solid velocities in the vicinity of the bottom of the tank with the increase in solid concentration.

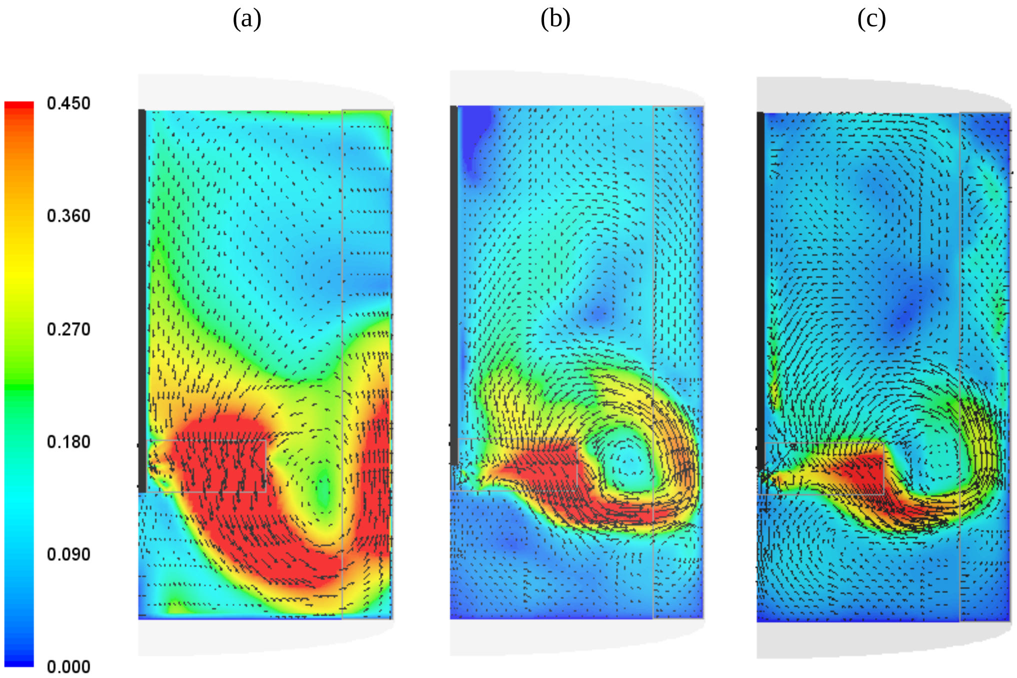

Figure 4.5. Normalised velocity maps and velocity vectors at mid-baffle plane using PBTD for N = N_{js} of (a) single phase, (b) solid phase (20 wt%) and (c) solid phase (40 wt%).

4.3.3 Analysis of Drag Models

The simulations were run using different drag models and the results were then compared with the experimental data. Guha et al. (2007) used CARPT technique, in which a single particle is introduced in the flow with the ability to mimic the motion in the phase of interest. Considering the limitation of CARPT technique which has a spatial resolution of the data is 7mm , the CFD results are reported on ensemble average basis in a 7 mm zone around the centerline of the measurement point.

The radial velocity of the solid particles at impeller plane is shown in Figure 4.6. On the x axis, r is the radial position, Ri is impeller radius and R is stirred tank radius. Out of the four drag models wide disparity with experimental data was observed when using the Wen and Yu and the Gidaspow model. These two models predicted the highest radial velocities. Guha et al.(2008) observed similar overprediction of radial velocities while using the Schiller-Nauman drag model. The Brucato drag model slightly overpredicted the radial velocity, whereas the predictions from the modified Brucato drag were in reasonable agreement with experimental data. The solid velocities are higher at the impeller tip. As the solids approach towards the wall, the velocity gradually decreases. Due to no slip condition on the wall, the velocity should gradually reach zero value at the wall. But, quantitatively, there is an over-prediction of the velocities in simulations in the near wall region. The disparity can be attributed to lesser number of data points available for averaging in experiments. The experiments clearly show a zero ensemble averaged value even at (r-Ri)/(R-Ri) = 0.8. The values of radial velocity should be high near the wall in the experiments and approach zero at wall. Its behaviour should be similar to the behaviour of radial velocity in Figure 4.10 and Figure 4.11. Such a decline in radial velocity is not reasonable.

At low solid concentrations, Gidaspow drag model acts like Wen and Yu model and at higher concentrations it takes the form of the Ergun equation. Therefore, both Wen and Yu model and Gidaspow models predict the same result. The modified Brucato drag model accounts for the effect of solid phase on the turbulence. At higher impeller speed, the role of turbulence in the calculation of drag is a vital factor, hence, the modified Brucato drag model predicts better results as compared to the other drag models.

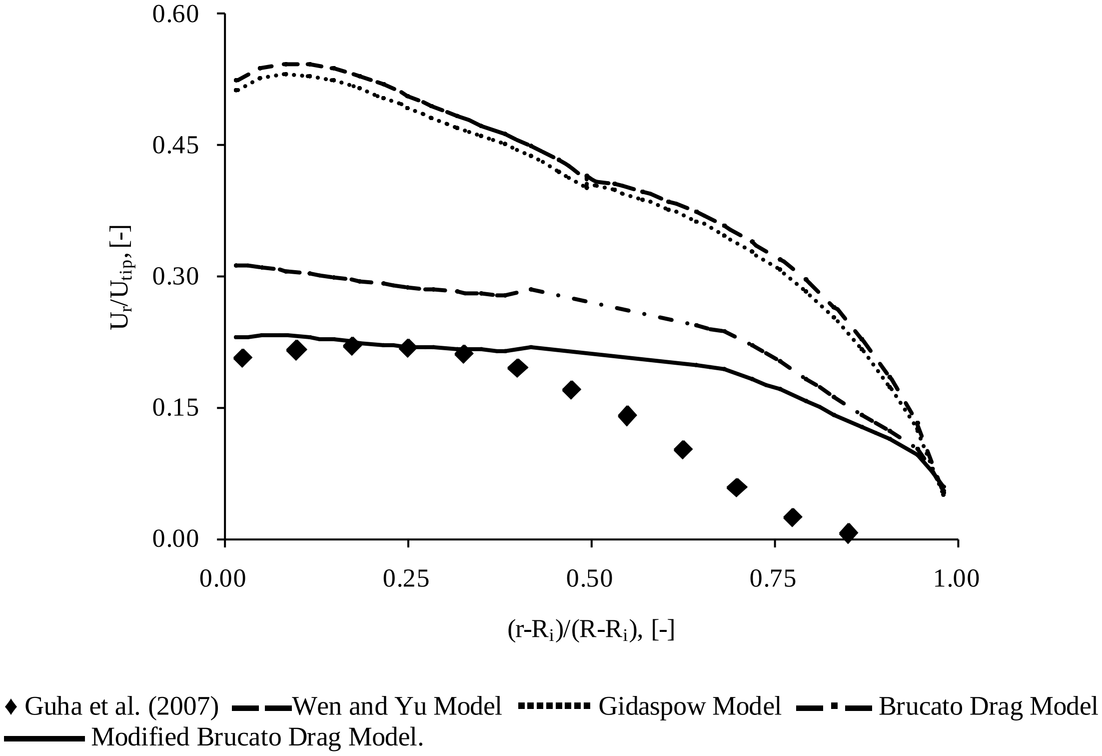

Figure 4.6. Radial velocity at the impeller plane for 0.01 solid volume fraction and 1000 RPM using RT.

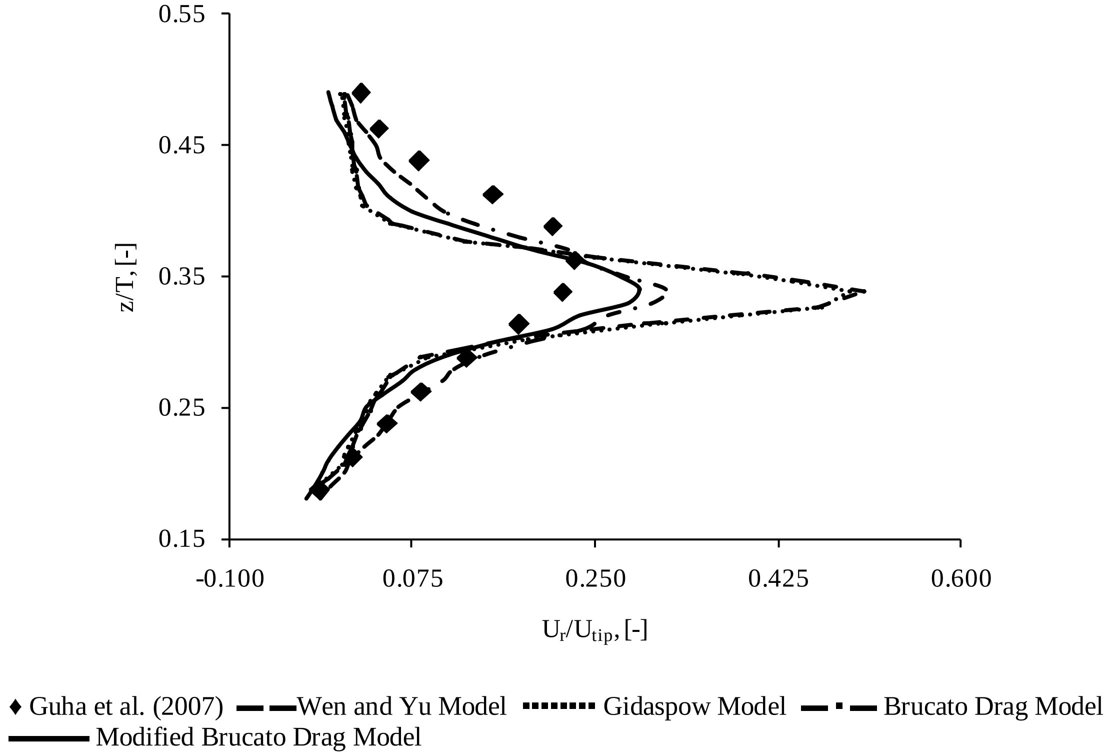

Figure 4.7. Radial velocity at axial plane r/R -0.5 for 0.01 solid volume fraction and 1000 RPM using RT.

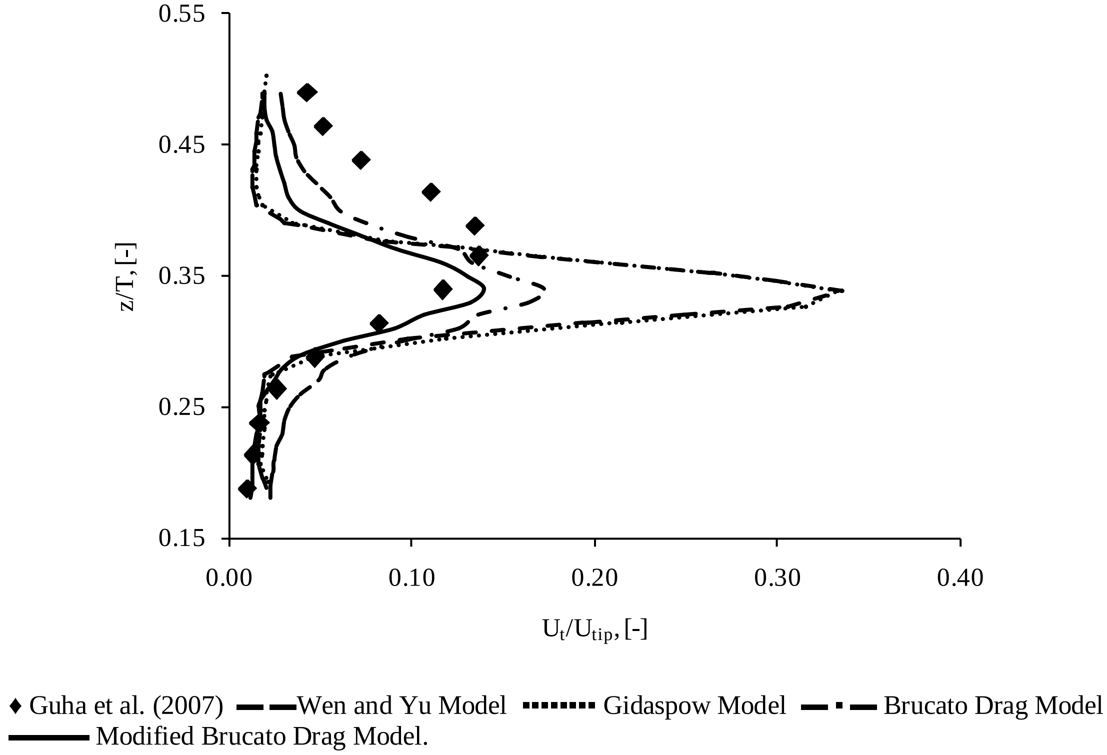

Figure 4.8. Tangential velocity at axial plane r/R – 0.5 for 0.01 solid volume fraction and 1000 RPM using RT.

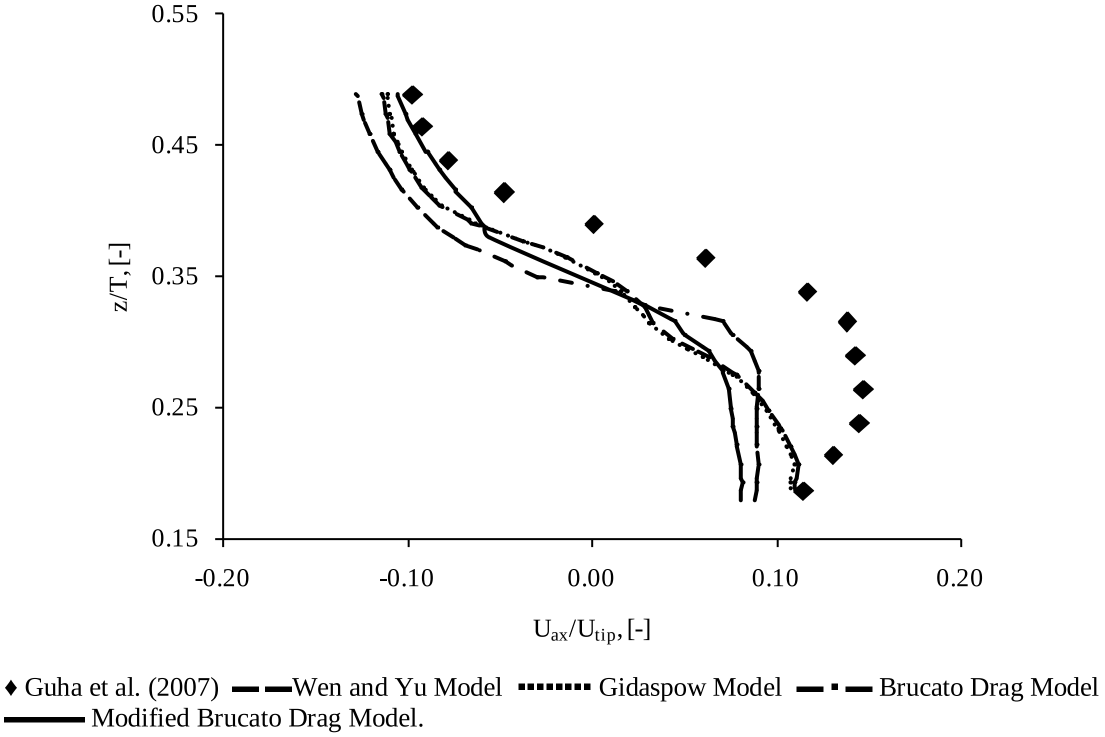

Figure 4.9. Axial velocity at axial plane r/R – 0.5 for 0.01 solid volume fraction and 1000 RPM using RT.

Figure 4.7 shows comparison between the simulation results and experimental data for radial velocity at axial plane r/R = -0.5. A positive radial velocity is expected in the upper zone of the impeller. As compared to the negative velocity in the region higher than the impeller zone where the magnitude of negative velocity is merely 2% of the maximum velocity attained by the solids, the negative radial velocity in the bottom of the tank is 10% of the maximum velocity. This corresponds to a relatively stronger flow towards the centre in the bottom of the tank. It indicates the presence of stronger clockwise currents. All the drag models could qualitatively capture this flow behaviour. For the experimental data, the highest tangential velocity is observed at z/T = 0.36 ± 0.04. This compares well the simulation result of z/T = 0.34. In the lower region of the stirred tank, where the effect of turbulence is not as prominent as the upper region, the predictions from all the drag models compared well with experimental data. In the upper region, the discrepancy was observed. Around the impeller zone, where, the turbulence and velocity fluctuations are higher, the Wen and Yu and Gidaspow drag models show show large overprediction compared to the experimental data. On the other hand, the Brucato and the modified Brucato drag show reasonable agreement. Figure 4.8 shows comparison between the simulation results and experimental data for tangential velocity at axial plane r/R = -0.5. Similar trend to that observed in radial velocity is observed.

The axial velocity profile is shown in Figure 4.9. The reversal of flow can be clearly seen. Above the impeller, the axial velocities are negative that means the flow is in the downward direction. It reverses in the region below the impeller. At the impeller, the axial velocity is zero and is distributed as the other two components of velocities viz. radial and tangential. All the drag models were able to capture the flow reversal qualitatively. Moreover, the predictions of all the drag models were comparable. The experiments show higher axial velocity in the lower region compared to the upper region. Whereas, the simulations predicted similar velocities in the lower and upper region of the impeller. Although this phenomenon is visible in Figure 4.4, the axial velocities shown in Figure 4.9 fail to predict it. It is because of the bigger circular loop in the lower region of the impeller clearly seen in Figure 4.4, which also affects the ensemble averaging of values in this particular zone. At the impeller plane, the axial velocity is zero as it is distributed as the other two components of velocities.

It is clear from the above discussion that for low solid holdups the modified Brucato drag model performs better compared to the other drag models. To assess the applicability at the higher particle Reynolds number as is the matter with the cases studied in this chapter, the initial simulations were conducted using this drag model and the results were compared with the axial, radial and tangential velocity components for the same set of conditions as are available in the literature (Guida et al., 2010). The spatial resolution of PEPT technology depends on the particle velocity (Chaouki et al., 1997). From the maximum particle velocity magnitude from the experiments, the resolution was found to be 4 mm. Considering this limitation, the CFD results are reported on the ensemble average basis in a 4 mm zone around the centre line of the measurement point.

The radial, axial and tangential velocities of solid particles at impeller discharge plane for 20 wt% and 40 wt% solids are shown in Figure 4.10 and Figure 4.11 respectively. The comparison shows the axial velocity as the dominant component out of the three as is expected for the PBTD. The axial velocity follows the trend shown in Figure 4.5. It reaches a maximum when the discharge flow passes through the plane. Therefore, the minimum axial velocity was found to around 0.46 of r/R.

Moving radially outwards, the axial velocity approaches zero and advances towards positive values due to the upward flow of the loop near the walls.

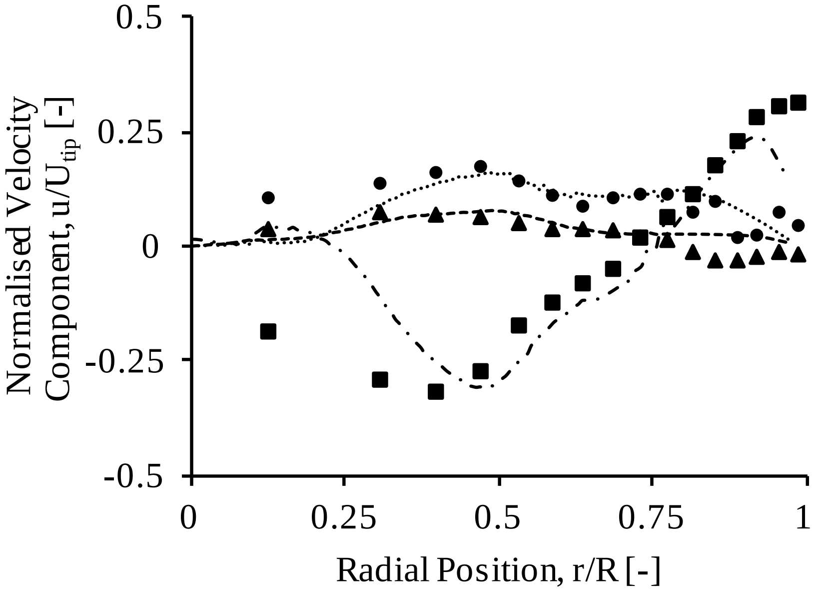

■ Experimental Axial Velocity ▬ ▪ ▬ ▪ Simulated Axial Velocity ▲ Experimental Radial Velocity ▬ ▬ Simulated Radial Velocity ● Experimental Tangential Velocity ▪▪▪▪▪▪▪▪ Simulated Tangential Velocity.

Figure 4.10. The three velocity components of solids in a horizontal plane at z/H = 0.2 for 20 wt% and N=N_{js} using PBTD.

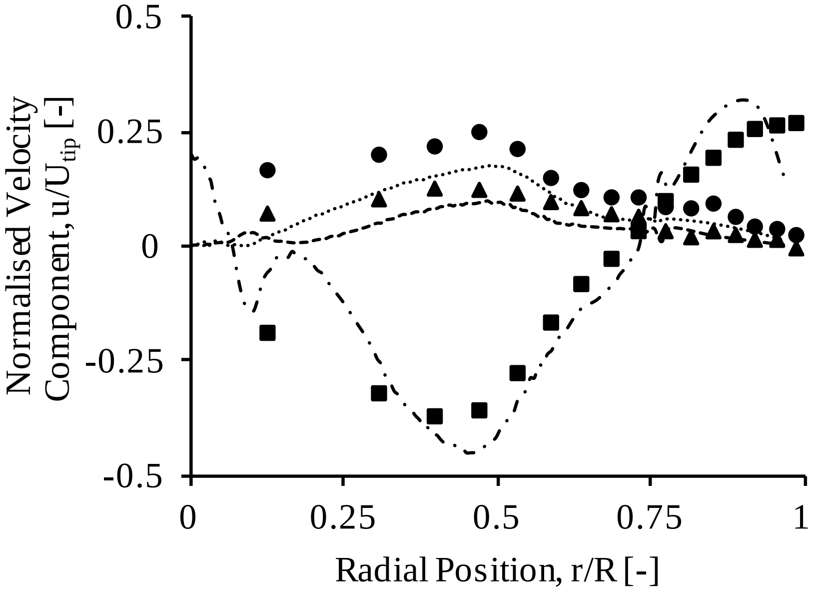

■ Experimental Axial Velocity ▬ ▪ ▬ ▪ Simulated Axial Velocity ▲ Experimental Radial Velocity ▬ ▬ Simulated Radial Velocity ● Experimental Tangential Velocity ▪▪▪▪▪▪▪▪ Simulated Tangential Velocity.

Figure 4.11. The three velocity components of solids in a horizontal plane at z/H = 0.2 for 40 wt% and N=Njs using PBTD.

The positive axial velocities near the centre of the tank are visible in the plots of Figure 4.10 and Figure 4.11. These positive values are a result of clockwise secondary loop observed in the low radius regions below the impeller (Figure 4.5b and c). The experimental data of Guida et al. (2010) were not able to capture it due to lower number of data points. But, similar behaviour has been captured and reported in few other studies (Guiraud et al., 1997, Pianko-Oprych et al., 2009). The radial and tangential velocity component are comparatively small. These components are found to be significant only in the impeller discharge region and tend to diminish when moving away from this field.

Interestingly, when comparing the axial velocity components for cases of 20 wt% and 40 wt% solids, the magnitude was higher for 40 wt% of solids. On detailed scrutiny, it was observed that the “false bottom effect” became more dominant in this case resulting in a lower concentration of solids in the impeller zone. Also, due to this reason, a further inclination of the jet was also observed in Figure 4.5. Therefore, the net decrease in the velocity in this particular region for 40 wt% solid is lesser than the dampening for 20wt% solid. As a result, the velocity of the discharge stream of 40wt % solids is higher than that for 20 wt% solids.

From the plot shown in Figure 4.10, the applicability of the modified Brucato drag model for this case is evident. The model is successfully able to predict the three velocity components quantitatively. However, there is a mismatch in the location of the peak value of maximum downward axial velocity. The peak in the simulation has shifted radially outwards. This is because of the change in angle and magnitude of the discharge jet. When compared with the experiments, the discharge jet in simulation has smaller axial component. Since this component has been distributed in the other two velocity components, there is an observed change in direction and hence, a shift is observed in the location of maximum downward axial velocity. The disparity is also observed in the near wall values of axial velocity which are supposedly to be approaching zero for the final data points at 137 mm and 142 mm radius. The experimental values are unable to reflect it, while CFD simulations are able to provide realistic results in this zone. In the regions lower than a quarter of the tank radius, difference in axial velocity is also observed. This disparity might be due to less data points in this region. A detailed scrutiny of the flow field shown in Figure 4.5 for this region reveals zone of very low axial velocities and clockwise circulation around it. Decreasing axial velocities in this region can also be observed in the figures showing flow field of solid phase given in the same paper (Guida et al., 2010).

Once satisfactory results were obtained for 20 % solids loading, the model was applied for a higher solid concentration of 40 wt%. The comparison with the experimental data is shown in Figure 4.11. While the simulation results matched well qualitatively with the experimental data, the simulations predicted lower radial and tangential velocities. However, it should be noted that the RMS error in the difference in value is 0.08 and is not significant as compared to the normalised velocity values. At this solids loading, distribution of axial components of velocity in other two components was not observed. This is probably due to the differences in the turbulence and turbulence dissipation predicted at such a high volume fraction of solids. It resulted in an over-prediction of drag as the drag is derived from the local values of ε.. The effect on the turbulence is discussed in the later part of the chapter. In the experimental results, the local solids concentration near the impeller was found to be lower for a 40 wt% solid case and therefore, the effect of reduction in velocity components was not that prominent as in the case of 20 wt% solids. The increase in solid concentration dampens the turbulence and therefore, the drag exerted on the particle (Ochieng and Onyango, 2008). Low local solid concentration in 40 wt% case in the impeller zone is the cause of this effect. Although, the simulations were able to predict the higher velocity components due to lower local solid concentration but in the present case, lower dissipation and higher turbulence values might have resulted in further increased values of the velocity components. The prediction of accurate levels of turbulence dampening is still erratic in the impeller region causing the deviation from expected behaviour (Derksen, 2003, Micheletti and Yianneskis, 2004).

Further scrutiny of the drag models was conducted by comparing the slip velocity in stirred tanks. The slip velocity in the stirred tanks was analysed using Gidaspow, Brucato and modified Brucato drag models. Since similar results for velocity components were obtained for Wen and Yu drag model and Gidaspow drag model, so only the results of Gidaspow drag model were used for the analysis. A significant difference in the magnitude of slip velocity was observed between Gidaspow and Brucato drag model in the impeller zone (Figure 4.12). The reason behind the disparity in the predictions of drag models is the basis on which drag is calculated. Brucato drag correlation is entirely dependent on the turbulence and is calculated from the ratio of diameter to Kolmogorov length scale. Gidaspow drag model is valid when the internal forces are negligible which means that the viscous forces dominate the flow behaviour. The flow in the stirred tank is mainly turbulent. Although k-ε turbulence model is not able to simulate turbulence effects at the Kolmogorov length scale, this effect has been taken into account in the modified Brucato drag model.

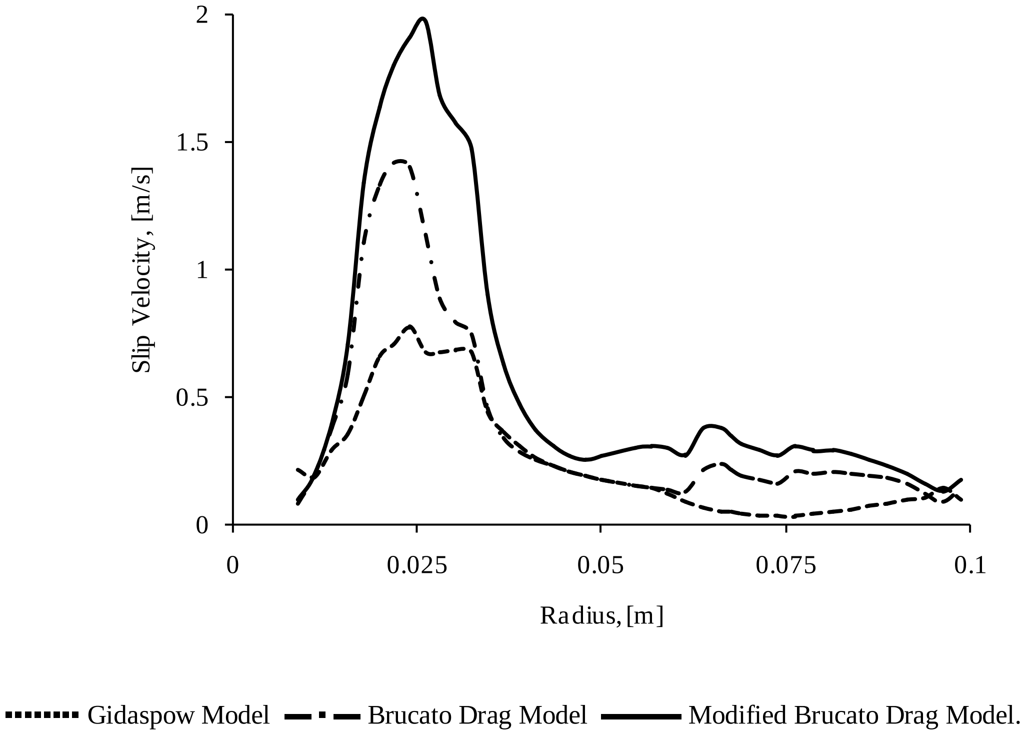

Figure 4.12. Slip velocity on an impeller plane for a solid volume fraction of 0.01 and 1000 RPM using RT.

Khopkar et al. (2006), while simulating the array of cylinders, have incorporated a source term in order to keep the Kolmogorov length scale of the order as is observed in a stirred tank. As a result, the underprediction of slip velocities in the impeller zone is addressed by using the Brucato and modified Brucato drag model. The magnitude of the drag increases with turbulence and hence, influences the slip velocity between primary and secondary phase. As seen from Figure 4.12, the Brucato drag modifies the drag to a greater extent than the modified Brucato drag, but still the value of slip velocity it is predicting is below that predicted by modified Brucato drag model. This is because of the impact of these models on the turbulence. Brucato drag, due to its magnitude, has a higher influence on the turbulence. The simulations show a high value of turbulent kinetic energy with the modified Brucato drag rather than the Brucato drag model. And the dissipation noticed in the former case was smaller than the latter case. It has a negative impact on the drag calculated and hence the drag is underpredicted due to the low turbulence calculated in the stirred tank. In the cases simulated, the maximum observed difference in dampening of turbulence was 10%. The impact of turbulence on drag is maximum visible in the impeller plane where turbulence is dominant. In this region, the ratio dp/λ is greater than 10 and for dp/λ>10, the interaction between energy dissipating eddies and particles become important for the solids concentration distribution (Ochieng and Onyango, 2008). Derksen et al. (2003) have compared the slip velocities in terms of linear and rotational Reynolds number and pointed out the dominance of high slip velocity in this impeller zone. When compared with the linear slip velocity values for vertical plane midway between two baffles, predictions by the Gidaspow and Brucato drag model were below the respective values from Derksen et al. (2003). The maximum slip velocity values obtained were 0.58, 0.63 and 0.72 for Gidaspow, Brucato and modified Brucato drag models respectively in the plane as compared to 0.75 in case of Derksen et al. (2003). Although, all the compared drag models were able to capture the high slip velocities in this region, only modified Brucato drag model predicted reasonable values of slip velocities.

From the above discussion, it is clear that the modified Brucato drag model can be successfully applied to higher solids concentration and particle Reynolds number. With this assertion, other parameters were analysed for the performance analysis of stirred tank.

4.3.4 Turbulent Kinetic Energy (TKE)

The flow in a stirred tank is turbulent flow that results in the fluctuating components of velocity due to formation of eddies. The k-ε model used in the RANS simulation assumes isotropic turbulence and uses the Boussinesq hypothesis to relate the Reynolds stresses to the mean velocity gradients (see Equation 4.3). The TKE represents the magnitude of turbulence present in the system. The presence of particles dampens turbulence. In order to assess the impact of particles at low solid loading, simulations were conducted for single phase, 1% solid loading and 7% solid loadings and the TKE was compared.

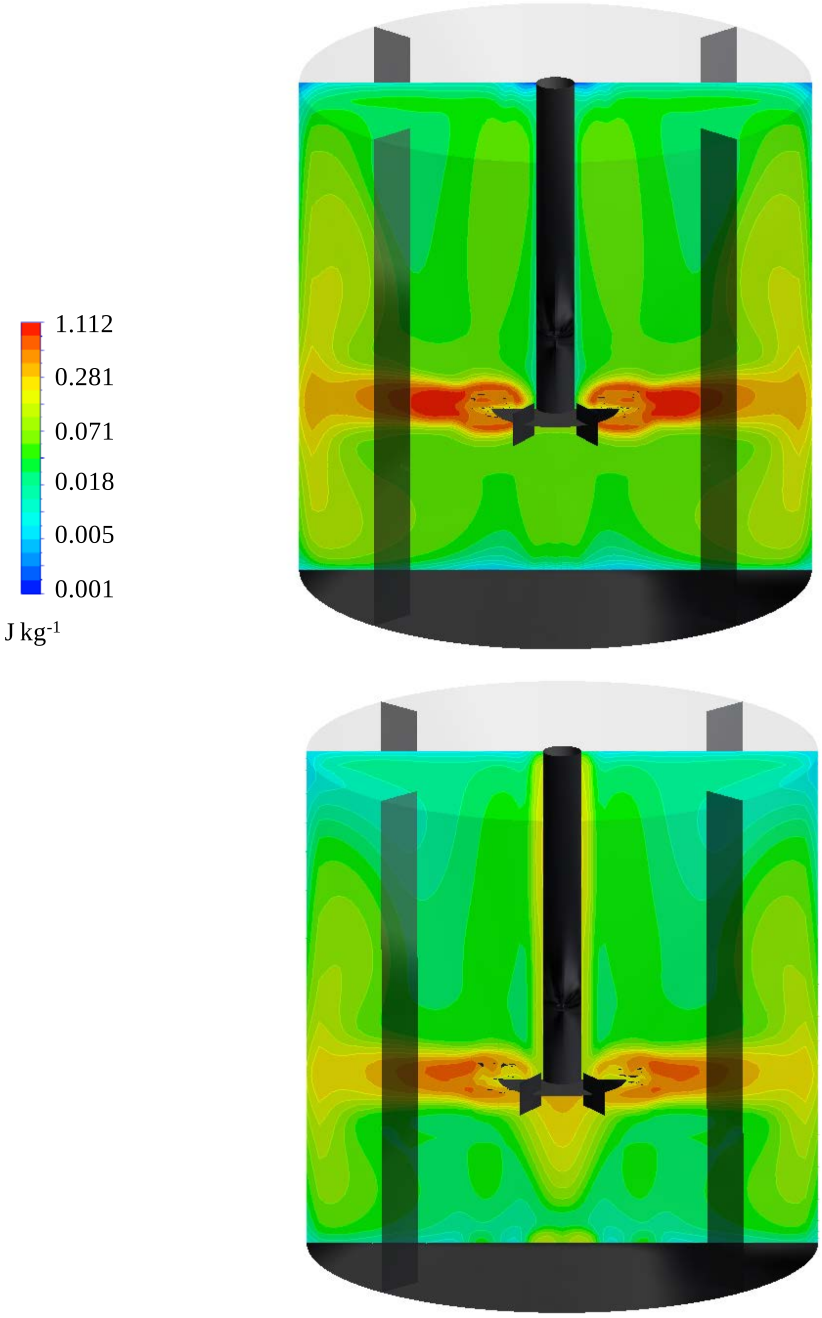

(a) Single Phase Flow (b) Solid- Liquid System (1% v/v)

Figure 4.13. Turbulent kinetic energy contours in stirred tanks at 1000 RPM using RT.

For a single phase system, the liquid is agitated by the impeller. The high velocity and trailing vortices result in large velocity fluctuations in the impeller plane. For this reason TKE was found to be the maximum at the blade tip (Figure 4.13a). As the velocity decreases radially in this plane, the TKE also decreases. The magnitude of TKE in the other parts of the tank is approximately 10^3 times lower than those in the impeller plane. Michelleti et al. (2004) used the LDA technique to measure dissipation rates at various points in the stirred tank and found the variation by more than 2 orders of magnitude between the impeller region and the bulk. Dissipation rate follows the same trend as TKE not only in the impeller region but in the other regions of the stirred tanks as well. The TKE, similar to the trend observed by Michelleti et al. (2004) for turbulence dissipation rate, is comparatively high near the walls and near the axially centre line where the axial velocity field is dominant. Similar behaviour is observed in the presence of particles (Figure 4.13b). However, the magnitude of TKE is much lower.

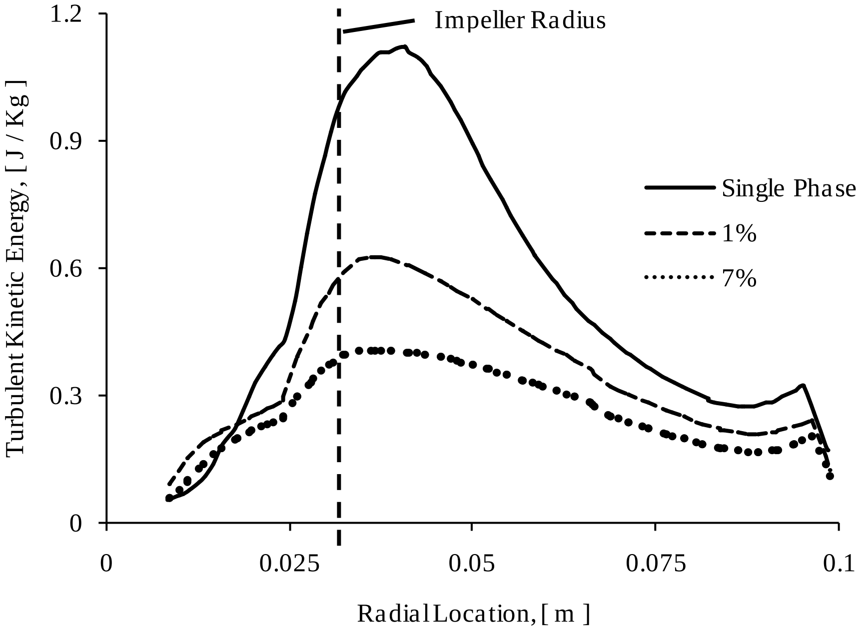

Figure 4.14. Turbulent kinetic energy profiles at impeller plane at 1000 RPM using RT.

Figure 4.14 shows the comparison between the TKE profile at impeller plane for 0%, 1% and 7% solids volume fraction. Within the impeller radius, the TKE increases due to the increase in turbulence. Initially, the rate of increase is lower as the impeller disc offers resistance. The impeller blades impart momentum to the fluid. The highly turbulent jet impinges radially out of the impeller. The vortices leaving the impeller blade also result in high magnitude fluctuating velocities. The high turbulence causes the formation of eddies of many different length scales. As a result, a hierarchy of scales appear in the flow (Falkovich and Sreenivasan, 2006). It results in the steep increase of TKE after the disc that reaches a maximum slightly beyond impeller radius. After this point, the TKE gradually decreases along the radius due to decrease in velocities. As the velocity jet hits the vessel wall, it creates eddies resulting in fluctuating velocities. As a result a small peak in the TKE is observed near the wall.

The kinetic energy in the liquid is imparted to solids resulting in the solids following the jet. It is also the reason for maximum energy dissipation in this zone. The comparison shows 50 % and 65 % decrease in the kinetic energy observed for 1% and 7% volume fraction of solids respectively in the impeller plane. The kinetic energy of the liquid is dissipated in the suspension and dispersion of solid particles. This results in the decrease in the level of turbulence and are visible as lower levels of TKE.

Nouri and Whitelaw (1992) measured and analysed liquid and solid phase velocities in stirred vessels with solid concentration upto 0.02 percent. The effect of presence of particles, particle concentration and density is studied on the slip velocities and turbulence and the turbulence was found to decrease by up to 25%. Specifically, they found the dampening in the turbulence in impeller zone. In the impeller zone, both the TKE and particle concentration are maximum. As a result, the dissipation of energy is the maximum in this region and leads to the maximum decrease in turbulence as particle concentration increases.

The dampening of turbulence found by Derksen et al. (2003) was around 15%. This value is far lower than as observed in this chapter. Similar observations were made by Michelleti et al. (2004) that presented the turbulence dampening values between 50 to 70%. The decrease in turbulence with increase in solid concentration was also observed by Barresi and Baldi (1987), Micheletti et al. (2003, 2004) and Ayazi Shamlou and Koutsakos (1989).

Micheletti et al. (2004) conducted experiments to study velocity characteristics in stirred solid liquid suspension. The flow field measurement in the presence of solids revealed a significant influence of their presence. The maximum difference was observed in the impeller plane that diminished with increasing radial distance. These points support the findings in this chapter where the turbulence is the maximum in the single phase flow and corresponding lower values of turbulence is observed for higher solid concentration. The difference in turbulence also decreases with the increase in the radial distance. In practical conditions, due to the increase in solids concentration, the dissipation of energy will be higher due to the high frequency of particle-particle, particle-wall and particle blades collision. The turbulence dampens in the presence of solids and the magnitude of vortices leaving the impeller decreases. For the same reason, a shift in the peak of TKE is observed with increase in solid concentration.

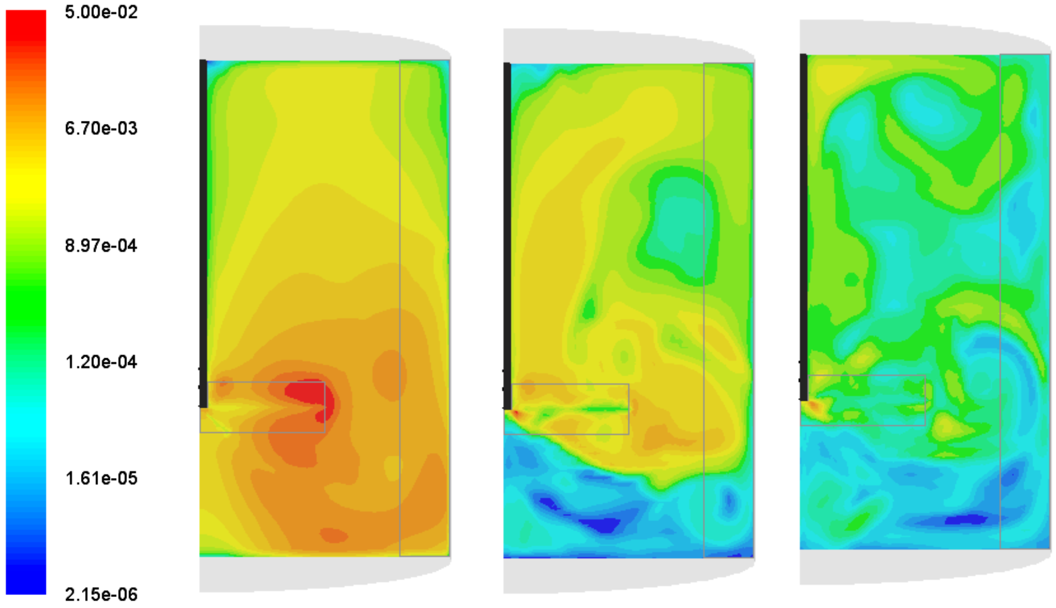

Figure 4.15. Normalised turbulent kinetic energy contours at mid-baffle plane using PBTD for N = N_{js} of (a) single phase, (b) solid phase (20 wt%) and (c) solid phase (40 wt%).

For high solid loading cases, normalised values of turbulent kinetic energy (TKE) were calculated by dividing the turbulent kinetic energy by the square of the tip velocity for the comparison of three cases viz. single phase, 20 wt% and 40 wt%. The simulation result shows very high value of kinetic energy in the impeller swept the region (Figure 4.15a). Since the value of TKE in the bulk was several orders of magnitude lower than that in the impeller region, therefore log scale was used in the colormap to show the change in even smaller values of TKE in the domain. Since the plane cuts the impeller blade, the magnitudes of TKE ahead of the impeller blade and that behind the impeller blade are also visible. The flow ahead of the impeller blade has at least double the TKE as that which follows the blade. The TKE is found to decrease with the advance of the flow loop and decreases by an order of magnitudes as the loop approaches wall. The difference in the TKE of the loop and the bulk is at least two orders of magnitude.

In order to understand the effect of solids on turbulence, its necessary to compare the results to those of single phase simulations. The direction of the flow loop changed in the presence of solids resulting in the observed drastic dissimilarity in the contours of TKE with and without solids (Figure 4.15). The high values followed the loop and were also observed in the upper portion of the tank rather than bottom as was seen in the single phase flow. The acute change of several orders of magnitudes in the TKE in the flow loop region is due to the simultaneous presence of high concentration of particles flowing along the loop. From Figure 4.15, the dampening of the turbulence and the increase in the dampening with the increase in particle concentration is evident. The same characteristic was also pointed out by studies in the literature (Guiraud et al., 1997, Bittorf and Kresta, 2003, Virdung and Rasmuson, 2007, Guida et al., 2010).

The turbulent structure provides energy to disperse the high concentration of solid particles, but at the same time the solid particles may result in the dampening of the turbulence (Barresi and Baldi, 1987, Nouri and Whitelaw, 1992, Bittorf and Kresta, 2003, Ochieng and Lewis, 2006). Turbulence produces eddies of different scales. These eddies generate eddies of smaller scales, where the gets ‘cascaded’ in smaller eddies. Kolmogorov microscales are the smallest scales in turbulent flow at which the cascade is terminated by viscosity (Falkovich and Sreenivasan, 2006). Only when the particle size is sufficiently close to the Kolmogorov microscale, the particle behaviour was unaffected by external turbulence. The eddy–particle interaction was reasoned as the basic mechanism for solids distribution in a stirred liquid (Pinelli et al., 2004). The settling velocity changes in the stirred tank in the conditions where the particle diameter is comparable to the Kolmogoroff microscale and eddies have significant influence on particle motion (Magelli et al., 1990). For $dp/\lambda > 10$, the interaction between energy dissipating eddies and particles become important for the solids concentration distribution (Ochieng and Onyango, 2008). In the cases studied in the chapter, the average value of this ratio was far higher than 10.

4.3.5 Slip Velocity

The data sampling for time statistics was opted in Fluent. The simulation data was time averaged for 2.5 s after the simulation got converged. Fluent computes the time averaged (mean) and root-mean-squares of instantaneous values sampled during calculations. The slip velocities for 1% volume fraction and 7% volume fraction at 1000 RPM were compared. All the parameters of the study were kept the same in the two cases except the solid volume fraction. Since, the velocity in the case of 1% volume fraction case was greater than the just suspension speed and that in the case of 7% volume fraction was below the speed of just suspension, a greater non-uniformity was observed in the solid concentration in the stirred tank. It resulted in an increased local value of the slip velocity in regions with a low solid concentration in the cases of higher average concentration of solids. Although the increase in concentration should result in the decrease in slip velocity, but in cases with impeller speed below and above the just suspension speed, local regions with higher slip velocities can be noticed. This behaviour was also observed by Sardeshpande et al. (2011). Another zone of higher slip velocities is the region in which the direction of axial velocities is upwards. In this zone, the velocity of the particles is against the force of gravity and increases the difference in the velocity of continuous phase and the dispersed phase. The observed phenomenon is exactly opposite in the regions with axial velocity vectors pointing downwards (Nouri and Whitelaw, 1992, Guiraud et al., 1997, Ljungqvist and Rasmuson, 2001, Ljungqvist and Rasmuson, 2004, Ochieng and Onyango, 2008, Pianko-Oprych et al., 2009).

The normalised slip velocities were calculated using the time averaged component of velocity of the two phases and is shown in Figure 4.16. The slip velocity was normalised by dividing the slip velocity by impeller tip velocity. The relaxation time for the particles has a very high value of 1.2425 s and the Stokes number was 9.94 and 12.21 for 20wt% and 40 wt% cases respectively. These values are an indicator of the presence of high slip velocities in the stirred tank. The high values of slip velocities were found in the impeller discharge region, vicinity of the side wall and near the impeller rod. The high values in the impeller discharge are expected due to the force exerted to the fluid accelerates it strongly but the particle acceleration is low due to the inertia. This supports the finding of Ljungqvist et al. (2004). High slip velocities near the side wall and impeller rod are mainly due to a combination of the effect of gravity and inertial forces. In the near wall region, high slip velocities located above the impeller plane are due to particles lagging the flow. In this region, the fluid flow is decelerating and due to a very high Stokes number the particles detach from the flow.

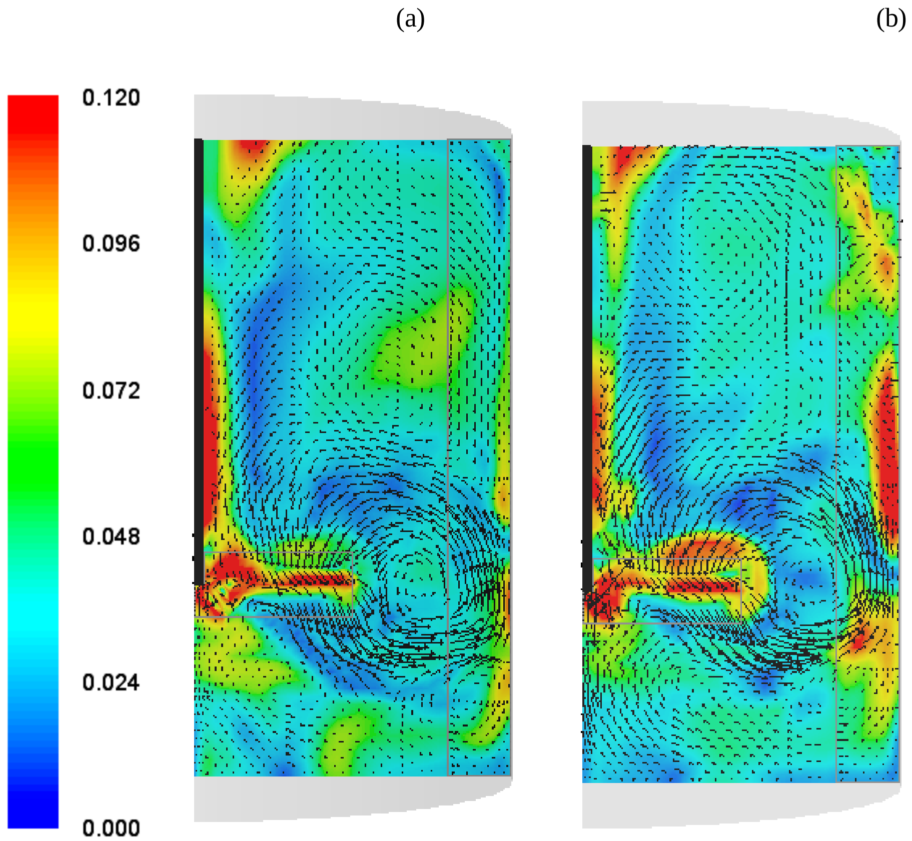

Figure 4.16. Normalised slip velocity maps and velocity vectors at mid-baffle plane using PBTD for N = Njs of (a) 20 wt% solid and (b) 40 wt% solids.

For the region below the impeller plane near the wall, the fluid leads and then lags the particle with the decreasing axial position. In the region of the loop where high fluid velocities encounter the wall, the fluid leads the solid. But below the loop, the fluid velocity approaches zero and the particles tend to settle down due to the absence of enough drag and presence of gravity, hence leaving the fluid behind. With careful examination, it can be observed that when the velocity vectors are pointing downwards (towards the gravity), the particles tend to gain velocity and lead the flow and when the velocity is in the opposite direction to the force of gravity, particle lags behind due to inertia and fluid lead the flow. This effect was also noticed and reported in the literature (Nouri and Whitelaw, 1992, Guiraud et al., 1997, Ljungqvist and Rasmuson, 2001, Ljungqvist and Rasmuson, 2004, Ochieng and Onyango, 2008, Pianko-Oprych et al., 2009).

A similar effect can also be observed in the near impeller region and in the clockwise secondary loop below the impeller. The dampening of the turbulence due to the increased solid concentration is the reason behind it. The modified Brucato drag model used in the simulation takes into account the turbulence effect at Kolmogorov length scale . Therefore, the simulations proved helpful in analysing the dampening of turbulence with increasing solid concentration. Its effect was noticed while comparing the slip velocity contours for the two cases. Due to this dampening, the magnitude of the slip velocity increased with the increase in concentration. When comparing the contours of TKE of Figure 4.15 (b) and (c) and corresponding slip velocities in Figure 4.16 (a) and (b), it is observed that the increase in solid concentration has dampened the turbulence in impeller zone. At the same time, the slip velocity in the zone has increased for 40 wt% case.

4.3.6 Cloud Height and Homogeneity

The velocities of the jet in the region above the impeller begin to decay after reaching a certain height. Negative buoyant jet behaviour is observed at this point and it results in a sudden concentration gradient and is termed as ‘cloud height’ (Ochieng and Lewis, 2006, Kasat et al., 2008, Fletcher and Brown, 2009). Beyond this height the velocity is not able to drag the solids. Apart from just suspension speed, the cloud height is an important parameter for the representation of homogeneity. The cloud height between 0.45-0.55T shows just suspension. The cloud height below this tank height shows poor homogeneity as very less solid concentration is present above this height. And a cloud height that reaches 0.9T or above shows the high quality of homogeneity. The cloud height was observed for the stirred tanks at volume fractions 0.01 and 0.07 using RT. In both the cases, the respective volume fraction of solids was patched over the entire volume. The cloud height in the stirred tank is shown as the iso-contours of the average volume fraction in the stirred tank Figure 4.17.

Fluctuations in the velocity and the solid concentration below the cloud height was observed to be negligible. Due to the sudden change in the flow field and concentration, a zone of high turbulent fluctuations and macroinstabilities forms at the cloud height. The velocity changes frequently and the cloud height fluctuates around a constant value.

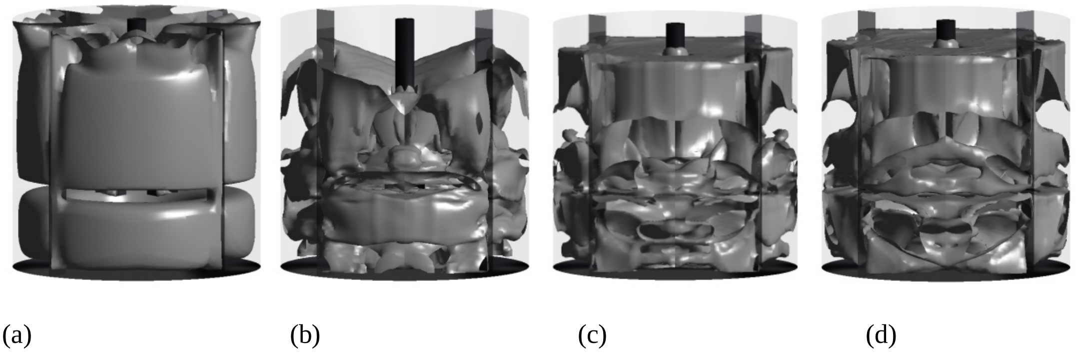

Figure 4.17. The cloud height in stirred tanks using RT. (a) 0.01 volume fraction 1000 RPM (b) 0.07 volume fraction 600 RPM (c) 0.07 volume fraction 800 RPM (d) 0.07 volume fraction 1000 RPM.

At low solid concentrations (0.01% v/v), the influence of solids on the liquid flow field is less. At the same time the kinetic energy dissipation of the continuous phase for the suspension of the dispersed phase is lesser as compared to the high loading systems. As a result, the magnitude of the axial velocity is not altered to a great extent. It implies that the level of turbulence was high and therefore, the drag observed by the particles was also high. This is reflected in the cloud height iso-contours for this case. Homogeneity in the stirred tank is achieved (Figure 4.17a). On a contrary, the dissipation of energy is more evitable in the case of high solid concentration. As a result, the turbulent kinetic energy in section 4.3.4 for 7% volume fraction is lower for the same impeller speed due to dampening of turbulence. This has a larger impact on the flow field resulting in a lesser drag experienced by the particles, hence lowering the cloud height. The cloud height is observed to be lower in the high solid loading system than the low solid loading system (see Figure 4.17a and d).

The decrease in the impeller speed not only resulted in the decrease in the cloud height but also the quality of suspension decreased. For the 7% volume fraction solid suspension and 600 RPM, the cloud height not only decreased but the solid concentration decreased drastically in regions right above the impellers. The reason behind such observation is the impeller speed which is far below the speed of just suspension and the prevailing. Therefore, the concentration in the bottom half of the tank is increasing resulting the dampening in the turbulence near the impeller blades. In the simulations, the solids uniformly present initially shift towards the bottom of the domain. Due to the high concentration of particles in the lower part, the recirculation is greatly affected in this region. While, in the region above the impeller, this impact is not significant. The recirculation created by the impeller in the region above it, forces the particles into the impeller zone creating a region void of solid particles (see Figure 4.17b).

Homogeneity is a measure of quality of suspension. The quality of the suspension increases with the impeller speed. The increase in the impeller speed results in a higher kinetic energy of the continuous phase which is available for disposal to the solids. A strong velocity field for continuous phase is present at high impeller speeds in various zones of a stirred tank. The velocity of the jet near the top surface is also larger. The magnitude of upward axial velocity near the walls is found to be higher when compared with those at lower impeller speeds. This result in the attainment of a higher cloud height at higher impeller speeds as is evident from Figure 4.17. It is in accordance with the results obtained by Sardeshpande et al. (2009) for impeller speeds above ‘speed of just suspension’. The non-monotonic behaviour in the cloud height is observed at very low impeller speeds (Sardeshpande et al., 2009). This effect is due to the presence of pseudo-bottom formed because of the accumulation of undispersed solids at the bottom causing ‘false-bottom’ effect. As a result the off-bottom clearance and the amount of suspended solids increases with increasing the impeller speed and hence, the cloud height decreases. Since, the impeller speeds studied were not very low that can cause ‘false bottom effect’, this non-monotonic behaviour was not observed. The height of the interface between the clear liquid layer and the solid suspension layer is lower in the region above the impeller as the recirculating jet forces solids downwards near the axis. This phenomenon is prominent at low impeller speeds due to the weak upward axial flow and the dominance of the drawing action right above the impeller.

4.3.7 Power Number

The power number is a global criterion providing an estimate for the power dispersed in mixing by an impeller. For the cases discussed for high solid loading systems, the increase in the power number with the increase in solids concentration was observed. Bubbico et al. (1998) performed experiments for investigation of effects of large particles suspension on the agitation power. They also observed the increase in the power number with the increase in concentration and accredited it to the increased drag in the case of large particles. However, the results obtained in the cases simulated in the chapter do not show a linear increase in the power number as is shown by Bubbico et al. (1998). The power number increases from 1.67 for single phase to 2.11 for 20 wt% solids and 2.34 for 40 wt% solids in the simulations. The power dissipated observed is non-linear and its value for 40 wt% falls below the expected extrapolated value of 2.55 as the Euler-Euler simulations are not able to include the energy lost due to the particle collisions and, therefore, underpredict power dissipation at higher solid concentration. Therefore, the increase in the collisional stress in the dispersed phase and fluctuations in velocity magnitude and direction due particle-particle and particle-wall collisions need to be included in the model for a more accurate representation of physics.

4.4 Simulation of CIL Tank

The choice of impeller type for a process depends on the problem it has to solve. In the CIL process, suspension of solid particles is a common problem. The turbulence is responsible for the suspension of particles. The local relative intensity of turbulence can provide an understanding of the solids suspension in a stirred tank (Montante et al., 2001). Compared to an axial flow impeller, radial flow impeller provides higher shear and turbulence levels with lower pumping (Paul et al., 2004). However, comparing the turbulence field generated by radial flow impeller and axial flow impeller shown in Figure 4.13 and Figure 4.15 respectively, the axial impeller appears to create high local turbulence at the bottom that do not allow the particles to settle. This is the reason that axial flow impellers are used in the industrial CIL tanks.

In this part of the chapter, the validated modified Brucato drag model is used for simulating laboratory scale geometry at N_{js} using the particle properties and concentration present in industrial CIL tanks. The dimensions of flat bottomed cylindrical tank with 6 bladed PBT used by Guida et al. (2010) was used for the laboratory scale geometry. The dimensions of the impellers and tank is tabulated in Table 4.1. The N_{js}, calculated using Zwietering's (1958) correlation, is 305 RPM. The concentration of ore particles in CIL tanks is between 45-50 wt% and average particle diameter is 75 μm. In simulations, the concentration of ore particles was taken as 50 wt% (23.6 % by volume). The particle diameter used in the simulations is 75μm.

Based on the simulation results, analysis is presented in the following sections of this chapter.

4.4.1 Flow Field and Velocity Components

The overall flow field observed was as expected in the case of PBTD (Figure 4.18). However, an anomaly was found in the region right below the impeller rod, where high velocity zone can be observed along with a strong clockwise loop. The jet approaches the bottom but the velocity seems to diminish before hitting the bottom and a change in jet direction is observed. The direction of the jet changes at a height of 0.1T from the bottom wall This is due to the presence of a bed of settled solids. The lesser clearance available to the jet and a lesser horizontal inclination has resulted in the formation of a strong secondary loop in the centre of the tank right below the impeller. Due to the low clearance, high velocity regions were found in the other parts of the tank as well. It is worth noticing that due to a higher concentration of solids, low velocity values are observed due to dampening of turbulence. A detailed scrutiny by considering the results from the flow field in conjunction with the turbulent kinetic energy contours is presented in Section 4.4.3.

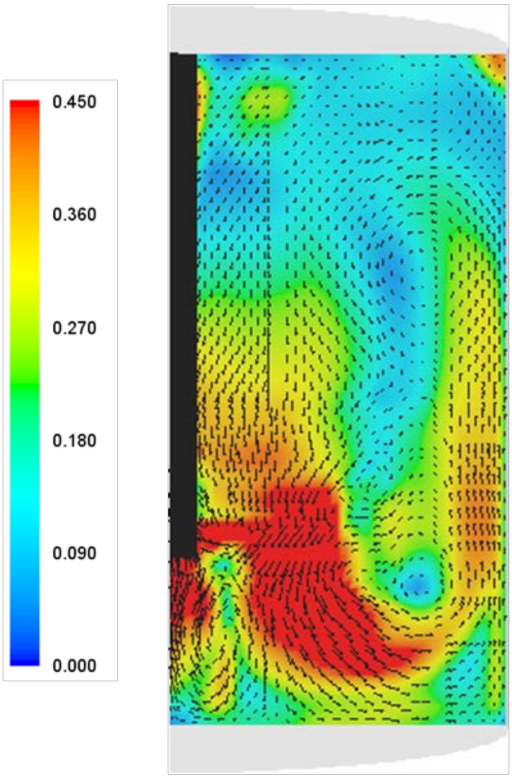

Figure 4.18. Normalised velocity maps and velocity vectors at mid-baffle plane using PBTD for N = Njs of CIL tanks (50 wt %).

Pinelli et al. (2004) reasoned that the eddy–particle interaction is the basic mechanism for solids distribution in a stirred liquid. Only when the particle size is sufficiently close to the Kolmogorov microscale, the particle behaviour was unaffected by external turbulence. As is determined by the simulation of CIL tanks, Kolmogorov microscale is of the order of 10^{-6}. The particle size is greater by an order of magnitude than the Kolmogorov scale. Smaller particles follow the streamlines of the fluid, thus dissipating its kinetic energy, while larger particles will result in a bigger wake, in turn resulting in more energy being transformed from the mean flow to turbulent kinetic energy (Virdung and Rasmuson, 2007). Therefore, the effect on the drag and turbulence significantly decreased with the decrease in the particle diameter. A combination of low turbulence damping and the settling of solids resulted in the high velocity field prevailing in the entire tank.

A high velocity field will help in keeping the particle suspended, for which a higher impeller speed will be required for the suspension of unsettled solids. A homogeneous suspension at small particle size and low concentration is obtained at low impeller speeds (Nasr-El-Din et al., 1996, Altway et al., 2001, Angst and Kraume, 2006, Sbrizzai et al., 2006, Sardeshpande et al., 2009). However, in the CIL tank, although the particle diameter was small (75 µm), the solid concentration was very high (50 wt%). The presence of the particle bed suggests that the impeller speed was not enough to suspend such high concentration of particles. Moreover, the just impeller speed calculated using Zweitering correlation was not accurate as the operating conditions in this case did not lie in the range in which the correlation is valid. Zweitering correlation is valid for particle diameter between 560 and 1800 µm and volume fraction between 0.5 and 20%. Higher impeller speed is desired for the suspension of settled particles.

The high value of velocities is also observed in the normalized axial, radial and tangential velocity components shown in Figure 4.19. Although an overall high concentration of particles is present, the amount of suspended solids is low. Therefore, the impact of solids on velocities is not dominant.

A higher mean axial velocity in the upward flow is observed for smaller particles because of the lower magnitude of the force due to gravity on particles (Nasr-El-Din et al., 1996, Guiraud et al., 1997, Ochieng and Lewis, 2006, Hosseini et al., 2010). A similar observation for the magnitude of axial velocity can be made from Figure 4.19. Moreover, due to the secondary loop shown in Figure 4.18, two peaks in the axial velocities are visible and a peak in the axial velocity near the centre also confirms the presence of strong recirculation.

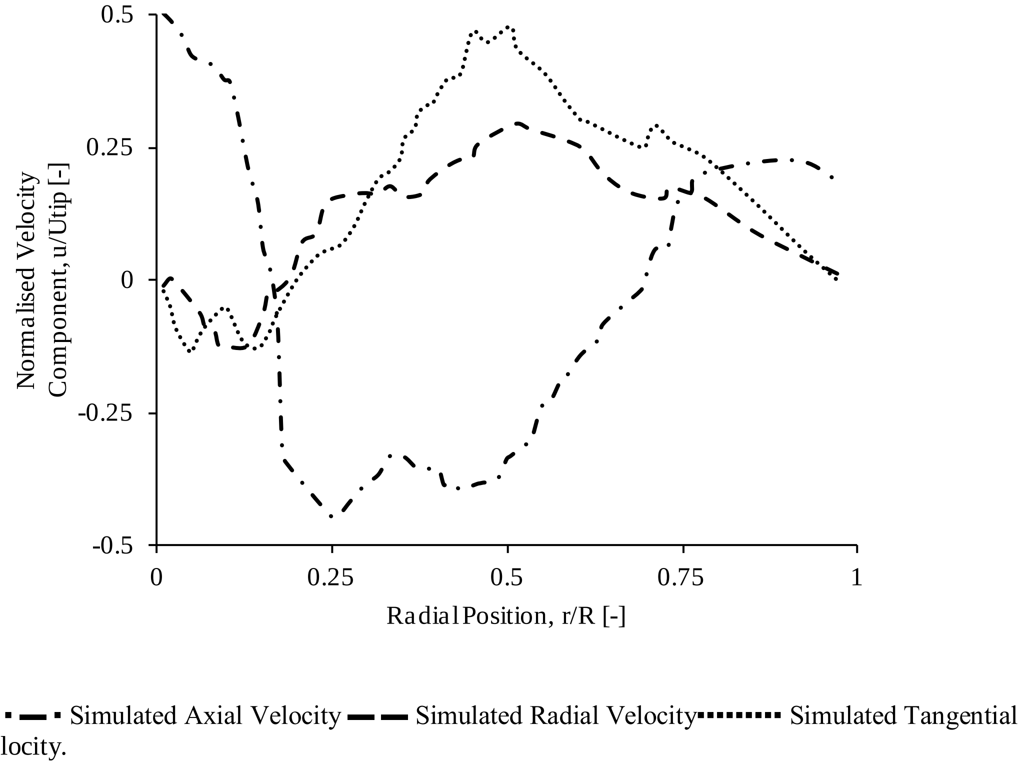

Figure 4.19. The three velocity components of solids in a horizontal plane at z/H = 0.2 for CIL tanks (50 wt%) and N=Njs.

The negative radial and tangential flow near the centre also suggest strong recirculation that forces the flow radially inwards and the presence of eddies and trailing vortices. The radial and tangential velocities increased radially as expected till the centre of the jet, then gradually reduces reaching near the eye of the loop, increases giving a small maxima for the upwards jet near the wall and then advances towards zero while approaching the wall.

4.4.2 Slip Velocity

Very few regions of high slip velocities can be noticed in the contour plot shown in Figure 4.20. In majority of the domain, the normalized slip velocity lies between 0.012 and 0.036 as compared to the values in the cases of 20 wt% and 40 wt% lying between 0.048 and 0.072. The reason for such a vast difference is the particle diameter. As is also mentioned in the previous section, smaller particles have a very little effect of the force due to gravity and have very less relaxation time. The force due to gravity is not enough to counteract the drag and result in particle settling. Therefore, small ore particles follow the trend of the fluid.

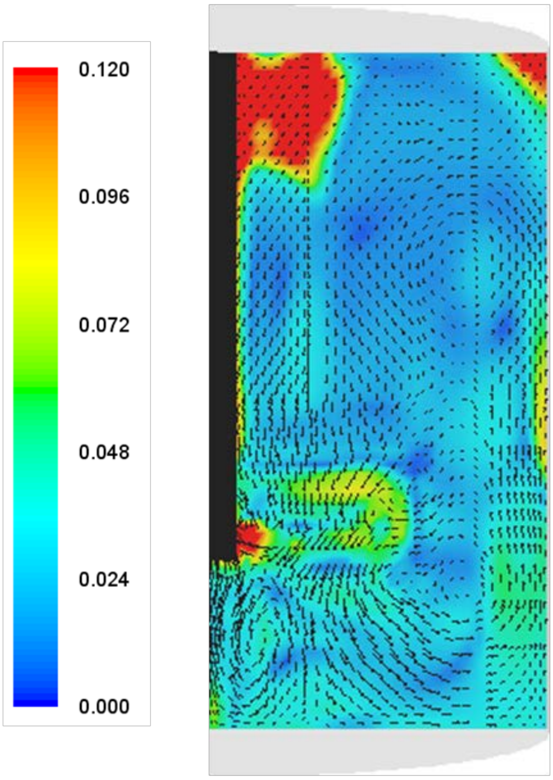

Figure 4.20. Normalised slip velocity maps and velocity vectors at mid-baffle plane for N = Njs of CIL tanks (50 wt %).

Although less, but there are regions of high slip velocity in the CIL tanks. High slip velocities are observed in the impeller region as the particles lag behind the liquid phase due to little but a finite relaxation time. Other than that, in the upper centre and near wall region of the stirred tank, the fluid velocities are very low. Therefore, the kinetic energy of the fluid in this region is also low, such that the kinetic energy of the continuous phase is not enough be transferred for the suspension of the dispersed phase. It is evident from the figure that in the regions of very high slip velocities except impeller region, either the solid phase velocities or solids concentration is negligible. In the near wall region, the moderate values of slip velocities are mainly due to a combination of the effect of gravity and inertial forces. But, since the gravity forces are not that dominant, the values of slip velocities did not rise to significant values. The mass transfer is directly related to the slip velocities. High mass transfers are observed in the regions of high slip velocities (Ljungqvist and Rasmuson, 2004). Since gravity has a little effect and the particles have a short relaxation time, a very high inertia developed by the impeller can result in high slip velocities favourable for leaching in CIL tanks.

4.4.3 Turbulence Kinetic Energy

The normalized turbulent kinetic energy in CIL tanks plotted on a logarithmic scale is shown in Figure 4.21. The normalized turbulent kinetic energy contours for CIL tanks when compared with that of the single phase flow shown in Figure 4.15a are qualitatively similar. Except, there is a difference of an order of magnitude quantatively, where the average value in bulk for single phase flow is 0.016 m^2/s^2

and for CIL tank is 0.0016 m^2/s^2. In the case of single phase flow, the high turbulence is also observed when the jet hits the bottom. This is not observed for the CIL tank due to the presence of solid bed. Moreover, when the values are compared quantitatively, the turbulence has significantly dampened due to the presence of solids. At the bottom of the CIL tank, the value drops to 0.00024 m^2/s^2 from the value of 0.02 m^2/s^2 in single phase.

Settled solids has resulted in the low turbulence at the bottom. The high solid concentration in the bottom centre also results very low turbulence in this region. This problem can be addressed by the use of mixed impeller and reducing the off-bottom clearance. Reducing off-bottom clearance will also result in fluid striking the bottom at high velocities causing the solids to suspend. However, for axial impellers, a very small off-bottom clearance may also result in a very low velocity zone at the bottom centre of the tank (Hosseini et al., 2010).

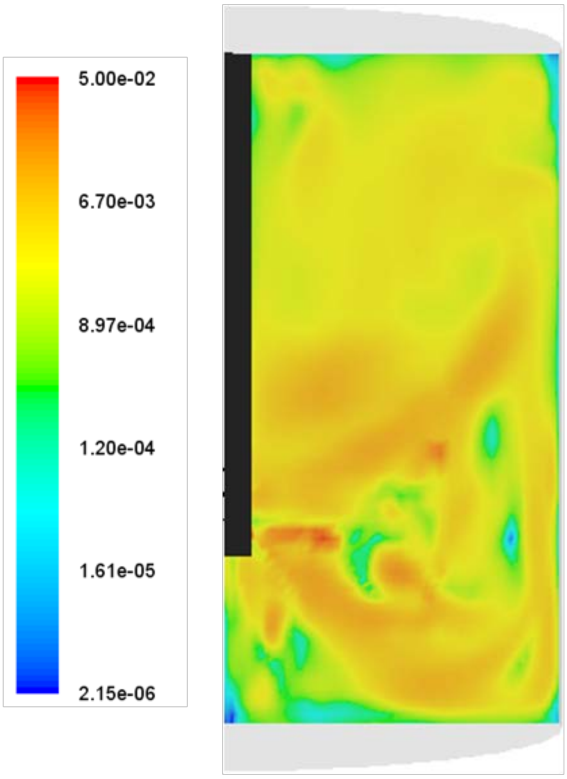

Figure 4.21. Normalised turbulent kinetic energy contours at mid-baffle plane for N = Njs of CIL tanks (50 wt %).

With respect to the impeller zone, the turbulence in the bulk decreases by several orders of magnitudes. The low turbulence in the bulk region results in higher mixing times because it denotes a weaker velocity region that takes more time to suspend the particles. The condition will worsen with higher impeller speeds, when the settled solids at the bottom will get suspended resulting in a further dampening of turbulence. Moreover with scale-up the gradient in the turbulence will increase exponentially. Therefore, multiple impellers are used and are recommended for use in CIL tanks to maintain the suspension and turbulence.

4.5 Conclusion

CFD simulations of solid suspension in stirred tank (CIL) are conducted for concentration 1% and 7% v/v and the impeller speeds above the “just suspension speed”. The predictions of four different drag models viz. Gidaspow, Wen & Yu, Brucato and modified Brucato drag models were compared. It is observed that the turbulence dispersion force had negligible effect due to a low volume fraction of solids. Moreover, high turbulence is found to increase the drag coefficient. The drag force was modified to account for the increase in drag at high turbulent intensities using Brucato and modified Brucato drag models. The modified drag law was found to be useful to simulate the low solids holdup in stirred tanks. Axial, radial and tangential velocities were compared at different axial locations. It was observed that all four models could qualitatively capture the flow in stirred tanks. The Wen and Yu and Gidaspow model showed biggest deviation from the experimental data while results from the modified Brucato drag model were in reasonable agreement for the liquid flow fields. Turbulent kinetic energy, homogeneity and cloud height in the stirred tanks are studied and discussed in the chapter. Maximum turbulence kinetic energy was found in the impeller zone. The turbulence dampens with the increase in the solids concentration and this effect was the most significant in this zone. The cloud height and homogeneity were found to increase with an increase in impeller speed. For achieving homogeneity at low loading stirred tanks, a low impeller speed is adequate. However, high impeller speed is needed for high solid loading systems such as CILs, as the energy dissipation is significant due to more number of particles and high frequency of particle-particle, particle-wall and particle-blade collisions.

CFD simulations were conducted for simulating stirred tanks with high solid concentration. The effect of high solid loading on the performance of stirred tank was conducted by the analysis of the flow field, velocity components, slip velocity, turbulence kinetic energy and power number. A careful application of drag model is recommended for the high concentration of solids in stirred tanks. Modified Brucato drag model worked well for the particle concentration of 20 wt% and 40 wt%. The increased solid concentration substantially changed the flow field. The ‘false bottom effect’ at very high solid concentration results in higher velocity values compared to moderate solid concentration cases. High slip velocity was found below the impeller, near the wall and near the impeller rod for PBTD. The magnitude of slip velocities increased due to increase in solid concentration. Dampening of turbulence was dominant due to the presence of particles. At higher concentration, significant power is required to counteract the dampening and for the dispersion of solids. The power number linearly increases with the increase in concentration. External forces need to be accommodated to incorporate the effect of energy dissipation due to particle collision at high solid concentration.

From the flow field, slip velocities and turbulence generated in CIL tanks by axial flow impellers, it can be concluded that velocities higher than Zweitering's correlation will be required for the complete suspension of particles. The gradient in the turbulence kinetic energy is too high, so multiple impellers can be a solution to maintain uniform turbulence and high slip velocities in the system.

The aim of the study was to gain insight of the hydrodynamics in CIL tanks. In the absence of consensus on drag models applicable for such systems, various drag models were assessed and appropriate drag model was used for simulation of CIL tank. The simulations presented in this chapter neglect presence of of carbon particles in CIL tanks. The concentration of these carbon particles (~1% v/v) is much lower than the ore particles (~ 25% v/v). Therefore the flow of carbon particles is affected by the ore particles and suitable drag models are required to accurately capture this interaction. No drag model is available that accounts for such a huge difference in volume fraction in bidisperse systems. Moreover, the drag experienced by the carbon particles is different in the presence of high concentration of ore than that in stagnant fluid. The next chapter discusses the evaluation of drag using MPM and the formulation of drag model for carbon particles present in a high concentration mixture of ore in liquid.

Chapter 5 Macroscopic Particle Model and Drag Formulation for Carbon Particles

As mentioned in the previous chapter, the drag experienced by the carbon particles is different in the presence of higher concentration of ore than that in stagnant fluid. Therefore, the same drag formulations cannot be used in such systems. In order to calculate drag on the carbon particles, a different approach is used. The system is treated as carbon particles present in non-Newtonian slurry of ore particles and cyanide solution. For simulations, RDPM approach is used. RDPM approach provides the accuracy at a comparatively lesser computational expense. In this study, a novel Macroscopic Particle Model (MPM) (Agrawal et al., 2009) is used, which is based on RDPM approach. MPM is incorporated in Fluent using UDFs.

Prediction of particle motion and terminal velocities in liquid is of critical importance. Terminal velocity was selected as the parameter for validating the model. In comparison with the voluminous literature available for the drag formulations and the movement of the sphere in quiescent Newtonian fluids, only a few papers related to yield-pseudoplastic non-Newtonian fluids are available. Current methods for predicting the terminal velocity are based on the extrapolations from known Newtonian behaviour or some empirical correlations for each individual fluid. Such estimations are full of uncertainties. Therefore, a review of papers is necessary to find a reliable data set required for the validation of results obtained from this novel approach. The motion of the particle in unbounded, stagnant Newtonian and non-Newtonian fluids using MPM approach is explained. The particle fall behaviour for these non-Newtonian calculations were then validated with experimental data (Wilson et al., 2003).

5.1 A brief review of particle motion in stagnant fluids

There are several studies on particles settling in Newtonian and non-Newtonian fluids (Cox and Brenner (1967), Bungay and Brenner (1973), Brunn (1982), Turton and Clark (1987), Madhav and Chhabra (1994), Atapattu (1995), Di Felice (1996), Beaulne (1997), Nguyen (1997), Chhabra (2003)). A state of the art review of the particle falling in both Newtonian and non-Newtonian fluids have been conducted by Chhabra (2006). A brief review relevant for the validation of MPM model is presented below:

5.1.1 Newtonian Fluids

For spherical particles, the resisting force observed by the particle is given as:

$$F_d = 3\pi\mu V_t d \qquad \text{………(5.1)}$$

where, μ is the fluid viscosity, V_t is the particle's terminal velocity and d is the diameter of the particle.

When the particle achieves terminal velocity, the weight of the particle is balanced by the sum of the buoyancy and the resisting force caused by the flow of the fluid around the particle.

$$\frac{1}{6}\pi d^3 \rho_p g = \frac{1}{6}\pi d^3 \rho_f g + 3\pi\mu V_t d \qquad \text{………(5.2)}$$

where, ρ_p and ρ_f are the densities of particle and water respectively, g is the acceleration due to gravity.

Solving the above equation provides the terminal velocity of the particle (also known as Stokes law velocity):

$$V_s = \frac{(\rho_p - \rho_f) g d^2}{18\mu} \qquad \text{……... (5.3)}$$

However, it is only valid for Reynolds number less than 0.1 (Flemmer and Banks, 1986). For the calculations for Reynolds number greater than 0.1, the drag force involving drag coefficient was used.

It involved a correlation between Reynolds number and drag coefficient and required iterative procedure to obtain a value of terminal velocity. The correlation is given as:

$$C_d = \frac{24}{\mathrm{Re}}\left(1 + 0.173\,\mathrm{Re}^{0.657}\right) \qquad \text{………(5.4)}$$

Although a huge disparity in the experimental data and the data from correlations at high Reynolds number was still a problem. Turton and Levenspiel (1986) modified the correlation and derived an expression that suited better for a wide range of Reynolds number. The correlation is given as:

$$\mathrm{C_d} = \frac{24}{\mathrm{Re}}\left(1 + 0.173\,\mathrm{Re}^{0.657}\right) + \frac{0.413}{1 + 16300\,\mathrm{Re}^{-1.09}} \qquad \text{………(5.5)}$$

Haider and Levenspiel (1989) developed correlations for the prediction of terminal velocities and drag coefficient for spherical and non-spherical particles. The correlation was similar to that given in Equation 5.5. Both of these correlations are valid for Reynolds number up to 20000.

Other than this, Nguyen et al. (1997) carried out an asymptotic analysis for calculating the terminal velocity of rigid spheres (V_t) from the Stokes law velocity (V_s) based on a relationship between Reynolds number and Archimedes number. They generated a three parameter model.

$$\frac{\mathrm{V_s}}{\mathrm{V_t}} = 1 + \frac{\mathrm{Ar}}{96}\left(1 + 0.079\mathrm{Ar}^{0.749}\right)^{-0.755} \qquad \text{………(5.6)}$$

where, Ar is Archimedes number. According to the author (Nguyen, 1997), this new model was capable of describing the terminal velocity for a wide range of Archimedes numbers ranging up to 80^3.

Few studies were conducted in order to find the influence of boundary walls on the velocity of sphere. Di Felice (1996) reported a relationship for prediction of bound terminal velocity (V_{tb}) in terms of unbound terminal velocities (V_s) and the ratio of particle to the cylinder diameter (λ) and they proposed it to be applicable to viscous, inertial and intermediate flow regimes:

$$\frac{V_{bt}}{V_s} = \left(\frac{1-\lambda}{1-0.33\lambda}\right)^{\alpha} \qquad \text{………(5.7)}$$

where, α is a constant derived from a correlation with Reynolds number ($Re_{t\infty}$) at terminal velocity for unbound fluid.

α is given as:

$$\frac{3.3-\alpha}{\alpha-0.85} = 0.1\text{Re}_{t\infty} \qquad \text{………(5.8)}$$

Since this correlation was not suitable for a wide range of Reynolds numbers, so Chhabra (2003) identified Reynolds numbers that marked the transitions from the viscous to intermediate and from the transitional to fully inertial flow regimes as functions of λ. The functional dependence of the wall factor on the sphere-to-tube diameter ratio (λ) and the sphere Reynolds number (Re) were examined. They derived a wall factor which was a function of λ and Re in the intermediate zone, and only a function of λ at very low and very high values of Re.

Out of the correlations discussed, the correlation proposed by Turton and Levenspiel (1986), which is applicable for a wide range of Reynolds number and predicts the terminal velocity with high accuracy for the unbound fluids, was used for the comparison with predictions of the MPM model for Newtonian cases.

5.1.2 Non-Newtonian Fluids

In non-Newtonian fluids, shear stress versus shear rate curve is not linear or if it is linear, it does not pass through the origin. The viscosity of such fluids is a function of the applied shear, i.e., with a change in the shear, there is a new value of apparent viscosity. The rate of shear of these fluids is purely a function of the current value of shear stress. The stress-strain curve of these fluids may be linear or nonlinear, once the yield stress has been achieved.

The fluid properties of yield pseudoplastic fluid can be given by different models. Two such models are the Casson equation and the Herschel – Bulkley equation, that are widely used to relate the stress and deformation in yield pseudoplastic fluids. The Casson model is a two parameter model:

For $\tau_{yx} > \tau_o^c$:

$$\left(\tau_{yx}\right)^{0.5} = \left(\tau_o^c\right)^{0.5} + \left(\mu_c \gamma_{yx}\right)^{0.5}$$ ……..(5.9)

For $\tau_{yx} < \tau_o^c$:

$$\gamma_{yx} = 0$$ ……..(5.10)

where, τ_{yx} is the shear stress, γ_{yx} is the shear rate, τ_o^c is yield stress and μ_c is the consistency parameter.

On the other hand, the Herschel-Bulkley equation is a three parameter model. It is given as:

For $\tau_{yx} > \tau_o^h$

$$\tau_{yx} = \tau_o^h + K_h \left(\gamma_{yx}\right)^n$$ ……..(5.11)

For $\tau_{yx} < \tau_o^h$:

$$\gamma_{yx} = 0$$ ……..(5.12)

where, τ_o^h is yield stress, K_h is the consistency index and n is the power-law index.

Note that when the shear stress falls below the yield stress, a solid structure is formed (un-yielded). Also when the power-law index is unity and the consistency index is equivalent to the plastic viscosity, the Herschel–Bulkley model reduces to the Bingham model.

For non-Newtonian fluids, Kelissidis (2004) determined correlations for predicting terminal velocities, and compared the results with previously published data (Turton and Clark, 1987, Kelessidis and Mpandelis, 2004), and derived:

$$U_* = \left[1 \Big/ \left\{ \left(\frac{18}{d_*^{1+n}}\right)^{0.824/n} + \left(\frac{0.321}{d_*}\right)^{0.412} \right\}\right]^{1.214}$$ ………(5.13)

where, U_* is the dimensionless velocity, d_* is dimensionless diameter and n is the power law index for non-Newtonian fluids.

d_* is written as:

$$d_* = d\left(\frac{g\Delta\rho}{\rho}\right)^{(2-n)/(2+n)}\left(\frac{\rho}{K}\right)^{2/2+n} \qquad \text{……..(5.14)}$$

where, ρ is density, K is consistency index, g is acceleration due to gravity and d is particle diameter.

and U_* is written as:

$$U_* = V\left[\frac{\rho^{n+1}}{g^n K \Delta\rho^n}\right]^{1/(2+n)} \qquad \text{……..(5.15)}$$

Motion of particles in non-Newtonian fluids is based on extrapolations of known Newtonian behaviour or calculated using a specific empirical correlation for each individual fluid. Such estimations are full of uncertainties. Moreover, Wilson et al. (2003) observed that predicting fall velocity using the existing correlations required an iterative procedure beginning with an initial estimate of the fall velocity which is employed to obtain a representative strain rate for use with the rheogram. Their methods also involve the customary plot of drag coefficient versus Reynolds number. The axes of this plot are poorly suited for the calculation of fall velocity, as it occurs in both the drag coefficient and Reynolds number. It, therefore, requires iteration even in the Newtonian case. In many of the cases that were tested, the iteration failed to close, or the predicted fall velocity was of the wrong sign. Therefore, Wilson et al. (2003) devised the concept of ‘equivalent Newtonian viscosity’ for non-Newtonian fluids on the basis of fluid rheology, which was then used for a direct prediction of terminal velocities. According to them, the accuracy of the predicted velocities was adequate for engineering purposes. The ‘equivalent Newtonian viscosity’ was given by:

$$\mu_{eq} = \frac{\tau}{\gamma'} \qquad \text{……..(5.16)}$$

where, τ is the shear stress and γ' is the shear rate at a particular τ and is determined by the rheogram.

τ is given by:

$$\tau = \xi\bar{\tau} \qquad \text{……..(5.17)}$$

where ξ is shape factor and $\bar{\tau}$ is the superficial shear stress.

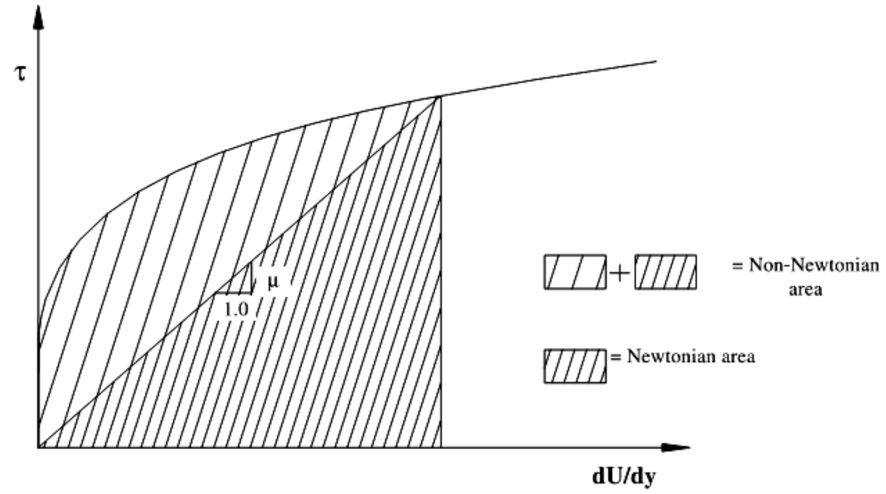

Figure 5.1. Schematic rheogram showing viscosities and shape factor areas. (Wilson et al., 2003)

The shape factor is based on the area beneath the portion of the rheogram to the left of the reference point (used at the intersection of rheogram and line of μ= 1). Shape factor is the ratio of non-Newtonian area to the Newtonian area (see Figure 5.1). The range of ξ lies from 1.0 (for a Newtonian fluid) to nearly 2.0 (which would apply for a plastic having τ constant rather than depending on strain rate). The position of ξ within these limits gives a measure of the degree of non-Newtonian behaviour (Wilson et al., 2003).

The superficial shear stress by:

$$\bar{\tau} = \frac{(\rho_p - \rho_f) g d_p}{6} \qquad \text{……..(5.18)}$$

Wilson et al. (2003) used a value of 0.3 for ξ to calculate the equivalent viscosity. This model provided reasonably accurate results for the prediction of the terminal velocity in non-Newtonian fluids, and therefore, it was chosen for the comparison of results obtained from MPM model.

Wilson et. al. (2003) conducted experiments for particles falling in stagnant non-Newtonian fluids. The rheology of these non-Newtonian fluids was represented using the Casson model.

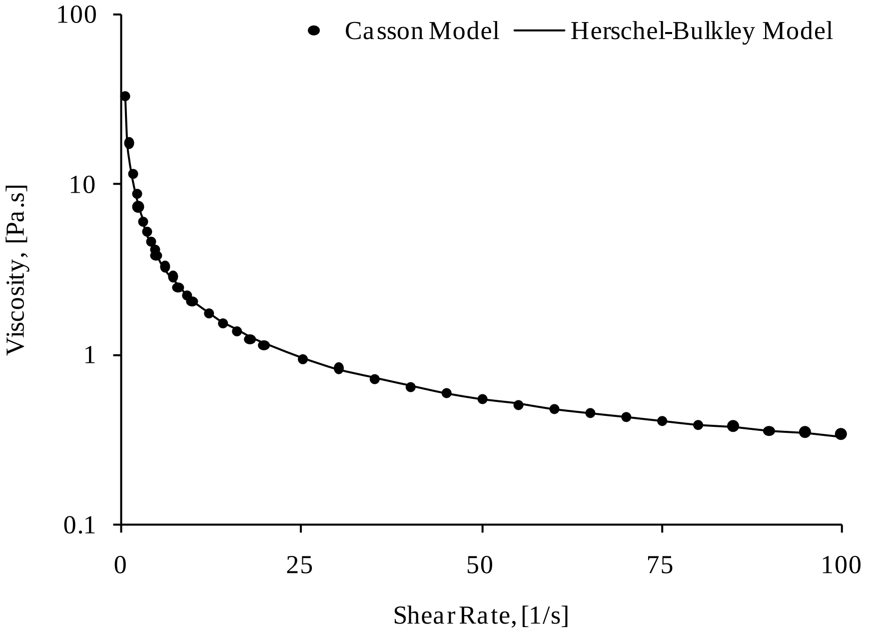

Figure 5.2. Apparent viscosity as a function of shear rate using the Casson and Herschel- Bulkley models.

The rheological property of a fluid can be incorporated in FLUENT in three different ways. Firstly, it can be treated as a constant; or it can be provided in the form of parameters of a model already available in FLUENT. Finally, it can be introduced as a user defined function, which provides the value of viscosity at each node of the geometry at each time step. Currently, Casson's rheological model, which is most appropriate for pseudoplastic fluids, is not available in FLUENT. Therefore, the rheological properties of the fluid were incorporated in FLUENT as a three parameter Herschel-Bulkley model. The stress versus strain data were collected from the Casson parameters and best fit parameters for the Herschel - Bulkley model were calculated using MATLAB®. The apparent viscosities using the Casson and Herschel-Bulkley model are compared in Figure 5.2. For the range of data studied, the RMS error between the predictions using two models was 0.0276, which is in tolerable limits.

5.2 Hydrodynamics Model

5.2.1 Continuity Equations

For the flow of non-Newtonian fluid, the laws of conservation apply in the same manner as for the Newtonian fluids. The conservation of mass can be described by the continuity equation (Versteeg and Malalasekera, 1995):

$$\frac{\partial \rho}{\partial t} + \nabla . \left(\rho \vec{v} \right) = S_m \qquad \text{……..(5.19)}$$

where, ρ is the density, v is the velocity vector and S_m is the mass added to the continuous phase from the dispersed phase. In this case, S_m is zero.

The equation for momentum conservation in three dimensions is as follows (Versteeg and Malalasekera, 1995):

x-component of momentum equation:

$$\rho\frac{Du}{Dt}=\frac{\partial\left(-p+\tau_{xx}\right)}{\partial x}+\frac{\partial\tau_{yx}}{\partial y}+\frac{\partial\tau_{zx}}{\partial z}+S_{Mx} \quad \text{……..(5.20)}$$

y-component of momentum equation:

$$\rho\frac{Dv}{Dt}=\frac{\partial\tau_{xy}}{\partial x}+\frac{\partial\left(-p+\tau_{yy}\right)}{\partial y}+\frac{\partial\tau_{zy}}{\partial z}+S_{My} \quad \text{……..(5.21)}$$

z-component of momentum equation:

$$\rho\frac{Dw}{Dt}=\frac{\partial\tau_{xz}}{\partial x}+\frac{\partial\tau_{yz}}{\partial y}+\frac{\partial\left(-p+\tau_{zz}\right)}{\partial z}+S_{Mz} \quad \text{……..(5.22)}$$

where u, v and w are the velocity components in x, y and z directions respectively, p is the normal stress (for pressure force), τ is the viscous stress (for viscous force) and S_{Mi} includes all body forces and drag.

The overall momentum equation is given by the following equation (ANSYS, 2009):

$$\frac{\partial}{\partial t}\left(\rho\vec{v}\right)+\nabla.\left(\rho\vec{v}\vec{v}\right)=-\nabla p+\nabla.\left(\overline{\overline{\tau}}\right)+S_M \quad \text{……..(5.23)}$$

where, $\overline{\overline{\tau}}$ is the stress tensor (described below).

The stress tensor is given by:

$$\overline{\overline{\tau}}=\mu\left[\left(\nabla\vec{v}+\nabla\vec{v}^T\right)-\frac{2}{3}\nabla.\vec{v}I\right] \quad \text{……..(5.24)}$$

where, μ is molecular viscosity, I is the unit tensor.

5.2.2 Fluid Rheology

5.2.3 Macroscopic Particle Model

The MPM is a quasi direct numerical simulation performed over static computational cells for capturing the precise hydrodynamics of particulate flows. This model is suitable for CFD solvers based on the finite volume method, This model is implemented in Fluent using UDFs and a customized user interface.

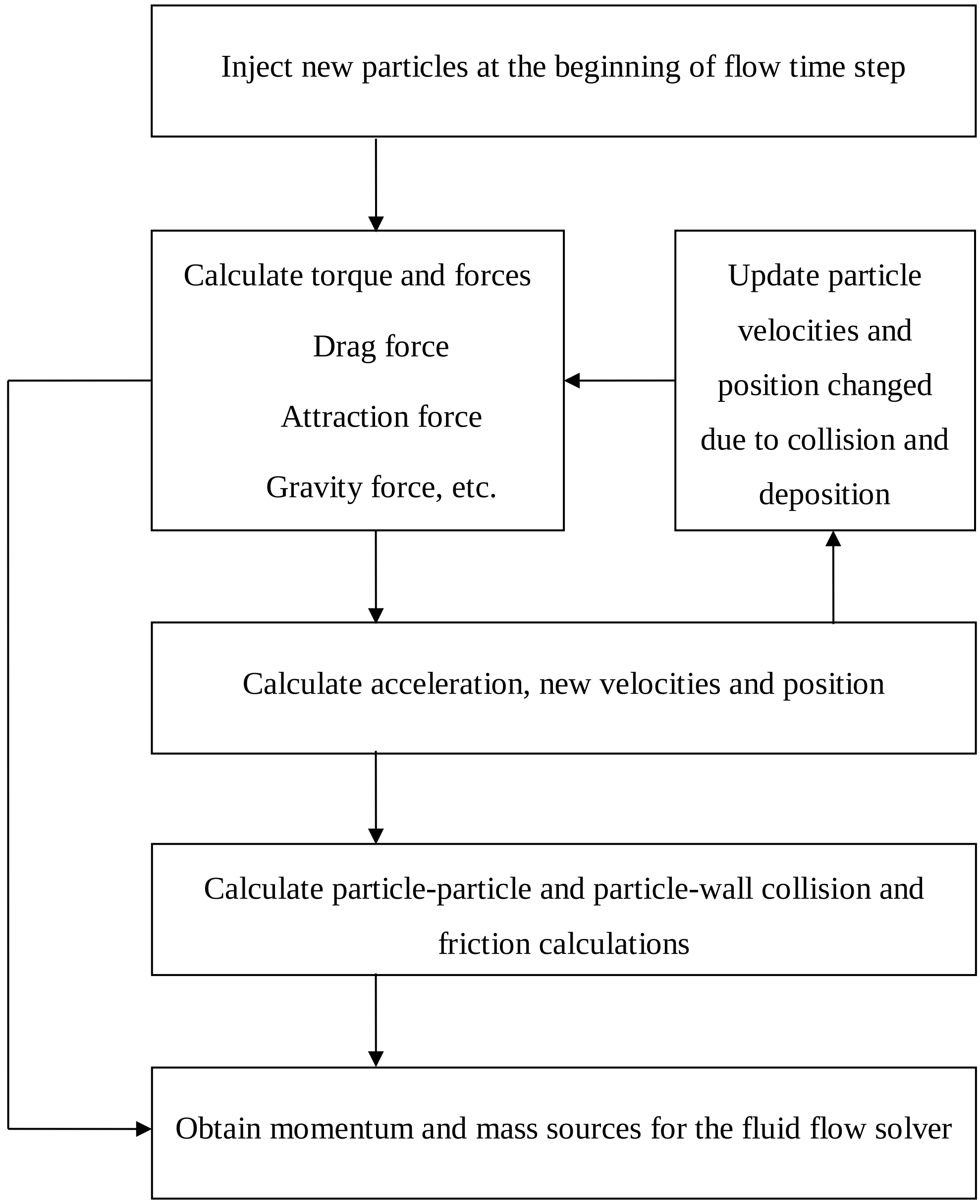

Figure 5.3. Flowchart showing calculation algorithm in MPM (Agrawal et al., 2009).

The flow chart of the calculations is shown in Figure 5.3. The model is based on the Lagrangian frame of reference in which the equations of motion are solved for the each individual particle, which are assumed to span several computational cells. Particle shape is assumed spherical. A solid body velocity that describes the particle motion (translational and rotational) is fixed in these cells to effectively transfer the momentum imparted to the liquid phase due to the particle motion. Drag and lift forces as well as the torque on the particle are explicitly calculated based on the velocity, pressure and shear stress distribution in the fluid cells around the particle. The pressure, viscous as well as the virtual mass components are included in the forces and torque calculations. The new velocity and position of the particle are calculated at each time step by taking the drag and lift forces into consideration. Cells that contain atleast one node with in the region occupied by the particle are considered as being ‘touched’ by the cell. At every time-step, a solid-body velocity that describes the particle motion is patched in the cells as shown in Figure 5.4. By patching the rigid body motion of the particle, momentum is effectively added to the fluid. For the calculation of drag between the particle and the surrounding fluid, a force balance on the particle was carried out, which consisted of viscous, pressure and virtual mass forces (Agrawal et al., 2009) .

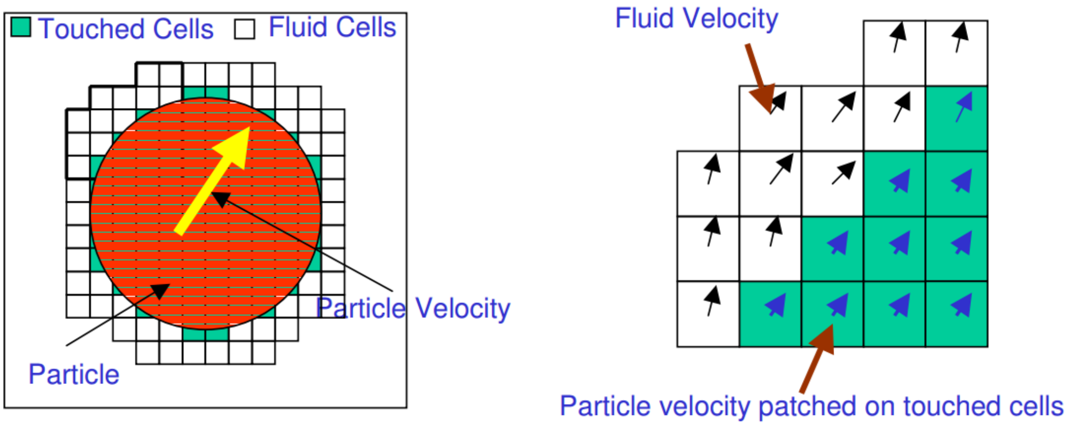

Figure 5.4. Fluid cells touched by particle and patching of particle velocity (Agrawal et al., 2004).

In MPM model, the viscous component is calculated on the basis of the shear stress distribution around the particle and is given by the equation:

$$F_{v,i} = \sum_{\substack{surface\\cells}} \sum_{j} \left[\vec{\tau}_{ji} d^2 \left(-\frac{\vec{r}.\vec{x}_j}{\left|\vec{r}.\vec{x}_j\right|} \right) \right]$$

……(5.25)

The pressure component is due to the pressure distribution in the fluid surrounding the particle. It is calculated using the nodal values of pressure in the cells surrounding the particle as given in equation (10):

$$F_{p,i} = \sum_{\substack{surface\\cells}} \left(Pd^2 \frac{\vec{r}}{\left|\vec{r}\right|}.\vec{x}_i \right)$$

……..(5.26)

Applying the momentum conservation on the system, the virtual mass component of the force on a particle is calculated. The integral of the rate of change of momentum is obtained by equation (11) considering the fluid cells within the particle volume.

$$F_{Vm,i} = \left(\sum_{\substack{\text{volume}\\\text{cells}}} m_f V_{f,i} - \sum_{\substack{\text{volume}\\\text{cells}}} m_f V_{p,i} \right) \frac{1}{\Delta t} \qquad \text{……..(5.27)}$$

The flow is governed by the usual conservation equations of mass and momentum (Equation 5.15 to 5.19) for an incompressible fluid under isothermal conditions.

5.3 Methodology

The physical domain comprised of a free falling spherical particle in quiescent Newtonian and non-Newtonian fluids without any wall effects. A structured meshed cylindrical geometry with dimensions 2 cm diameter and 6 cm height was constructed in Gambit. These cases were then simulated in FLUENT 6.1 using MPM.

Table 5.1. Details of cases simulated using MPM model.

Run	Fluid	Fluid Density (in kg / m^3)	Particle Density (in kg / m^3)	Parrticle Diameter (in mm)	Equivalent Viscosity (Pa.s)
1	A	999	8876	6.35	0.905
2	A	999	7792	6	3.015
3	A	999	7792	7.94	0.434
4	A	999	7792	8	0.66
5	A	999	7638	7.94	0.736
6	A	999	7638	9.53	0.421
7	A	999	7792	10	0.355
8	B	999	7792	8	1.698
9	B	999	7792	10	0.599
10	B	999	7638	7.94	2.093
11	B	999	7638	9.53	0.782
12	B	999	8876	6.35	3.223
13	B	999	8876	7.94	0.82
14	C	999	8000	7	2.616
15	C	999	8000	8	1.306
16	C	999	8000	9	0.8454
17	C	999	8000	10	0.6225

The carbon particles in CIL tanks are of 0.003 m diameter. For validation, the particle diameters between 0.002 m to 0.01 m and having density in the range of 7638 kg / m^3 to 8876 kg / m^{-3} were investigated. The particles were initially positioned right at the centre of the domain to minimize any impact due to walls. With all these parameters defined, the MPM model was initiated by injecting the particles in a similar way as in DPM.

Both Newtonian and non-Newtonian cases having a constant fluid density of 999 kg / m^3 and same “equivalent viscosity” were studied. In non-Newtonian fluids, it was defined using the Herschel-Bulkley model and for the Newtonian case, the equivalent viscosity of the fluid was calculated using the method of Wilson et al. (2003). The non-Newtonian fluids chosen for the simulations had similar rheological properties as that of slurry in CIL tanks as analysed by Osan (1990). The simulations were conducted using three fluids. The H-B parameters for Fluid A were τ_h= 16.0635, K_h= 1.4219 and n=0.5434, Fluid B were τ_h= 20.0589, K_h= 1.5198 and n=0.5374, and fluid C were τ_h= 18.1359, K_h= 1.7133 and n=0.566. The details of cases simulated is tabulated in Table 5.1.

Before running simulations with the non-Newtonian method, initial simulations were run for different grid sizes, time steps and domain size for a Newtonian fluid.

5.4 Results and Discussions

5.4.1 Effect of Simulation Parameters

Figure 5.5(a) shows the initial position of a spherical particle with a diameter of 0.01m falling in the domain under the effect of gravity. Since there was no other force acting on the particle, it moved down along the axis without any lateral deviation. The particle also imparted momentum to the fluid in its vicinity. A longitudinal cross-section of the velocity contours during the fall is shown in Figure 5.5(b).

The velocity at each time-step was noted and the simulation was run until the terminal velocity reached a plateau. The velocity versus time data for d_p = 0.00635 m is plotted in Figure 5.6. The rate of change of particle velocity was initially high and as the particle approached near the terminal velocity, it asymptotically reached zero.

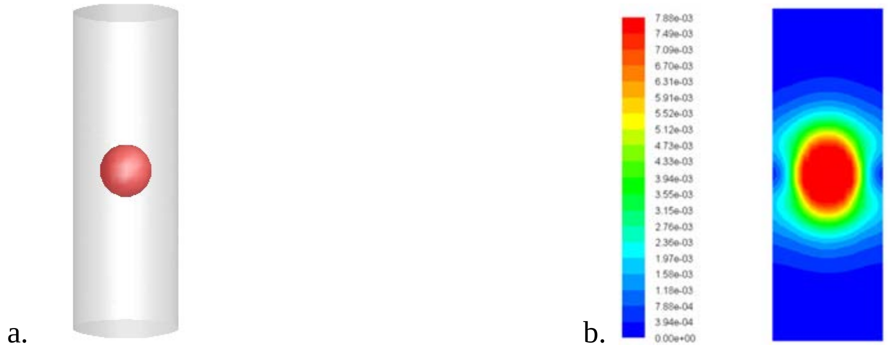

Figure 5.5. (a) Initial position of the particle. (b) Contours of fluid velocity around the particle.

In order to ensure the simulation results are independent of the time-step size, simulations were conducted with various time-step sizes ranging between 10^{-3} and 10^{-5} s (see Figure 5.7). A larger time-step consumes less computational power but its accuracy is low, but on the other hand, the lower time steps although rendered more accuracy, they need very high computational power and time. As can be seen from Figure 4, the time step of 10^{-3} s showed a greater deviation in the terminal velocities from the values calculated using the Stokes law as compared to those with the time step sizes of 10^{-4} s and 10^{-5} s, both of which provided very similar results. Therefore, a time-step size of 10^{-4} s was considered as optimum for the rest of this study.

Similarly, simulations were conducted to study the effect of grid size on model predictions. In the MPM, a high number of grid points per particle can provide more accurate results at the expense of increased computational requirements. So, it becomes necessary to find an optimum grid resolution without compromising the numerical accuracy. Figure 5.8 shows that all three grid resolutions gave nearly similar results. Therefore, it may be concluded that for this study, a mesh having 10 grid-points per particle was adequate as higher grid points per particle only resulted in higher computational requirements without any considerable improvement in the accuracy. Therefore, for the remaining simulations in this study a mesh with 10 grid-points per particle was used.

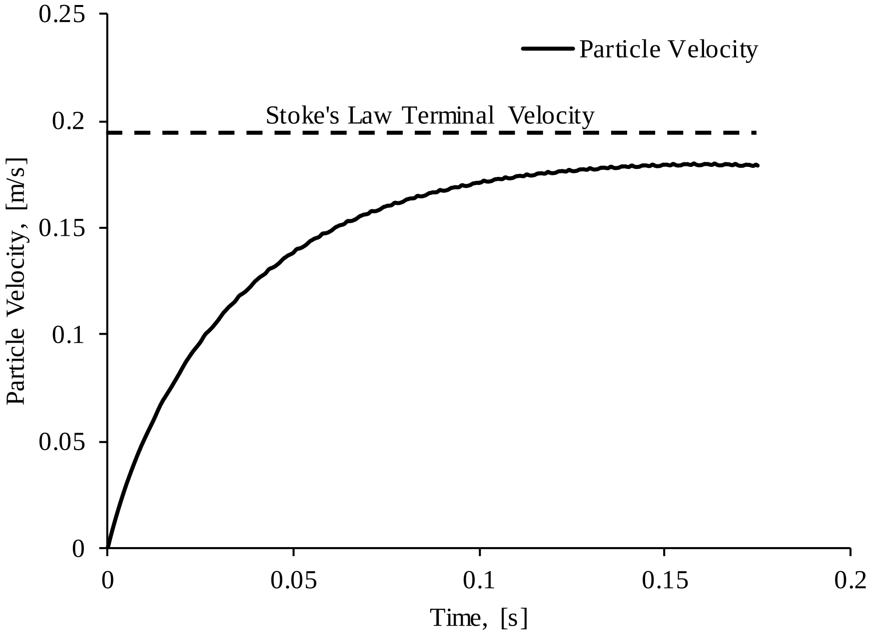

Figure 5.6. Particle velocity as a function of time ($\rho_p = 8876$ kg/m^3, $\rho_f = 999$ kg/m^3, $\mu = 0.905$ Pa.s, $d_p = 0.00635$ m).

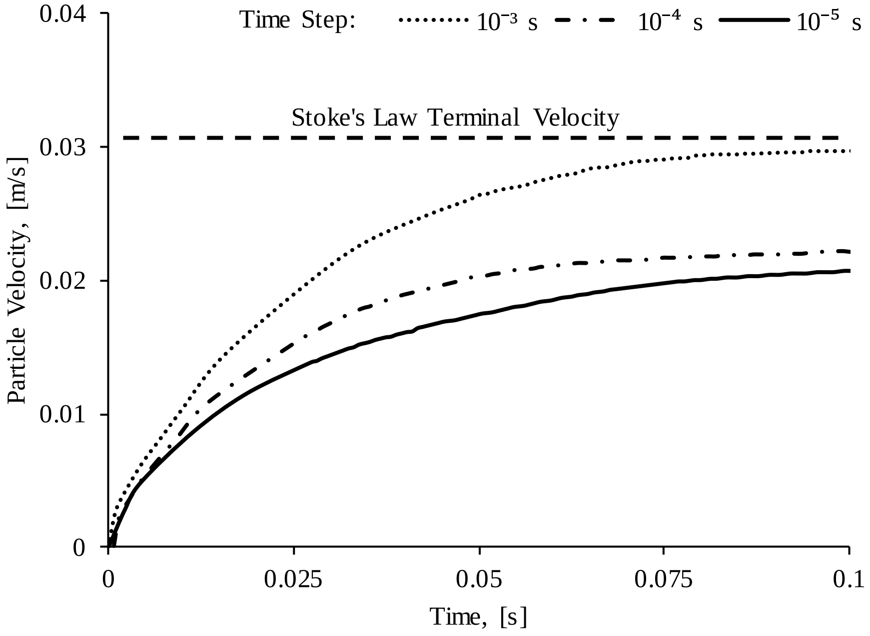

Figure 5.7. Effect of time-step size on simulation predictions ($\rho_p = 1550$ kg/m^3, $\rho_f = 999$ kg/m^3, $\mu = 1$ Pa.s, $d_p = 0.01$ m).

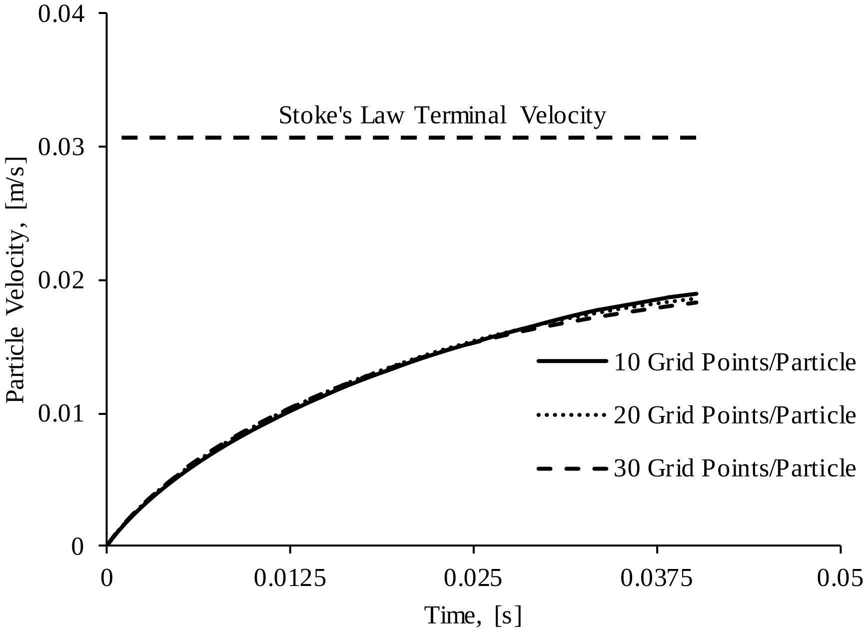

Figure 5.8. Effect of mesh size on simulation predictions (ρ_p = 1550 kg/m^3, ρ_f= 999 kg/m^3, μ = 1 Pa.s, d_p=0.01 m).

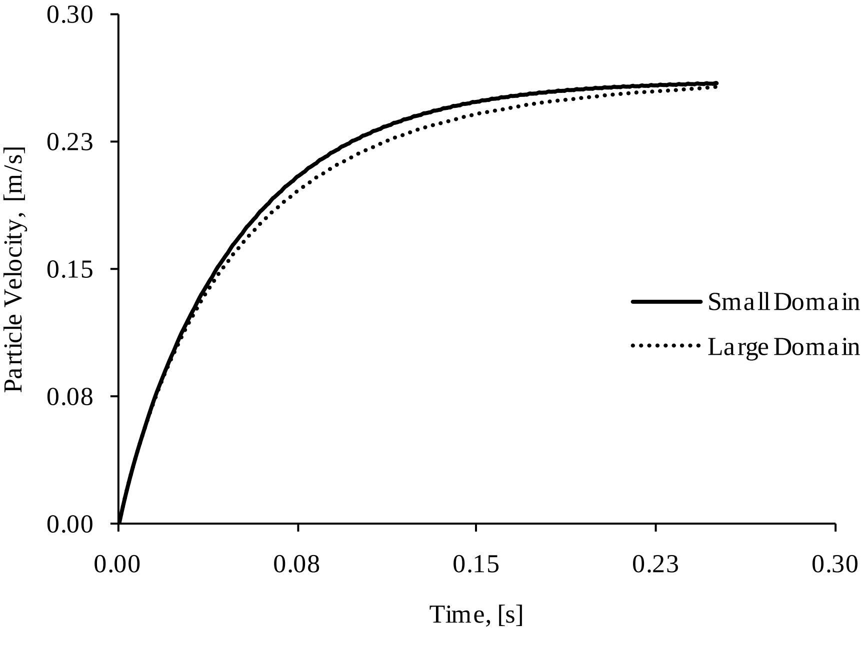

Figure 5.9. Effect of domain extent on the particle velocity prediction for Newtonian Fluids (ρ_p = 7638 kg/m^3, ρ_f = 999 kg/m^3, μ = 0.736 Pa.s, d_p = 0.00794 m).

Attapattu (1990) showed that the domain size may affect the motion of falling bodies in pseudoplastic fluid. Therefore, the vessel walls were treated as pressure outlets to avoid the effect of the wall on the motion of falling sphere, and simulations were conducted to study the effect of domain size. Figure 5.9 compares the velocity profile of a particle in a Newtonian fluid inside a 2 cm diameter cylindrical domain (D-2cm, H- 6cm) with a relatively larger cuboidal domain (L-5cm, W-5cm, H-15cm). It is clear that increasing the domain size did not have any noticeable effect on the velocity profiles as the RMS error between the two curves was only 0.0061. The maximum allowable error is 5% of 0.3 i.e. 0.015. Therefore, the error in the result is within tolerable limits. Larger domain had over half a million grid points as compared to 26000 for smaller domain. Larger domain used 20 times more computational time producing same result as smaller domain. Therefore, for the simulation of particles in the Newtonian fluid the smaller domain was adequate, as it required significantly less computational power as compared to the larger domain which had over half a million grid points.

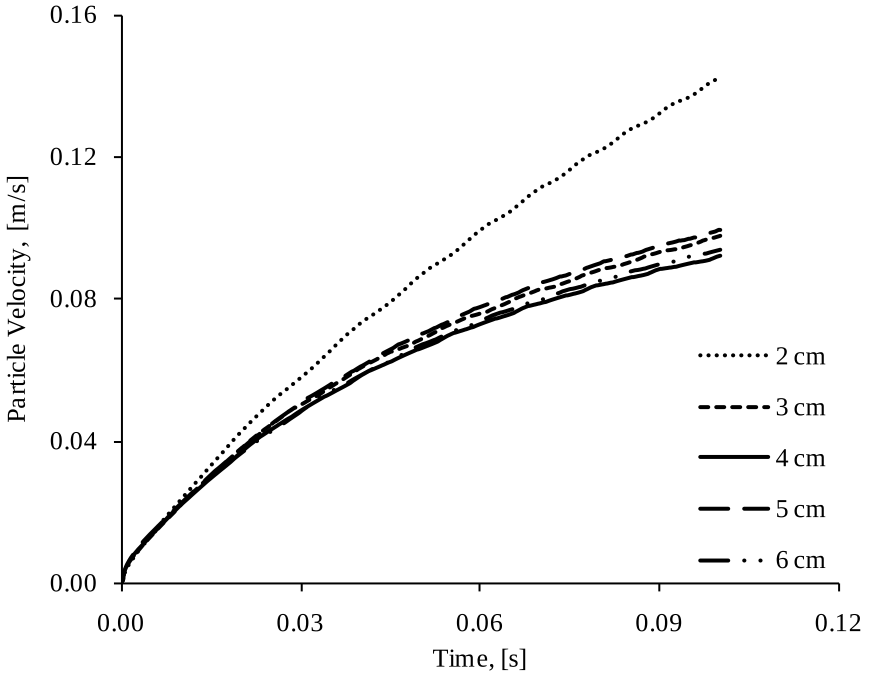

Figure 5.10. Effect of domain extent on the particle velocity prediction for Non-Newtonian Fluids ($\rho_p = 7638$ kg/m^3, $\rho_f = 999$ kg/m^3, $d_p = 0.00794$ m).

As shown in Figure 5.10, similar simulations were performed for the motion of particles in non-Newtonian fluids which showed a very high sensitivity towards the change in the domain size. Cuboid domains having a fixed height of 15 cm with widths (and depths) of 2cm, 3cm, 4 cm, 5cm and 6cm were investigated. From the Figure 5.10, the overprediction of velocity in domains with width and depth of 2 cm when compared with the larger domains is evident. The smaller domain does not provide enough clearance diametrically around the particle to resolve the flow. Increasing the cross-sectional area of domain solves this problem. So, all the domains with widths and depths greater than 4cm gave nearly identical results. Therefore, for simulations using non-Newtonian fluids, larger domains must be used. Therefore, for the remaining simulations for non-

Newtonian fluids in this study, a cuboidal domain with 4 cm width and depth (L-4 cm, W-4 cm, H15 cm) was used.

5.4.2 Comparison with Experimental Data

The simulations for non-Newtonian fluids were conducted using the operating conditions from Wilson et al. (2003). Two different fluids with different rheologies were taken into consideration, and were modelled using the Herschel-Bulkley model. The Herschel-Bulkley parameters for Fluid A were τ_h= 16.0635, K_h= 1.4219 and n=0.5434, and that of Fluid B were τ_h= 20.0589, K_h= 1.5198 and n=0.5374.The main difference in these two fluids was the yield stress a particle has to overtake in order to move. With these parameters, Fluid B would always be more viscous for any similar instance but would also have a higher rate of decrease of viscosity than Fluid A once the yield stress is overcome.

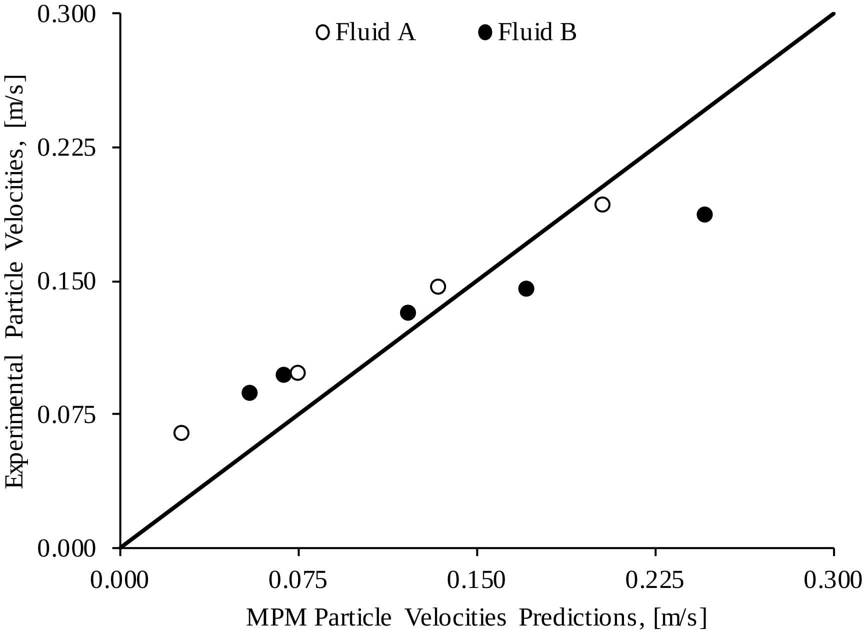

Figure 5.11. The Validation of terminal velocity predictions for Non-Newtonian Fluids by MPM model with the experimental values provided by Wilson et. al. (2003).

Simulated terminal velocities in these two fluids were plotted (see Figure 5.11) against the experimental results of Wilson et al. (2003). Since most of the simulated data points lie in the vicinity of the diagonal line, it may be concluded that the MPM approach was adequate for predicting the motion of particles in non-Newtonian fluids. As can be seen from the graph, that for the larger terminal velocities, the model is over-predicting the terminal velocity and the deviation is increasing with the increasing velocities. The possible reason for the deviation might be the inapplicability of the model under certain conditions such as particle diameter, etc. Therefore, further simulations were conducted for the variation in prediction with particle diameter.

5.4.3 Effect of Particle Diameter on Terminal Velocity in Newtonian Fluids

As can be seen in Figure 5.12, that for particle diameters of 0.009 m and less, there was a reasonable agreement between the MPM predictions of terminal velocity and those calculated using Stokes law. A further increase in the diameter resulted in a deviation from the calculated value. This deviation shows the inapplicability of MPM model for particles greater than 0.009 m. However, the size of the carbon particles used in CIL tanks is around 2 to 3 mm. This size is well within the range in which the MPM model is applicable. Therefore, although the MPM model is applicable for a certain range, still it is useful and accurate for the predictions to be used in the study of drag.

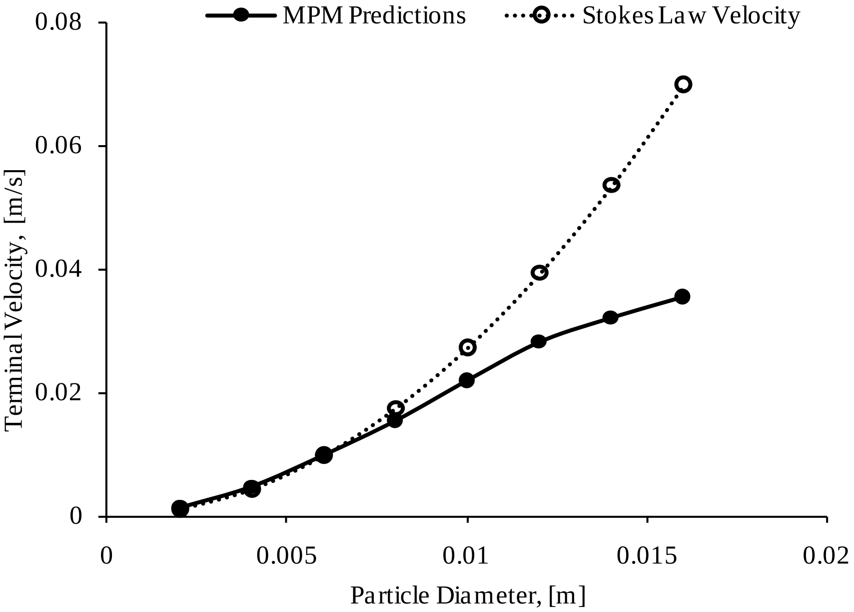

Figure 5.12. Variation in terminal velocity predictions with particle diameter for Newtonian fluids ($\rho_p = 1500$ kg/m^3, $\rho_f = 999$ kg/m^3, $\mu = 1$ Pa.s).

5.4.4 Effect of Particle Diameter, Particle Density and Fluid Properties on Terminal Velocity in non-Newtonian Fluids

To further test the applicability of the MPM model in non-Newtonian fluids, other parameters of the simulation were varied and analysed whether it shows the expected behaviour or not. The simulations were conducted using three fluids. The H-B parameters for Fluid A were τ_h= 16.0635, K_h= 1.4219 and n=0.5434, Fluid B were τ_h= 20.0589, K_h= 1.5198 and n=0.5374, and fluid C were τ_h= 18.1359, K_h= 1.7133 and n=0.566. Fluid A and fluid B had similar properties except the difference in their yield stress values. Fluid C had an intermediate yield stress, but is different in terms of consistency index and power law index. With the increase in shear stress, its shear rate increases rapidly and therefore, it had more dominant shear thinning. Particles of different diameters were dropped in fluid A and Fluid C and their terminal velocities were plotted in Figure 5.13.

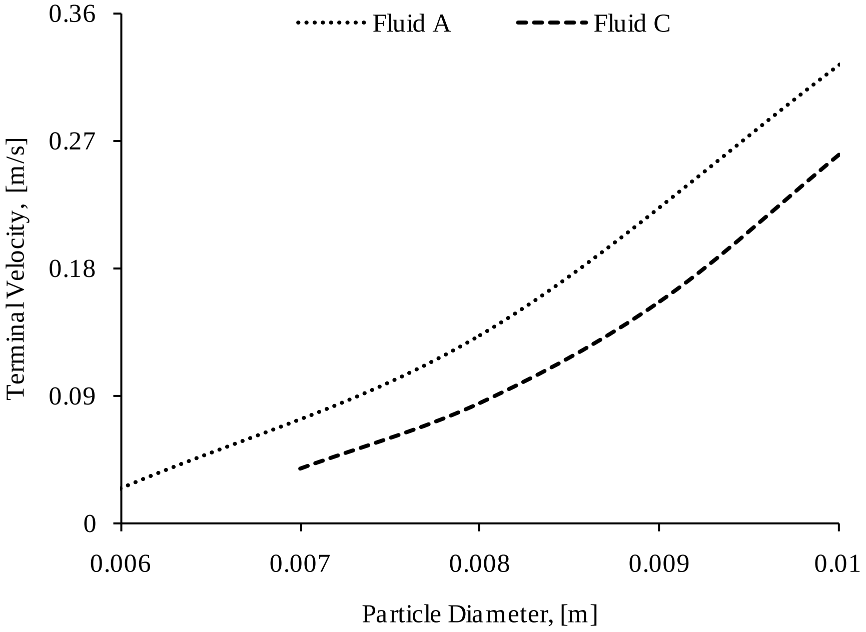

Figure 5.13. The Comparison of velocity predictions for the non-Newtonian fluids and their variation with particle diameter. (ρ_f = 999 kg/m3).

As expected, the terminal velocity in all three cases increased with the particle diameter which is consistent with the experimental results of Reynolds and Jones (1989). Moreover, since the apparent viscosity in the case of fluid C will always be greater than that of fluid A, therefore a higher drag is expected to result in slower motion of particles. The particle when suspended in fluid A showed a higher terminal velocity when compared to that in fluid C under the same conditions. This prediction shows that the local calculation of force is consistent in MPM and is accurate even if fluid with different property is used in domain. It means that although the fluid properties are changed, the influence of force applied on the particle can be calculated accurately using the pressure and viscous forces around the particle.

Both particle diameter and density directly contribute to the shear applied to the fluid. It is, therefore, expected that an increase in density should also result in an increase in terminal velocity. Expected results were obtained when only the particle densities were changed and the velocities were compared for particles having the same diameter falling in fluid B (see Figure 5.14). It was observed that the increase in particle density had a similar influence on the velocities to that of particle diameter.

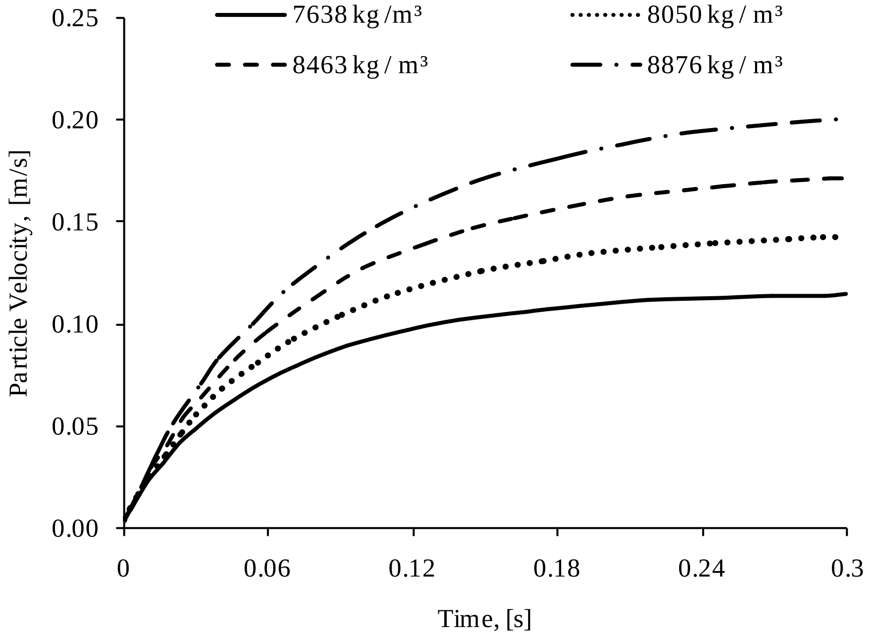

Figure 5.14. The Comparison of velocity predictions for the non-Newtonian fluids and their variation with fluid properties. (d_p = 0.00794 m, ρ_f = 999 kg/m3, µ = 0.736 Pa.s)

5.4.5 Comparison of Fall Velocities for Newtonian and Non-Newtonian Fluids

Wilson et al. (2003) conducted experiments using non-Newtonian fluids and evaluated an “equivalent viscosity” for predicting the particle terminal velocities. Using the same constant viscosity value and fluid density, simulations were conducted for the Newtonian fluid as well. The plots for the velocities were compared and are shown in Figure 5.15. The terminal velocity in case of the non-Newtonian fluids were significantly lower when compared to the corresponding Newtonian fluid. It was possibly because of the presence of high viscosity due to the yield stress of viscoplastic fluid in the undisturbed fluid. The increase of the velocity of particle results in the shear thinning of the fluid, due to which, the apparent viscosity surrounding the sphere decreased and a bounded region of finite viscosity was formed. As a result, the rate of displacement increased, and gradually the velocity of the sphere reached to a terminal velocity. The rate of this process was slower when compared with the constant viscosity case of Newtonian fluids.

For the same ‘equivalent viscosity’, the Newtonian fluid should predict same terminal velocity as that of non-Newtonian fluids. This reason for such a disparity can be determined by examining the drag experienced by particles in both the cases.

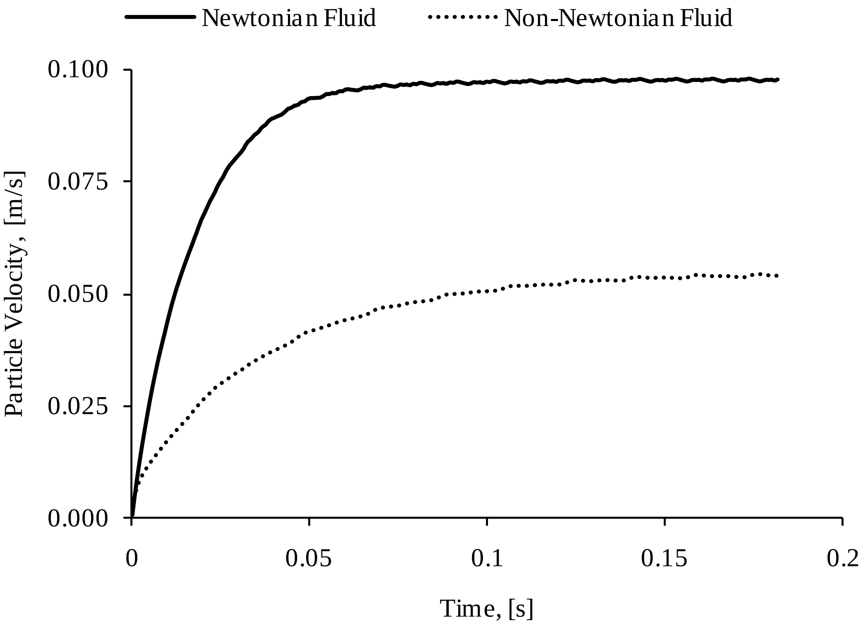

Figure 5.15. Sphere free fall velocity in non-Newtonian and Newtonian fluid with corresponding equivalent viscosity (2.093 Pa. s).

5.4.6 Comparison of Drag Coefficient for Newtonian and Non-Newtonian Fluids

The drag coefficient in the case of Newtonian fluids was compared with the drag coefficient from an earlier study (Turton and Levenspiel, 1986) and the corresponding drag coefficient of non-Newtonian fluids. The calculated drag coefficient at the terminal velocity of the each particle was plotted as a function of the Re number. It is clear from Figure 5.16 that the predictions for the terminal velocities in the case of Newtonian fluids were in close agreement with those calculated using the correlation of Turton and Levenspiel given in Equation 5.4. However, it can be observed that the drag experienced by the particles in non-Newtonian fluids were far greater than that for Newtonian fluids with ‘equivalent viscosity’. Therefore, a new drag model needs to be proposed that can predict the drag experienced by the particle in non-Newtonian fluids by using the properties of Newtonian fluids with ‘equivalent viscosity’. This drag model will, therefore, be directly applicable in the multiphase simulation of carbon particle in CIL tanks.

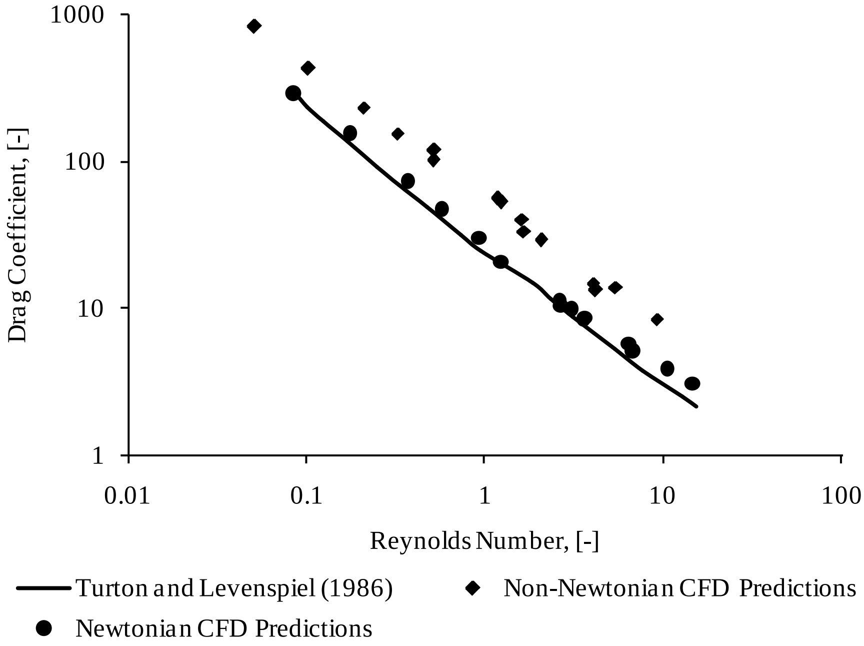

Figure 5.16. Drag coefficient as a function of particle Reynolds number.

Table 5.2. Results from the cases simulated using MPM model.

Run	Terminal Velocity		Drag force	Drag Coefficient	Reynolds Number
	Newtonian	Non-Newtonian			
1	0.179133	0.074284	0.007943	92.81181	0.507543
2	0.043127	0.025524	0.006145	696.297	0.048632
3	0.396877	0.202408	0.016259	16.0844	3.805808
4	0.294473	0.132946	0.01336	30.20258	1.602396
5	0.25946	0.114964	0.013383	33.61762	1.47885
6	0.468488	0.246183	0.025488	11.80843	5.746477
7	0.539141	0.324026	0.029777	7.333747	9.53489
8	0.123255	0.06787	0.014527	126.406	0.31154
9	0.395624	0.245771	0.02708	11.42775	4.149461
10	0.097621	0.054403	0.013824	188.8739	0.201534
11	0.146	0.322	0.021925	21.26044	2.066808
12	0.051364	0.074034	0.008461	664.939	0.054715
13	0.273264	0.121202	0.015549	42.79724	1.167099
14	0.065523	0.038827	0.010234	361.4348	0.099293
15	0.155588	0.085421	0.014428	78.75481	0.496895
16	0.29107	0.156735	0.020073	25.71408	1.58563
17	0.42757	0.261315	-	-	-

5.5 Drag model

The MPM has provided reasonable results, and it can be used for the modelling drag coefficient that can be applied in the multiphase simulation of CIL tanks. As is described in the first chapter, the ore and carbon particles are simultaneously present in the CIL tanks. The drag on carbon particles will be much more than that experienced by the ore particles because of the presence of high concentration of ore particles. The drag experienced by carbon particles is calculated by treating the slurry as a non-Newtonian fluid. The drag is, then, modelled on the basis of the method used by Attapatu (1989), so that it is applicable when the carbon particles are present in Newtonian fluid and ore particles.

The MPM model calculates the value of drag force using the equations given in section 5.3. However, the drag force on a spherical particle is given as:

$$F_D = C_D\left(\rho V^2/2\right)\left(A_p\right) \qquad \text{……..(5.28)}$$

where C_D is the drag coefficient, ρ is the liquid density, A_p is the projected area of particle in the plane perpendicular to the flow direction.

The value of drag coefficient is calculated by using the drag force and terminal velocity calculated by MPM simulations. The Reynolds number is calculated as is calculated for Power law fluids. The Reynolds number is defined as:

$$\mathrm{Re}_{PL} = \frac{d_p^n V^{2-n}\rho}{K_h} \qquad \text{……..(5.29)}$$

The drag coefficient was related to a factor Q, that was dependent on Reynolds number and Bingham number, (Bi_{HB}). Atapattu (1989) defined Bingham number as:

$$Bi_{HB} = \frac{\tau_o^h}{K_h(V/d)^n} \qquad \text{……..(5.30)}$$

and Q was defined as:

$$Q = \frac{\mathrm{Re}_{PL}}{1+\frac{7\pi}{24}Bi_{HB}} \qquad \text{……..(5.31)}$$

The drag coefficient from a number of cases with different particle diameter and rheological characteristics studied is plotted against the Reynolds number. The nature of the scatter indicates a log-log relationship between the two. Therefore, a graph with logarithmic axes is plotted (Figure 5.17). The relationship between drag coefficient and Q given by Atapattu (1989) is as follows:

$$C_D = \frac{24}{Q} \quad \text{……..(5.32)}$$

However, the model under-predicted the drag coefficient with maximum deviations between experimental data and predictions for the cases studied in the chapter were 24%. The under-prediction was found to increase with the increasing Reynolds number and therefore, the equation did not hold good for Q greater than 1. This is apparently because the model proposed by Atapattu (1989) was based on data with value of Q less than 1. The relationship was remodeled and the error was reduced to 15%. The new relationship between Q and C_D is given below:

$$C_D = \frac{24}{Q}\left(1 + 0.15Q^{0.5813}\right) \quad \text{……..(5.33)}$$

This drag model can be used for the simulation of carbon particles in ore filled slurry.

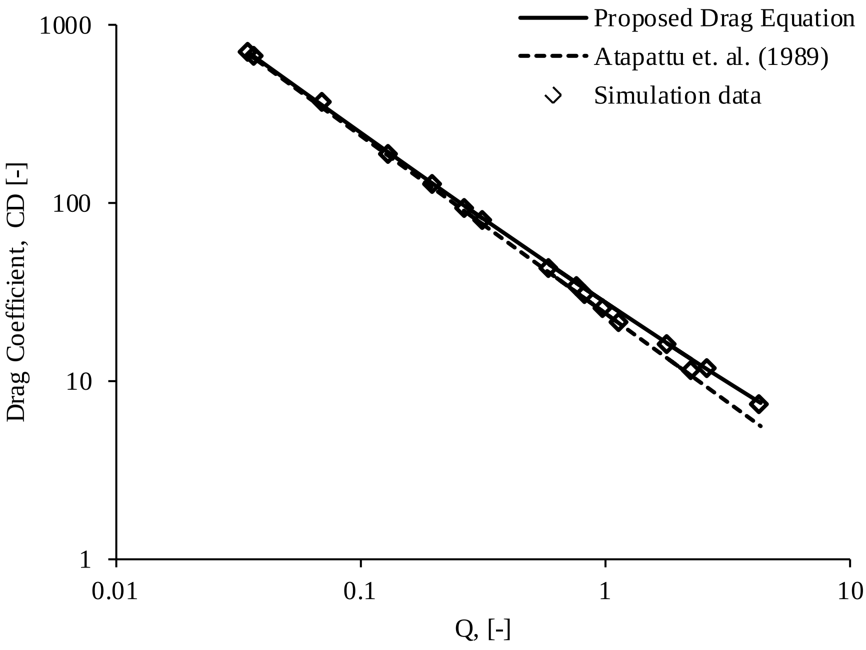

Figure 5.17. Drag coefficient versus Reynolds number for a range of particle and fluid properties.

5.6 Conclusion

In this chapter, a drag model was proposed for the carbon particles that can be used in the Eulerian-Eulerian simulation of stirred tank. For obtaining the drag force, a novel macroscopic particle model (MPM) based on RDPM approach was used after validation. Drag and lift forces as well as the torque on the particle were explicitly calculated based on the velocity, pressure and shear stress distribution in the fluid cells around the particle. The motion of particles in Newtonian and non-Newtonian fluids have been investigated and the experimental values of terminal velocities were used for validation. The rheological parameters of Wilson et al. (2003) were fitted into the Herschel - Bulkley model. The simulation results were assessed for the effect of time step, domain size and grid points per particle. A time-step size of 10^{-4} s and grid size consisting of 10 grid points per particle were found to be adequate. Domains with a diameter of at least twice the particle diameter in Newtonian case and four times in the case of non-Newtonian fluid were required to alleviate the effect of bounded region. The predictions from the MPM model were compared with available experimental data (Wilson et al., 2003). It was found that MPM model over predicted the fall velocity of particle with a diameter greater than 0.009 m. It was also observed that the particle velocities for Newtonian fluids were greater than those in the case of non-Newtonian fluids for the same ‘equivalent viscosity’, as higher drag is observed by the particles in non-Newtonian fluids. The drag results of the simulations were validated using the experimental data from the literature (Turton and Levenspiel, 1986). Based on the increased drag observed for non-Newtonian fluids, a new drag model was proposed. This drag model can be used for more detailed hydrodynamic simulations of ore and carbon particles in stirred tank along with a modified Brucato drag model for ores.

Chapter 6 Closure

The objectives of the thesis as stated in Chapter 1 were to develop a full mechanistic phenomenological model of Carbon-in-Leach series using first principles method, gain insight of the hydrodynamics in CIL tanks and develop a drag model that can be used in simulating large carbon particles in CIL tanks. To achieve the objectives, a phenomenological model of the CIL circuit was modelled and simulated. Effect of critical model parameters was investigated for improving the performance of the CIL circuit. Simulations were also conducted to understand the hydrodynamics of CIL stirred tanks. Due to lack of consensus on the appropriate drag model, simulation results using different drag models were compared. The flow in CIL tanks was simulated using the most appropriate drag model. The flow of carbon particles in CIL tanks is affected by the ore particles. Appropriate drag models are necessary that account this interaction. Therefore, a drag model was formulated that can appropriately evaluate the drag observed by the carbon particles. The conclusions derived from these studies are summarised below:

6.1.1 Phenomenological Modelling of Carbon in Leach Circuit

A dynamics phenomenological model to simulate the performance of CIL circuit was developed. Comprehensive kinetics for for the cyanidation and adsorption reactions were used. . The parameters of leaching rate were fitted to match the Mintek rate data. The model was validated by comparing the results of dynamic simulations with the literature data. The validated model was used for investigating the effect of critical parameters. The conclusions from the study are listed below:

a) The particle size and cyanide concentration are critical for the gold leaching. Decrease in the particle size and increase in cyanide concentration results in an increase in the efficiency of the process.
b) Oxygen concentration did not show significant effect on the efficiency.
c) The residence time and the number of tanks are interrelated. The current study shows the increase in the recovery with the increase in residence time and the number of tanks.
d) Increased recovery with increased carbon transfer interval is obtained. The increased carbon transfer interval may result in increased capital costs if the tank configurations are changed. Low carbon transfer interval incurs higher operating costs.

6.1.2 Hydrodynamic Simulation of CIL Tanks

Four different drag models were evaluated for use in CIL tanks. The validated drag model was used for the study of the flow field, velocity components, slip velocity and turbulence for radial and axial flow impellers. The conclusions from the study are listed below:

a) The turbulence dispersion force had negligible effect at a low volume fraction of solids.
b) Axial, radial and tangential velocities were compared at different axial locations for the four drag models. All four models could qualitatively capture the flow in stirred tanks.
c) Results from the modified Brucato drag model were in reasonable agreement for the liquid flow fields.
d) Maximum turbulence kinetic energy was found in the impeller zone. The turbulence dampens with the increase in the solids concentration and this effect was the most significant in this zone.
e) The cloud height and homogeneity were found to increase with an increase in impeller speed. For achieving homogeneity at low loading stirred tanks, a low impeller speed is adequate.

f) Modified Brucato drag model worked well up to the particle concentration of 20 wt% and a Reynolds number of 1.91×10^5. The predictions of the drag model deviated while predicting the velocity components of cases with higher solid concentration (40 wt %) due to an under - prediction of the drag.

g) The increased solid concentration substantially changed the flow field. The ‘false bottom effect’ at very high solid concentration results in higher velocity values compared to moderate solid concentration cases.

h) High slip velocities were found below the impeller, near the wall and near the impeller rod for PBTD. The magnitude of slip velocities increased due to increase in solid concentration.

i) Dampening of turbulence was dominant due to the presence of particles. At higher concentration, significant power is required to counteract the dampening and for the dispersion of solids.

j) The use of axial flow impellers with high impeller rotation speed is recommended for CIL tanks.

k) The velocities higher than Zweitering’s correlation will be required for the complete suspension of particles.

l) Multiple impellers may be required for maintaining high turbulence and high slip velocities in the system.

6.1.3 Macroscopic Particle Model and Drag Formulation for Carbon Particles

The CIL tanks are bidisperse systems containing large carbon particles and small ore particles. The MPM model was used to simulate carbon particles in the ore slurry after validation. The simulation results were assessed for the effect of time step, domain size and grid points per particle. A drag formulation was devised that can be applied in the E-E simulations along with ore particles and liquid in stirred tank system from the data obtained from the MPM simulation. The conclusions from the study are listed below:

a) For obtaining the drag force, a novel macroscopic particle model (MPM) based on RDPM approach was used after validation.

b) A time-step size of 10^{-4} s and grid size consisting of 10 grid points per particle were found to be adequate.

c) Domains with a diameter of at least twice the particle diameter in Newtonian case and four times in the case of non-Newtonian fluid were required to alleviate the effect of bounded region.
d) The predictions from the MPM model were compared with available experimental data (Wilson et al., 2003). It was found that MPM model over predicted the fall velocity of particle with a diameter greater than 0.009 m.
e) The particle velocities for Newtonian fluids were greater than those in the case of non-Newtonian fluids for the same ‘equivalent viscosity’, as higher drag is observed by the particles in non-Newtonian fluids.
f) The drag results of the simulations were validated using the experimental data from the literature (Turton and Levenspiel, 1986). Based on the increased drag observed for non-Newtonian fluids, a new drag model was proposed.

6.2 Recommendations for future work

During the course of research, the following areas have been identified as worthy of further research:

a) Phenomenological modeling

The current thesis carried out significant work in the development, validation and parametric study for CIL circuits. The output parameters from the hydrodynamic simulations such as extent of homogeneity or residence time can be incorporated explicitly in the phenomenological model.

b) Hydrodynamic Simulations

The simulations presented in the thesis provided insight of the hydrodynamics in CIL tanks. This in-depth understanding is essential for the development of Distributed parameter models, based on the actual flow fields in the mixing tanks. This model will need to take into account the extent of mixing in different regions of CIL tanks. Since, the extent of mixing will vary with the scale-up and in the presence of carbon particles, its modeling in an industrial scale CIL tanks will be a challenging task. Moreover, it will require simulation of industrial scale CIL tank using Modified Brucato drag model and the drag model for carbon particles.

The output from such study can be used for the continual improvement of the phenomenological model. Research on the lines of these recommendations can form the basis of another PhD study.

Appendix I. MATLAB Code for Phenomenological Model

```
function CILtanks = Tanks6Sim(t,y)
CILtanks = zeros(24,1);    % a column vector
C = zeros(6,1);
G = zeros(6,1);
Q = zeros(6,1);
CN = zeros(6,1);
carb = zeros(6,1);
vfc = zeros(6,1);
vfo = zeros(6,1);
W = zeros(6,1);
M = zeros(6,1);
Csc = zeros(6,1);
Cso = zeros(6,1);
Leach = zeros(6,1);
Ads = zeros(6,1);
Preg = zeros(6,1);
Cyan = zeros(6,1);
dCdt = zeros(6,1);
dGdt = zeros(6,1);
dQdt = zeros(6,1);
dCNdt = zeros(6,1);

k = mod (t,43200);

if ((k <= 900 || k > 42300) && t > 3600)
        Qs = 750/3600;
        Qf = 0;
else
        Qf=750/3600;
        Qs = 0;
end

Qfs=Qf+Qs;

V=750;
```

```
% Particles properties
ROc=900;
ROo=2550;
dc=0.0014;
dav = 30; %75;

% Initial values
C1=0;  %6;
Q6=0.0;
oxy = 28;  %28;
CN1 = 280;  %280;
G1=0.001;

vfl=0.75;

%Constants for isotherms
A=18.5;
B=4.65;
a=2.4;
%b=0;%0.64;
%c=0;%2.4;
%d=0.64;
Dj=0.2;
mj=0.1;

% Constants for leaching reactions
kf1=0.00001;
kau1=1;
kau2 = 2.28*10^-10;
theta = 2.93;
alpha = 2.13;
beta = 0.961;
gamma = 0.228;
Auinf = 0.0357*(1-1.49*exp(-0.0176*dav));
kau = 0.00513*(kau1 - kau2*dav.^theta);
```

```
% Constants for cyanide dissolving reactions
kcn1 = 1.69*10^-8;
kcn2 = 6.4;
phi = 0.547;
kcn = kcn1/(dav^phi-kcn2);

% Constants for pregrobbing reactions
kp1=0.0;%0.00000002;
%kp2=0;%0.00000002;

% y[1] = Gold concentration in liquid
% y[2] = Gold concentration on ore
% y[3] = Gold concentration on carbon
% y[4] = Cynide concentration in liquid
for i = 1: 6

     C(i) = y(4*i-3);
     G(i) = y(4*i-2);
     Q(i) = y(4*i-1);
     CN(i) = y(4*i);
     carb(i)=25; % 11.5 and 12
     vfc(i)=carb(i)/ROc;
     vfo(i)=1-(vfl+vfc(i));
     W(i)=V*carb(i);
     M(i)=vfo(i)*V*ROo;
     Csc(i) = (Q(i)*B)/((A-a*Q(i))*B);
     if Csc(i)>C(i)
          Csc(i) = C(i);
     end
     Cso(i) = (G(i)/Dj).^(1/mj);

end

for i = 1:6


%Reaction rate equations for leaching
```

```
Leach(i) = (M(i)*(kau*(G(i)*1000-Auinf).^alpha*CN(i).^beta*oxy
.^gamma))/(3600000);

%Reaction rate equations for adsorption
Ads(i) = 6*kf1*W(i)*(C(i)-Csc(i))/(ROc*dc);

%Reaction rate equations for pregrobbing
Preg(i) = 6*kp1*M(i)*(C(i)-Cso(i))/(ROo*(dav/1000000));

%Reaction rate equations for cyanide consumption
Cyan(i) = kcn*((CN(i))^3.71);

     if (i == 1)
          QfsIn = Qf+Qs ;
          QfsOut = Qfs  ;
          QsOut = Qs    ;
          Qsin = Qs    ;
          vfcIn = vfc(i+1);
          vfoIn1 = vfo(i) ;
          vfoIn2 = vfo(i+1) ;
          Cin1 = C1;
          Cin2 = C(i+1);
          Gin1 = G1;
          Gin2 = G(i+1);
          CNin1 = CN1  ;
          CNin2 = CN(i+1);
          Qin = Q(i+1);
     elseif (i == 6)
          QfsIn = Qfs ;
          QfsOut = Qf ;
          QsOut = Qs  ;
          Qsin = 0    ;
          vfcIn = vfc(i);
          vfoIn1 = vfo(i-1) ;
          vfoIn2 = 0;
          Cin1 = C(i-1);
          Cin2 = 0;
```

```
          Gin1 = G(i-1);
          Gin2 = 0;
          CNin1 = CN(i-1) ;
          CNin2 = 0;
          Qin = Q6;
     else
          QfsIn = Qfs ;
          QfsOut = Qfs  ;
          QsOut = Qs  ;
          Qsin = Qs    ;
          vfcIn = vfc(i+1);
          vfoIn1 = vfo(i-1) ;
          vfoIn2 = vfo(i+1) ;
          Cin1 = C(i-1);
          Cin2 = C(i+1);
          Gin1 = G(i-1);
          Gin2 = G(i+1);
          CNin1 = CN(i-1) ;
          CNin2 = CN(i+1);
          Qin = Q(i+1);
     end


dCdt(i)   =   (vfl*QfsIn*Cin1/(vfl+vfoIn1)+vfl*Qsin*Cin2/(vfl+
vfoIn2)-vfl*(QfsOut+QsOut)*C(i)/(vfl+vfo(i))+Leach(i)-Ads(i)-
Preg(i))/(vfl*V);

dGdt(i) = (vfoIn1*QfsIn*ROo*Gin1/(vfl+vfoIn1)+vfoIn2*Qsin*ROo*
Gin2/(vfl+vfoIn2)-vfo(i)*(QfsOut+QsOut)*ROo*G(i)/(vfl+vfo(i))-
Leach(i)+Preg(i))/M(i);

dQdt(i) = (vfcIn*Qs*ROc*Qin-vfc(i)*Qs*ROc*Q(i)+Ads(i))/W(i);

dCNdt(i)  =  (vfl*QfsIn*CNin1/(vfl+vfoIn1)+vfl*Qsin*CNin2/(vfl+
vfoIn2)-vfl*(QfsOut+QsOut)*CN(i)/(vfl+vfo(i))-0.001*Cyan(i)*V)
/ ( vfl*V );
```

```
end

for i = 1:6
     CILtanks(4*i-3) = dCdt(i);
     CILtanks(4*i-2) = dGdt(i);
     CILtanks(4*i-1) = dQdt(i);
     CILtanks(4*i) = dCNdt(i);
end
end
```

Appendix II. UDF for Modified Brucato Drag Model

```
#include "udf.h"
#include "mem.h"
#include "stdio.h"

#define diam2 0.0003

DEFINE_EXCHANGE_PROPERTY(custom_drag,cell,mix_thread,s_col,f_c
ol)
{
 Thread *thread_g, *thread_s;
 real x_vel_g, x_vel_s, y_vel_g, y_vel_s,z_vel_g, z_vel_s,
abs_v, slip_x, slip_y, slip_z, rho_g, rho_s, rho_mix, mu_mix,
eps_mix, reyp, eps_g;
 real lemda, cdo, k_g_s, mu_nu, mu_g, void_g, drag_coeff;

 /* find the threads for the gas (primary) */
 /* and solids (secondary phases)          */

 thread_g = THREAD_SUB_THREAD(mix_thread, s_col);/* gas phase
*/
 thread_s = THREAD_SUB_THREAD(mix_thread, f_col);/* solid
phase*/

 /* find phase velocities and properties*/

 x_vel_g = C_U(cell, thread_g);
 y_vel_g = C_V(cell, thread_g);
 z_vel_g = C_W(cell, thread_g);

 x_vel_s = C_U(cell, thread_s);
 y_vel_s = C_V(cell, thread_s);
 z_vel_s = C_W(cell, thread_s);

 slip_x = x_vel_g - x_vel_s;
```

```
 slip_y = y_vel_g - y_vel_s;
 slip_z = z_vel_g - z_vel_s;

 rho_g = C_R(cell, thread_g);
 rho_s = C_R(cell, thread_s);
 rho_mix = C_R(cell, mix_thread);

 mu_mix = C_MU_EFF(cell, mix_thread);

 mu_g = C_MU_L(cell, thread_g);

 eps_g = C_D(cell, thread_g);

 void_g = C_VOF(cell, thread_g);/* gas vol frac*/

 /*compute slip*/
 abs_v = sqrt(slip_x*slip_x + slip_y*slip_y + slip_z*slip_z);

 /*compute Reynold's number*/
 reyp = rho_g*abs_v*diam2/mu_g;

 /*kinematic viscosity calculation*/
 mu_nu = mu_mix/rho_mix;

 /*compute Kolmogorov length scale*/
 lemda = pow((pow(mu_nu,3)/eps_g), 0.25);

 /* compute Cdo */
 cdo = 24*(1+0.15*pow((void_g*reyp),0.687))/(reyp*void_g);
 drag_coeff = (8.76*pow(10,-5)*pow((diam2/lemda),3)+1)*cdo;
 k_g_s = drag_coeff*3*rho_g*(1-void_g)*abs_v*abs_v/(4*diam2);

 return k_g_s;
}
```

References

Adams, M. D. (1990). "The mechanism of adsorption of aurocyanide onto activated carbon, 1. Relation between the effects of oxygen and ionic strength." Hydrometallurgy **25**(2): 171-184.

Adams, M. D., et al. (1992). "The mechanism of adsorption of Au(CN)4- onto activated carbon." Hydrometallurgy **31**(3): 265-275.

Adams, M. D., et al. (1987). "Models for the adsorption of aurocyanide onto activated carbon. Part III: Comparison between the extraction of aurocyanide by activated carbon, polymeric adsorbents and 1-pentanol." Hydrometallurgy **19**(1): 95-115.

Agrawal, M., et al. (2004). Macroscopic Particle Model- Tracking Big Partcles in CFD. AIChE 2004 Annual Meeting, Austin, Texas, USA.

Agrawal, M., et al. (2009). Drag Force Formulation in Macroscopic Particle Model and Its Validation. The Proceedings of AiChE 2009 Annual Meeting, Nashville, TN, http://apps.aiche.org/proceedings.

Ahmed, F. E., et al. (1992). "Comparison and modelling of the adsorption kinetics of gold cyanide onto activated carbon and resin in a silica slurry." Hydrometallurgy **30**(1-3): 257-275.

Altway, A., et al. (2001). "Effect of Particle Size on Simulation of Three-Dimensional Solid Dispersion in Stirred Tank." Chemical Engineering Research and Design **79**(8): 1011-1016.

Angst, R. and M. Kraume (2006). "Experimental investigations of stirred solid/liquid systems in three different scales: Particle distribution and power consumption." Chemical Engineering Science **61**(9): 2864-2870.

ANSYS (2009). Fluent User Guide, ANSYS Inc.: Canonsburg, PA, www. fluent. com.

Atapattu, D. D. (1995). "Creeping sphere motion in Herschel-Bulkley fluids: flow field and drag." Journal of non-Newtonian fluid mechanics **59**(2-3): 245.

Atapattu, D. D., et al. (1990). "Wall effect for spheres falling at small reynolds number in a viscoplastic medium." Journal of non-Newtonian fluid mechanics **38**(1): 31-42.

Baldi, G., et al. (1978). "Complete suspension of particles in mechanically agitated vessels." Chemical Engineering Science **33**(1): 21-25.

Barigou, M. (2004). "Particle Tracking in Opaque Mixing Systems: An Overview of the Capabilities of PET and PEPT." Chemical Engineering Research and Design **82**(9): 1258-1267.

Barresi, A. and G. Baldi (1987). "Solid dispersion in an agitated vessel." Chemical Engineering Science **42**(12): 2949-2956.

Bates, R. L., et al. (1963). "Examination of Some Geometric Parameters of Impeller Power." Industrial & Engineering Chemistry Process Design and Development **2**(4): 310-314.

Beaulne, M. and Beaulne (1997). "Creeping motion of a sphere in tubes filled with Herschel–Bulkley fluids." Journal of non-Newtonian fluid mechanics **72**(1): 55.

Beetstra, R., et al. (2006). "A lattice-Boltzmann simulation study of the drag coefficient of clusters of spheres." Computers & fluids **35**(8): 966-970.

Bittorf, K. J. and S. M. Kresta (2003). "Prediction of Cloud Height for Solid Suspensions in Stirred Tanks." Chemical Engineering Research and Design **81**(5): 568-577.

Brittan, M. (2008). "Kinetic and equilibrium effects in gold ore cyanidation." Minerals & Metallurgical Processing **25**(3): 117-122.

Brittan, M. I. (1975). "Variable activation energy model for leaching kinetics." International Journal of Mineral Processing **2**(4): 321-331.

Brucato, A., et al. (2010). "Particle suspension in top-covered unbaffled tanks." Chemical Engineering Science **65**(10): 3001-3008.

Brucato, A., et al. (1998). "Particle drag coefficients in turbulent fluids." Chemical Engineering Science **53**(18): 3295-3314.

Brunazzi, E., et al. (2004). "An Impedance Probe for the Measurements of Flow Characteristics and Mixing Properties in Stirred Slurry Reactors." Chemical Engineering Research and Design **82**(9): 1250-1257.

Brunn, P. (1982). "The motion of rigid particles in viscoelastic fluids." Journal of non-Newtonian fluid mechanics **7**(4): 271-288.

Bubbico, R., et al. (1998). "Agitation power for solid-liquid suspensions containing large particles." The Canadian Journal of Chemical Engineering **76**(3): 428-432.

Bujalski, W., et al. (1999). "Suspension and Liquid Homogenization in High Solids Concentration Stirred Chemical Reactors." Chemical Engineering Research and Design **77**(3): 241-247.

Bungay, P. M. and H. Brenner (1973). "The motion of a closely-fitting sphere in a fluid-filled tube." International Journal of Multiphase Flow **1**(1): 25-56.

Buurman, C., et al. (1986). "Scaling-up rules for solids suspension in stirred vessels." Chemical Engineering Science **41**(11): 2865-2871.

Chaouki, J., et al. (1997). "Noninvasive tomographic and velocimetric monitoring of multiphase flows." Industrial & engineering chemistry research **36**(11): 4476-4503.

Chhabra, R. P. (2003). "A note on wall effect on the terminal falling velocity of a sphere in quiescent Newtonian media in cylindrical tubes." Powder Technology **129**(1-3): 53.

Chhabra, R. P. (2006). Bubbles, drops, and particles in non-Newtonian fluids, CRC Press.

Cho, E. H., et al. (1979). "The kinetics of gold cyanide adsorption on activated charcoal." Metallurgical and Materials Transactions B **10**(2): 185-189.

Chudacek, M. W. (1985). "Solids suspension behaviour in profiled bottom and flat bottom mixing tanks." Chemical Engineering Science **40**(3): 385-392.

Coetzee, J. W. and S. Lalloo (2005). "A CIP simulation technique using excel built-in functionality." Minerals Engineering **18**(8): 845-848.

Cook, R., et al. (1989). "An XPS study of the adsorption of gold (I) cyanide by carbons." Hydrometallurgy **22**(1-2): 171-182.

Cox, R. G. and H. Brenner (1967). "The slow motion of a sphere through a viscous fluid towards a plane surface--II Small gap widths, including inertial effects." Chemical Engineering Science **22**(12): 1753-1777.

Crundwell, F. K. and S. A. Godorr (1997). "A mathematical model of the leaching of gold in cyanide solutions." Hydrometallurgy **44**(1-2): 147-162.

Cundall, P. A. and O. D. L. Strack (1979). "A discrete numerical model for granular assemblies." Geotechnique **29**(1): 47-65.

Derksen, J., et al. (1999). "Large eddy simulations on the flow driven by a Rushton turbine." AIChE Journal **45**(2): 209-221.

Derksen, J. J. (2003). "Numerical simulation of solids suspension in a stirred tank." American Institute of Chemical Engineers. AIChE Journal **49**(11): 2700-2700.

Deschenes, G., et al. (2002). "Reactions of gold and sulfide minerals in cyanide media." Minerals & Metallurgical Processing **19**(4): 169-177.

Deschenes, G. and G. Wallingford (1995). "Effect of oxygen and lead nitrate on the cyanidation of a sulphide bearing gold ore." Minerals Engineering **8**(8): 923-931.

Deventer, J. S. J. v. (1986). "Kinetic model for the reversible adsorption of gold cyanide on activated carbon." Chemical Engineering Communications **44**(1): 257.

Deventer, J. S. J. v., et al. (2004). "Dynamic modelling of a carbon-in-leach process with the regression network." Chemical Engineering Science **59**(21): 4575-4589.

Deventer, J. S. J. v. and V. E. Ross (1991). "The dynamic simulation of carbon-in-pulp systems: A review of recent developments." Minerals Engineering **4**(7-11): 667-681.

Ding, J. and D. Gidaspow (1990). "A bubbling fluidization model using kinetic theory of granular flow." AIChE Journal **36**(4): 523-538.

Dixon, S., et al. (1976). The interaction between gold cyanide, silver cyanide, and high surface area charcoal. AIChE Meeting, Chicago, IL.,.

Don Dudley, A. (1989). Sphere motion in viscoplastic fluids. Dept. of Chemical, Engineering, Monash University. **Thesis PhD**.

Elsner, L. (1946). "Über das Verhalten verschiedener Metalle in einer wässrigen Lösung von Cyankalium." J. Prakt. Chem **37**: 440-446.

Ergun, S. (1952). "Fluid flow through packed columns." Chemical Engineering Progress **48**(2): 89-94.

Evans-Pritchard, A. (2009). Barrick shuts hedge book as world gold supply runs out. Telegraph.co.uk.

Fajner, D., et al. (2008). "Solids distribution and rising velocity of buoyant solid particles in a vessel stirred with multiple impellers." Chemical Engineering Science **63**(24): 5876-5882.

Falkovich, G. and K. R. Sreenivasan (2006). "Lessons from hydrodynamic turbulence." Physics Today **59**: 43.

Fan, L., et al. (2005). "Numerical simulation of turbulent solid-liquid two-phase flow and orientation of slender particles in a stirred tank." Chemical Engineering Science **60**(24): 7045-7056.

Felice, R. d. (1996). "A relationship for the wall effect on the settling velocity of a sphere at any flow regime." International Journal of Multiphase Flow **22**(3): 527-533.

Ferreira, P. J., et al. (1994). "A new approach to measuring solids concentration in mixing tanks." Advanced Powder Technology **5**(1): 15-24.

Finkelstein, N. P. (1972). "The chemistry of the extraction of gold from its ores." Gold Metallurgy on the Witwatersrand, South Africa, Adamson, RJ (Ed.), Cape and Transvaal Printers Ltd, Cape town.

Fleming, C. A. and M. J. Nicol (1984). "The absorption of gold cyanide onto activated carbon. Ill. Factors influencing the." Journal of the South African Institute of Mining and Metallurgy: 85.

Fleming, C. A., et al. (1980). The optimization of a carbon-in-pulp adsorption circuit based on the kinetics of extraction of aurocyanide by activated carbon.

Flemmer, R. and C. Banks (1986). "On the drag coefficient of a sphere." Powder Technology **48**(3): 217-221.

Fletcher, D. F. and G. J. Brown (2009). "Numerical simulation of solid suspension via mechanical agitation: effect of the modelling approach, turbulence model and hindered settling drag law." International journal of computational fluid dynamics **23**(2): 173-187.

Fradette, L., et al. (2007). "CFD phenomenological model of solid-liquid mixing in stirred vessels." Computers & Chemical Engineering **31**(4): 334-345.

Geisler, R. K., et al. (1993). "Scale-up of the necessary power input in stirred vessels with suspensions." The Chemical Engineering Journal **51**(1): 29-39.

Goodall, W. R., et al. (2005). "A new method for determination of preg-robbing in gold ores." Minerals Engineering **18**(12): 1135-1141.

Guha, D. (2007). Hydrodynamics and Mixing in Single Phase and Liquid-Solid Stirred Tank Reactors. Department of Energy, Environmental and Chemical Engineering. Missouri, Washington University**:** 211.

Guha, D. (2008). "Evaluation of large Eddy simulation and Euler-Euler CFD models for solids flow dynamics in a stirred tank reactor." American Institute of Chemical Engineers. AIChE Journal **54**(3): 766-778.

Guha, D., et al. (2007). "Flow field of suspended solids in a stirred tank reactor by Lagrangian tracking." Chemical Engineering Science **62**(22): 6143-6154.

Guida, A., et al. (2009). "Positron emission particle tracking in a mechanically agitated solid-liquid suspension of coarse particles." Chemical Engineering Research and Design **87**(4): 421-429.

Guida, A., et al. (2010). "PEPT measurements of solid-liquid flow field and spatial phase distribution in concentrated monodisperse stirred suspensions." Chemical Engineering Science **65**(6): 1905-1914.

Guiraud, P., et al. (1997). "Local measurements of fluid and particle velocities in a stirred suspension." Chemical Engineering Journal **68**(2-3): 75-86.

Guo, H., et al. (2005). "Leaching kinetics and mechanisms of surface reactions during cyanidation of gold in the presence of pyrite or stibnite." Minerals and Metallurgical Processing **22**(2): 89-95.

Guzman, L., et al. (1999). "Electrochemistry of conventional gold cyanidation." Electrochimica Acta **44**(15): 2625-2632.

Guzman, L., et al. (1999). "Gold cyanidation using hydrogen peroxide." Hydrometallurgy **52**(1): 21-35.

Habashi, F. (1966). "The theory of cyanidation." Transactions of the Society of Mining Engineers of AIME **235**: 236-239.

Haider, A. (1989). "Drag coefficient and terminal velocity of spherical and nonspherical particles." Powder Technology **58**(1): 63.

Hoef, M. A. v. d., et al. (2008). "Numerical Simulation of Dense Gas-Solid Fluidized Beds: A Multiscale Modeling Strategy." Annual Review of Fluid Mechanics **40**(1): 47-70.

Hosseini, S., et al. (2010). "Study of solid-liquid mixing in agitated tanks through electrical resistance tomography." Chemical Engineering Science **65**(4): 1374-1384.

Ibrado, A. S. and D. W. Fuerstenau (1992). "Effect of the structure of carbon adsorbents on the adsorption of gold cyanide." Hydrometallurgy **30**(1-3): 243-256.

Ibrahim, S. and A. W. Nienow (1999). "Comparing Impeller Performance for Solid-Suspension in the Transitional Flow Regime with Newtonian Fluids." Chemical Engineering Research and Design **77**(8): 721-727.

Jeffrey, M. I. and I. M. Ritchie (2001). "The Leaching and Electrochemistry of Gold in High Purity Cyanide Solutions." Journal of the Electrochemical Society **148**(4): D29-D36.

Jenne, M. and M. Reuss (1999). "A critical assessment on the use of k–ε turbulence models for simulation of the turbulent liquid flow induced by a Rushton-turbine in baffled stirred-tank reactors." Chemical Engineering Science **54**(17): 3921-3941.

Jia, Y. F., et al. (1998). "Mechanism of adsorption of gold and silver species on activated carbons." Carbon **36**(9): 1299-1308.

Jones, R. L. and R. R. Horsley (2000). "Viscosity Modifiers in the Mining Industry." Mineral Procesing and Extractive Metallurgy Review **20**(1): 215-223.

Jordi, R. G., et al. (1991). "Gold adsorption on activated carbon and the effect of suspended solids and dissolved silicon dioxide." Chemical Engineering Communications **102**(1): 127-147.

Kasat, G. R., et al. (2008). "CFD simulation of liquid-phase mixing in solid-liquid stirred reactor." Chemical Engineering Science **63**(15): 3877-3885.

Kelessidis, V. C. and Kelessidis (2004). "An explicit equation for the terminal velocity of solid spheres falling in pseudoplastic liquids." Chemical Engineering Science **59**(21): 4437.

Kelessidis, V. C. and G. Mpandelis (2004). "Measurements and prediction of terminal velocity of solid spheres falling through stagnant pseudoplastic liquids." Powder Technology **147**(1-3): 117-125.

Khopkar, A. R., et al. (2006). "Computational Fluid Dynamics Simulation of the Solid Suspension in a Stirred Slurry Reactor." Industrial & Engineering Chemistry Research **45**(12): 4416-4428.

Kiranoudis, C. T., et al. (1998). "Modelling and optimization of carbon-in-pulp gold recovery processs." IMA J Management Math **9**(1): 35-54.

Kiranoudis, C. T., et al. (1998). "Modelling and optimization of carbon-in-pulp gole recovery processs." IMA J Management Math **9**(1): 35-54.

Kondos, P. D., et al. (1995). "Process optimization studies in gold cyanidation." Hydrometallurgy **39**(1-3): 235-250.

Kongolo, K., et al. (1997). "Electrophoretic studies of the adsorption of gold and silver from aqueous cyanide solutions onto activated carbon." Hydrometallurgy **44**(1-2): 191-202.

Kraume, M. (1992). "Mixing times in stirred suspensions." Chemical Engineering & Technology **15**(5): 313-318.

Lagerge, S., et al. (1999). "Comparative Study on the Adsorption of Cyanide Gold Complexes onto Different Carbonaceous Samples: Measurement of the Reversibility of the Process and Assessment of the Active Surface Inferred by Flow Microcalorimetry." Langmuir **15**(14): 4803-4811.

Lane, G. L., et al. (2005). "Numerical modelling of gas and liquid flow in stirred tanks." Chemical Engineering Science **60**(8): 2203-2214.

Lavezzo, V., et al. (2009). "Ekman pumping and intermittent particle resuspension in a stirred tank reactor." Chemical Engineering Research and Design **87**(4): 557-564.

Le Roux, J. D., et al. (1991). "A comparison of several kinetic models for the adsorption of gold cyanide onto activated carbon." Journal of the South African Institute of Mining and Metallurgy **91**(3): 95-103.

Lima, L. R. P. and D. Hodouin (2005). "Optimization of reactor volumes for gold cyanidation." Minerals Engineering **18**(7): 671-679.

Lima, L. R. P. d. A. (2006). "Some remarks on the reactor network synthesis for gold cyanidation." Minerals Engineering **19**(2): 154-161.

Lima, L. R. P. d. A. (2007). "Dynamic Simulation of the Carbon-in-pulp and Carbon-in-leach Processes." Brazilian Journal of Chemical Engineering **24**(4): 623-635.

Lima, L. R. P. d. A. and D. Hodouin (2005). "A lumped kinetic model for gold ore cyanidation." Hydrometallurgy **79**(3-4): 121-137.

Lima, L. R. P. d. A. and D. Hodouin (2006). "Simulation study of the optimal distribution of cyanide in a gold leaching circuit." Minerals Engineering **19**(13): 1319-1327.

Lin, H. K. and X. Chen (2001). "Electrochemical study of gold dissolution in cyanide solution." Minerals and Metallurgical Processing(USA) **18**(3): 147-153.

Ling, P., et al. (1996). "An improved rate equation for cyanidation of a gold ore." Canadian Metallurgical Quarterly **35**(3): 225-234.

Ljungqvist, M. and A. Rasmuson (2001). "Numerical Simulation of the Two-Phase Flow in an Axially Stirred Vessel." Chemical Engineering Research and Design **79**(5): 533-546.

Ljungqvist, M. and A. Rasmuson (2004). "The Two-Phase Flow in an Axially Stirred Vessel Investigated Using Phase-Doppler Anemometry." The Canadian Journal of Chemical Engineering **82**(2): 275-288.

Mabrouk, R., et al. (2007). "Effective drag coefficient investigation in the acceleration zone of an upward gas–solid flow." Chemical Engineering Science **62**(1–2): 318-327.

MacTaggart, R. S., et al. (1993). "A conductivity probe for measuring local solids concentration in a slurry muxing tank." Separations Technology **3**(3): 151-160.

Madhav, G. V. and R. P. Chhabra (1994). "Settling velocities of non-spherical particles in non-Newtonian polymer solutions." Powder Technology **78**(1): 77-83.

Magelli, F., et al. (1990). "Solid distribution in vessels stirred with multiple impellers." Chemical Engineering Science **45**(3): 615-625.

Mark, A. O. (1990). The rheological and mineralogical characteristics of Western Australian gold ore slurries and the effectiveness of viscosity modifiers by Mark A. Osan, Thesis MEng--Curtin University of Technology.

Marsden, J. and I. House (2006). The chemistry of gold extraction, Society for Mining Metallurgy.

McDougall, G. J., et al. (1980). "The Mechanism of the Adsorption of Gold Cyanide on Activated Carbon." Journal of the South African Institute of Mining and Metallurgy **80**(9): 344-356.

Micale, G., et al. (2002). "Assessment of Particle Suspension Conditions in Stirred Vessels by Means of Pressure Gauge Technique." Chemical Engineering Research and Design **80**(8): 893-902.

Micale, G., et al. (2004). "CFD Simulation of Particle Suspension Height in Stirred Vessels." Chemical Engineering Research and Design **82**(9): 1204-1213.

Micale, G., et al. (2000). "CFD Simulation of Particle Distribution in Stirred Vessels." Chemical Engineering Research and Design **78**(3): 435-444.

Micheletti, M. (2003). "Particle Concentration and Mixing Characteristics of Moderate-to-Dense Solid- Liquid Suspensions." Industrial & Engineering Chemistry Research **42**(24): 6236-6236.

Micheletti, M., et al. (2004). "On Spatial and Temporal Variations and Estimates of Energy Dissipation in Stirred Reactors." Chemical Engineering Research and Design **82**(9): 1188-1198.

Micheletti, M. and M. Yianneskis (2004). "Study of fluid velocity characteristics in stirred solid-liquid suspensions with a refractive index matching technique." Proceedings of the Institution of Mechanical Engineers, Part E: Journal of Process Mechanical Engineering **218**(4): 191-204.

Montante, G., et al. (2001). "Experiments and CFD Predictions of Solid Particle Distribution in a Vessel Agitated with Four Pitched Blade Turbines." Chemical Engineering Research and Design **79**(8): 1005-1010.

Montante, G., et al. (2003). "Scale-up criteria for the solids distribution in slurry reactors stirred with multiple impellers." Chemical Engineering Science **58**(23-24): 5363-5372.

Murthy, B. N. and J. B. Joshi (2008). "Assessment of standard , RSM and LES turbulence models in a baffled stirred vessel agitated by various impeller designs." Chemical Engineering Science **63**(22): 5468-5495.

N. Sharma, R. and A. A. Shaikh (2003). "Solids suspension in stirred tanks with pitched blade turbines." Chemical Engineering Science **58**(10): 2123-2140.

Nasr-El-Din, H. A., et al. (1996). "Local solids concentration measurement in a slurry mixing tank." Chemical Engineering Science **51**(8): 1209-1220.

Nguyen, A. V. (1997). "An improved formula for terminal velocity of rigid spheres." International Journal of Mineral Processing **50**(1-2): 53.

Nicol, M. J. (1980). "The Anodic Behaviour of Gold. II.--Oxidation in Alkaline Solutions." Gold Bulletin **13**(3): 105-111.

Nicol, M. J., et al. (1984). "The absorption of gold cyanide onto activated carbon. II: Application of the kinetic model to multistage absorption circuits." Journal of the South African Institute of Mining and Metallurgy **84**(3): 70-78.

Nicol, M. J., et al. (1984). "Absorption of Gold Cyanide onto Activated Carbon: I. The Kinetics of Absorption from Pulps." Journal of the South African Institute of Mining and Metallurgy **84**(2): 50-54.

Nouri, J. M. and J. H. Whitelaw (1992). "Particle velocity characteristics of dilute to moderately dense suspension flows in stirred reactors." International Journal of Multiphase Flow **18**(1): 21-33.

Ochieng, A. and A. E. Lewis (2006). "CFD simulation of solids off-bottom suspension and cloud height." Hydrometallurgy **82**(1-2): 1-12.

Ochieng, A. and A. E. Lewis (2006). "Nickel solids concentration distribution in a stirred tank." Minerals Engineering **19**(2): 180-189.

Ochieng, A. and M. S. Onyango (2008). "Drag models, solids concentration and velocity distribution in a stirred tank." Powder Technology **181**(1): 1-8.

Paul, E. L., et al. (2004). Handbook of Industrial Mixing: Science and Practice, John Wiley & Sons.

Pianko-Oprych, P., et al. (2009). "Positron emission particle tracking (PEPT) compared to particle image velocimetry (PIV) for studying the flow generated by a pitched-blade turbine in single phase and multi-phase systems." Chemical Engineering Science **64**(23): 4955-4968.

Pinelli, D., et al. (2004). "Dispersion coefficients and settling velocities of solids in slurry vessels stirred with different types of multiple impellers." Chemical Engineering Science **59**(15): 3081-3089.

Rasteiro, M. G., et al. (1994). "Modelling slurry mixing tanks." Advanced Powder Technology **5**(1): 1-14.

Rees, K. L. and J. S. J. v. Deventer (2000). "The mechanism of enhanced gold extraction from ores in the presence of activated carbon." Hydrometallurgy **58**(2): 151-167.

Rees, K. L. and J. S. J. v. Deventer (2000). "Preg-robbing phenomena in the cyanidation of sulphide gold ores." Hydrometallurgy **58**(1): 61-80.

Rees, K. L. and J. S. J. v. Deventer (2001). "Gold process modelling. I. Batch modelling of the processes of leaching, preg-robbing and adsorption onto activated carbon." Minerals Engineering **14**(7): 753-773.

Rees, K. L., et al. (2001). "Gold process modelling. II. The effect of ore type on leaching and adsorption dynamics at telfer gold mine." Minerals Engineering **14**(8): 887-900.

Resources, N. (2010). PHOTO: Nevsun's Bisha Mining in Eritrea Tefsea News. http://www.tesfanews.net/archives/874, Nevsun Resources Ltd.

Reuter, M. A., et al. (1991). "The application of knowledge-based systems to the simulation of gold extraction processes." Minerals Engineering **4**(2): 103-119.

Reynolds, P. A. and T. E. R. Jones (1989). "An experimental study of the settling velocities of single particles in non-Newtonian fluids." International Journal of Mineral Processing **25**(1-2): 47-77.

Rieger, F. (2002). "Effect of particle content on agitator speed for off-bottom suspension." Chemical Engineering and Processing **41**(4): 381-384.

Roy, S., et al. (2002). "Optimal design of radioactive particle tracking experiments for flow mapping in opaque multiphase reactors." Applied Radiation and Isotopes **56**(3): 485-503.

Sardeshpande, M. V., et al. (2011). "Solid suspension in stirred tanks: UVP measurements and CFD simulations." The Canadian Journal of Chemical Engineering **89**(5): 1112-1121.

Sardeshpande, M. V., et al. (2009). "Solid Suspension and Liquid Phase Mixing in Solid-Liquid Stirred Tanks." Industrial & engineering chemistry research **48**(21): 9713-9713.

Sbrizzai, F., et al. (2006). "Direct numerical simulation of turbulent particle dispersion in an unbaffled stirred-tank reactor." Chemical Engineering Science **61**(9): 2843-2851.

Schubert, J. H., et al. (1993). "Performance evaluation of a carbon-in-pulp plant by dynamic simulation." Journal of the South African Institute of Mining and Metallurgy **93**(11/12): 293-299.

Senanayake, G. (2005). "Kinetics and reaction mechanism of gold cyanidation: Surface reaction model via Au(I)-OH-CN complexes." Hydrometallurgy **80**(1-2): 1-12.

Sessiecq, P., et al. (1999). "Solid Particles Concentration Profiles in an Agitated Vessel." Chemical Engineering Research and Design **77**(8): 741-746.

Shamlou, P. A. and E. Koutsakos (1989). "Solids suspension and distribution in liquids under turbulent agitation." Chemical Engineering Science **44**(3): 529-542.

Spidla, M., et al. (2005). "Solid particle distribution of moderately concentrated suspensions in a pilot plant stirred vessel." Chemical Engineering Journal **113**(1): 73-82.

Stange, W. (1991). "The optimization of the CIP process using mathematical and economic models." Minerals Engineering **4**(12): 1279-1295

Stevenson, R., et al. (2010). "Analysis of partial suspension in stirred mixing cells using both MRI and ERT." Chemical Engineering Science **65**(4): 1385-1393.

Tamburini, A., et al. (2009). "Dense solid-liquid off-bottom suspension dynamics: Simulation and experiment." Chemical Engineering Research and Design **87**(4): 587-597.

Turton, R. and N. N. Clark (1987). "An explicit relationship to predict spherical particle terminal velocity." Powder Technology **53**(2): 127-129.

Turton, R. and O. Levenspiel (1986). "A short note on the drag correlation for spheres." Powder Technology **47**(1): 83-86.

Unadkat, H., et al. (2009). "Application of fluorescent PIV and digital image analysis to measure turbulence properties of solid-liquid stirred suspensions." Chemical Engineering Research and Design **87**(4): 573-586.

Vegter, N. M. (1992). "The distribution of gold in activated carbon during adsorption from cyanide solutions." Hydrometallurgy **30**(1-3): 229-242.

Versteeg, H. K. and W. Malalasekera (1995). An Introduction to CFD. The Finite Volume Method, Longman, London.

Virdung, T. and A. Rasmuson (2007). "Measurements of Continuous Phase Velocities in Solid-Liquid Flow at Elevated Concentrations in a Stirred Vessel Using LDV." Chemical Engineering Research and Design **85**(2): 193-200.

Wadsworth, M. E. (2000). "Surface processes in silver and gold cyanidation." International Journal of Mineral Processing **58**(1-4): 351-368.

Wadsworth, M. E., et al. (2000). "Gold dissolution and activation in cyanide solution: kinetics and mechanism." Hydrometallurgy **57**(1): 1-11.

Walt, T. J. v. d. and J. S. J. v. Deventer (1992). "Non-ideal behaviour in counter-current in-pulp adsorption cascades." Minerals Engineering **5**(10-12): 1401-1420.

Walton, O. R. (1993). Numerical simulation of inelastic, frictional particle-particle interactions, Chap. **25:** 884-911.

Wen, C. Y. and Y. H. Yu (1966). Mechanics of Fluidization.

Wichterle, K. (1988). "Conditions for suspension of solids in agitated vessels." Chemical Engineering Science **43**(3): 467-471.

Wilson, K. C., et al. (2003). "Direct prediction of fall velocities in non-Newtonian materials." International Journal of Mineral Processing **71**(1-4): 17-30.

Woollacott, L., et al. (1990). "Towards more effective simulation of CIP and CIL processes. 1. A modelling of adsorption and leaching." Journal of the South African Institute of Mining and Metallurgy **90**(10): 275-282.

Woollacott, L. C. and G. N. d. Guzman (1993). "The combined influence of oxygen and cyanide on adsorption isotherms in carbon-based gold extraction systems." Minerals Engineering **6**(3): 251-265.

Wu, J., et al. (2001). "Impeller Geometry Effect on Velocity and Solids Suspension." Chemical Engineering Research and Design **79**(8): 989-997.

Yamazaki, H., et al. (1986). "Concentration profiles of solids suspended in a stirred tank." Powder Technology **48**(3): 205-216.

Yamazaki, H., et al. (1992). "Measurement of local solids concentration in a suspension by an optical method." Powder Technology **70**(1): 93-96.

Zurilla, R. W., et al. (1978). "The Kinetics of the Oxygen Reduction Reaction on Gold in Alkaline Solution." Journal of the Electrochemical Society **125**: 1103.

Zwietering, T. N. (1958). "Suspending of solid particles in liquid by agitators." Chemical Engineering Science **8**(3–4): 244-253.

Every reasonable effort has been made to acknowledge the owners of copyright material. I would be pleased to hear from any copyright owner who has been omitted